

**VARIATIONAL METHODS AND APPLICATIONS FOR
TURBULENT SINGLE AND TWO-PHASE
FLUID-STRUCTURE INTERACTION**

VAIBHAV JOSHI

(B.Tech., Mechanical Engineering)

**A THESIS SUBMITTED
FOR THE DEGREE OF DOCTOR OF PHILOSOPHY
DEPARTMENT OF MECHANICAL ENGINEERING
NATIONAL UNIVERSITY OF SINGAPORE**

2018

Supervisors:

Assistant Professor Rajeev K. Jaiman

Examiners:

Professor Koh Chan Ghee

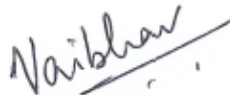
Associate Professor Tan Beng Chye, Vincent

Professor Roger Ohayon, National Conservatory of Arts and Crafts

DECLARATION

I hereby declare that this thesis is my original work and it has
been written by me in its entirety. I have duly
acknowledged all the sources of information which
have been used in the thesis.

This thesis has also not been submitted for any degree
in any university previously.

A handwritten signature in black ink, appearing to read "Vaibhav Joshi". It is written in a cursive style with a diagonal line through the end of the signature.

Vaibhav Joshi

24 May 2018

This page is intentionally left blank

Acknowledgements

I am blessed to have the presence of several people during my journey at the National University of Singapore. I would like to acknowledge their role in making my journey smooth and enjoyable. First and foremost, I would like to thank my supervisor Assistant Professor Rajeev K. Jaiman for giving me the prestigious opportunity to pursue Ph.D. under his guidance. I especially thank him for his suggestions to improve my technical writing and presentation, which is a crucial aspect of scientific research. I express my gratitude for his constructive criticism and advice which kept me motivated throughout the four years, resulting in the current piece of work.

I would like to appreciate the support I received from my friend and colleague Pardha for the meaningful discussions we had, both academic and non-academic. Discussions with him helped me to understand the intricacies of the in-house solver. I would also like to thank my friends Amit, Manali, and Smarth for providing moral support and always being there in difficult times.

I would like to emphasize the importance of a supportive family in research. You hit your highs and lows during your Ph.D., and a supportive family gives you the confidence and courage to never give up. I owe this Ph.D. to my late grandparents who taught me valuable lessons in my childhood and transformed me into the person I am today. Blessings of my parents, and love from my sister kept me working towards my goal and become successful in my endeavors in this journey.

Finally, I would like to thank the National University of Singapore, National Research Foundation and Keppel Corporation for supporting this work done in the Keppel-NUS Corporate Laboratory and providing the financial support towards the completion of the present dissertation. I would also like to acknowledge the National Supercomputing Centre, Singapore and High Performance Computing at NUS, which provided for the computational resources for the simulation performed in the current work.

This page is intentionally left blank

Contents

Summary	ix
List of Tables	xi
List of Figures	xiii
Nomenclature	xxvii
1 Introduction	1
1.1 Background and motivation	1
1.2 Objectives and methodology	3
1.3 Contributions	4
1.4 Organization of the thesis	5
2 Literature Review	7
2.1 Convection-diffusion-reaction equation	7
2.2 Two-phase flow description	11
2.3 Two-phase fluid-structure interaction	17
2.4 Turbulent flow FSI	18
2.5 Riser VIV and ship hydrodynamics	19
2.5.1 VIV of long risers	20
2.5.2 Ship hydrodynamics	22
3 The Positivity Preserving Variational Method	23
3.1 The convection-diffusion-reaction equation	23
3.1.1 Strong differential form	23

Contents

3.1.2	Semi-discrete variational form	24
3.2	The proposed method	26
3.2.1	Linear stabilization	27
3.2.2	Positivity and nonlinear stabilization	27
3.2.2.1	The positivity condition	28
3.2.2.2	Enforcement of positivity condition in one-dimension	29
3.2.2.3	Extension to multi-dimensions	34
3.2.2.4	Characteristic element length scale	37
3.3	Convergence and stability analysis	38
3.3.1	Dependence of error on the non-dimensional parameters	39
3.3.2	Two-dimensional Fourier analysis	41
3.3.3	Mesh convergence study	44
3.4	Numerical results	47
3.4.1	One-dimensional cases	47
3.4.2	Two-dimensional cases	53
3.4.3	Non-uniform unstructured and anisotropic meshes	58
3.5	Summary	62
4	Variational Fluid-Structure Framework	63
4.1	Coordinate systems	63
4.2	The Navier-Stokes equations for two-phase flow	64
4.2.1	Strong differential form	64
4.2.2	Equations in the ALE framework	65
4.2.3	Semi-discrete variational form	66
4.3	The structural equation	68
4.3.1	Strong differential form	69
4.3.2	Semi-discrete variational form	70
4.3.2.1	Rigid body	71
4.3.2.2	Linear flexible body	71
4.3.2.3	Nonlinear flexible multibodies	73
4.4	The fluid-structure interface	73

Contents

4.5	The fluid-fluid interface	73
4.6	ALE mesh motion	74
4.7	Summary	75
5	Phase-Field Formulation for Two-Phase Flows	76
5.1	Background	76
5.2	The Allen-Cahn equation	78
5.2.1	Strong differential form	78
5.2.2	Semi-discrete variational form	79
5.3	Partitioned iterative coupling for two-phase flows	82
5.3.1	Coupled linearized matrix form	82
5.3.2	Implementation details	83
5.4	Numerical tests	85
5.4.1	Verification of the Allen-Cahn implementation	85
5.4.2	Laplace-Young law	88
5.4.3	Sloshing tank problem	90
5.4.3.1	Effectiveness of the PPV technique	90
5.4.3.2	Effect of the number of elements in the equilibrium interfacial thickness (N_ε)	92
5.4.3.3	Effect of the time step size (Δt)	93
5.4.3.4	Effect of the interfacial thickness parameter (ε)	94
5.4.4	Two-dimensional dam-break problem	96
5.4.5	Three-dimensional dam-break with obstacle	98
5.5	Application to wave-structure interaction	100
5.6	Summary	107
6	Mesh Adaptive Procedure for Phase-Field Formulation	108
6.1	Adaptive variational Allen-Cahn procedure	108
6.1.1	Residual error estimates for the conservative Allen-Cahn equation	109
6.1.2	The adaptive algorithm	111
6.1.3	The nonlinear adaptive variational partitioned (NAVP) procedure	112

Contents

6.2	Convergence and performance study	114
6.2.1	Spinodal decomposition in a complex curved geometry	115
6.2.2	Volume conserved motion by curvature	117
6.2.3	Liquid sloshing in a tank	119
6.2.3.1	Background mesh convergence	119
6.2.3.2	Assessment of the nonlinear adaptive variational partitioned (NAVP) procedure	121
6.2.3.3	Advantage of the PPV technique	122
6.2.3.4	Relationship between tol_R and ε	123
6.2.3.5	Role of the interfacial thickness parameter ε	125
6.3	Application to dam-break problem	126
6.4	Summary	127
7	Two-Phase Fluid-Structure Interaction	130
7.1	The nonlinear partitioned iterative FSI coupling	130
7.1.1	Coupled linearized matrix form	131
7.1.2	Implementation details	133
7.1.3	General remarks	135
7.2	Numerical tests	136
7.2.1	Heave decay test under translation	136
7.2.2	Decay test under rotation along free-surface	140
7.3	Application to flexible riser FSI with internal two-phase flow	142
7.3.1	Amplitude response and flow patterns	145
7.3.2	Relationship between VIV and internal flow patterns	147
7.4	Summary	149
8	PPV based Hybrid RANS/LES Turbulence Application	150
8.1	Background	150
8.2	Turbulence transport equation	151
8.2.1	Strong differential form	151
8.2.2	Semi-discrete variational form	152

Contents

8.3	Flow across circular cylinder at $Re=3,900$ and $Re=140,000$	154
8.3.1	Mesh characteristics	155
8.3.2	Hydrodynamic coefficients	157
8.3.3	Flow visualization	160
8.3.4	Comparison of flow statistics	160
8.4	VIV of an offshore riser	163
8.4.1	Key fluid-structure parameters	163
8.4.2	Mesh characteristics	163
8.4.3	Amplitude response	166
8.4.4	Spectral analysis of response amplitude	169
8.4.5	Trajectory along the riser	170
8.4.6	Flow visualization	173
8.5	Summary	174
9	Application to Coupled Vessel Riser System	176
9.1	Flow across a Wigley hull	176
9.2	Ship hydrodynamics	180
9.2.1	Boundary conditions and key parameters	180
9.2.2	Mesh characteristics	181
9.2.3	Results and discussion	182
9.3	Drillship-riser system	183
9.3.1	Boundary conditions and key parameters	184
9.3.2	Mesh characteristics	186
9.3.3	Results and discussion	186
9.4	Summary	190
10	Conclusions and Recommendations	192
10.1	Concluding remarks	192
10.2	Future recommendations	193
Bibliography		195

Contents

A One-dimensional analysis of the local element matrix	217
B The positivity condition for convective transport equation	219
C Fourier analysis of the CDR equation in one-dimension	221
C.1 Semi-discrete analysis	222
C.2 Fully discrete analysis	224
D Fourier analysis of the CDR equation in two-dimensions	228
E Exact solutions of the CDR equation in one-dimension	233
F Discrete energy stability proof for the Allen-Cahn equation	234
G Discrete mass conservation for the Allen-Cahn equation	236
H Temporal accuracy of the discrete Allen-Cahn equation	238
I Residual error estimates for the Allen-Cahn equation	242

Summary

Single and two-phase fluid-structure interactions are commonly observed phenomena in industries as well as daily life. While two-phase fluid-structure interaction finds its applications ranging from small-scale droplet interactions, microstructural phase evolution, flows in oil pipelines and heat exchangers, to large-scale ocean wave-current interaction with offshore structures; flow across an aircraft wing and subsea pipelines subjected to undersea current are some of the canonical examples of single-phase flow. These applications involve complex multiscale and coupled nonlinear dynamics which can be quite challenging to predict and analyze via physical experiments and theoretical ways. The kinematic and dynamic effects of these flows can directly impact the design conditions of industrial systems, which makes their study essential from both experimental and computational points of view. Of particular interest to the present study is the system of an offshore drilling vessel and long pipelines called risers which connect a floating vessel to the ocean floor. This system is subjected to turbulent ocean current, wind streams and free-surface waves which may lead to complex fluid-structure interaction and coupled instabilities associated with waves and vortex dynamics. Development of a novel three-dimensional multifield and flexible multibody computational framework based on the continuum mechanics laws is the focus of the present dissertation.

The proposed coupled continuum system is governed by the partial differential equations of Navier-Stokes, Allen-Cahn phase-field, turbulence transport, and the structural equations for rigid and flexible components of the flexible multibody system. The most canonical form of these equations is the convection-diffusion-reaction (CDR) equation, which poses numerical challenges with regard to stability, conservation and positivity preservation of solution field. To resolve these challenges, we begin by one of the novel contributions of this dissertation on the design of a nonlinear and positivity preserving variational (PPV) Petrov-Galerkin technique.

Summary

In comparison to state-of-the-art methods, the proposed PPV scheme provides a superior accuracy and stability of the complex CDR system for a broad range of physical effects. We then extend the PPV-based Petrov-Galerkin technique to the phase-field Allen-Cahn equation which is coupled with the Navier-Stokes equations to model two-phase flows involving high density and viscosity ratios. The accuracy of the order parameter is further enhanced via an adaptive mesh procedure based on the residual error estimates of the Allen-Cahn equation. The adaptive algorithm is based on the newest vertex bisection algorithm and avoids complex tree data structure in its implementation. For the first time, the structural equations are coupled with the two-phase Navier-Stokes and Allen-Cahn variational formulation via a hybrid Allen-Cahn/arbitrary Lagrangian-Eulerian (ALE) scheme which has the feature of sharp interface-tracking of the fluid-structure interface via ALE and interface-capturing of the fluid-fluid interface. The interface-capturing handles any topological changes of fluid-fluid interfaces at turbulent flow condition. This coupling is carried out in a novel partitioned block-iterative manner which ensures flexibility and ease of implementation in the 3D parallel variational solver. The developed PPV technique has also been implemented for the hybrid RANS/LES method to resolve turbulence effects at high Reynolds number. The resultant integrated turbulent single and two-phase fluid-structure interaction framework is found to be robust and stable for high density and viscosity ratios of two fluid phases, and low structure-to-fluid mass ratios. The developed partitioned coupling leads to a block-type format which eases the implementation of the algorithm to existing variational solvers with little effort. The study is concluded by demonstrating the practical application of the drilling vessel-riser system with turbulent ocean current, wind streams and free-surface waves, combining all the elements developed thus far in the study. This application has a high impact on the offshore industry where hydrodynamic analyses of the drilling vessel and riser system are very expensive to undertake experimentally. The present framework not only provides the response amplitudes of the different multibodies but also outputs the integrated hydrodynamic forces on the structures, thus giving a comprehensive data for such large-scale two-phase fluid-structure systems for machine learning and data-driven computing.

List of Tables

3.1	Differential operators on the weighting function for stabilization methods	26
3.2	Quantification of the minimum and maximum values of the variable φ in different test cases in two-dimensions.	58
3.3	Quantification of the minimum and maximum values of the variable φ in different test cases in two-dimensions: Unstructured and anisotropic meshes.	61
3.4	The range of non-dimensional parameters: Unstructured and anisotropic meshes. .	61
5.1	Percentage error in the final radii of the two circles for different mesh resolutions.	87
5.2	Bounds in the solution of interface evolution at the left boundary with and without PPV consideration.	91
5.3	Error (e_3) in the solution for different N_ε	93
5.4	Error (e_3) in the solution for different Δt	94
5.5	Error (e_3) in the solution for different ε	94
6.1	Bounds of the solution of interface evolution over the whole domain for different techniques.	123
7.1	Non-dimensional parameters for the two cases considered for the present study. .	144
8.1	Comparison of the hydrodynamic parameters pertaining to the flow across a circular stationary cylinder at $Re = 3,900$ (Laminar Separation).	157
8.2	Comparison of the hydrodynamic parameters pertaining to the flow across a circular stationary cylinder at $Re = 140,000$ (Turbulent Separation).	157
8.3	Mesh details for flexible riser with $L/D = 481.5$ in a uniform current flow at $Re = 4000$	165

List of Tables

9.1	Different mesh resolutions for flow across a Wigley hull.	178
9.2	Non-dimensional frequencies (fL_{pp}/U_∞) of the displacement response.	187

List of Figures

1.1	Schematic for the methodology to develop the single-/two-phase fluid-structure interaction framework.	4
3.1	Sketch of the residual-based stabilization inside a generic element with ABCD sub-domain boundary: (a) Four-node quadrilateral element with convection velocity and the added diffusions k_s^{add} and k_c^{add} in the streamline and crosswind directions respectively; (b) added diffusions and solution gradient ($\nabla\varphi$) shown for designing positivity. Solid (red) and dashed (blue) lines represent the streamline and crosswind directions of the convection field respectively while solid (blue) line is the solution gradient vector.	35
3.2	Dependence of non-dimensionalized L^2 error on non-dimensional numbers as a function of: Da for convection-reaction equation with number of elements- (a) and (c); and ψ for diffusion-reaction problem- (b) and (d). Number of elements is kept constant at 10 for (a-b) and 40 for (c-d) with a domain length $L = 1$. . .	40
3.3	Variation of phase velocity and damping ratios with α_k for different $Kh_x/\pi \in [0, 1]$ for convection-diffusion-reaction problem for the present method: Phase velocity ratio for (a) positive reaction, (c) negative reaction; Damping ratio for (b) positive reaction, (d) negative reaction.	43
3.4	Mesh convergence study for various finite element methods through dependence of non-dimensionalized L^2 error as a function of uniform mesh refinement h : (a) convection-reaction; (b) diffusion-reaction; (c) CDR (destruction) and (d) CDR (production) problem. Number of elements is increased by decreasing h	46
3.5	Variation of scalar field φ of the steady CDR equation in one-dimension in	

List of Figures

the three canonical regimes: (a) Convection-diffusion ($Pe = 1$, $f = 1$, $(0, 0)$); (b) Convection-reaction ($Da = 10$, $f = 1$, inlet Dirichlet condition = 0); (c) Diffusion-reaction ($\psi = 10$, $f = 1$, $(0, 0)$).	48
3.6 Solution of the scalar field φ of the steady CDR equation in one-dimension by setting the source term, $f \neq 0$: (a) $Pe = 0.01$, $Da = 100$, $f = 1$, $(0, 0)$; (b) $Pe = 1.0$, $Da = 10$, $f = 1$, $(0, 0)$; (c) $Pe = 10$, $Da = 1.0$, $f = 1$, $(0, 0)$	49
3.7 Solution of the scalar field φ of the steady CDR equation in one-dimension by setting the source term, $f = 0$: (a) $Pe = 0.1$, $Da = 10$, $(0, 1)$; (b) $Pe = 1.0$, $Da = 10$, $(8, 3)$; (c) $Pe = 10$, $Da = 10$, $(0, 1)$; (d) $Pe = 10$, $Da = 10$, $(1, 0)$; (e) $Pe = 10$, $Da = 0.1$, $(1, 0)$; (f) $Pe = 10$, $Da = 0.2$, $(8, 3)$; (g) $Pe = 10$, $Da = 1.0$, $(8, 3)$; (h) $Pe = 1.0$, $Da = 60$, $(8, 3)$	50
3.8 Solution of the steady CDR equation in one-dimension in the exponential regime: (a) $Pe = 1.0$, $Da = -0.4$, $f = 0$, $(0, 1)$; (b) $Pe = 1.5$, $Da = -0.5$, $f = 1$, $(0, 0)$; (c) $Pe = 9.0$, $Da = -0.15$, $f = 0$, $(0, 1)$; (d) $Pe = 9.0$, $Da = -0.15$, $f = 0$, $(1, 0)$. The Galerkin solution is very oscillatory and hence is shown partially in Figs. 3.8(c) and 3.8(d).	51
3.9 Solution of the steady CDR equation in one-dimension in the propagation regime: (a) $Pe = 0.05$, $Da = -3.0$, $f = 0$, $(0, 1)$; (b) $Pe = 0.1$, $Da = -6.0$, $f = 0$, $(0, 1)$; (c) $Pe = 0.15$, $Da = -9.0$, $f = 0$, $(0, 1)$; (d) $Pe = 0.15$, $Da = -9.0$, $f = 0$, $(1, 0)$.	52
3.10 Solution of the transient CDR equation in one-dimension: Transient convection of two rectangular pulses, $u = 1$, $k = s = f = 0$	52
3.11 Schematic diagrams of the two-dimensional steady-state test cases: (a) convection- diffusion problem with unit skewed convection velocity, $s = 0$, $f = 0$; (b) convection-diffusion problem with constant source term, $s = 0$, $f = 1$; (c) diffusion-reaction problem with constant source term, $s = 1$, $f = 1$; (d) convection- diffusion problem with varying velocity and constant source term, $s = 0$, $f = 1$; (e) convection-diffusion problem with discontinuous source term, $s = 0$, $f(x \leq 0.5, y) = 1, f(x > 0.5, y) = -1$. The diffusion coefficient (k) is taken constant with a value of 10^{-8} for all the cases.	53
3.12 Solution of the steady-state CDR equation in two-dimensions at 20×20 and	

List of Figures

80 × 80 mesh resolutions: Convection-diffusion problem with unit convection velocity skewed at- (a) 0°; (b) 30°; (c) 45°; (d) 60°; (e) 90°; and (f) 90° (Codina [1]).	55
3.13 Solution of the steady-state CDR equation in two-dimensions at 20 × 20 and 80 × 80 mesh resolutions: (a) Convection-diffusion problem with constant source term; (b) Diffusion-reaction problem with constant source term; (c) Convection-diffusion problem with varying velocity and constant source term; (d) Convection-diffusion problem with discontinuous source term.	56
3.14 Solution of the transient CDR equation in two-dimensions: Transient convection of a circular bubble with the convection velocity at an angle of 45° with the X-axis, $k = 10^{-30}$, $s = 0$, $f = 0$ at- (a) $t = 1\text{s}$; (b) $t = 2\text{s}$, (c) $t = 3\text{s}$; (d) $t = 4\text{s}$. . .	57
3.15 Three representative unstructured and anisotropic grids: (a) Mesh A, (b) Mesh B, (c) Mesh C. Results of the steady-state CDR equation in two-dimensions for skewed convection-diffusion problem at 60° (second row); Convection-diffusion problem with constant source term (third row); Diffusion-reaction problem (fourth row).	60
4.1 Schematic of two-phase fluid-structure interaction at (a) the initial configuration $t = 0$, and (b) some deformed configuration of the structure at time $t > 0$. $\Omega^f(0)$, Ω^s and $\Omega^f(t)$, $\Omega^s(t)$ are the fluid and the structural domains at $t = 0$ and some time $t > 0$ respectively with (c) sharp fluid-structure interface, and (d) diffused fluid-fluid interface, smeared using the internal length scale parameter ε . Γ^{fs} and Γ^{ff} denote the fluid-structure and fluid-fluid interfaces, respectively.	64
5.1 Evolution of the radii of two-dimensional circles: (a) Schematic diagram showing the computational domain, (b) Validation of the evolution of the radii of the two circles with the literature [2], and the contour plots of the order parameter ϕ at (c) $t = 0$, and (d) $t = 100$. In (a), Ω_1^f and Ω_2^f are the two phases with periodic boundary conditions imposed on all the sides.	86
5.2 Convergence study for the present method through dependence of non-dimensionalized L^2 error (e_2) as a function of: (a) uniform mesh refinement h , and (b) uniform temporal refinement Δt	88

List of Figures

5.3 Laplace-Young law: (a) Schematic diagram showing the computational domain, (b) Comparison of the pressure difference across the interface in a static bubble obtained from the simulation with the Laplace-Young law. In (a), Ω_1^f and Ω_2^f are the two fluid phases with densities $\rho_1^f = 1000$ and $\rho_2^f = 1$, viscosities $\mu_1^f = 10$, $\mu_2^f = 0.1$ and acceleration due to gravity $\mathbf{g} = (0, 0, 0)$ and all the boundaries have periodic boundary condition.	89
5.4 Sloshing in a rectangular tank: (a) Schematic diagram showing the computational domain, (b) Contour plot of the order parameter ϕ at $t = 0$. In (a), Ω_1^f and Ω_2^f are the two fluid phases with densities $\rho_1^f = 1000$ and $\rho_2^f = 1$, viscosities $\mu_1^f = 1$, $\mu_2^f = 0.01$ and acceleration due to gravity $\mathbf{g} = (0, -1, 0)$ and the walls of the tank have slip boundary condition with $p = 0$ at the upper boundary.	91
5.5 Sloshing tank problem: Effect of using the PPV technique on the evolution of the interface. $\varepsilon = 0.01$, $\Delta t = 0.001$ and $N_\varepsilon = 3$. The reference solution is obtained at $N_\varepsilon = 8$	92
5.6 Sloshing tank problem: Effect of N_ε on the evolution of the interface. $\varepsilon = 0.01$ and $\Delta t = 0.001$ are kept constant.	93
5.7 Sloshing tank problem: Effect of Δt on the evolution of the interface. $\varepsilon = 0.01$ and $N_\varepsilon = 4$ are kept constant.	94
5.8 Sloshing tank problem: Effect of ε on the evolution of the interface. $\Delta t = 0.01$ and $N_\varepsilon = 4$ are kept constant.	95
5.9 Comparison of the solution considering $N_\varepsilon = 4$, $\Delta t = 0.01$ and $\varepsilon = 0.01$ with XFEM-based level set approach in [3].	95
5.10 Two-dimensional dam-break problem: (a) schematic diagram showing the computational domain, and (b) the contour plot of the order parameter ϕ at $t = 0$. In (a), Ω_1^f and Ω_2^f are the two phases with $\rho_1^f = 1000$, $\rho_2^f = 1$, $\mu_1^f = 10^{-3}$ and $\mu_2^f = 10^{-5}$ and acceleration due to gravity is taken as $\mathbf{g} = (0, -9.81, 0)$	96
5.11 Two-dimensional dam-break problem: temporal evolution of non-dimensional water column (a) width and (b) height.	97
5.12 Interface profiles for two-dimensional dam-break problem: (a) $t = 0.0$, (b) $t = 0.2$, (c) $t = 0.4$, (d) $t = 0.6$, (e) $t = 0.8$ and (f) $t = 1.0$. The profile shown depicts	

List of Figures

the contour of the order parameter cutoff below 0, i.e., it only shows the domain consisting water.	98
5.13 Schematic diagram showing the computational domain for three-dimensional dam-break with obstacle. Ω_1^f and Ω_2^f are the two phases with $\rho_1^f = 1000$, $\rho_2^f = 1.225$, $\mu_1^f = 1.002 \times 10^{-3}$ and $\mu_2^f = 1.983 \times 10^{-5}$, acceleration due to gravity is taken as $\mathbf{g} = (0, -9.81, 0)$ and slip boundary condition is imposed on all the boundaries.	99
5.14 Three-dimensional dam-break problem: temporal evolution of the pressure at the probe points: (a) P1 and (b) P2.	99
5.15 Three-dimensional dam-break problem: temporal evolution of the height at the probe points: (a) H1 and (b) H2.	100
5.16 Three-dimensional dam-break problem: temporal evolution of the iso-contours of water ($\phi > 0$) at time: (a) 0.125s, (b) 0.75s, (c) 1.125s, (d) 2s, (e) 2.5s and (f) 3s.	101
5.17 Notations and coordinate system in the description of the second-order Stokes wave theory: $\eta(x, t)$ is the profile of the free-surface, d is the water depth, A is the amplitude of the wave, $H = 2A$ is the height of the wave and λ is the wavelength.	102
5.18 A schematic of the wave-structure problem. The computational setup and boundary conditions are shown for the Navier-Stokes equations. Here, $\mathbf{u}^f = (u, v, w)$ denotes the components of the fluid velocity which are given by Eqs. (5.45) and (5.46) with $v = 0$. Stress-free boundary condition with zero pressure is given at the top surface of the wave tank. Slip boundary condition is imposed at the X-Z plane at $y = -1$ and $y = 1$. All other boundaries have the no-slip condition. Moreover, zero Neumann boundary condition is imposed for the order parameter ϕ on all the boundaries.	103
5.19 Three-dimensional computational mesh and contours of order parameter for the run-up problem: (a) refined interfacial region with unstructured finite element mesh, (b) contour plot of order parameter ϕ superimposed with the unstructured mesh.	104
5.20 Water wave run-up on a truncated cylinder: Snapshots of iso-contours $\phi = 0$ colored by the free-surface elevation for two representative wave steepness pa-	

List of Figures

parameters at $t/T = 8.926$: (a) $kA = 0.1837$, and (b) $kA = 0.2146$.	105
5.21 Water wave run-up on a truncated cylinder: Time histories of the free-surface elevations at the probe locations for three representative wave steepness parameters: (a) $kA = 0.0779$, (b) 0.1381, (c) 0.2146, and (d) comparison of the wave run-up ratio with the results from the literature at $ka = 0.208$: The first- and second-order results are from frequency domain potential theory, the experimental results are from the campaign in [4] and the ALE results are from the free-surface ALE solver in [5]. Time and free-surface elevation are non-dimensionalized by time period T and wave amplitude A respectively.	106
6.1 A schematic of the newest vertex bisection algorithm for refinement: (a) marked element for refinement, (b) bisection of the largest edge, (c) bisection of the other marked edges, (d) inclusion of more elements to remove hanging nodes.	111
6.2 Spinodal decomposition in a spiral domain: (a) schematic diagram showing the computational domain and (b) initial triangular mesh at $t = 0$. In (a), the coordinates of O, A and B are $(0, 0)$, $(0.5, 0)$ and $(1, 0)$ respectively and r denotes the radius of the spiral curve varying with angle θ as given in Eq. (6.11).	115
6.3 Decay of the total discrete energy with time for the spinodal decomposition in a spiral domain. The contours of the order parameter are shown at different time instances $t \in [2, 5, 8]$. The total energy decreases with time making the scheme energy stable.	116
6.4 Solution of the spinodal decomposition in a spiral domain at $t = 100$: (a) the adapted mesh and (b) the contours of the order parameter ϕ .	117
6.5 Assessment of volume conservation during the interface evolution according to mean curvature flow: the adaptive mesh at (a) $t = 0$, (b) $t = 400$, (c) validation of the evolution of the radii of the two circles with the literature [2], and (d) the variation of the total mass of the order parameter ϕ with time.	118
6.6 Background mesh convergence for the sloshing tank problem: evolution of the interface at the left boundary with $\varepsilon = 0.01$ and different background mesh sizes.	120
6.7 Contours of the order parameter ϕ (top) and the adaptive mesh (bottom) for the sloshing tank problem with background mesh $\Delta x = 0.04$ and $\varepsilon = 0.01$ at	

List of Figures

t/T_{oscill} : (a) 0.55, (b) 1.94, (c) 3.6 and (d) 5.	120
6.8 Variation of the measured quantities with time in the sloshing tank problem: (a) the error in mass conservation evaluated using Eq. (6.16), (b) the residual error η , (c) the number of degrees of freedom or unknowns, and (d) the cumulative elapsed time.	122
6.9 Variation of the measured quantities with tol_R in the sloshing tank problem: (a) the total mass loss, (b) the average number of degrees of freedom and (c) the average error in solving the Allen-Cahn equation (\bar{e}_{AC}).	123
6.10 Variation of the interface at the left boundary in the sloshing tank problem: (a) $tol_R = 1 \times 10^{-3}$, (b) $tol_R = 5 \times 10^{-3}$ and (c) $tol_R = 5 \times 10^{-4}$	124
6.11 Variation of the measured quantities with time in the sloshing tank problem for varying interface thickness parameter ε : (a) mass evaluated using Eq. (6.14), (b) degrees of freedom or unknowns, and (c) residual error indicator η	125
6.12 Contours of the order parameter ϕ (a and c) and the adaptive mesh (b and d) for the sloshing tank problem at $t/T_{oscill} = 5$ for: $\varepsilon = 0.005$ (a and b), and $\varepsilon = 0.0025$ (c and d).	125
6.13 Two-dimensional dam-break problem: (a) the contour plot of the order parameter ϕ at $t = 0$, and (b) the initial refined mesh at $t = 0$	126
6.14 Two-dimensional dam-break problem: temporal evolution of non-dimensional water column (a) width and (b) height. The results from the present method are in good agreement with the literature.	127
6.15 Contours of the order parameter ϕ (left) and the adaptive mesh (right) for the dam-break problem at $t\sqrt{(2g/a)}$: (a) 2.32, (b) 4.64, (c) 9.96 and (d) 11.60. . . .	128
7.1 Schematic of the decay response of a cylinder of diameter D under gravity in the $X-Y$ cross-section. The computational domain extends a distance of $17D$ in the Z -direction.	137
7.2 Mesh employed for the decay response of a cylinder interacting with the free-surface: (a) the refined mesh around the cylinder to capture the flow vortices near the structure, and (b) the boundary layer mesh around the cylinder with $y^+ \sim 1$ for hybrid RANS/LES modeling.	138

List of Figures

7.3	Temporal convergence study for the decay test of a circular cylinder: (a) heave motion employing temporal refinement, and (b) the dependence of non-dimensionalized L^2 error (e_1) as a function of uniform temporal refinement Δt	139
7.4	Dependence of spatial grid convergence on the interfacial thickness parameter ε for the decay test of a circular cylinder at free-surface.	139
7.5	Decay test of a circular cylinder under translation along the free-surface: (a) validation of the heave motion of the cylinder at the free-surface with the experimental [6] and simulation [7] studies, and (b) Z -vorticity contours around the cylinder at $t = 1.5$ s with the free-surface indicated at $\phi = 0$	140
7.6	Rotation of a rectangular barge under gravity: (a) schematic of the computational setup of a barge of length $L = 0.3$, height $H = 0.2$ and width $W = 3L$ in the $X-Y$ cross-section, and (b) zoom-in view of the computational mesh near the barge with boundary layer. The computational domain extends a distance of $3L$ in the Z direction.	141
7.7	Decay test under rotation: (a) validation of the rotational motion of the rectangular barge at the free-surface with the experimental [8] and simulation [7] studies, and (b) Z -vorticity contours around the barge at $t = 1.4$ s with the free-surface indicated at $\phi = 0$	142
7.8	Schematic of the uniform flow past a flexible riser with an internal two-phase flow: (a) the $X - Z$ cross-section of the flexible riser with the internal flow velocity profile at the inlet and outlet of the pipe, and (b) the computational setup and boundary conditions employed for the demonstration. Here, $\mathbf{u}^f = (u, v, w)$ denotes the components of the fluid velocity and the hatched area shows the flexible structure (riser).	143
7.9	Computational mesh for the VIV of a riser with an internal two-phase flow: (a) three-dimensional view of the mesh, and (b) two-dimensional cross-section of the mesh with refined wake region behind the riser and refined internal region of the riser to capture the interface between the two phases in the internal flow accurately.	144
7.10	The response amplitude at the mid-point of the riser ($z/L = 0.5$) exposed to external uniform flow with internal two-phase flow: (a) Case 1 ($Re = 100$), and	

List of Figures

(b) Case 2 ($Re = 1000$).	146
7.11 Response amplitudes of the riser along the span with non-dimensional time tU_∞/D for Case 1: (a) cross-flow, and (b) in-line.	146
7.12 Response amplitudes of the riser along the span with non-dimensional time tU_∞/D for Case 2: (a) cross-flow, and (b) in-line.	147
7.13 Contour plots for the VIV of a riser at $Re = 100$ with internal two-phase flow at tU_∞/D : (a) 80, (b) 90 and (c) the internal flow along the riser. The Z - vorticity contours are shown at three cross-sections along the riser, viz., $z/L \in$ $[0.25, 0.5, 0.75]$ and are colored with red for positive vorticity and blue for negative vorticity. The inset figure provides the velocity magnitude at the mid-section of the riser. The interior two-phase flow of the riser is visualized by the contours of order parameter $\phi > 0$ at an arbitrary plane passing through the axis of the deformed riser.	147
7.14 Contour plots for the VIV of a riser at $Re = 1000$ with internal two-phase flow at tU_∞/D : (a) 40, (b) 50 and (c) the internal flow along the riser. The Z - vorticity contours are shown at three cross-sections along the riser, viz., $z/L \in$ $[0.25, 0.5, 0.75]$ and are colored with red for positive vorticity and blue for negative vorticity. The inset figure provides the velocity magnitude at the mid-section of the riser. The interior two-phase flow of the riser is visualized by the contours of order parameter $\phi > 0$ at an arbitrary plane passing through the axis of the deformed riser.	148
8.1 A schematic of the flow past a three-dimensional circular cylinder at high Reynolds number. The computational setup and boundary conditions are shown for the Navier-Stokes and DDES equations. Here, $\mathbf{u}^f = (u, v, w)$ denotes the components of the fluid velocity, LS and TS denote the laminar separation and turbulent sep- aration cases respectively.	155
8.2 Mesh characteristics for the flow past a circular cylinder: (a) mesh in the full computational domain in the cross-sectional $X-Y$ plane, (b) various mesh regions around the cylinder for the well-designed DES mesh. While the elements in the LES focus region are isotropic and well resolved for capturing the wake dynamics,	

List of Figures

the viscous RANS region maintains $y^+ < 1$ close to the cylinder surface.	156
8.3 Time histories of the hydrodynamic force coefficients for the flow past a circular stationary cylinder at two subcritical Reynolds numbers: (a) $Re = 3,900$, and (b) $Re = 140,000$	158
8.4 Spectrum of the lift coefficient C_L for the stationary circular cylinder at: (a) $Re = 3,900$, (b) $Re = 140,000$	159
8.5 Flow past a stationary circular cylinder: Variation of C_p along the circumference with angle θ at (a) $Re = 3,900$: (—) Present simulation, (- -) Present (no PPV method), (○) Experiment [9], (---) Dynamic LES [10]; (b) $Re = 140,000$: (—) Present simulation, (○) Experiment at $Re = 8.5 \times 10^6$ [11], (Δ) Experiment at $Re = 7.6 \times 10^6$ [12], (- -) DES [13], (---) DES [13]. Here the angle $\theta = 0$ denotes the stagnation point.	159
8.6 Flow past a stationary circular cylinder at subcritical Reynolds numbers: Vortical wake structures of iso-surfaces of $Q^+ = 0.25$ colored by $ \mathbf{u}^f /U_\infty$ at $tU_\infty/D = 150$: Three-dimensional view at (a) $Re = 3,900$ and (c) $Re = 140,000$. Top-view- The rolls with the braid region consisting of small-scale structures and the ribs can be observed at (b) $Re = 3,900$ and (d) $Re = 140,000$	161
8.7 Flow past a stationary circular cylinder: Spectra of the transverse velocity and the Kolmogorov's rule at (a) $Re = 3,900$, (b) $Re = 140,000$	162
8.8 Mean velocity at three locations in the wake of the stationary circular cylinder at $Re = 3,900$: (a) Streamwise velocity; (b) Transverse velocity. (—) Present simulation, (- -) LES [14], (---) B-Spline simulation [15], (●) PIV experiment [14], (■) Experiment [16].	162
8.9 A long flexible riser model in uniform current flow along the Z -axis: (a) Pinned-pinned tensioned riser with uniform flow, (b) Sketch to illustrate the computational setup and boundary conditions for the PPV-based DDES on flow past a flexible riser. Here, $\mathbf{u}^f = (u, v, w)$ denotes the fluid velocity components. Consistent with the experimental measurement, a tensioned beam with the pinned at both ends and free to oscillate in the IL (X) and CF (Y) directions is employed in the numerical simulation.	164

List of Figures

8.10 Uniform flow past a long flexible riser model: Two-dimensional mesh in the X - Y plane employed in the computation of flexible riser VIV. This mesh is extruded in the third dimension to obtain the three-dimensional mesh.	165
8.11 Uniform current flow past a flexible riser model $L/D = 481.5$ at $(Re, m^*, U_r) = (4000, 2.23, 5.6)$: Dependence of riser response at $z/L = 0.55$ with spanwise resolution for 800 layers: (a) cross-flow response and (b) in-line response.	166
8.12 Uniform current flow past a flexible riser model $L/D = 481.5$ at $(Re, m^*, U_r) = (4000, 2.23, 5.6)$: Variation of the root mean square amplitude along the span of the riser for different employed meshes: (a) Cross-flow amplitude; (b) In-line amplitude. The first mode (fundamental) response for the CF and the second mode for the IL can be seen.	167
8.13 Riser response envelope with spanwise resolution of 800 layers for uniform current flow past a flexible riser model at $(Re, m^*, U_r) = (4000, 2.23, 5.6)$: (a) Cross-flow and (b) In-line directions. The riser is vibrating in the fundamental mode in the CF and the second mode for the IL directions.	168
8.14 Standing wave response of flexible riser VIV with spanwise resolution of 800 layers for uniform current flow past a flexible riser model at $(Re, m^*, U_r) = (4000, 2.23, 5.6)$: (a) Cross-flow and (b) In-line directions. While the CF resonant response is at the fundamental mode, the IL wave response has a second mode pattern.	168
8.15 Oscillation frequencies and orbital trajectory at different locations $z/L \in [0.22, 0.88]$ along the span of the riser in the time window $tU_\infty/D \in [400, 470]$. The horizontal row corresponds to the same location of the riser with the first and second column giving the power spectra of cross-flow and in-line amplitudes respectively.	171
8.16 Oscillation frequencies and orbital trajectory at different locations $z/L \in [0.22, 0.88]$ along the span of the riser in the time window $tU_\infty/D \in [600, 670]$. The horizontal row corresponds to the same location of the riser with the first and second column giving the power spectra of cross-flow and in-line amplitudes respectively.	172
8.17 Orbital trajectory at different locations along the span of the riser $(Re, m^*, U_r) = (4000, 2.23, 5.6)$: Comparison of experimental trajectory (left column) with the	

List of Figures

simulation in the time window $tU_\infty/D \in [440, 460]$ (right column)	173
8.18 Flow visualization along the flexible riser undergoing VIV at $(Re, m^*, U_r) = (4000, 2.23, 5.6)$: Vibration amplitude along the riser with Z -vorticity contours in various sections- red and blue color indicate the positive and negative vorticity respectively: (a) $tU_\infty/D = 460$ and (b) $tU_\infty/D = 650$. The vorticity contours are plotted for different locations along the riser corresponding to $z/L \in [0.11, 0.88]$	174
9.1 Schematic of the Wigley hull with the computational domain. Γ_{in} and Γ_{out} denote the inlet and outlet boundaries with freestream velocity at Γ_{in} . Slip boundary conditions are satisfied on the boundaries including Γ_{side} , Γ_{bottom} , Γ_{top} and Γ_{symm} . No-slip condition is imposed on the hull surface Γ_{hull}	177
9.2 Computational Mesh 2 for the flow across a Wigley hull with the top and side view. The mesh consists of half of the Wigley hull with symmetric boundary condition.	178
9.3 Wave profile elevation along the Wigley hull: comparison between the experimental data and numerical results at (a) $Fr = 0.25$ and (b) $Fr = 0.316$	178
9.4 Wave elevation contours along the Wigley hull at (a) $Fr = 0.25$ and (b) $Fr = 0.316$. The contours are mirrored along the $X - Z$ plane owing to the symmetry in the hull geometry.	179
9.5 Schematic of the ship model 5415 with the computational domain. Γ_{in} and Γ_{out} denote the inlet and outlet boundaries with a combination of linear Airy waves and current at the inlet. Slip and no-slip boundary conditions are satisfied at the sides Γ_{side} and the ship hull surface Γ_{ship} respectively. Atmospheric condition is satisfied at Γ_{top} with no-slip condition at Γ_{bottom}	181
9.6 Computational mesh for the ship hull model 5415 with the top and side view. The mesh is refined near the fluid-fluid interface. The inset provides the discretization of the ship hull.	182
9.7 Heave displacement response (η_z^s/L_{pp}), heaving velocity ($\dot{\eta}_z^s/U_\infty$) and the vertical fluid force ($F_z/(\rho_1^f U_\infty^2 L_{pp}^2)$) on the ship model 5415 subjected to free-surface waves.	183
9.8 Heave motion of the 5415 vessel model at (a) $tU_\infty/L_{pp} = 3.27$, (b) $tU_\infty/L_{pp} = 6.22$ and (c) $tU_\infty/L_{pp} = 3.6$. The free-surface of the waves is represented by the	

List of Figures

iso-surface of the order parameter at $\phi = 0$ colored by the elevation. The ship surface is colored by the non-dimensional heave displacement.	184
9.9 Schematic of the full-scale DTMB 5415 with the computational domain. Γ_{in} and Γ_{out} denote the inlet and outlet boundaries with a combination of nonlinear Stokes waves and current at the inlet. Slip and no-slip boundary conditions are satisfied at the sides Γ_{side} and the surfaces Γ_{ship} , Γ_{riser} respectively. Atmospheric condition is satisfied at Γ_{top} with no-slip condition at Γ_{bottom}	185
9.10 Computational mesh for the drillship-riser system with full-scale DTMB 5415 as the drillship. The mesh is refined near the fluid-fluid interface. The inset provides the discretization of the ship hull.	187
9.11 Displacement response (η_{ship}^s/L_{pp}) of the drillship in the surge (x), sway (y) and heave (z) directions.	188
9.12 Fluid force ($F/(\rho_1^f U_\infty^2 L_{pp}^2)$) on the drillship in the surge (x), sway (y) and heave (z) directions.	188
9.13 Displacement response (η_{riser}^s/D) of the riser of diameter D in the surge (x), sway (y) and heave (z) directions at the midpoint of the riser at $z/L = 0.5$	189
9.14 Response envelope along the span of the riser in (a) in-line (x) direction, and (b) cross-flow (y) direction.	189
9.15 Coupled vessel riser system subjected to free-surface waves and ocean current at $tU_\infty/L_{pp} = 1.535$. The free-surface of the waves is represented by the iso-surface of the order parameter at $\phi = 0$ colored by the elevation. The inset provides the Z-vorticity contours along the riser surface with red and blue colors representing positive and negative vorticities respectively.	190
C.1 Variation of phase velocity, damping and group velocity ratios with $\bar{K} = Kh$ for convection-diffusion-reaction problem for different numerical schemes: Phase velocity ratio for (a) positive reaction, (d) negative reaction; Damping ratio for (b) positive reaction, (e) negative reaction; Group velocity ratio for (c) positive reaction, (f) negative reaction. The plots for the proposed method will be similar to those of GLS method for positive reaction and those of SGS method for negative reaction.	223

List of Figures

C.2	Contours of the magnitude of the amplification factor ($ \zeta^h $), the phase velocity ratio (c^h/c) and the group velocity ratio (v_g^h/c) for GLS and SGS methods when the reaction coefficient is positive ($s > 0$).	225
C.3	Contours of the magnitude of the amplification factor ($ \zeta^h $), the phase velocity ratio (c^h/c) and the group velocity ratio (v_g^h/c) for GLS and SGS methods when the reaction coefficient is negative ($s < 0$).	226
D.1	Variation of phase velocity and damping ratios with α_k for different $Kh_x/\pi \in [0, 1]$ for convection-diffusion-reaction problem with positive reaction: Phase velocity ratio for (a) GLS, (b) SGS; Damping ratio for (c) GLS, (d) SGS. The plots for the proposed method will be similar to those of GLS method in this regime. . .	230
D.2	Variation of phase velocity and damping ratios with α_k for different $Kh_x/\pi \in [0, 1]$ for convection-diffusion-reaction problem with negative reaction: Phase velocity ratio for (a) GLS, (b) SGS; Damping ratio for (c) GLS, (d) SGS. The plots for the proposed method will be similar to those of SGS method in this regime. . .	231

Nomenclature

Abbreviations

2D	Two-dimensional
3D	Three-dimensional
ALE	Arbitrary Lagrangian-Eulerian
FSI	Fluid-structure interaction
SUPG	Streamline upwind Petrov-Galerkin
GLS	Galerkin/least-squares
SGS	Subgrid-scale
PPV	Positivity preserving variational
CDR	Convection-diffusion-reaction
AC	Allen-Cahn
RANS	Reynolds averaged Navier-Stokes
LES	Large eddy simulation
S-A	Spalart-Allmaras
DDES	Delayed detached eddy simulation

Domains

Ω	General domain
Ω^f	Fluid domain
Ω^s	Structural domain
$\Gamma_D^{(\cdot)}$	Dirichlet boundary for variable (\cdot)
$\Gamma_H^{(\cdot)}$	Neumann boundary for variable (\cdot)
Γ^{ff}	Fluid-fluid interface

Nomenclature

Γ^{fs} Fluid-structure interface

Mathematical spaces

$\mathcal{S}_{(\cdot)}^{\text{h}}$ Space of trial solution for variable (\cdot)
 $\mathcal{V}_{(\cdot)}^{\text{h}}$ Space of test function for variable (\cdot)

Physical parameters

ρ^{f} Fluid density
 μ^{f} Fluid dynamic viscosity
 ε Phase-field interface thickness parameter
 ρ^{s} Structural density
 U_{∞} Freestream velocity
 p_{∞} Far-field pressure
 P Axial tension on the beam
 EI Flexural rigidity of the beam

Non-dimensional parameters

Pe Peclet number
 Da Damköhler number
 Re Reynolds number
 m^* Structure-to-fluid mass ratio
 U_r Reduced velocity
 C_D Drag coefficient
 C_L Lift coefficient
 C_{pb} Base pressure coefficient
 St Strouhal number
 ρ^* Density ratio of the two fluid phases
 μ^* Dynamic viscosity ratio of the two fluid phases
 P^* Non-dimensional axial tension
 EI^* Non-dimensional flexural rigidity

Nomenclature

EA^* Non-dimensional axial rigidity

Operators

$\text{tr}(\cdot)$	Tensor trace operator
$\partial_t(\cdot)$	Partial time derivative operator
$\nabla(\cdot)$	Gradient operator
$\nabla \cdot (\cdot)$	Divergence operator
$\ \cdot\ _2$	L^2 norm operator
$\max(\cdot)$	Maximum of (\cdot)
$\min(\cdot)$	Minimum of (\cdot)
rand	Uniformly distributed random numbers in the interval $(0, 1)$
$\overline{(\cdot)}$	Mean value of (\cdot)

Variables

t	Temporal variable
\boldsymbol{x}^f	Spatial coordinates for the domain Ω^f
\boldsymbol{x}^s	Lagrangian coordinates for the domain Ω^s at $t = 0$
$\boldsymbol{\chi}$	ALE referential coordinates
φ	General transport variable
\boldsymbol{u}	General convection velocity
k	General diffusion coefficient
s	General reaction coefficient
f	General source term
\boldsymbol{u}^f	Fluid velocity
\boldsymbol{u}^m	Mesh velocity
p	Fluid pressure
\boldsymbol{u}^s	Structural velocity
ϕ	Phase indicator (or order parameter)
$\tilde{\nu}$	Eddy viscosity
$\boldsymbol{\varphi}$	Position vector mapping for the structure

Nomenclature

η^s	Displacement of the structure
η^f	Displacement of the fluid mesh
w	Finite element test function for general transport variable φ
ψ^f	Finite element test function for fluid velocity
q	Finite element test function for fluid pressure
ψ^s	Finite element test function for structural velocity
\hat{w}	Finite element test function for order parameter
\tilde{w}	Finite element test function for eddy viscosity
σ^f	Fluid Cauchy stress tensor
σ^s	First Piola-Kirchhoff stress tensor
I	Identity matrix tensor
$(\cdot)_D$	Dirichlet condition on variable (\cdot)
$h^{(\cdot)}$	Neumann condition on variable (\cdot)
$(\cdot)_0$	Initial condition on variable (\cdot)
$\mathbf{n}^{(\cdot)}$	Unit normal to Neumann boundary for variable (\cdot)
$A_{(\cdot)}$	Displacement amplitude in (\cdot) direction

Chapter 1

Introduction

1.1 Background and motivation

Fluid-structure interaction (FSI) involving single and two phases is omnipresent. Two-phase FSI finds its application in small-scale droplet interactions [17], phase separation and microstructural evolution [18], bubbly and slug flows in oil and natural gas pipelines [19], heat exchangers [20], to large-scale ocean waves and wave breaking [21, 22, 23]. Some canonical examples of single phase flow are flow across an aerofoil and ocean current impinging on subsea pipelines. Fluid flow over slender flexible structures finds a special interest in the offshore engineering due to the strong interactions of ocean currents with drilling and production risers, mooring lines, tendons and subsea pipelines [24]. These applications involve complex multiscale and nonlinear phenomena which can be quite challenging to understand and analyze via physical experiments and theoretical ways. The kinematic and dynamic effects of these flows can directly impact the design conditions of industrial systems, which makes their study essential from both experimental and computational point of view.

Of particular interest to the present study are the offshore platforms and pipeline systems. Oil and natural gas under the seabed are extracted with the help of offshore platforms such as jack-up drills, tension-leg platforms, semi-submersibles, and drillships. The potential oil reserve under the seabed is first surveyed and analyzed. Once the capability and potential of the reservoir in terms of the natural resource have been quantified, the drilling of the seabed commences. It is a very time-consuming process which initiates by forming the wellhead, then the conductor

Chapter 1. Introduction

casing and finally the production casing for laying the foundation for the production process. Since the seabed is quite a distance from the sea-level, long tubular structures called drilling risers are employed for transporting the drill bit to the seabed as well as pulling out the drilling mud from the seabed. The length of these risers can be from 500 m (shallow water drilling) to 3500 m (ultra deepwater drilling). After the drilling process is complete, the production risers are set up to extract the resources from the reserves.

Due to the drastic and chaotic ocean conditions, the risers are subjected to turbulent ocean current with Reynolds number of the order of $10^5 - 10^7$. These offshore structures may undergo self-excited vibrations and fluid-elastic instabilities [24, 25] which are a result of unsteady fluid forces that arise from the asymmetric vortices shed behind the structure, known as vortex-induced vibrations (VIV). During VIV, the phenomenon of frequency lock-in occurs for a certain range of fluid and structural parameters and the preferred frequency of wake deviates from its expected value determined by the Strouhal relation while being close to the value of the natural frequency of the structure. This complex frequency lock-in phenomenon leads to high amplitude of vibrations, typically around one cross-sectional unit of the structure [24]. Based on the marine environment and structural properties, VIV can cause significant dynamic bending stresses, the drag force amplification and large deflections on the riser from a short-term perspective. From the long-term viewpoint for production risers, rapid accumulation of fatigue damage may lead to structural failure if the vibrations are left unchecked. Consequently, it is imperative for the safety of offshore operations that VIV response is adequately predicted on these long flexible cylinders. In addition, the physical understanding of vibrating flexible cylinders can help in developing devices and methods to suppress VIV.

On the other hand, the offshore platform at the free-surface can interact with the ocean waves (two-phase flow involving air and water) consisting of high amplitude and multi-frequency waves, causing wave-structure interaction. The response of the platform can reach high amplitudes depending on the characteristics of the ocean waves. Drifting of the platform is not desired in such cases since it hinders the drilling process and induces high bending stresses on the riser joints. Furthermore, the effect of the VIV of the risers on these platforms and the effect of wave-induced effects of the platforms on the risers is relatively a novel area to explore.

Though there have been many experimental as well as computational studies dealing with

Chapter 1. Introduction

small-scale flexible cylinders in the literature, understanding such long risers and large-scale drilling vessels is experimentally very expensive. Therefore, offshore operators rely on the semi-empirical data obtained from simplified theoretical models during the drilling operation, which are very conservative. Computational fluid dynamics (CFD) offers an option to accurately solve these large-scale problems. High-fidelity numerical simulations can play an important role to understand the nonlinear coupled physics as well as to provide guidelines for engineering design and optimization. The current work is an attempt to develop such computational framework to solve large-scale problems with application to a drillship-riser system in the offshore environment.

1.2 Objectives and methodology

The main objective of the current work is the development of a computational framework based on variational techniques to solve single and two-phase fluid-structure interaction problems. Physical systems in a continuum are governed by conservative transport equations ranging from Navier-Stokes, Helmholtz, heat and mass transfer, Allen-Cahn, Cahn-Hilliard, level-set to turbulence transport equations. The most canonical form of these equations can be expressed as a convection-diffusion-reaction (CDR) equation. Getting an exact solution of these equations in three-dimensions is an open problem to the researchers, especially the Navier-Stokes equations which are among the seven Clay Mathematics Institute Millennium Prize problems. The difficulties in finding the solution to these equations arise due to the inherent nonlinearities. Moreover, the onset of turbulence in the Navier-Stokes equations further complicates the issue. Therefore, numerical methods are employed, where the equations are solved on finite degrees of freedom in contrast to the infinite degrees existing in nature. By doing so, we introduce numerical errors in the solution and do not capture some of the crucial physical phenomena.

The current study begins with identifying these challenges in the context of a scalar convection-diffusion-reaction equation, reviewing the studies carried out thus far and developing a novel variational method (the positivity preserving variational method) to improve the solution. The developed formulation is then applied to the conservative Allen-Cahn equation to model the two-phase flows along with a mesh adaptive procedure to improve the accuracy of the solution. Progressing towards a two-phase fluid-structure interaction framework depicted in Fig.

Chapter 1. Introduction

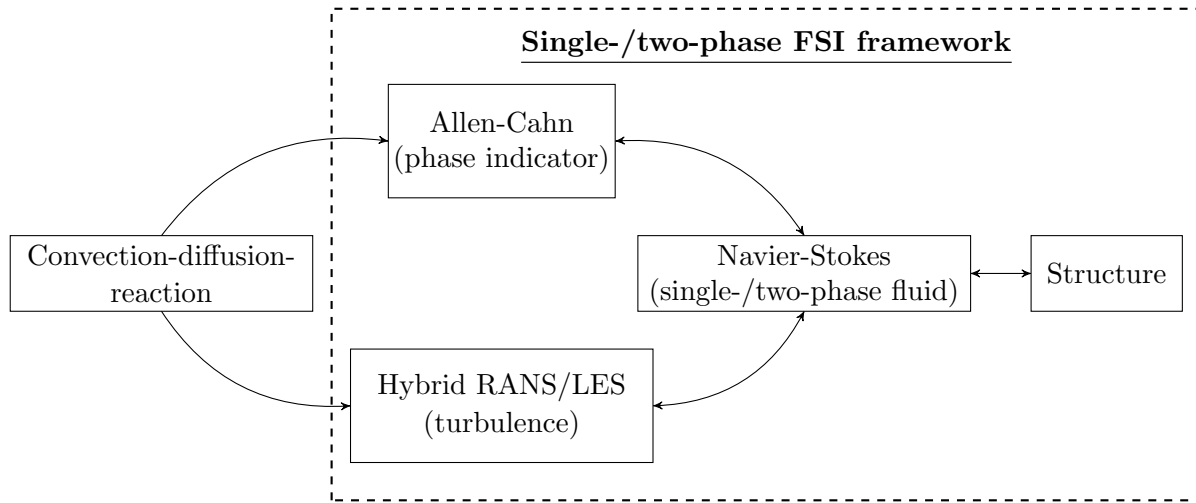


Figure 1.1: Schematic for the methodology to develop the single-/two-phase fluid-structure interaction framework.

1.1, the coupling between the different fluid and structural equations is presented leading to an efficient, robust and stable computational framework. The turbulence transport equation is also formulated via the positivity preserving method and closes the loop for considering highly turbulent flows. Finally, the practical problems of flow across a drilling riser and the coupled drillship-riser system are demonstrated to establish the capabilities of the framework. Some of the targeted numerical characteristics of the framework are robustness, consistency, stability, efficiency, computational scalability, flexibility, and ease of implementation.

1.3 Contributions

Based on the numerical analyses of the developed techniques in the present work, the computational framework offers significant contributions to the research community as well as the industries. The work carried out in this study is multi-disciplinary and covers areas such as computational mathematics, numerical analysis, fluid mechanics and finite element analysis. Some of the major contributions from the development of the framework can be summarized as:

- A novel positivity preserving variational method to solve a convection-diffusion-reaction equation,
 - A conservative and energy-stable two-phase formulation based on phase-field models em-

Chapter 1. Introduction

ploying the Allen-Cahn equation,

- A grid-adaptive algorithm for the two-phase formulation,
- A partitioned iterative coupling algorithm for the two-phase fluid-structure interaction,
- A positivity preserving hybrid RANS/LES turbulence model, and
- An integrated, stable and robust turbulent two-phase FSI solver.

1.4 Organization of the thesis

The thesis is organized in-line with the contributions stated in the previous section. Chapter 2 discusses the challenges in the computational modeling of a CDR equation and single-/two-phase FSI and some of the recent works from the literature.

We begin the study by analyzing the scalar CDR equation and design a novel positivity preserving variational (PPV) method in Chapter 3. It describes in detail the proposed methodology to solve the canonical CDR equation which finds application in many areas from heat and mass transfer, phase-field modeling to turbulence transport equations. The governing equation and its variational form are reviewed. With the help of Fourier analysis, the shortcomings of the Galerkin/least-squares (GLS) and the subgrid-scale (SGS) methods are discussed with the proposed linear stabilization methodology. A nonlinear stabilization strategy is proposed while maintaining the positivity preserving property at the element matrix level. Convergence and stability analyses are carried out to assess the proposed method and its properties. Finally, some one-dimensional and two-dimensional cases are tested and compared with the exact solution.

Chapter 4 reviews the fundamentals of the variational fluid-structure framework which form the preliminaries for the FSI problems discussed in the subsequent chapters.

The developed PPV method is then applied to the conservative Allen-Cahn equation to model the two-phase flows in Chapter 5 which introduces the concept and advantages of the diffuse-interface description in the two-phase flows. The positivity preserving and convergence properties are analyzed by numerical tests involving standalone Allen-Cahn verification, Laplace-Young law and liquid sloshing in a tank. The ability of the formulation to handle any topological changes of the fluid-fluid interface is demonstrated by two- and three-dimensional

Chapter 1. Introduction

dam breaking tests. Finally, a wave-structure interaction problem of wave run-up on a truncated circular cylinder is demonstrated and conclusions are drawn.

Chapter 6 extends the accuracy in the solution of the Allen-Cahn equation by including the mesh adaptive algorithm. A nonlinear adaptive variational procedure for adapting the computational mesh along the fluid-fluid interface is presented based on the residual error estimates of the Allen-Cahn equation. Numerical tests on sloshing tank reveal a reduction in the computational resources and elapsed time for the adaptive case compared to its non-adaptive counterpart. The adaptive algorithm is then demonstrated on a two-dimensional dam-break problem.

Two-phase fluid-structure interaction is the subject of discussion in Chapter 7 in which a partitioned iterative coupling algorithm is proposed. The partitioned-block nature of the coupling eases the computational implementation of different solves such as Navier-Stokes, Allen-Cahn, and structure. A nonlinear iterative force correction scheme is employed for stability in low structure-to-fluid mass ratio regimes for the FSI problems. Natural decay motion under heave and rotation for a circular cylinder and a rectangular barge are studied and validated respectively. The two-phase FSI framework is then applied to a riser with internal two-phase flow experiencing vortex-induced vibration due to an external uniform current flow.

The application of the PPV method to the hybrid RANS/LES turbulence modeling is discussed in Chapter 8 where the turbulence transport equation is expressed as a CDR equation. Uniform flow across a circular cylinder is validated with the numerical and experimental data from the literature before demonstrating the flow across a marine riser at high Reynolds number.

Chapter 9 deals with the ultimate demonstration of the turbulent two-phase fluid-structure interaction applied to the objective problem of the offshore vessel-riser system. First, wave profiles for flow across a Wigley hull are simulated and the results are compared with that of the experiments. Then, we present some results for a free heave motion of a navy combatant vessel under free-surface ocean waves and finally, we demonstrate the capability of the developed framework to solve the large-scale problem of a full-scale drilling vessel-riser system.

Lastly, some conclusions and recommendations for the future work are summarized in Chapter 10.

Chapter 2

Literature Review

Following the step-by-step methodology towards the single-/two-phase turbulent fluid-structure interaction framework shown in Fig. 1.1, we develop the scientific understanding of each component based on the research studies carried out in the past in this chapter. We first discuss the history and state-of-the-art of the canonical convection-diffusion-reaction equation which will lay down the fundamental numerical challenges in solving a scalar transport equation. Then, we introduce the concept of phase-field methods to model two-phase flows and compare them with the conventional techniques utilized to capture the fluid-fluid interface of two-phase flows. We highlight the advantages of employing the Allen-Cahn based phase-field methodology in capturing the fluid-fluid interface. Furthermore, some of the methods to increase the accuracy of the two-phase flow solution based on adaptive grid refinement are also discussed. After identifying the challenges in solving the two-phase flow problems, we dive into the studies carried out so far on the two-phase fluid-structure interaction and some of the issues related to the coupling at the fluid-structure interface. Finally, we review the experimental and numerical studies on the vortex-induced vibrations of long slender risers and ship hydrodynamics.

2.1 Convection-diffusion-reaction equation

We start by understanding the convection-diffusion-reaction (CDR) equation which forms the canonical equation for any continuum transport system. Numerical discretization inevitably introduces errors in the solution since the discrete computational domain cannot capture all the

Chapter 2. Literature Review

effects of the continuous equation. Of particular interest of this work is a generic CDR equation:

$$\frac{\partial \varphi}{\partial t} + \mathbf{u} \cdot \nabla \varphi - \nabla \cdot (\mathbf{k} \nabla \varphi) + s\varphi = f, \quad (2.1)$$

defined on a d -dimensional domain $\Omega(t) \subset \mathbb{R}^d$, where φ is the unknown scalar variable, \mathbf{u} , \mathbf{k} , s and f are the convection velocity, diffusivity tensor ($\mathbf{k} = k\mathbf{I}$ for isotropic diffusion, k and \mathbf{I} being the diffusion coefficient and identity tensor respectively), reaction coefficient and source respectively. The first-order spatial derivatives in the equation constitute the convection which transports any information along the characteristic curves with a certain velocity \mathbf{u} , the second-order spatial derivatives represent the diffusion which spreads the information throughout the domain and the term $s\varphi$ denotes the reaction effect, which produces or destructs the information. The exact solution of Eq. (2.1) in one-dimension can be characterized based on the roots of the characteristic polynomial (the sign of $D = |\mathbf{u}|^2 + 4ks$), if $D \geq 0$ it is said to fall under the exponential regime with production for $s < 0$, and dissipation (or destruction) with $s \geq 0$, and for $D < 0$, the solution constitutes the propagation regime. After discretization, the numerical solution of the CDR problem exhibits distinctive properties depending upon which physical effect of the equation is dominant and the applied boundary conditions, and may manifest a boundary layer-like behavior near the regions with high gradients. The layers formed along the outflow boundaries are known as exponential layers while those along the tangential boundaries to the flow direction are termed as parabolic or characteristic boundary layers. Moreover, such layers can also manifest close to any sharp discontinuity inside the computational domain, referred to as parabolic or characteristic internal layers [26].

It is known that the standard Galerkin weighted residual method produces spurious node to node oscillations in the numerical solution when convection effects are dominant [27]. One of the reasons is the inability of the scheme to resolve the high gradient layers, which manifests as numerical oscillations in the computational domain. Therefore, several methods have been proposed to stabilize the solution through the Petrov-Galerkin perturbation based on a stabilization parameter (τ) of the underlying variational formulation which tends to capture the subscale physical phenomena missed out by insufficient mesh resolution. The perturbed term acts as an upwinding function by removing the influence of outflow boundary condition on the convection term. This upwinding causes excessive crosswind diffusion and therefore, it was limited to the streamline direction. A streamline upwind Petrov-Galerkin (SUPG) method

Chapter 2. Literature Review

was developed in [28] which introduces upwinding of the convection, transient as well as source terms. In the generalization of the analysis from one- to two-dimensions, the streamline direction may not be the most appropriate upwind direction [29]. It is observed that SUPG method does not avert overshooting and undershooting in the vicinity of the sharp layers (boundary and internal layers) in multi-dimensions. Furthermore, due to the loss of conservation of physical quantities at the discrete level and discontinuities in the domain, the numerical solution may be oscillatory or unbounded. The discrete maximum principle (DMP) preserves this positivity by avoiding any maxima or minima inside the domain. The algorithm proposed in [29] focused on making the local element matrix non-negative to satisfy the DMP condition but was restricted only for linear triangular elements. Another effort towards monotone methods with conservation properties was performed in [30] where element geometry and flow rates were interpolated to approximate the convection term. Unfortunately, the above method was also limited to bilinear quadrilateral elements.

Nonlinear methods depending on the solution and satisfying the DMP condition were put forward to circumvent the Godunov's theorem for finite difference approximation, which restricts the accuracy of a linear monotone method to first-order [31]. In the field of finite element method, one of the successful attempts to satisfy the DMP was achieved in [32] whereby a nonlinear discontinuity capturing term was added to the variational formulation acting in the direction of the solution gradient. A further modification to the discontinuity capturing term was carried out in consistent approximate upwind (CAU) method [33]. This method manifested excessive diffusion in the regions of regular solution. Improving the drawbacks of the CAU method, the streamline approximate upwind Petrov-Galerkin (SAUPG) method was proposed in [34] which behaved as SUPG near the regular solution and as CAU in proximity to the boundary layers. To improve the stability and convergence properties while maintaining accuracy, the least-squares framework was introduced in Galerkin/least-squares (GLS) method [35]. The gradient Galerkin/least-squares (GGLS) method was proposed in [36] which considered the least-square form of the gradient of the Euler-Lagrange equation for the stabilization. In another study [37], GLS with discontinuity capturing term was generalized to the Euler and Navier-Stokes equations with a simplified formula for the stabilization parameter. A need for crosswind diffusion rather than an isotropic diffusion for the discontinuity capturing term

Chapter 2. Literature Review

was suggested in [1], which provided relatively accurate results with improved convergence. A comprehensive analysis of the performance of linear stabilization methods such as SUPG, space-time Galerkin/least-squares (ST-GLS), subgrid-scale (SGS), characteristic Galerkin (CG) and Taylor-Galerkin (TG) was performed in [38].

The origin of the stabilization parameter was reviewed in [39, 40] using the subgrid-scale phenomena. While the large scales are resolvable by the variational finite element method, the small unresolvable scales are modeled via Fourier representation of the Green's function of the subscale problem. The residual-based variational multiscale (RBVMS) concept arises from the same multiscale phenomena described above. The details of the method and its application to the Navier-Stokes equations can be found in [41, 42]. Another attempt in explaining the stabilization parameter was carried out with the aid of Taylor series and the concept of flow balance in a finite domain, which derived expressions using the finite increment calculus (FIC) method in [43, 44, 45]. FIC method was extended to multi-dimensional systems in [46]. Apart from the formulations presented above, the concept of flux-corrected schemes (FEM-FCT) and total variational diminishing schemes (FEM-TVD) pertaining to finite element method were proposed in [47, 48, 49] which captured the discontinuities and shocks by adding an anti-diffusive flux to the first-order accurate (excessively diffusive) method generated by the discrete upwinding of the scheme, which are generally referred to as high resolution methods for finite-difference/finite-volume approximations [50].

Extension of the finite element stabilization to the transport equation containing reaction effects was carried out in [51] by adding a term depending on the magnitude of the solution gradient, known as SUPG with diffusion for reaction-dominated regions (SUPG+DRD). This method performed well for standalone convection- and reaction-dominated regimes, but was inaccurate when both the effects were dominant. Solving the issue posed by the method above, SUPG with centered Petrov-Galerkin (SU+C)PG was proposed in [52] which satisfied the DMP and added a separate term for reaction dominated problems. Furthermore, the Galerkin/least-squares/gradient least-squares (GLS/GLS) method for convection-diffusion equation with production was presented in [53] and transient convection-diffusion equation was shown to behave in a similar way as the transport equation with reaction effects in [54]. The expression for the stabilization parameter (τ) for the CDR equation was derived to satisfy the DMP in [38],

Chapter 2. Literature Review

however, it was concluded that none of the compared methods therein generated a non-negative matrix in multi-dimensions. With the advent of the subgrid-scale phenomena explaining the origins of τ , methods based on this model were proposed for the reaction-dominated regime like the algebraic subgrid-scale method (SGS) [55], unusual stabilized finite element method (USFEM) and its variants [56], and methods employing the Green's function approach [57, 58]. A comparison between the effects of the expression of τ derived using variational multiscale (VMS) strategy and τ proposed in [38, 37] was performed in [59]. Generalization of the CDR equation for distorted meshes employing the VMS approach of adding diffusion to the direction of maximum instability (where the element Peclet and Damköhler numbers are large) was carried out in [60]. Some of the recent works in the stabilization of CDR equation has been studied in [61, 62] which employed the discrete upwind operator to maintain positivity in the solution (DMP condition) and proposed a nonlinear method to stabilize the solution in most of the convection- and reaction-dominated regimes.

Summarizing, based on the challenges discussed, some of the possible room for improvement in the stabilization of the CDR equation can be:

- Combining the effects of the GLS and SGS methods to improve the linear stabilization,
- Maintaining positivity in the solution through nonlinear stabilization strategy,
- Reducing the phase and amplitude errors in the solution, and
- Obtaining a solution with second-order accuracy.

2.2 Two-phase flow description

Now, we concentrate on the description of the methods for modeling the fluid-fluid interface in two-phase flows. It is well known that the numerical treatment of two-phase flow involving immiscible fluids poses certain challenges owing to the physical complexity in the representation and the evolution of the fluid-fluid interface [63]. The representation of the continuum interface between the two phases can be considered by either interface-tracking or interface-capturing techniques. For the interface-tracking, a boundary between the two fluid sub-domains is explicitly tracked, for example, front-tracking [64], [particle tracking](#) [65] and arbitrary Lagrangian-Eulerian [66] methods. While these methods can accurately locate the interface position by

Chapter 2. Literature Review

tracking the moving boundary or markers on the interface, they may lead to numerical difficulties for relatively larger interface motion and topological changes. During the topological changes, remeshing can be computationally expensive for interface-tracking methods in three-dimensions. In the case of interface-capturing, no explicit representation of the interface is considered, instead the interface is represented implicitly using a field function throughout the computational domain on an Eulerian grid, such as level-set, volume-of-fluid, and phase-field approaches. Through an implicit evolution of the interface field function, topological changes such as merging and breaking of interfaces can be naturally handled by the interface-capturing methods. During the evolution of interface, the discontinuous nature of physical quantities such as density, viscosity, and pressure can also pose difficulties during the numerical treatment of the interface. In particular, these discontinuities in the properties may lead to unphysical and spurious oscillations in the solution which can eventually result in the unbounded behavior of multiphase flow system. The background fixed mesh has to be sufficiently resolved to capture these discontinuities leading to high computational cost. Furthermore, surface tension effects or capillary forces along the interface need to be accurately modeled. Several models have been discussed in the literature to evaluate the surface tension, one of which is the continuum surface force method [67]. The conservation of mass is another challenge which is crucial for a physically consistent solution of multiphase flow.

Among the types of interface-capturing methods, the level-set and volume-of-fluid (VOF) are the most popular methods. The VOF method utilizes a volume-of-fluid function to extract the volume fraction of each fluid within every computational cell. While the VOF method conserves mass accurately for incompressible flows, the calculation of interface curvature and normal from volume fractions can be quite complex due to interface reconstruction [68, 64, 69]. In addition, the smearing of the interface by numerical diffusion causes additional difficulty. On the other hand, the level-set approach can provide a non-smeared interface by constructing a signed-distance function (level-set function) of a discretization point to the interface [70]. The zero-level-set of the distance function provides a sharp-interface description and the curvature of the interface can be approximated with high accuracy. However, the level-set method does not conserve mass. The reasons behind the inability of level-set to conserve mass are numerical dissipation introduced due to discretization and re-initialization process to keep the

Chapter 2. Literature Review

level-set function as a signed distance function [71]. Although methods including high-order discretization scheme [72], improved re-initialization [72, 73, 74], coupled particle tracking/level-set [75, 76, 77], and coupled level-set/volume-of-fluid [78, 79, 80] have been proposed to deal with the mass conservation issue, these hybrid treatments make the overall scheme much more complex and computationally expensive. To improve the mass conservation property, a conservative level-set method was proposed in [81, 82] whereby the signed distance function was replaced with a hyperbolic tangent function. However, the re-initialization was necessary to maintain the width of the hyperbolic tangent profile in this case. One of the recent improvements in the level-set approach is the extended finite element method (XFEM) which utilizes the enrichment of shape functions of the elements along the interface region [3]. Both the level-set and the volume-of-fluid techniques utilize some kind of geometric reconstruction for the modeling of the fluid-fluid interface, which can be quite tedious to implement in three-dimensions for unstructured grids over complex geometries.

Interface-capturing for two-phase flows can be further classified into sharp-interface and diffuse-interface descriptions. For the sharp-interface description, the interface between the two phases is treated as infinitely thin with the physical properties such as density and viscosity having a bulk value until the interface discontinuity. In the diffuse-interface description, however, a gradual and smooth variation of the physical properties is assumed across the phase interface of a finite thickness. The physical properties are a function of a conserved order parameter which is solved by minimizing a free energy functional based on thermodynamic arguments [83]. Similar to the VOF and level-set methods, the interface location is defined by the contour levels of the phase-field order parameter. Unlike the sharp-interface description, the phase-field formulation does not require to satisfy the jump conditions at the interface and there are rapid but smooth variations of the order parameter and other physical quantities in the thin interfacial region. The diffuse-interface description has been shown to approach the sharp-interface limit asymptotically [84].

The phase-field models originate from the thermodynamically consistent theories of phase transitions via minimization of gradient energy across the diffuse-interface. The phases are indicated by an order parameter (ϕ) (e.g., $\phi = 1$ in one phase and $\phi = -1$ in another phase) which is solved over an Eulerian mesh and the interface is evolved. As these models fall under

Chapter 2. Literature Review

the diffuse-interface description, no sharp conditions at the interface between the two phases are required to be satisfied explicitly. The surface tension and capillary effects can be modeled as a function of the phase-field order parameter depending on the minimization of the Ginzburg-Landau energy functional. Therefore, these methods do not require any re-initialization or reconstruction at the interface. Furthermore, the mass conservation property can be imparted in a relatively simple manner. The topology changes in the interface can be handled by the phase-field models easily given that the mesh is refined enough to capture these phenomena. Overall, the phase-field models offer attractive physical properties for the modeling of multiphase systems for a broad range of conditions with topological changes while maintaining the mass conservation property.

In the phase-field models, the interface is evolved by solving a transport equation formulated in the form of a gradient flow of the energy functional, either in the $L^2(\Omega)$ norm for the Allen-Cahn (AC) equation [85] or in the $H^{-1}(\Omega)$ norm for the Cahn-Hilliard (CH) equation [86]. Although the CH equation conserves mass naturally, the fourth-order of the differential equation imposes the requirement for longer stencils or higher-order polynomial approximation to obtain a stable solution. With the discretization using lower-order polynomials, the CH equation thus has to be split as a set of two coupled equations, which increases the degrees of freedom. On the other hand, the AC equation is a second-order differential equation and avoids the requirement of equation splitting. Furthermore, the mass conservation property can be imposed by a Lagrange multiplier in the conventional AC equation. Owing to the simplicity of the differential form, we consider the Allen-Cahn phase-field equation for our two-phase computations.

For the phase-field models, the energy stability and the mass conservation properties are strongly influenced by the treatments of the nonlinearity of the double-well potential function and the Lagrange multiplier, respectively. As reviewed in [87], the nonlinearities in the phase-field methods can be handled in various ways to obtain an energy-stable scheme. The mid-point approximation of the derivative of the double-well potential produces an unconditional energy-stable scheme [88]. With regard to imposing the mass conservation in the AC equation, a technique employing global and time-dependent Lagrange multiplier was suggested in [89, 90]. Some of the recent works which have used the conservative AC equation and coupled it with the Navier-Stokes equations are [91, 92, 93]. These works employed only a global Lagrange

Chapter 2. Literature Review

multiplier, however, the need for a multiplier having spatial and temporal dependency was suggested in [94, 95] to capture the geometrical features more accurately. An operator splitting technique employing such multiplier under the finite difference framework was carried out in [96, 97]. These methods were at most first-order accurate in time. For problems consisting of complicated domains, the performance of the finite element method was found to be superior to the finite difference schemes in [98]. In the present phase-field formulation, we consider space and time-dependent Lagrange multiplier within the finite element framework.

The AC phase-field equation mathematically represents a complex nonlinear convection-diffusion-reaction (CDR) equation. The solution of this equation can exhibit oscillations when the convection or reaction effects are dominant. One of the basic strategies for the finite difference and finite volume discretizations to deal with such instabilities is a classical upwinding technique. Although the algorithm is stable, it is only first-order accurate and leads to smearing of the solution. Some of the works which deal with reducing these oscillations and thus preserving the positivity property of the solution in the variational framework are [99, 1] which focus on stabilizing the solution for convection-dominated regimes.

While interface-capturing methods can handle breaking and merging of the interface in a simple manner compared to interface-tracking, the absence of prior knowledge of the location of the convecting fluid interface forces the user to refine the computational grid throughout the domain. This, in turn, increases the number of unknowns, increasing the computational cost for a desired spatial accuracy of the underlying fluid-fluid interface problem. Refining the computational mesh adaptively with the evolving interface during the run-time is a promising way to reduce the degrees of freedom and to increase accuracy and efficiency of interface-capturing methods.

Some of the refinement strategies are mesh movement or repositioning (r -methods), mesh enrichment (h/p -methods) and adaptive remeshing (m -methods) [100]. Among these methods, h -refinement is particularly attractive and deals with the addition of extra degrees of freedom near a region of interest in the computational domain and p -refinement elevates the order of approximation by using higher-order polynomials. The h -refinement is preferred for the current study since it conserves the physical quantity and can be easily vectorized and parallelized. It can be carried out by either subdivision of the elements into equal parts or by recursive

Chapter 2. Literature Review

subdivision of the largest edge side of the element. To optimize the degrees of freedom and the underlying mesh, the error indicators based on *a posteriori* residual estimates are constructed. The indicators can be based on gradients of the concerned quantities or the residuals of the equation being solved. Some of the commonly used error estimators are residual-based, hierarchical-based [101] and ZZ-type [102] error estimators. A review of the mathematical theory behind the error estimates derived for a variety of equations can be found in [103, 104, 105]. Basic strategies and algorithms for adaptive methods from a computational perspective are discussed in [106].

Some of the works dealing with the error estimates for the non-conservative Allen-Cahn equation are [107, 108, 109, 110, 111, 112]. On the other hand, mesh refinement of the conservative Allen-Cahn equation coupled with the Navier-Stokes equations has been the topic of some of the recent works [93, 91, 113]. One of recent works in [93] utilized the open-source library [114] for the adaptive mesh refinement, which utilizes a tree data structure to store the refinement hierarchy; while a mesh distribution strategy was used in [91, 113]. A tree-type data structure for the hierarchical mesh can cover a good amount of the computational storage space. The algorithm of [115] avoids such data structures thereby easing the implementation of the algorithm. Moreover, most of the past literature has dealt with structured mesh adaptivity algorithms, restricting the use of unstructured grids for practical geometries.

Based on the challenges in the modeling of two-phase flow systems, the numerical methodology can be further improved by:

- Imparting the positivity property to the conservative Allen-Cahn equation for the reaction-dominated regimes,
- Improving mass conservation and energy stability properties,
- Spatial and temporal discretization with second-order accuracy,
- Adaptive mesh refinement of the underlying grid to reduce the computational cost, and
- Simplified and stable partitioned coupling of the Navier-Stokes and the Allen-Cahn equations.

2.3 Two-phase fluid-structure interaction

Two-phase FSI involves complex nonlinear interface dynamics and the difficulties associated with the boundary conditions, viz., the evolution of the fluid-fluid interface with complex surface phenomena, the no-slip condition at the structure in the neighborhood of highly-deformable fluid-fluid interface, and the precise movement of the fluid-structure interface. The fluid-fluid interface has to be evolved with the deformation of the structure while satisfying the no-slip condition at the fluid-structure interface. This can be achieved by either considering the structural domain as Lagrangian and then solving the two-phase flow equations in the arbitrary Lagrangian-Eulerian (ALE) coordinates, or with the help of an immersed boundary technique where the equations are solved in an Eulerian grid with boundary conditions represented by a fictitious force field [116, 117]. The modeling of boundary-layer vorticity flux and near-wall turbulence at the fluid-structure interface is accurate if one considers a boundary-conforming grid (e.g., ALE framework) to track the fluid-structure interface. Furthermore, the robust and efficient modeling of the three-dimensional fluid-fluid interface using a sharp-interface description via ALE-type interface-tracking technique is a non-trivial task, especially in problems involving any topological changes of the interface. Therefore, it can be more advantageous if one considers the diffuse-interface description based phase-field method for the fluid-fluid interface.

Methods employing the boundary-conforming grid for the fluid-structure interaction can be classified into monolithic and partitioned schemes. In a monolithic approach [118, 119, 120], the fluid and structural equations are assembled into a single block matrix and the fluid and structural variables are solved simultaneously. These methods are robust and stable for low structure-to-fluid mass ratio of the structures, but are quite computationally expensive. They lack the advantage of flexibility and modularity in utilizing the existing fluid and structural solvers [118, 119, 120, 121]. A partitioned approach, on the other hand, solves the fluid and structural equations in a sequential manner, becoming flexible and facilitating the use of existing fluid and structural solvers with minimal changes to the code.

Large-scale simulations of offshore structures involving free-surface ocean waves coupled with the flexible multibody structures require an efficient and general numerical approach. While the flow can be modeled as viscous, incompressible two-phase fluid and can include

Chapter 2. Literature Review

turbulence effects, the offshore structures can include rigid bodies, shells, beams, cables, etc. For solving such complex and diverse system via the monolithic approach, substantial efforts and restructuring at the levels of linear algebra and finite element formulation for the fluid and the structural solvers are required. However, a partitioned decoupled scheme finds some attractive advantages in iterative solvers, preconditioning strategies, scalability and parallel processing. Furthermore, the spatial and temporal discretizations of the structural and flow solvers can be chosen independently for such methods. Therefore, partitioned decoupling of the fluid-structure equations is preferred for such large-scale applications.

Based on the discussion above, the following characteristics are expected to be exhibited by a two-phase fluid-structure interaction framework:

- Stable and consistent formulation with the capability to handle low structure-to-fluid mass ratios,
- Stability for high density and viscosity ratios of the two phases of the fluid,
- Robustness in capturing the topological changes in the fluid-fluid interface with the moving structure, and
- Ease of implementation and flexibility due to the partitioned decoupling.

2.4 Turbulent flow FSI

In this section, we discuss the closure problem for the modeling of turbulent flows. To capture the complex wake flow dynamics along the long slender risers at high Reynolds numbers, the turbulent effects have to be modeled correctly. This can be broadly carried out via three approaches, viz., direct numerical simulation (DNS), unsteady Reynolds averaged Navier-Stokes (RANS), and large eddy simulation (LES). The DNS and LES approaches are computationally expensive due to massively separated turbulent wake flow and the requirement of spanwise resolution for large aspect ratio applications. Since both DNS and LES for such large-scale applications are beyond the capacity of current computer hardware and URANS is not reliable for massively separated vortex flows [122], a hybrid RANS/LES approach, known as delayed detached eddy simulation (DDES) [123, 124] offers a practical avenue by treating near-wall

Chapter 2. Literature Review

turbulent boundary layer and near-wall turbulence effects through the Spalart-Allmaras (S-A) URANS equation.

The underlying S-A equation of DDES is phenomenological and poses several numerical challenges while dealing with its variational discretization using the finite element formulation, namely (a) the inclusion of the reaction terms, (b) the production and destruction effects, and (c) spurious oscillations near the boundary and internal layers. The turbulent viscosity variable of the transport equation should exhibit non-negative values for the positive boundary and initial conditions. However, discretizing the equation using numerical methods may result in the oscillations in the solution. This is the similar phenomenon that one observes when solving the convection-diffusion-reaction equation using the classical streamline upwind Petrov-Galerkin or Galerkin/least-squares methodology without any discontinuity capturing. The negative solutions can be prevented through simple clipping, but such clipping causes serious damage to the convergence and accuracy properties of evolving residual of the partial differential equation. Many methods have been proposed to limit these negative values of the eddy viscosity in the solution of the S-A model, which are mentioned in [125]. In [126], discrete operators are used in making a first-order accurate positive scheme. The method in [127] deals with treating the convection part and the source term by the finite volume method and the diffusion terms by the finite element approach. Modification of the differential equation for the S-A model itself was carried out in [128] to preserve the positivity and the negative S-A model was proposed in [125].

One of the possible improvements in the numerical methodology which is dealt with in this work is to obtain a positivity preserving and bounded solution of the turbulence transport equation via nonlinear stabilization of the S-A transport equation.

2.5 Riser VIV and ship hydrodynamics

Here, we discuss some of the large-scale applications of single-/two-phase FSI, viz., vortex-induced vibrations (VIV) of long flexible risers and ship hydrodynamics. Understanding these two phenomena will pave way for a coupled FSI simulation of the vessel-riser system which forms the motivation for the current study.

2.5.1 VIV of long risers

For slender and flexible cylinders, it has been observed that the response dynamics of VIV is chaotic, complex and consists of unrepeatable motions [129]. This dynamic complexity arises from the fact that several response modes on the structure can get excited by the wake flow simultaneously making it a multi-frequency and multi-modal response. The vibrating flexible cylinder in cross-flow can generate a complex vortex wake that has a profound role on the response trajectories, the phase lock-in between fluid force and motion, and the interaction of the in-line (IL) and the cross-flow (CF) responses. This kind of chaotic response of the riser has been generally attributed to the competition between the different kinds of wake vortex modes (symmetric and asymmetric) in [130, 131]. Moreover, a mixed standing and traveling wave response is usually associated with this chaotic behavior [129]. The ratio between the in-line and cross-flow frequency was observed to be two in the resonance condition and the transverse amplitude was found to be much larger than that in the in-line direction [132]. From the two degree-of-freedom experiment for elastically mounted cylinders [133], it was found that the preferred direction of the cylinder in the figure-8 motion tends to be upstream at the extreme transverse amplitudes during VIV lock-in. The interaction between the in-line and cross-flow responses can be quite complex along the riser span under various incoming flow conditions. The loads on the flexible structure can be strongly dependent on the response trajectories or the phase angles between the in-line and the cross-flow motions. The spatial-temporal regions of energy transfer from the surrounding fluid flow to the riser structure are a function of local motion trajectories, whereby the counter-clockwise trajectories relate to the wake excitation region and the energy transfer from the fluid flow to the structure, and the damping and energy loss is connected with the clockwise motion trajectories.

Various fluid-structure interaction experiments have been performed to understand the behavior of the risers with the incoming subsea uniform and shear currents. The model test VIV experiments conducted by Norwegian Deepwater Programme [134] ($L/D = 1400$) and Exxon-Mobil [135] ($L/D = 482$) considered both uniform as well as sheared ocean currents with bare and straked configurations of the riser, where L denotes the length of the riser and D is the cross-sectional diameter. The time series of displacements were extracted by acceleration measurements along the span of the flexible structure, which have provided a significant information

Chapter 2. Literature Review

about the response amplitude of vibration and the mode excitation. To understand the effects of higher harmonics and the traveling wave induced fatigue damage, the field experiments by the Deepstar sponsored VIV experiment campaign [136] with $L/D = 4200$ and by British Petroleum [137] with $L/D = 300\text{-}1700$ were conducted. The focus of the high L/D experiment campaign was to obtain data from an instrumented riser model to provide an understanding of traveling wave and higher mode VIV excitations to improve semi-empirical codes. However, these model tests and field experiments could not establish physical relations among the phase-locked traveling wave along the span, the figure-8 trajectory motion and the vortex shedding dynamics behind the vibrating flexible cylinder. Due to the complexity of the hydroelasticity associated with the cylinder-wake interaction [138], theoretical and semi-empirical models remain incomplete for vibrating flexible cylinders in the fluid flow. In particular, the complex interactions among various response modes of vibrations are not accounted properly in the semi-empirical models, thus necessitating the use of fully-coupled Navier-Stokes based VIV analysis with a high-fidelity turbulence modeling.

Some progress has been made in the understanding of VIV of a long single cylinder using fully three-dimensional (3D) fluid flow simulations with a simple structural model [139, 140, 141]. With the flexible characteristic of the structure, the amplitude response can be quite complex and vary along the span of the structure. Recently, fully-coupled numerical simulation has emerged as an effective tool with high accuracy for studying VIV at high Reynolds numbers. Therefore, the process of developing an efficient and robust numerical methodology for vibrating flexible structures and a systematic validation of the numerical results with full-scale measurements has a great significance to the offshore industry. For example, a finite element method was used in [139, 142] while a spectral element method was utilized in [143] to simulate the VIV of the flexible riser. A similar study with finite analytic method was carried out in [144] with the aspect ratio of 482. A comparison of the numerical results with that of the experiment [135] was performed for linear and sheared currents in [145] using a commercial multi-field solver. It was observed that in all the cases, the in-line response frequency was almost twice that of the cross-flow response frequency marking a case of dual resonance. We try to shed some light on the response patterns and trajectories along the riser subjected to a uniform current flow in the present study with the developed FSI framework. This will enhance the understanding of

Chapter 2. Literature Review

the VIV of risers to some extent and will be beneficial for the research community as well as offshore industry.

2.5.2 Ship hydrodynamics

The hydrodynamic forces on a ship hull are crucial for the offshore operators to estimate the ship resistance as well as the drift. These pieces of information are valuable to mitigate the drift in case of drilling vessels where it is required by the vessel to minimize its motion for the drilling process to be continuous. Complex ocean environment may cause high amplitude motion of the vessel, leading to large drift from the drilling center, thus hampering the drilling operation.

There have been several experimental and numerical studies to quantify the hydrodynamics of a ship hull. Starting from the basic geometries of a Wigley hull, the experimental and numerical studies were carried out in [146] and [147, 148, 149] respectively. The ship hull considered in the present work, the US Navy DTMB 5415 has been extensively studied in the literature. The hull resistance, pitch angle, and heave displacement were quantified at varying Froude numbers experimentally in [150], which formed a rigorous dataset for the numerical studies [151, 152].

As per the knowledge of the author, there does not exist a coupled drilling vessel-riser numerical study, which is the ultimate practical application of the developed numerical framework in this dissertation. The present work will demonstrate the capability of the framework to handle such large-scale FSI systems, paving way for high-fidelity simulations for enhanced design and technical understanding.

Chapter 3

The Positivity Preserving Variational Method*

In this chapter, we present a positivity preserving variational method to solve the canonical convection-diffusion-reaction equation. The method is designed by satisfying the positivity condition at the finite element local matrix level while being nonlinear to iteratively correct the discretization error. The technique is then extended to multi-dimensions and assessed by extensive error analyses and numerical tests.

3.1 The convection-diffusion-reaction equation

The convection-diffusion-reaction (CDR) equation forms the most canonical form for a transport system with reaction effects. We review the differential form as well as the semi-discrete variational form for the equation in this section.

3.1.1 Strong differential form

Consider a d -dimensional spatial domain $\Omega(t) \subset \mathbb{R}^d$ with the Dirichlet and Neumann boundaries denoted by $\Gamma_D^\varphi(t)$ and $\Gamma_H^\varphi(t)$ respectively. The CDR equation (with φ as the scalar variable) is

*Parts of this chapter have been published in “V. Joshi and R.K. Jaiman, A positivity preserving variational method for multi-dimensional convection-diffusion-reaction equation, *Journal of Computational Physics*, 339, Pg. 247-284 (2017).”

written in the strong form as

$$\frac{\partial \varphi}{\partial t} + \mathbf{u} \cdot \nabla \varphi - \nabla \cdot (\mathbf{k} \nabla \varphi) + s\varphi = f, \quad \text{on } \Omega(t), \quad (3.1)$$

$$\varphi = \varphi_D, \quad \forall \mathbf{x} \in \Gamma_D^\varphi(t), \quad (3.2)$$

$$\mathbf{k} \nabla \varphi \cdot \mathbf{n}^\varphi = h^\varphi, \quad \forall \mathbf{x} \in \Gamma_H^\varphi(t), \quad (3.3)$$

$$\varphi = \varphi_0, \quad \text{on } \Omega(0), \quad (3.4)$$

where $\varphi = \varphi(\mathbf{x}, t)$ is the scalar unknown which depends on the spatial coordinates \mathbf{x} at time t , \mathbf{u} is the convection velocity, \mathbf{k} is the diffusivity tensor, s and f are the reaction coefficient and the source term respectively. It is assumed that the diffusivity tensor \mathbf{k} is isotropic, i.e., $\mathbf{k} = k\mathbf{I}$, \mathbf{I} being the identity tensor and k is a scalar positive quantity defined as the diffusion coefficient of the problem. The Dirichlet and Neumann boundary conditions are given by φ_D and h^φ respectively and \mathbf{n}^φ denotes the unit normal to the Neumann boundary. The initial condition on the scalar variable is represented by φ_0 .

3.1.2 Semi-discrete variational form

The CDR equation is discretized in time by the generalized- α method [153]. It enables a user-defined high-frequency damping which is desirable for coarser discretization in space and time, which is achieved by controlling a parameter called the spectral radius ρ_∞ . The following expressions are employed for the discretization:

$$\varphi^{n+1} = \varphi^n + \Delta t \partial_t \varphi^n + \gamma \Delta t (\partial_t \varphi^{n+1} - \partial_t \varphi^n), \quad (3.5)$$

$$\partial_t \varphi^{n+\alpha_m} = \partial_t \varphi^n + \alpha_m (\partial_t \varphi^{n+1} - \partial_t \varphi^n), \quad (3.6)$$

$$\varphi^{n+\alpha} = \varphi^n + \alpha (\varphi^{n+1} - \varphi^n), \quad (3.7)$$

where γ , α and α_m are the generalized- α parameters defined by

$$\alpha_m = \frac{1}{2} \left(\frac{3 - \rho_\infty}{1 + \rho_\infty} \right), \quad \alpha = \frac{1}{1 + \rho_\infty}, \quad \gamma = \frac{1}{2} + \alpha_m - \alpha. \quad (3.8)$$

In the present chapter, we fix the parameters as $\alpha = \alpha_m = \gamma = 0.5$ which correspond to $\rho_\infty = 1$ so that $\partial_t \varphi^{n+\alpha_m} = (\varphi^{n+\alpha} - \varphi^n)/(\alpha \Delta t)$. The temporally discretized CDR equation can then be written as

$$\partial_t \varphi^{n+\alpha_m} + \mathbf{u} \cdot \nabla \varphi^{n+\alpha} - \nabla \cdot (\mathbf{k} \nabla \varphi^{n+\alpha}) + s\varphi^{n+\alpha} = f(t^{n+\alpha}), \quad (3.9)$$

$$\frac{\varphi^{n+\alpha} - \varphi^n}{\alpha \Delta t} + \mathbf{u} \cdot \nabla \varphi^{n+\alpha} - \nabla \cdot (\mathbf{k} \nabla \varphi^{n+\alpha}) + s \varphi^{n+\alpha} = f(t^{n+\alpha}). \quad (3.10)$$

Equation (3.10) can also be expressed as

$$\mathbf{u} \cdot \nabla \varphi^{n+\alpha} - \nabla \cdot (\mathbf{k} \nabla \varphi^{n+\alpha}) + \left(s + \frac{1}{\alpha \Delta t} \right) \varphi^{n+\alpha} = \left(f + \frac{1}{\alpha \Delta t} \varphi^n \right). \quad (3.11)$$

The above equation can be considered as a steady-state equation with modified reaction coefficient and source term. Let the modified coefficients be given by $\tilde{\mathbf{u}}$, $\tilde{\mathbf{k}}$, \tilde{s} and \tilde{f} defined as

$$\tilde{\mathbf{u}} = \mathbf{u}, \quad \tilde{\mathbf{k}} = \mathbf{k}, \quad \tilde{s} = s + \frac{1}{\alpha \Delta t}, \quad \tilde{f} = f + \frac{1}{\alpha \Delta t} \varphi^n. \quad (3.12)$$

Therefore, we will now discretize the following equation in the spatial domain:

$$\tilde{\mathbf{u}} \cdot \nabla \varphi^{n+\alpha} - \nabla \cdot (\tilde{\mathbf{k}} \nabla \varphi^{n+\alpha}) + \tilde{s} \varphi^{n+\alpha} = \tilde{f} \quad \text{on } \Omega(t). \quad (3.13)$$

Discretization of the domain $\Omega(t)$ into n_{el} number of elements is performed such that $\Omega(t) = \cup_{e=1}^{n_{el}} \Omega^e$ and $\emptyset = \cap_{e=1}^{n_{el}} \Omega^e$. Defining the space of trial solution as \mathcal{S}_φ^h and that of the test function as \mathcal{V}_φ^h such that

$$\mathcal{S}_\varphi^h = \{ \varphi_h \mid \varphi_h \in H^1(\Omega(t)), \varphi_h = \varphi_D \text{ on } \Gamma_D^\varphi(t) \}, \quad (3.14)$$

$$\mathcal{V}_\varphi^h = \{ w_h \mid w_h \in H^1(\Omega(t)), w_h = 0 \text{ on } \Gamma_D^\varphi(t) \}, \quad (3.15)$$

the variational statement for the CDR equation is given as: find $\varphi_h(\mathbf{x}, t^{n+\alpha}) \in \mathcal{S}_\varphi^h$ such that $\forall w_h \in \mathcal{V}_\varphi^h$,

$$\int_{\Omega(t)} \left(w_h (\tilde{\mathbf{u}} \cdot \nabla \varphi_h) - w_h \nabla \cdot (\tilde{\mathbf{k}} \nabla \varphi_h) + w_h \tilde{s} \varphi_h \right) d\Omega = \int_{\Omega(t)} w_h \tilde{f} d\Omega, \quad (3.16)$$

Using the divergence theorem and the fact that $w_h = 0$ on $\Gamma_D^\varphi(t)$, Eq. (3.16) becomes

$$\int_{\Omega(t)} \left(w_h (\tilde{\mathbf{u}} \cdot \nabla \varphi_h) + \nabla w_h \cdot (\tilde{\mathbf{k}} \nabla \varphi_h) + w_h \tilde{s} \varphi_h \right) d\Omega = \int_{\Omega(t)} w_h \tilde{f} d\Omega + \int_{\Gamma_H^\varphi(t)} w_h h^\varphi d\Gamma. \quad (3.17)$$

Since the Galerkin finite element method is prone to spurious global oscillations and is unstable for large convection and reaction effects, various stabilization methods have been proposed of which the most commonly used are SUPG and GLS. The stability is introduced by the effect of upwinding through perturbation of the test function. The standard variational formulation

Chapter 3. The Positivity Preserving Variational Method

for such methods is: find $\varphi_h(\mathbf{x}, t^{n+\alpha}) \in \mathcal{S}_\varphi^h$ such that $\forall w_h \in \mathcal{V}_\varphi^h$:

$$\begin{aligned} \int_{\Omega(t)} \left(w_h (\tilde{\mathbf{u}} \cdot \nabla \varphi_h) + \nabla w_h \cdot (\tilde{\mathbf{k}} \nabla \varphi_h) + w_h \tilde{s} \varphi_h \right) d\Omega + \sum_{e=1}^{n_{el}} \int_{\Omega_e} \mathcal{L}^m w_h \tau (\tilde{\mathcal{L}} \varphi_h - \tilde{f}) d\Omega \\ = \int_{\Omega(t)} w_h \tilde{f} d\Omega + \int_{\Gamma_H^\varphi(t)} w_h h^\varphi d\Gamma, \end{aligned} \quad (3.18)$$

where \mathcal{L}^m is the operator on the weighting function given in Table 3.1 and the expression for the stabilization parameter τ is [37]

$$\tau = \left[\left(\frac{1}{\alpha \Delta t} \right)^2 + 9 \left(\frac{4k}{h^2} \right)^2 + \left(\frac{2|\mathbf{u}|}{h} \right)^2 + s^2 \right]^{-1/2}, \quad (3.19)$$

where h is the characteristic element length and $|\mathbf{u}|$ is the magnitude of the convection velocity. The expression for τ has been thoroughly studied in the past with several definitions and its dependence on the equation coefficients and the mesh size can be estimated through the error analysis. The generality of the expression is discussed in Section 3.2.2.4. The residual of the CDR equation is given as

$$\mathcal{R}(\varphi_h) = \tilde{\mathbf{u}} \cdot \nabla \varphi_h - \nabla \cdot (\tilde{\mathbf{k}} \nabla \varphi_h) + \tilde{s} \varphi_h - \tilde{f} = \tilde{\mathcal{L}} \varphi_h - \tilde{f}, \quad (3.20)$$

where $\tilde{\mathcal{L}}$ is the differential operator corresponding to the differential Eq. (3.13).

Table 3.1: Differential operators on the weighting function for stabilization methods

Method	Stabilization operator (\mathcal{L}^m)
SUPG	$\mathcal{L}_{adv} = \tilde{\mathbf{u}} \cdot \nabla$
GLS	$\tilde{\mathcal{L}} = \tilde{\mathbf{u}} \cdot \nabla - \nabla \cdot (\tilde{\mathbf{k}} \nabla) + \tilde{s}$
SGS	$-\tilde{\mathcal{L}}^* = \tilde{\mathbf{u}} \cdot \nabla + \nabla \cdot (\tilde{\mathbf{k}} \nabla) - \tilde{s}$

3.2 The proposed method

We present the positivity preserving variational technique in this section where we design the stabilization terms to maintain positivity in the solution and thereby reduce oscillations which remain after the linear stabilization of SUPG and GLS discussed in the previous section.

3.2.1 Linear stabilization

First, we start by analyzing the linear stabilization terms which are based on SUPG, GLS and SGS methods, by focusing on the reaction coefficient (\tilde{s}), which can become positive or negative depending on the destruction or production effects respectively. We perform Fourier analysis to analyze GLS and SGS methods, the details of which are given in Appendix C and D. We observe that the SGS method performs well in the regime when the reaction coefficient (\tilde{s}) is negative, however, it loses accuracy when $\tilde{s} \gg 0$ due to excessive dissipation [57]. While GLS method is not as diffusive as SGS for $\tilde{s} \geq 0$, it suffers with phase error when $\tilde{s} < 0$. Therefore, we propose a combination of these two methods to benefit in both the production and the destruction regimes. Since linear and multilinear elements are employed in the study, the effect of the diffusion term is assumed negligible in the differential operator. The second term in Eq. (3.18) can thus be modified as

$$\sum_{e=1}^{n_{el}} \int_{\Omega^e} \mathcal{L} w_h \tau (\tilde{\mathcal{L}} \varphi_h - \tilde{f}) d\Omega, \quad (3.21)$$

where $\mathcal{L} = \tilde{\mathbf{u}} \cdot \nabla - \nabla \cdot (\tilde{\mathbf{k}} \nabla) + |\tilde{s}|$. Here, the absolute value function $\mathcal{F}(x) = |x|$ is defined as

$$\mathcal{F}(x) = \begin{cases} x, & \text{if } x > 0, \\ 0, & \text{if } x = 0, \\ -x, & \text{if } x < 0. \end{cases} \quad (3.22)$$

The above method will behave as GLS method for $\tilde{s} \geq 0$ and as SGS when $\tilde{s} < 0$. We next present the design of the positivity condition and nonlinear stabilization of our variational procedure for the CDR equation.

3.2.2 Positivity and nonlinear stabilization

Although SUPG and GLS methods are successful in reducing the spurious oscillations observed in the Galerkin method, some overshoots and undershoots are observed where the gradient of the solution is high or where a sharp discontinuity is present. This is because neither of the above two methods is monotone or positivity preserving [1]. Physical solutions in nature should maintain the sign of their neighbor, precluding such oscillations. Therefore, we look into some of the key criteria to enforce this property at the discrete level.

3.2.2.1 The positivity condition

We next describe the positivity condition in the context of Galerkin finite element formulation for the convection-dominated problems. The positivity preserving condition for the Eq. (3.1) can be defined as follows. Consider a simplified form of Eq. (3.1) with only convection effects:

$$\partial_t \varphi + \mathbf{u} \cdot \nabla \varphi = 0. \quad (3.23)$$

The finite element Galerkin approximation for an explicit scheme of a one-dimensional element between $i - 1$ and i can be written as

$$\frac{\varphi_i^{n+1} - \varphi_i^n}{\Delta t} = - \int_{\Omega(t)} w_h \left(u \frac{\partial \varphi_h}{\partial x} \right) d\Omega = - \int_{\Omega(t)} N^T u \frac{\partial N}{\partial x} d\Omega \begin{bmatrix} \varphi_{i-1}^n \\ \varphi_i^n \end{bmatrix} = - \frac{u}{2h} \begin{bmatrix} -1 & 1 \\ -1 & 1 \end{bmatrix} \begin{bmatrix} \varphi_{i-1}^n \\ \varphi_i^n \end{bmatrix}, \quad (3.24)$$

where N is the row-vector of Lagrangian linear shape functions for one-dimensional elements satisfying the partition of unity property. Therefore, after assembly of the elements for a uniform grid, the finite element based stencil can be expressed as follows

$$\frac{\varphi_i^{n+1} - \varphi_i^n}{\Delta t} = - \frac{u}{2h} (\varphi_{i+1}^n - \varphi_{i-1}^n), \quad (3.25)$$

which is same as the central difference scheme. Any scheme which can be written in the following form

$$\frac{\varphi_i^{n+1} - \varphi_i^n}{\Delta t} = C^+ (\varphi_{i+1}^n - \varphi_i^n) - C^- (\varphi_i^n - \varphi_{i-1}^n), \quad (3.26)$$

satisfies the positivity preserving property if the coefficients C^+ and C^- satisfy [50]

$$C^+ \geq 0, \quad C^- \geq 0, \quad C^+ + C^- \leq 1. \quad (3.27)$$

We observe that the Galerkin approximation (Eq. (3.25)) does not satisfy this condition. The scheme has to be modified by adding the stabilization terms to satisfy the positivity property, as suggested by [50] for finite difference approximations.

An implicit numerical method for solving a differential equation can be expressed as a system of linear equations of the form $\mathbf{A}\varphi = \mathbf{b}$ where \mathbf{A} is the left-hand side matrix, \mathbf{b} is the right-hand side vector or force vector and φ is the vector of unknowns. The definition for the positivity preservation can be generalized to the implicit matrix form of the scheme by transforming the matrix $\mathbf{A} = \{a_{ij}\}$ to an M-matrix which ensures the positivity and convergence with the

following properties [154]

$$a_{ii} > 0, \forall i, \quad (3.28)$$

$$a_{ij} \leq 0, \forall j \neq i, \quad (3.29)$$

$$\sum_j a_{ij} = 0, \forall i. \quad (3.30)$$

These are the sufficient conditions for imparting the positivity property to the matrix \mathbf{A} . This transformation to an M-matrix is carried out by the addition of the discrete upwind matrix $\mathbf{D} = \{d_{ij}\}$ which has the following properties [49]:

$$\begin{aligned} d_{ij} &= d_{ji} = -\max\{0, a_{ij}, a_{ji}\}, \\ d_{ii} &= -\sum_{j \neq i} d_{ij}. \end{aligned} \quad (3.31)$$

Remark 1. Galerkin, SUPG, and GLS are not positivity preserving methods [1]. We know that the Galerkin solution leads to spurious global oscillations in the convection-dominated regime. Addition of the linear stabilization term in SUPG and GLS does not satisfy the conditions in Eqs. (3.28-3.30) and therefore they are not positivity preserving methods. The proposed method takes the combined GLS-SGS approach as the linear stabilization (which is not positivity preserving) and adds a nonlinear stabilization term to impart the desired positivity preserving property (which is presented in Section 3.2.2.2).

3.2.2.2 Enforcement of positivity condition in one-dimension

Consider the steady-state CDR equation in one-dimension:

$$u \frac{d\varphi}{dx} - k \frac{d^2\varphi}{dx^2} + s\varphi = f, \quad u \geq 0. \quad (3.32)$$

For simplicity, assume that only Dirichlet boundary conditions are specified and $f = 0$. The variational formulation gives: find $\varphi_h(\mathbf{x}) \in \mathcal{S}_\varphi^h$ such that $\forall w_h \in \mathcal{V}_\varphi^h$:

$$\int_\Omega \left(w_h u \frac{d\varphi_h}{dx} + \frac{dw_h}{dx} k \frac{d\varphi_h}{dx} + w_h s \varphi_h \right) d\Omega + \sum_{e=1}^{n_{el}} \int_{\Omega_e} \mathcal{L} w_h \tau(\tilde{\mathcal{L}} \varphi_h) d\Omega = 0, \quad (3.33)$$

where \mathcal{L} is the differential operator of the proposed method, i.e., in one-dimension, $\mathcal{L} = u \frac{d}{dx} + |s|$ (diffusion term is neglected here pertaining to the linear finite elements), which gives

$$\int_{\Omega} \left(w_h u \frac{d\varphi_h}{dx} + \frac{dw_h}{dx} k \frac{d\varphi_h}{dx} + w_h s \varphi_h \right) d\Omega + \sum_{e=1}^{n_{el}} \int_{\Omega^e} \left(u \frac{dw_h}{dx} + |s| w_h \right) \tau \left(u \frac{d\varphi_h}{dx} + s \varphi_h \right) d\Omega = 0. \quad (3.34)$$

Let $\mathbf{A}_c^e = [a_{c\{ij\}}^e]$, $\mathbf{A}_d^e = [a_{d\{ij\}}^e]$ and $\mathbf{A}_r^e = [a_{r\{ij\}}^e]$ be the local element matrices for the first three terms in Eq. (3.34) corresponding to convection, diffusion and reaction effects respectively. Assuming that the elements employed in the discretization are two-node linear elements and $w_i = N_i$ be the shape functions at the corresponding nodes of the finite element, the matrices can be written as

$$a_{c\{ij\}}^e = \int_{\Omega^e} N_i u \frac{dN_j}{dx} d\Omega, \quad a_{d\{ij\}}^e = \int_{\Omega^e} \frac{dN_i}{dx} k \frac{dN_j}{dx} d\Omega, \quad a_{r\{ij\}}^e = \int_{\Omega^e} N_i s N_j d\Omega,$$

which are computed to be

$$\mathbf{A}_c^e = \frac{u}{2} \begin{bmatrix} -1 & 1 \\ -1 & 1 \end{bmatrix}, \quad \mathbf{A}_d^e = \frac{k}{h} \begin{bmatrix} 1 & -1 \\ -1 & 1 \end{bmatrix}, \quad \mathbf{A}_r^e = \frac{sh}{6} \begin{bmatrix} 2 & 1 \\ 1 & 2 \end{bmatrix}, \quad (3.35)$$

where h is the characteristic length of the element. Similarly, we can write each expression in Eq. (3.34) in the matrix form. The element level matrix \mathbf{A}^e is thus given by

$$\mathbf{A}^e = \begin{bmatrix} -\frac{u}{2} + \frac{k}{h} + \frac{sh}{3} + \frac{\tau u^2}{h} - \frac{u\tau s}{2} - \frac{u\tau|s|}{2} + \frac{\tau s|s|h}{3} & \frac{u}{2} - \frac{k}{h} + \frac{sh}{6} - \frac{\tau u^2}{h} - \frac{u\tau s}{2} + \frac{u\tau|s|}{2} + \frac{\tau s|s|h}{6} \\ -\frac{u}{2} - \frac{k}{h} + \frac{sh}{6} - \frac{\tau u^2}{h} + \frac{u\tau s}{2} - \frac{u\tau|s|}{2} + \frac{\tau s|s|h}{6} & \frac{u}{2} + \frac{k}{h} + \frac{sh}{3} + \frac{\tau u^2}{h} + \frac{u\tau s}{2} + \frac{u\tau|s|}{2} + \frac{\tau s|s|h}{3} \end{bmatrix}. \quad (3.36)$$

The discrete upwind operator corresponding to \mathbf{A}^e is expressed as

$$\mathbf{D}^e = \begin{bmatrix} \max \left\{ \frac{|u - u\tau s + u\tau|s||}{2} - \frac{k + \tau u^2}{h} + \frac{(s + \tau s|s|)h}{6}, 0 \right\} & -\max \left\{ \frac{|u - u\tau s + u\tau|s||}{2} - \frac{k + \tau u^2}{h} + \frac{(s + \tau s|s|)h}{6}, 0 \right\} \\ -\max \left\{ \frac{|u - u\tau s + u\tau|s||}{2} - \frac{k + \tau u^2}{h} + \frac{(s + \tau s|s|)h}{6}, 0 \right\} & \max \left\{ \frac{|u - u\tau s + u\tau|s||}{2} - \frac{k + \tau u^2}{h} + \frac{(s + \tau s|s|)h}{6}, 0 \right\} \end{bmatrix} \quad (3.37)$$

$$= \frac{k^{\text{add}}}{h} \begin{bmatrix} 1 & -1 \\ -1 & 1 \end{bmatrix}, \quad (3.38)$$

where k^{add} is

$$k^{\text{add}} = \max \left\{ \frac{|u - \tau us + \tau u|s||h}{2} - (k + \tau u^2) + \frac{(s + \tau s|s|)h^2}{6}, 0 \right\} \quad (3.39)$$

Chapter 3. The Positivity Preserving Variational Method

This matrix \mathbf{D}^e , when added to \mathbf{A}^e converts it into an M-matrix, imparting the positivity property. The addition of this matrix can be considered as a diffusion effect to the linear stabilized form of the problem, whereby a simple example of this matrix construction is shown in Appendix A. To counteract the loss of accuracy due to the diffusion, there is a need for a nonlinear regulation of this diffusion to selective elements. This regulation is provided by a solution-dependent parameter which makes the method nonlinear, adding the diffusion only to those elements where a non-regular solution is present in the high gradient regions. As a result, the loss of accuracy is avoided in the regions of smooth solution where the nonlinear term has a small contribution owing to the negligible residual.

In one-dimension, the proposed discrete formulation for steady-state CDR equation is: find $\varphi_h(x) \in \mathcal{S}_\varphi^h$ such that $\forall w_h \in \mathcal{V}_\varphi^h$:

$$\begin{aligned} & \int_{\Omega} \left(w_h \left(u \frac{d\varphi_h}{dx} \right) + k \frac{dw_h}{dx} \frac{d\varphi_h}{dx} + w_h s \varphi_h \right) d\Omega + \sum_{e=1}^{n_{el}} \int_{\Omega_e} \mathcal{L} w_h \tau (\tilde{\mathcal{L}} \varphi_h - f) d\Omega \\ & + \sum_{e=1}^{n_{el}} \int_{\Omega_e} \chi \frac{|\mathcal{R}(\varphi_h)|}{|\nabla \varphi_h|} k^{\text{add}} \frac{dw_h}{dx} \frac{d\varphi_h}{dx} d\Omega = \int_{\Omega} w_h f d\Omega + \int_{\Gamma_H^\varphi} w_h h^\varphi d\Gamma, \end{aligned} \quad (3.40)$$

where $\mathcal{R}(\varphi_h)$ is the residual of the given equation and χ is an expression depending on the problem constants (u , k , s and h) yet to be defined which non-dimensionalizes $\frac{|\mathcal{R}(\varphi_h)|}{|\nabla \varphi_h|}$ by scaling it. The above added expression has been the standard canonical form to add nonlinearity or discontinuity capturing to the linear stabilized equation in the literature. To define the parameter χ , we look into the variation of $\frac{|\mathcal{R}(\varphi_h)|}{|\nabla \varphi_h|}$ with s , u , k and h inside a finite element. We adopt a similar approach as taken in [61]. Consider a pure-reaction problem ($s\varphi = f$). When applying the discrete upwind operator to the left-hand side of the matrix system in this case, we obtain a lumped mass matrix. Gibbs oscillations can be prevented by using the lumped mass technique to solve such problems. Therefore, we determine $\frac{|\mathcal{R}(\varphi_h)|}{|\nabla \varphi_h|}$ by assuming that the solution approaches its lumped mass matrix approach counterpart. For that purpose, we consider a canonical example by defining the source $f(x)$ as a step function

$$f(x) = \begin{cases} 0, & \forall x \in [0, 0.25 + \eta h], \\ q, & \text{elsewhere}, \end{cases} \quad (3.41)$$

where h is the element length, η is the location of the discontinuity in the function $f(x)$. The

Chapter 3. The Positivity Preserving Variational Method

lumped mass matrix solution is then given by

$$\varphi = \left(\frac{q}{s}\right) \left\{ 0, \dots, 0, \frac{(1-\eta)^2}{2}, \frac{(2-\eta^2)}{2}, 1, \dots, 1 \right\}. \quad (3.42)$$

Let us observe how $\frac{|\mathcal{R}(\varphi_h)|}{|\nabla \varphi_h|}$ behaves inside the element containing the discontinuity at η . For this particular element,

$$\mathcal{R}(\varphi_h) = s\varphi_h - f = q \left(\frac{(1-\xi)(1-\eta)^2}{2} + \frac{(1+\xi)(2-\eta^2)}{2} \right) - f, \quad (3.43)$$

$$\nabla \varphi_h = \frac{q}{2sh} (2\eta - 2\eta^2 + 1), \quad (3.44)$$

which gives

$$\frac{|\mathcal{R}(\varphi_h)|}{|\nabla \varphi_h|} = \left| \frac{\mathcal{R}(\varphi_h)}{\nabla \varphi_h} \right| = \left| \frac{sh}{2} \frac{(1-\xi)(1-\eta)^2 + (1+\xi)(2-\eta^2)}{2\eta - 2\eta^2 + 1} - \frac{2fsh}{q(2\eta - 2\eta^2 + 1)} \right|. \quad (3.45)$$

Considering the above ratio for all the elements, it is observed that

$$\frac{|\mathcal{R}(\varphi_h)|}{|\nabla \varphi_h|} = \frac{|s\varphi_h - f|}{|\nabla \varphi_h|} = \left| \frac{sh}{2} p(\eta, \xi) \right|, \quad (3.46)$$

where $p(\eta, \xi)$ is a function depending on the location of the discontinuity η inside an element and the natural coordinate ξ and is defined as

$$p(\eta, \xi) = \begin{cases} \frac{(1-\xi)(1-\eta)^2 + (1+\xi)(2-\eta^2)}{2\eta - 2\eta^2 + 1} - \frac{4f}{q(2\eta - 2\eta^2 + 1)}, & \text{elements with discontinuity,} \\ (1+\xi) - \frac{4f}{q(1-\eta)^2}, & \text{elements adjoining discontinuity,} \\ 0, & \text{elsewhere.} \end{cases} \quad (3.47)$$

The added positivity preserving integral can be expressed as

$$\int_{\Omega_e} \chi \frac{|\mathcal{R}(\varphi_h)|}{|\nabla \varphi_h|} k^{\text{add}} \frac{dw_h}{dx} \frac{d\varphi_h}{dx} d\Omega = \int_{\Omega_e} \chi \left| \frac{sh}{2} p(\eta, \xi) \right| k^{\text{add}} \frac{dw_h}{dx} \frac{d\varphi_h}{dx} d\Omega. \quad (3.48)$$

After the finite element discretization, let the local element matrix corresponding to the above term be denoted by $\mathbf{K}_{\text{add}}^e$ which can be written as

$$\mathbf{K}_{\text{add}}^e = \frac{k^{\text{add}} \chi}{h} \int_{\Omega_e} \left| \frac{sh}{2} p(\eta, \xi) \right| d\Omega \begin{bmatrix} 1 & -1 \\ -1 & 1 \end{bmatrix}. \quad (3.49)$$

The above function can be integrated by using the property of the absolute function (Eq. (3.22)).

After some algebraic arrangements, the above integral simplifies to

$$\int_{\Omega^e} \left| \frac{sh}{2} p(\eta, \xi) \right| d\Omega = \begin{cases} \frac{|s|h^2}{2} r(\eta), & \text{elements with discontinuity,} \\ \frac{|s|h^2}{2}, & \text{elements adjoining discontinuity,} \\ 0, & \text{elsewhere,} \end{cases} \quad (3.50)$$

where $r(\eta)$ is a function of the location of the discontinuity inside the element ($0 \leq \eta \leq 1$) given as [61]

$$r(\eta) = \left[\frac{1 + 2\eta(1 - \eta)[1 - 2\eta(1 - \eta)]}{1 + 2\eta(1 - \eta)} \right]. \quad (3.51)$$

Now, we turn our attention to the undefined scaling parameter χ . Since the change of the variable in the integration to the local coordinates introduces a factor equal to the Jacobian of the element ($h/2$ in one-dimensional case), we do not consider this factor in defining χ because of its geometry-dependent property. Therefore, we scale the integral as $\chi = 2/(|s|h)$ so that the regulatory term depends purely on the function $r(\eta)$, which is essentially geometry independent.

Let us consider two cases:

Case 1: For the convection-diffusion problem with $f = 0$,

$$\frac{|\mathcal{R}(\varphi_h)|}{|\nabla \varphi_h|} = \frac{|u \nabla \varphi_h|}{|\nabla \varphi_h|} = |u|. \quad (3.52)$$

In this case, we define $\chi = 1/|u|$.

Case 2: For the diffusion-reaction equation, we construct the same expression for the integral as Eq. (3.48) which gives $\chi = 2/(|s|h)$. The Laplacian operator is exactly zero for linear elements. However, it is very small for bilinear and trilinear finite elements and has been neglected in this case. Therefore, we can conclude that for the reaction-dominated problems ($u \rightarrow 0$), $\chi \rightarrow 2/(|s|h)$ and for the convection-dominated problems ($s \rightarrow 0$), $\chi \rightarrow 1/|u|$. Thus, χ can be defined as a combined expression as follows:

$$\boxed{\chi = \frac{2}{|s|h + 2|u|}} \quad (3.53)$$

Remark 2. Notice that we have not made any assumption on the sign of the reaction coefficient s . The above evaluated integral will adjust itself accordingly. The absolute function takes care of the change in the sign of the reaction coefficient.

The above steps complete the formulation of the positivity condition and the nonlinear

stabilization in one-dimension. The positivity bounds (Eq. (3.27)) for the PPV formulation have been shown for some particular cases in Appendix B. We next proceed to generalize the procedure to multi-dimensional CDR equation.

3.2.2.3 Extension to multi-dimensions

In multi-dimensions, the discrete form of the proposed formulation for steady-state CDR equation is: find $\varphi_h(\mathbf{x}) \in \mathcal{S}_\varphi^h$ such that $\forall w_h \in \mathcal{V}_\varphi^h$:

$$\begin{aligned} & \int_{\Omega} \left(w_h (\mathbf{u} \cdot \nabla \varphi_h) + \nabla w_h \cdot (\mathbf{k} \nabla \varphi_h) + w_h s \varphi_h \right) d\Omega + \sum_{e=1}^{n_{el}} \int_{\Omega_e} \mathcal{L} w_h \tau (\tilde{\mathcal{L}} \varphi_h - f) d\Omega \\ & + \sum_{e=1}^{n_{el}} \int_{\Omega_e} \chi \frac{|\mathcal{R}(\varphi_h)|}{|\nabla \varphi_h|} k_s^{\text{add}} \nabla w_h \cdot \left(\frac{\mathbf{u} \otimes \mathbf{u}}{|\mathbf{u}|^2} \right) \cdot \nabla \varphi_h d\Omega \\ & + \sum_{e=1}^{n_{el}} \int_{\Omega_e} \chi \frac{|\mathcal{R}(\varphi_h)|}{|\nabla \varphi_h|} k_c^{\text{add}} \nabla w_h \cdot \left(\mathbf{I} - \frac{\mathbf{u} \otimes \mathbf{u}}{|\mathbf{u}|^2} \right) \cdot \nabla \varphi_h d\Omega = \int_{\Omega} w_h f d\Omega + \int_{\Gamma_H^\varphi} w_h h^\varphi d\Gamma, \end{aligned} \quad (3.54)$$

where k_s^{add} and k_c^{add} are the diffusion in the streamline and the crosswind directions respectively. The diffusion required to satisfy the discrete maximum principle for the proposed stabilized method in one-dimension is given in Eq. (3.39). We will directly extend this formula to multi-dimensions by working in two principal directions namely, streamline and crosswind (Fig. 3.1). Implementation of the procedure requires only minor modifications to existing stabilized finite element codes.

Remark 3. *The present PPV method adds diffusion in both the streamline and the crosswind directions consistently so that in the case of velocity being perpendicular to the solution gradient, sufficient diffusion is added to maintain positivity and local boundedness (see Fig. 3.1(b)). We will show the effectiveness of the proposed treatment through a range of numerical experiments in Section 3.4.*

First, we consider the streamline direction. The following expression adds diffusion in the streamline direction while maintaining the positivity property:

$$\text{Stabilization term}_s = \sum_{e=1}^{n_{el}} \int_{\Omega_e} \chi \frac{|\mathcal{R}(\varphi_h)|}{|\nabla \varphi_h|} k_s^{\text{add}} \nabla w_h \cdot \left(\frac{\mathbf{u} \otimes \mathbf{u}}{|\mathbf{u}|^2} \right) \cdot \nabla \varphi_h d\Omega, \quad (3.55)$$

where k_s^{add} is the diffusion in the streamline direction, given by

$$k_s^{\text{add}} = \max \left\{ \frac{||\mathbf{u}| - \tau |\mathbf{u}| s + \tau |\mathbf{u}| |s| |h|}{2} - (k + \tau |\mathbf{u}|^2) + \frac{(s + \tau s |s|) h^2}{6}, 0 \right\}. \quad (3.56)$$

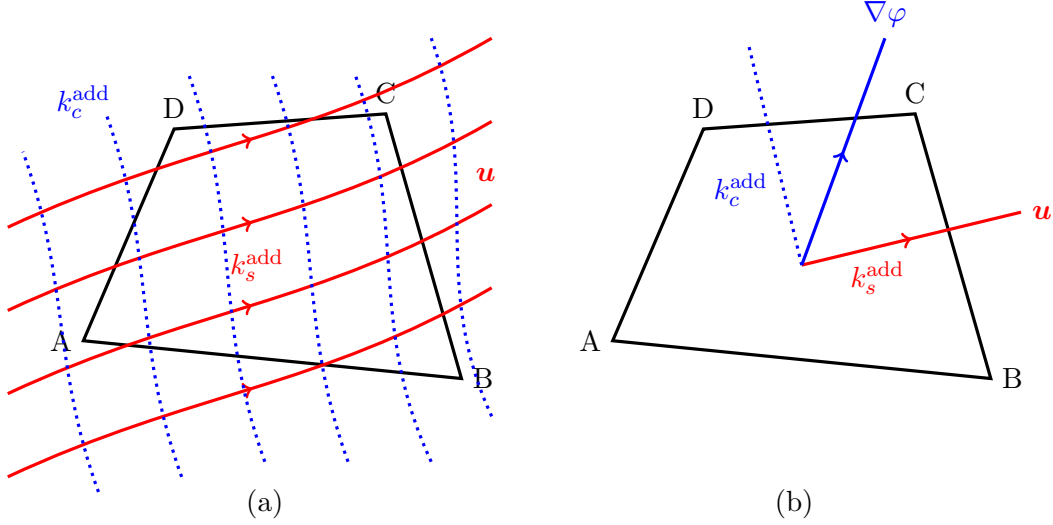


Figure 3.1: Sketch of the residual-based stabilization inside a generic element with ABCD sub-domain boundary: (a) Four-node quadrilateral element with convection velocity and the added diffusions k_s^{add} and k_c^{add} in the streamline and crosswind directions respectively; (b) added diffusions and solution gradient ($\nabla \varphi$) shown for designing positivity. Solid (red) and dashed (blue) lines represent the streamline and crosswind directions of the convection field respectively while solid (blue) line is the solution gradient vector.

While in the crosswind direction, we will add the following term:

$$\text{Stabilization term}_c = \sum_{e=1}^{n_{\text{el}}} \int_{\Omega_e} \chi \frac{|\mathcal{R}(\varphi_h)|}{|\nabla \varphi_h|} k_c^{\text{add}} \nabla w_h \cdot \left(\mathbf{I} - \frac{\mathbf{u} \otimes \mathbf{u}}{|\mathbf{u}|^2} \right) \cdot \nabla \varphi_h d\Omega, \quad (3.57)$$

where k_c^{add} is the diffusion in the crosswind direction, given by

$$k_c^{\text{add}} = \max \left\{ \frac{|\mathbf{u}| + \tau |\mathbf{u}| |s| h}{2} - k + \frac{(s + \tau s |s|) h^2}{6}, 0 \right\}. \quad (3.58)$$

Here, $|\mathbf{u}| = \sqrt{u_i u_i}$ is the magnitude of the multi-dimensional velocity vector.

Remark 4. The formula derived in one-dimension for k^{add} has been directly extended to multi-dimensions. In one-dimension, there is no sense of the crosswind direction. Therefore, k^{add} in Eq. (3.39) is added along the streamline. In multi-dimensions, the proposed expression for streamline diffusion is same as that in Eq. (3.39) pertaining to the streamline, but for the crosswind diffusion in Eq. (3.58), the terms associated with the linear stabilization and convection velocity have been omitted. Assume that linear stabilization is added in streamline direction (SUPG), the terms in Eq. (3.39) depicting this streamline stabilization are $-\tau |\mathbf{u}| s |h| / 2$ and $\tau |\mathbf{u}|^2$. In crosswind direction, these terms will not be present, resulting in Eq. (3.58). This case is elaborated as follows. Suppose that we have SUPG stabilization in one-dimension, then the

Chapter 3. The Positivity Preserving Variational Method

added term in the linear stabilization is

$$\sum_{e=1}^{n_{\text{el}}} \int_{\Omega^e} u \frac{dw_h}{dx} \tau \left(u \frac{d\varphi_h}{dx} + s\varphi_h - f \right) d\Omega. \quad (3.59)$$

The left-hand side of the stabilized expression after the finite element discretization can be written in the matrix form at the local element level as

$$\begin{bmatrix} \frac{\tau u^2}{h} - \frac{u\tau s}{2} & -\frac{\tau u^2}{h} - \frac{u\tau s}{2} \\ -\frac{\tau u^2}{h} + \frac{u\tau s}{2} & \frac{\tau u^2}{h} + \frac{u\tau s}{2} \end{bmatrix} \quad (3.60)$$

When we write the k^{add} expression for the SUPG method, these extra terms will correspond to the diffusion in the streamline direction. Therefore, the terms relating to the expressions above are omitted from the crosswind diffusion in Eq. (3.58).

Remark 5. The PPV method takes care of gradients in the solution in any direction. Previous methods added null discontinuity capturing term when the convection velocity is perpendicular to the solution gradient. The present method adds the discontinuity capturing term in both the crucial directions and reduces any unwanted oscillations in the solution.

Remark 6. The present PPV method is slightly more diffusive than that proposed in [1, 61, 62]. Neglecting the effects of the added nonlinear diffusion in the streamline direction, the method can be simplified to that of [1] by using a factor of 0.7 rather than 1 in the first term of the k_c^{add} for the convection-diffusion equation:

$$k_c^{\text{add}} = \max \left\{ \frac{0.7|\mathbf{u}|h}{2} - k, 0 \right\}. \quad (3.61)$$

We take the constant as 1 rather than 0.7 for maintaining positivity throughout the computational domain. With 0.7 as the multiplying factor, a non-regular solution near the boundary for 90° convection case is obtained, which is shown in the subsequent section describing the test results (Fig. 3.12(f)).

Remark 7. We have made only two assumptions in the above description of the method: (i) the diffusion is isotropic and (ii) higher-order derivatives in the variational form and the differential operator of the stabilization term are neglected due to the use of linear and multilinear finite elements.

Remark 8. Since the nonlinear expression has the absolute function, the computation of the derivative of this function is required for evaluating the Jacobian for implicit and nonlinear

methods. Here, we have used Picard fixed-point procedure for the nonlinear iterations, meaning that the factor $|\mathcal{R}(\varphi_h)|/|\nabla \varphi_h|$ is evaluated using the values of the variable φ_h at the previous nonlinear step.

3.2.2.4 Characteristic element length scale

A general and precise definition of the element length scale poses a difficulty to the error analysis of the residual-based stabilization of the Galerkin formulation. In the one-dimensional problem, it is straightforward to select the characteristic element length. Finding an appropriate length for an element in multi-dimensions is a challenging task, particularly for highly irregular and anisotropic elements. It was shown in [37] that under generalized isoparametric transformation, the formula for the stabilization parameter τ is given by

$$\tau = \left[\left(\frac{1}{\alpha \Delta t} \right)^2 + \mathbf{u} \cdot \mathbf{G} \mathbf{u} + C_I k^2 \mathbf{G} : \mathbf{G} + s^2 \right]^{-1/2}, \quad (3.62)$$

where C_I is a constant derived from inverse estimates [155] and \mathbf{G} is the element contravariant metric tensor for isoparametric mapping given by

$$\mathbf{G} = \frac{\partial \boldsymbol{\xi}^T}{\partial \mathbf{x}} \frac{\partial \boldsymbol{\xi}}{\partial \mathbf{x}}, \quad (3.63)$$

where $\boldsymbol{\xi}$ and \mathbf{x} are the vectors of natural and global coordinates, respectively. The above formula for τ reduces to Eq. (3.19) in case of one-dimension. Therefore, in one-dimension

$$\mathbf{u} \cdot \mathbf{G} \mathbf{u} = \left(\frac{2u}{h} \right)^2. \quad (3.64)$$

One can define the characteristic element length in multi-dimensions such that one-dimensional equivalent streamline length scale is obtained. Such length scale has been used in the literature [156, 157, 158]:

$$h_u = \frac{2|\mathbf{u}|}{\sqrt{\mathbf{u} \cdot \mathbf{G} \mathbf{u}}}, \quad (3.65)$$

where h_u is the streamline element length and $|\mathbf{u}| = \sqrt{u_i u_i}$. The above length scale or the expression for τ in Eq. (3.62) does not take into account the anisotropic character of the finite element, in particular when there is a large directionality mismatch between the equation coefficients and the wave vector associated to subscale physics. Due to this reason, when the element is anisotropic, we observe oscillations in the numerical solution for some of the cases. This was studied in [60] where a generalized Fourier analysis of the CDR equation was carried

out. We will highlight some of the crucial points from that analysis.

It has been discussed in the Chapter 2 that the origin of the stabilization parameter comes from the multiscale phenomenon in which we model the unresolved subgrid scales via residual-based stabilization. The approximation of stabilization parameter τ arises from the Fourier representation of the Green's function for a subscale problem at the element level whereby the subscale term vanishes on the element boundary. Using the inverse Fourier transform, the stabilization parameter τ for the subscale problem can be written as [60]

$$\tau = \left[(K_i K_j k_{ij}^r + s)^2 + (K_j u_j^r)^2 \right]^{-1/2}, \quad (3.66)$$

where K_i and K_j are the components of the wave vector \mathbf{K} from the Fourier analysis, u_j^r and k_{ij}^r are the convection velocity and the diffusion coefficient of the transformed CDR equation in the local coordinates, i.e., $u_i^r = u_j J_{ij}^{-T}$ and $k_{lm}^r = J_{mi}^{-T} k_{ij} J_{lj}^{-T}$, J being the Jacobian of a finite element. If we neglect the directionality of the wave vector and write the terms in the above expression for τ , we get

$$K_i K_j k_{ij}^r \approx \|\mathbf{K}\|^2 \sqrt{k_{ij}^r k_{ij}^r}, \quad (3.67)$$

$$K_j u_j^r \approx \|\mathbf{K}\| \|u^r\|, \quad (3.68)$$

where $\|\cdot\|$ is the invariant of the vector. When $s = 0$, the above expression is similar to Eq. (3.62). However, neglection of the directionality of the wave vector has consequences on an anisotropic grid with variable coefficients. A heuristic approach to finding the direction where maximum instability occurs based on the element Peclet and Damköhler numbers was proposed in [60]. We employ a similar definition of the element length scale and demonstrate the method for anisotropic and unstructured grids in Section 3.4.3. For generality, the preceding developments can be extended to the time-dependent case by considering the transient term and deriving the diffusion expressions similar to the above procedure.

3.3 Convergence and stability analysis

In this section, we systematically analyze the different methods for solving the one-dimensional CDR equation and assess the convergence, accuracy, and stability properties of the proposed method. This comparison is conducted by means of computed solutions for a wide range of char-

acteristic dimensionless parameters. First, to understand the behavior of different methods with the non-dimensional numbers, the variation of non-dimensionalized L^2 error with $Da = sh/u$ (for the convection-reaction case) and with $\psi = sh^2/k$ (for the diffusion-reaction case) is analyzed. Then, the stability properties of the proposed method are described on the basis of Fourier analysis with quantification of the algorithmic damping and phase velocity (or algorithmic frequency) ratios. Finally, the mesh convergence study is performed to demonstrate the accuracy of a variety of methods for the steady-state convection-reaction, diffusion-reaction and CDR equations. Throughout the error analysis, the non-dimensionalized L^2 error is computed for a fixed number of sample nodal points as

$$\text{Error} = \frac{\|\varphi_{\text{numerical}} - \varphi_{\text{exact}}\|_2}{\|\varphi_{\text{exact}}\|_2}, \quad (3.69)$$

where φ_{exact} is the analytical value defined in Appendix E for the convection-reaction, the diffusion-reaction and the convection-diffusion equations and $\|\cdot\|_2$ is the L^2 norm.

3.3.1 Dependence of error on the non-dimensional parameters

We consider the one-dimensional problem for the error analysis by varying the non-dimensional numbers and keeping the element length to 0.1 (number of elements = 10 with domain length, $L = 1$) and 0.025 (number of elements = 40 with the same domain length). Without the loss of generality, the left-hand side Dirichlet condition is set to 1 with $f = 0$ for the convection-reaction case (since only one Dirichlet condition is required to solve the problem), while the left-hand side and right-hand side nodal values are 8 and 3 respectively with $f = 0$ for the diffusion-reaction case. One can observe from Figs. 3.2(a) and 3.2(c) that in the convection-dominated regime ($Da < 1$), all the methods give a monotonically decreasing error, while for high Da , methods other than the present method behave like an asymptote to a constant value of the computed error. The present method minimizes the error even in the reaction-dominated regime ($Da > 1$). Moreover, the error decreases with the increase in Da . This is due to the reduction in the undershoots and overshoots of the solution near the boundary layers. The maximum error occurs around $Da \approx 10$ for the coarse mesh and at around $Da \approx 1$ for the fine mesh case. Similarly, from Figs. 3.2(b) and 3.2(d), SGS method behaves quite well for diffusion-dominated regime ($\psi < 1$) with the same behavior of monotonically decreasing error

Chapter 3. The Positivity Preserving Variational Method

with decreasing ψ . All the methods tend to achieve an asymptotic error at higher ψ , while the error norm decreases monotonically for the proposed method in the reaction-dominated regime ($\psi > 1$). The performance of the PPV is very similar to that of SUPG and GLS in the diffusion dominated regime. The maximum error for the present method occurs around $\psi \approx 5$ and $\psi \approx 1$ for the coarse and fine meshes respectively. One can observe the improvement in the error norm for the proposed method with increasing Da and ψ for the reaction-dominated effects. This is mainly due to the preservation of the positivity property and the reduction of oscillations near the boundary layer.

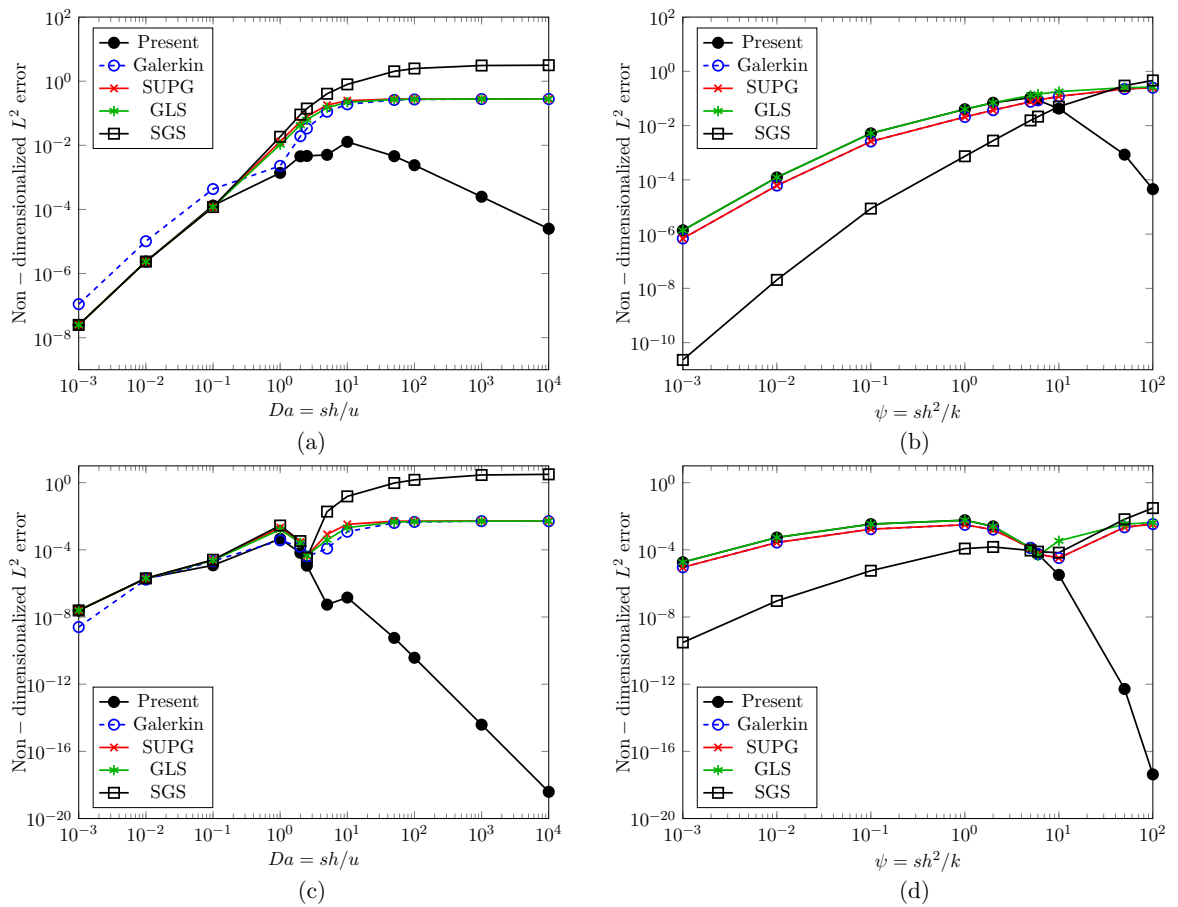


Figure 3.2: Dependence of non-dimensionalized L^2 error on non-dimensional numbers as a function of: Da for convection-reaction equation with number of elements- (a) and (c); and ψ for diffusion-reaction problem- (b) and (d). Number of elements is kept constant at 10 for (a-b) and 40 for (c-d) with a domain length $L = 1$.

The trend of an increase in the computed error at the middle of the regime of the non-dimensional numbers can be explained by the fact that with the increase in Da (or ψ), the boundary layer in the exact solution becomes sharper. Since we consider a fixed number of

finite elements in the domain, the error depends on the behavior of each node to resolve the boundary layer. At lower Da (or ψ), the reaction effects are small showing less error. With the increase in the non-dimensional numbers, the ability of the method to resolve the layer is tested, which introduces some errors as the node of the element falls near the edge of the layer. Due to the efficacy of the positivity preservation, reduction of oscillations as well as the fixed number of elements, the error decreases for large dimensionless parameters for the present method as it approaches the nodally exact solution and the edge of the boundary layer recedes away from the node. The high error at the middle range of the non-dimensionalized parameters can be reduced through an adaptive refinement as shown in the finer mesh (Fig. 3.2(c-d)) where we observe a similar trend.

3.3.2 Two-dimensional Fourier analysis

It is now known that the assumption in the von Neumann analysis regarding the error dynamics following the discrete equation needs improvement [159, 160]. In the von Neumann analysis, one does not observe any dispersion errors. Therefore, in this study, we employ the Fourier analysis assessing the dispersion as well as diffusion errors introduced by the discretization. We present the Fourier analysis of the PPV method without the nonlinear stabilization term. To analyze the stability and accuracy measures, the analysis has also been performed for the GLS and SGS methods in Appendices C and D for one- and two-dimensions respectively. Assuming the exact solution of the one-dimensional transient CDR equation as a Fourier series $\varphi = Ae^{\nu t+iKx}$, where K is the spatial wave number and ν represents the evolution of the solution with time. ν can be expressed as $\nu = -\xi - i\omega$, ξ and ω being the damping coefficient and frequency respectively and $i = \sqrt{-1}$. From the continuous equation, one can obtain

$$\xi = s + kK^2, \quad (3.70)$$

$$\omega = uK. \quad (3.71)$$

The group velocity of the continuous equation is given as $v_g = \partial\omega/\partial K = u$. Similarly, expressing the discrete solution in terms of Fourier series, $\varphi_h(x_j, t) = Ae^{\nu^h t+iK_j h}$, where $\nu^h = -\xi^h - i\omega^h$, ξ^h and ω^h being the discrete counterparts of ξ and ω termed as algorithmic damping coefficient and algorithmic frequency respectively. It is assumed that there is a negligible error in the

Chapter 3. The Positivity Preserving Variational Method

time discretization. The Fourier analysis of the proposed method in one-dimension leads to the following amplification factor:

$$\nu_{\text{Present}}^h = \frac{2(\cos(Kh) - 1)(k + u^2\tau) - \frac{sh^2}{3}(\cos(Kh) + 2)(1 + |s|\tau) - ih\sin(Kh)(1 - s\tau + |s|\tau)}{\frac{h^2}{3}(\cos(Kh) + 2)(1 + |s|\tau) - ihu\tau\sin(Kh)}. \quad (3.72)$$

The above formula reduces to that of GLS method (Eq. (C.10)) when $s \geq 0$ and to that of SGS method (Eq. (C.11)) when $s < 0$. Refer to the Appendix C for detailed steps.

The accuracy of the present scheme can be analyzed by expanding ξ^h and ω^h as follows:

$$\omega_{\text{Present}}^h = uK + ukK^3\tau - \left(\frac{uK^5}{180}\right)h^4 + \mathcal{O}(\tau\Delta t, \Delta t^2, \tau^2, h^6), \quad (3.73)$$

$$\xi_{\text{Present}}^h = s + kK^2 - |s|kK^2\tau + \left(\frac{kK^4}{12}\right)h^2 + \mathcal{O}(\tau\Delta t, \Delta t^2, \tau^2, h^4). \quad (3.74)$$

The above expressions show that the accuracy of the algorithmic damping coefficient (ξ^h) and the algorithmic frequency (ω^h) with respect to h will depend on the stabilization parameter τ when $u \neq 0$. Therefore, depending on which phenomenon among convection, diffusion and reaction is dominant, τ varies with h , according to Eq. (3.19). Further analysis is carried out by evaluating the algorithmic damping ratio (ξ^h/ξ), the algorithmic frequency ratio (ω^h/ω) and the group velocity ratio (v_g^h/c) which is the ratio of the group velocity of the numerical scheme to that of the continuous differential equation. The plots of these ratios are given in Appendix C.1. The proposed PPV method has a relatively less damping than the SGS counterpart when $s \geq 0$ and it behaves very similar to the GLS method. When $s < 0$, the proposed method adds appropriate damping compared to GLS which has a larger negative damping. In this range, the behavior of PPV is similar to that of the SGS method. Therefore, the behavior of the present method will be the same as that of GLS for positive reaction and that of SGS for negative reaction. The variation of algorithmic frequency and algorithmic damping ratios with Kh are shown in Fig. C.1 for GLS and SGS methods. Further details of the Fourier analysis are given in Appendix C where we have also considered the fully discrete form of the equation.

Similarly, in two dimensions, the exact solution is assumed as $\varphi = Ae^{\nu t+i\mathbf{K}\cdot\mathbf{x}}$, where $\mathbf{K} = K\cos\alpha_k\mathbf{i} + K\sin\alpha_k\mathbf{j}$ and \mathbf{x} are the wave vector and the position vector respectively. For simplicity, it is assumed that the velocity vector $\mathbf{u} = u\mathbf{i} + v\mathbf{j}$ has the same direction as that of the wave

Chapter 3. The Positivity Preserving Variational Method

vector. The damping coefficient and frequency for the continuous CDR equation are given by

$$\xi = s + kK^2, \quad (3.75)$$

$$\omega = |\mathbf{u}|K. \quad (3.76)$$

The detailed analysis in two-dimensions is presented in Appendix D. The amplification factor

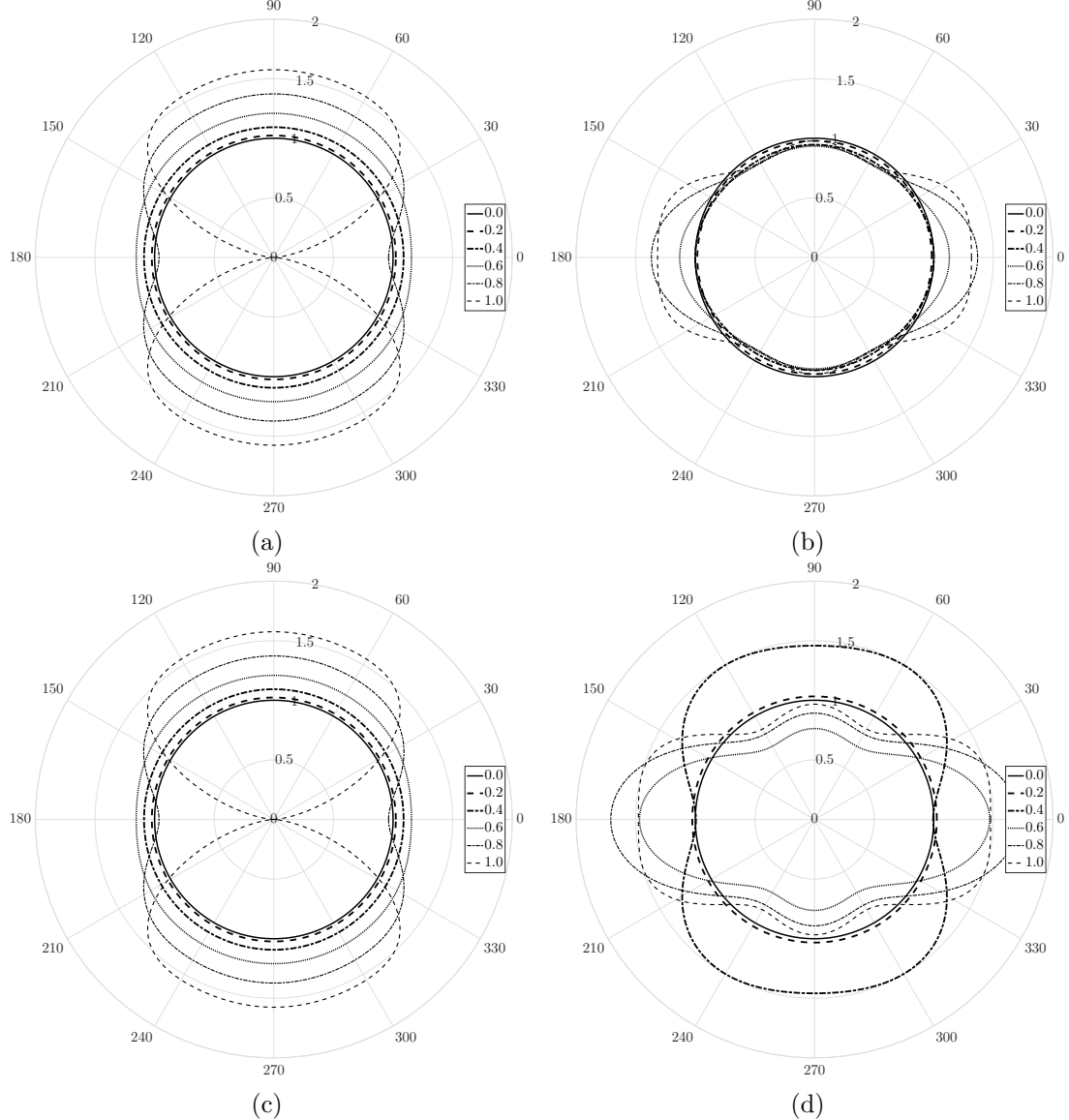


Figure 3.3: Variation of phase velocity and damping ratios with α_k for different $Kh_x/\pi \in [0, 1]$ for convection-diffusion-reaction problem for the present method: Phase velocity ratio for (a) positive reaction, (c) negative reaction; Damping ratio for (b) positive reaction, (d) negative reaction.

in two-dimensions for the present method can be expressed as

$$\begin{aligned} \nu_{\text{Present}}^h = & \frac{1}{\gamma_k h_x^2 M_x M_y (1 + |s|\tau) - i\tau h_x (u\gamma_k M_y \sin\alpha_x + v M_x \sin\alpha_y)} \times \\ & \left[\frac{2M_x(\cos\alpha_y - 1)}{\gamma_k} (k + \tau v^2) + 2M_y(\cos\alpha_x - 1)\gamma_k (k + \tau u^2) - 2\tau u v \sin\alpha_x \sin\alpha_y \right. \\ & \left. - s\gamma_k h_x^2 M_x M_y (1 + |s|\tau) - i h_x u \gamma_k M_y \sin\alpha_x (1 - s\tau + |s|\tau) - i h_x v M_x \sin\alpha_y (1 - s\tau + |s|\tau) \right], \end{aligned} \quad (3.77)$$

where h_x , γ_k , α_x , α_y , M_x and M_y are defined in Appendix D. The above expression can be reduced to its one-dimensional counterpart if the wave vector is considered along the coordinate directions. The phase velocity ratio is defined as ω^h/ω and the damping ratio as ξ^h/ξ . The polar plots of the phase velocity ratio and the damping ratio are given in Fig. 3.3. From the analysis carried out in Appendix D, one can make a similar inference as that for the one-dimensional case. SGS method is more diffusive and has more phase error when $s \geq 0$, while it behaves well for $s < 0$. We next turn our attention to the accuracy of the new variational scheme, in particular, with regard to the convergence rate of various stabilized finite element methods.

3.3.3 Mesh convergence study

The truncation error in a discretization scheme can be obtained by expanding the stencil using Taylor series and then subtracting the given differential equation from it. Herein, we consider the linear stabilized (GLS) discretized form of steady-state CDR equation:

$$\begin{aligned} & \left(-\frac{u}{2h} - \frac{k}{h^2} + \frac{s}{6} - \frac{u^2\tau}{h^2} + \frac{u\tau s}{2h} - \frac{u\tau s}{2h} + \frac{s^2\tau}{6} \right) \varphi_{h,j-1} + \left(\frac{2k}{h^2} + \frac{2s}{3} + \frac{2u^2\tau}{h^2} + \frac{2s^2\tau}{3} \right) \varphi_{h,j} \\ & + \left(\frac{u}{2h} - \frac{k}{h^2} + \frac{s}{6} - \frac{u^2\tau}{h^2} - \frac{u\tau s}{2h} + \frac{u\tau s}{2h} + \frac{s^2\tau}{6} \right) \varphi_{h,j+1} = 0. \end{aligned} \quad (3.78)$$

Expanding $\varphi_{h,j+1}$ and $\varphi_{h,j-1}$ around $\varphi_{h,j}$ and rearranging, we obtain the modified equation which is solved by the numerical method [161] as

$$\begin{aligned} & u \frac{d\varphi}{dx} - k \frac{d^2\varphi}{dx^2} + s\varphi + \left(-u^2 \frac{d^2\varphi}{dx^2} + s^2\varphi \right) \tau + \frac{k}{12} \frac{d^4\varphi}{dx^4} h^2 \\ & + \left(-\frac{u^2}{12} \frac{d^4\varphi}{dx^4} + \frac{s^2}{6} \frac{d^2\varphi}{dx^2} \right) \tau h^2 + \mathcal{O}(\tau^2, h^4) = 0. \end{aligned} \quad (3.79)$$

Chapter 3. The Positivity Preserving Variational Method

The local truncation error of the scheme is defined as the difference between the modified equation and the actual differential equation, which can be written as follows

$$\epsilon_{\text{GLS}} = \left(-u^2 \frac{d^2\varphi}{dx^2} + s^2\varphi \right) \tau + \frac{k}{12} \frac{d^4\varphi}{dx^4} h^2 + \left(-\frac{u^2}{12} \frac{d^4\varphi}{dx^4} + \frac{s^2}{6} \frac{d^2\varphi}{dx^2} \right) \tau h^2 + \mathcal{O}(\tau^2, h^4). \quad (3.80)$$

In the convection-reaction regime ($k = 0$), the coefficient corresponding to τ becomes zero using rearrangement and substitution from the original convection-reaction equation. This makes the leading error of the order τh^2 . Since τ is of the order h when the mesh is refined, GLS is formally third-order accurate in this regime. Galerkin method is fourth-order accurate since $\tau = 0$ and $k = 0$. While in the diffusion-reaction regime ($u = 0$), GLS is second-order accurate since τ will be of order h^2 as the mesh is refined.

Similarly, the truncation error for the SGS method can be written as

$$\begin{aligned} \epsilon_{\text{SGS}} = & \left(-u^2 \frac{d^2\varphi}{dx^2} - 2us \frac{d\varphi}{dx} - s^2\varphi \right) \tau + \frac{k}{12} \frac{d^4\varphi}{dx^4} h^2 \\ & + \left(-\frac{u^2}{12} \frac{d^4\varphi}{dx^4} - \frac{us}{3} \frac{d^3\varphi}{dx^3} - \frac{s^2}{6} \frac{d^2\varphi}{dx^2} \right) \tau h^2 + \mathcal{O}(\tau^2, h^4). \end{aligned} \quad (3.81)$$

For the SGS method, we observe a third-order of accuracy in the convection-reaction regime which is related to the cancellation of the coefficient of τ in the truncation error. Although in the diffusion-reaction regime, we observe a peculiar fourth-order of accuracy for the SGS method. This could be seen if we manipulate the terms in the error such that the second-order terms get canceled. Assuming that refinement of mesh could be interpreted as an increase in the diffusion effects of the equation, we can approximate the stabilization parameter as

$$\tau \approx \frac{h^2}{12k}. \quad (3.82)$$

Substituting this term in $-s^2\tau\varphi$ above and manipulating $\frac{k}{12} \frac{d^4\varphi}{dx^4} h^2$, we observe that these terms indeed get canceled. Moreover, the order of τ is h^2 in this case leading to the order of truncation as τh^2 which makes the solution fourth-order accurate.

For the proposed method, the truncation error in the steady-state model problem is given by

$$\begin{aligned} \epsilon_{\text{Present}} = & -\chi \frac{|\mathcal{R}(\varphi)|}{|\nabla\varphi|} k^{\text{add}} \frac{d^2\varphi}{dx^2} + \left(-u^2 \frac{d^2\varphi}{dx^2} - us \frac{d\varphi}{dx} + u|s| \frac{d\varphi}{dx} + s|s|\varphi \right) \tau \\ & + \left(\frac{k}{12} \frac{d^4\varphi}{dx^4} - \frac{1}{12} \chi \frac{|\mathcal{R}(\varphi)|}{|\nabla\varphi|} k^{\text{add}} \frac{d^4\varphi}{dx^4} \right) h^2 \end{aligned}$$

Chapter 3. The Positivity Preserving Variational Method

$$+ \left(-\frac{u^2}{12} \frac{d^4 \varphi}{dx^4} - \frac{us}{6} \frac{d^3 \varphi}{dx^3} + \frac{u|s|}{6} \frac{d^3 \varphi}{dx^3} + \frac{s|s|}{6} \frac{d^2 \varphi}{dx^2} \right) \tau h^2 + \mathcal{O}(\tau^2, h^4). \quad (3.83)$$

The proposed method is at least second-order accurate in all the regimes except the convection-

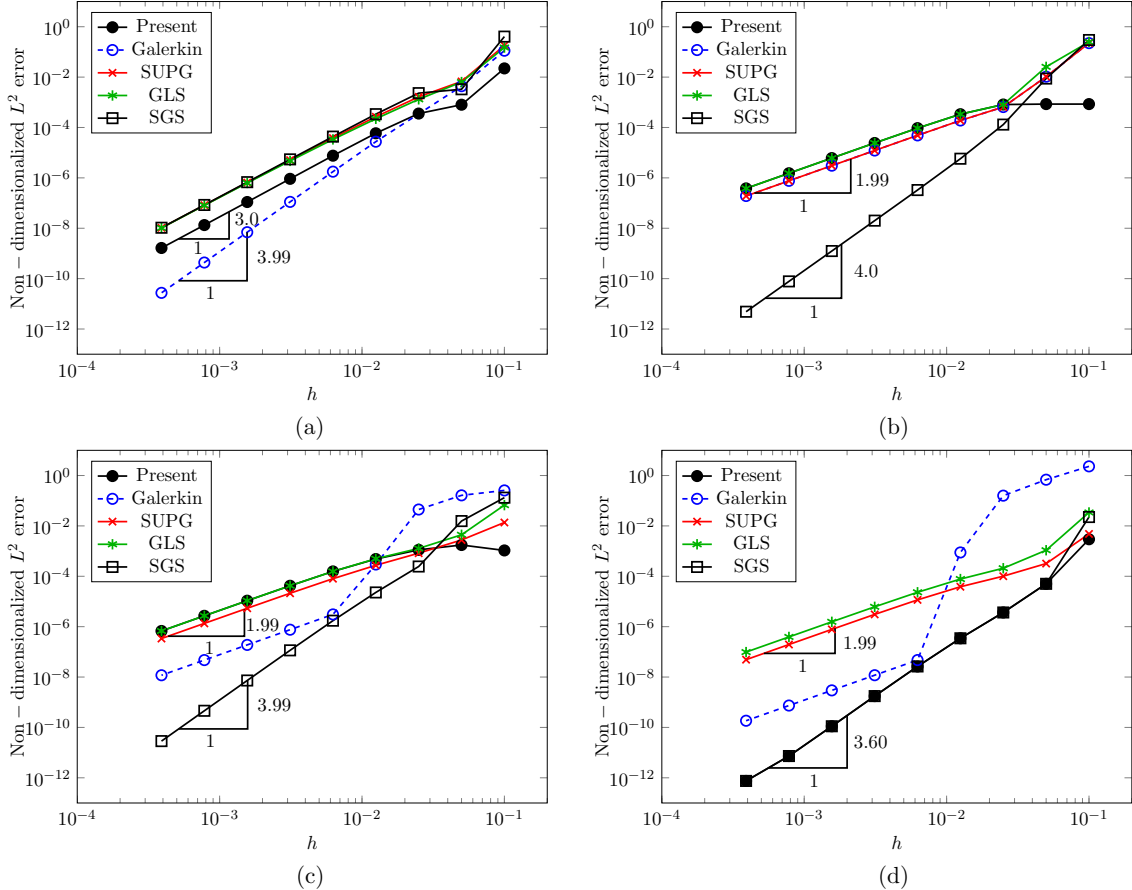


Figure 3.4: Mesh convergence study for various finite element methods through dependence of non-dimensionalized L^2 error as a function of uniform mesh refinement h : (a) convection-reaction; (b) diffusion-reaction; (c) CDR (destruction) and (d) CDR (production) problem. Number of elements is increased by decreasing h .

reaction where we see a third-order of accuracy and in the propagation regime where a fourth-order of accuracy is observed. This can be explained as follows. Under the asymptotic convergence regime, the residual of the equation tends to be negligible leading to the behavior of the method to be that of its parent linear method, i.e., GLS when $s \geq 0$ and SGS when $s < 0$. This is observed in the convergence plots as the trend of the error follows that of the parent method. The properties shown above about the accuracy are confirmed by the mesh convergence plots in Fig. 3.4. The parameters such as convection velocity (u), diffusion coefficient (k) and reaction coefficient (s) are kept constant while varying the element length (h) during the uniform mesh refinement in the convergence study. The convergence of solution with respect to element size

(h) is shown in Figs. 3.4(a), 3.4(b), 3.4(c) and 3.4(d) for the convection-reaction, the diffusion-reaction, the CDR with destruction and production cases respectively. For the CR equation, $u = 1$, $s = 50$, $f = 0$ with left-hand node assigned value of 1; while for the DR equation, $k = 0.01$, $s = 50$, $f = 0$, left-hand and right-hand nodes have values of 8 and 3 respectively. $u = 4$, $k = 0.01$ and $f = 1$ with Dirichlet condition of 0 is imposed at both the extreme nodes with $s = 60$ for the CDR equation with destruction effects and $s = -6$ for the CDR equation with production effects. The number of elements is increased by a factor of 2 from 10 to 2560. Three comments can be made from the mesh convergence plots. Firstly, the measured slope of the PPV method is higher than 2 for the steady-state convection-reaction equation, as shown in Fig. 3.4(a). Secondly, the GLS, SUPG and the present PPV methods provide second-order accuracy for the diffusion-reaction and the CDR equations. Finally, the SGS shows an order of accuracy up to 4 for the diffusion-reaction and the CDR equations, as shown in Figs. 3.4(b)-(d). Although the mesh convergence study has been done for the steady CDR equation, Fourier analysis of the transient CDR equation has been carried out in Appendix C and D and Section 3.3.2.

3.4 Numerical results

To further assess the accuracy of the PPV scheme and compare against other stabilized finite element methods, we present detailed results for one-dimensional and two-dimensional cases for wide-ranging conditions of the CDR equation. Furthermore, we demonstrate the generality of the method for unstructured and anisotropic two-dimensional meshes.

3.4.1 One-dimensional cases

First, we test several one-dimensional steady-state cases for verification. A domain of length $L = 1$ is discretized with 10 linear one-dimensional elements. The categories of various cases are described as follows:

- Canonical forms
 - Convection-diffusion equation: $Pe = 1$ with $f = 1$ and $(0, 0)$ (Fig. 3.5(a))

Chapter 3. The Positivity Preserving Variational Method

- Convection-reaction equation: $Da = 10$ with $f = 1$ and inlet condition = 0 (Fig. 3.5(b))
- Diffusion-reaction equation: $\psi = 10$ with $f = 1$ and $(0, 0)$ (Fig. 3.5(c))

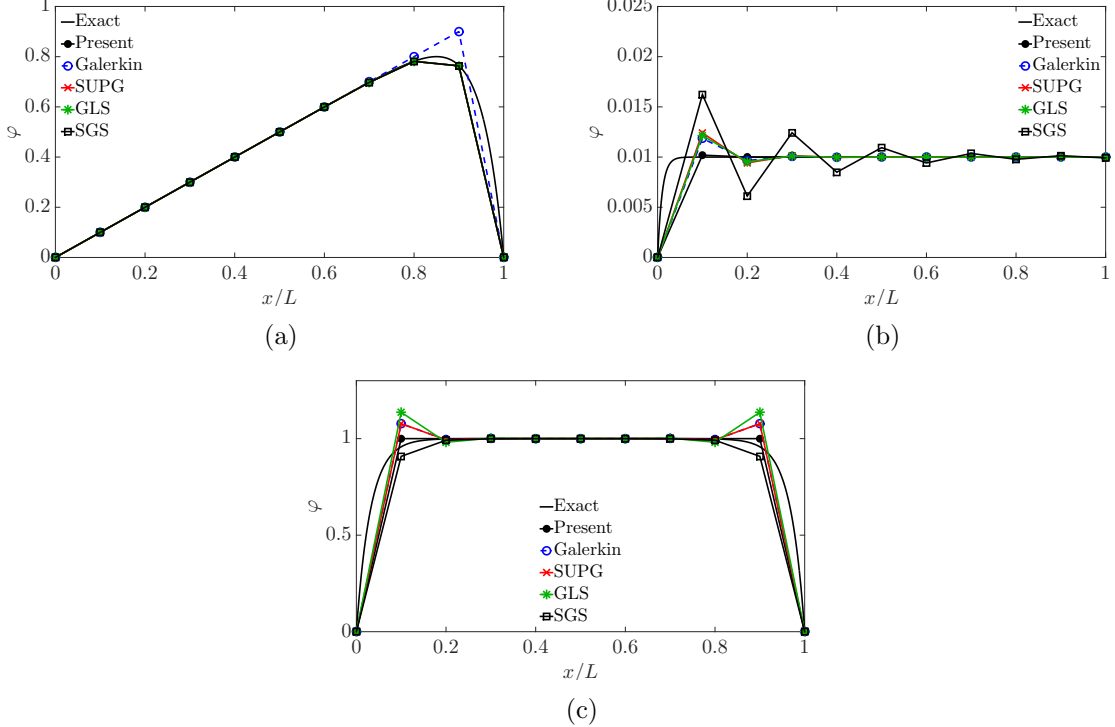


Figure 3.5: Variation of scalar field φ of the steady CDR equation in one-dimension in the three canonical regimes: (a) Convection-diffusion ($Pe = 1$, $f = 1$, $(0,0)$); (b) Convection-reaction ($Da = 10$, $f = 1$, inlet Dirichlet condition = 0); (c) Diffusion-reaction ($\psi = 10$, $f = 1$, $(0,0)$).

- With source term ($f \neq 0$)
 - $Pe = 0.01$ and $Da = 100$ with $(0,0)$ (Fig. 3.6(a))
 - $Pe = 1$ and $Da = 10$ with $(0,0)$ (Fig. 3.6(b))
 - $Pe = 10$ and $Da = 1$ with $(0,0)$ (Fig. 3.6(c))
- Without source term ($f = 0$)
 - $Pe = 0.1$ and $Da = 10$ with $(0,1)$ (Fig. 3.7(a))
 - $Pe = 1$ and $Da = 10$ with $(8,3)$ (Fig. 3.7(b))
 - $Pe = 10$ and $Da = 10$ with $(0,1)$ and $(1,0)$ (Figs. 3.7(c) and 3.7(d))
 - $Pe = 10$ and $Da = 0.1$ with $(1,0)$ (Fig. 3.7(e))

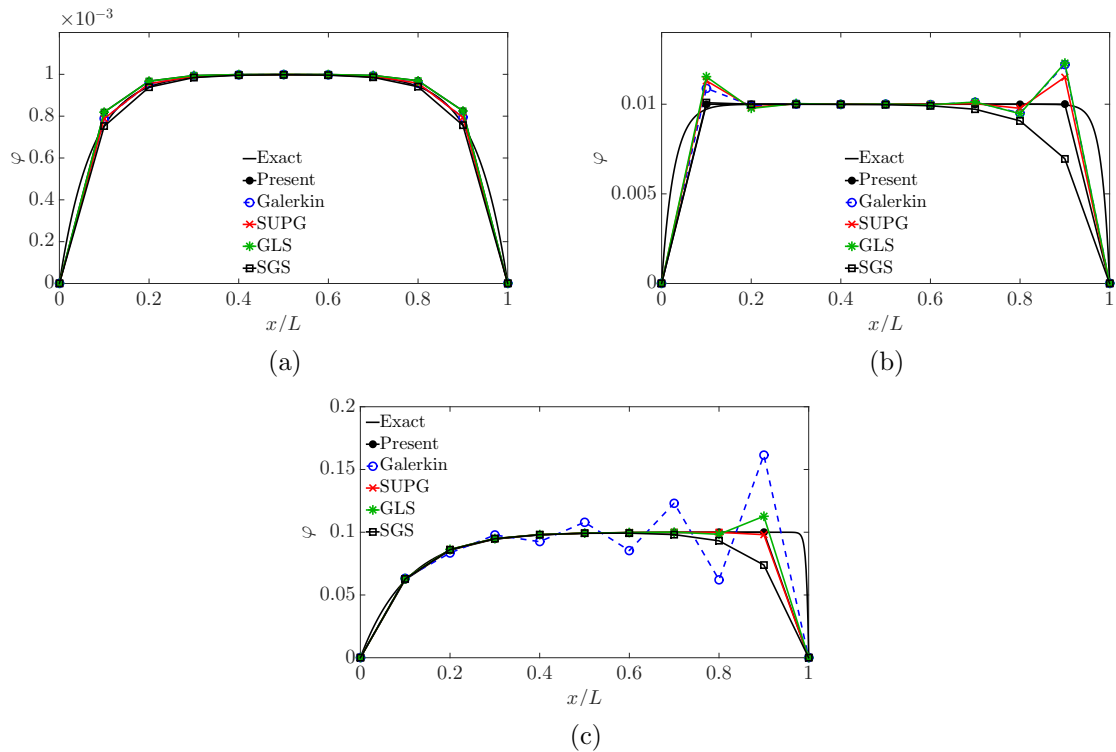


Figure 3.6: Solution of the scalar field φ of the steady CDR equation in one-dimension by setting the source term, $f \neq 0$: (a) $Pe = 0.01$, $Da = 100$, $f = 1$, $(0, 0)$; (b) $Pe = 1.0$, $Da = 10$, $f = 1$, $(0, 0)$; (c) $Pe = 10$, $Da = 1.0$, $f = 1$, $(0, 0)$.

- $Pe = 10$ and $Da = 0.2$ with $(8, 3)$ (Fig. 3.7(f))
 - $Pe = 10$ and $Da = 1$ with $(8, 3)$ (Fig. 3.7(g))
 - $Pe = 1$ and $Da = 60$ with $(8, 3)$ (Fig. 3.7(h))
 - Production regime ($s < 0$)
 - Exponential regime ($u^2 + 4ks \geq 0$)
 - * $Pe = 1$ and $Da = -0.4$ with $(0, 1)$ (Fig. 3.8(a))
 - * $Pe = 1.5$ and $Da = -0.5$ with $f = 1$ and $(0, 0)$ (Fig. 3.8(b))
 - * $Pe = 9$ and $Da = -0.15$ with $(0, 1)$ and $(1, 0)$ (Figs. 3.8(c) and 3.8(d))
 - Propagation regime ($u^2 + 4ks < 0$)
 - * $Pe = 0.05$ and $Da = -3$ with $(0, 1)$ (Fig. 3.9(a))
 - * $Pe = 0.1$ and $Da = -6$ with $(0, 1)$ (Fig. 3.9(b))
 - * $Pe = 0.15$ and $Da = -9$ with $(0, 1)$ and $(1, 0)$ (Figs. 3.9(c) and 3.9(d))

Chapter 3. The Positivity Preserving Variational Method

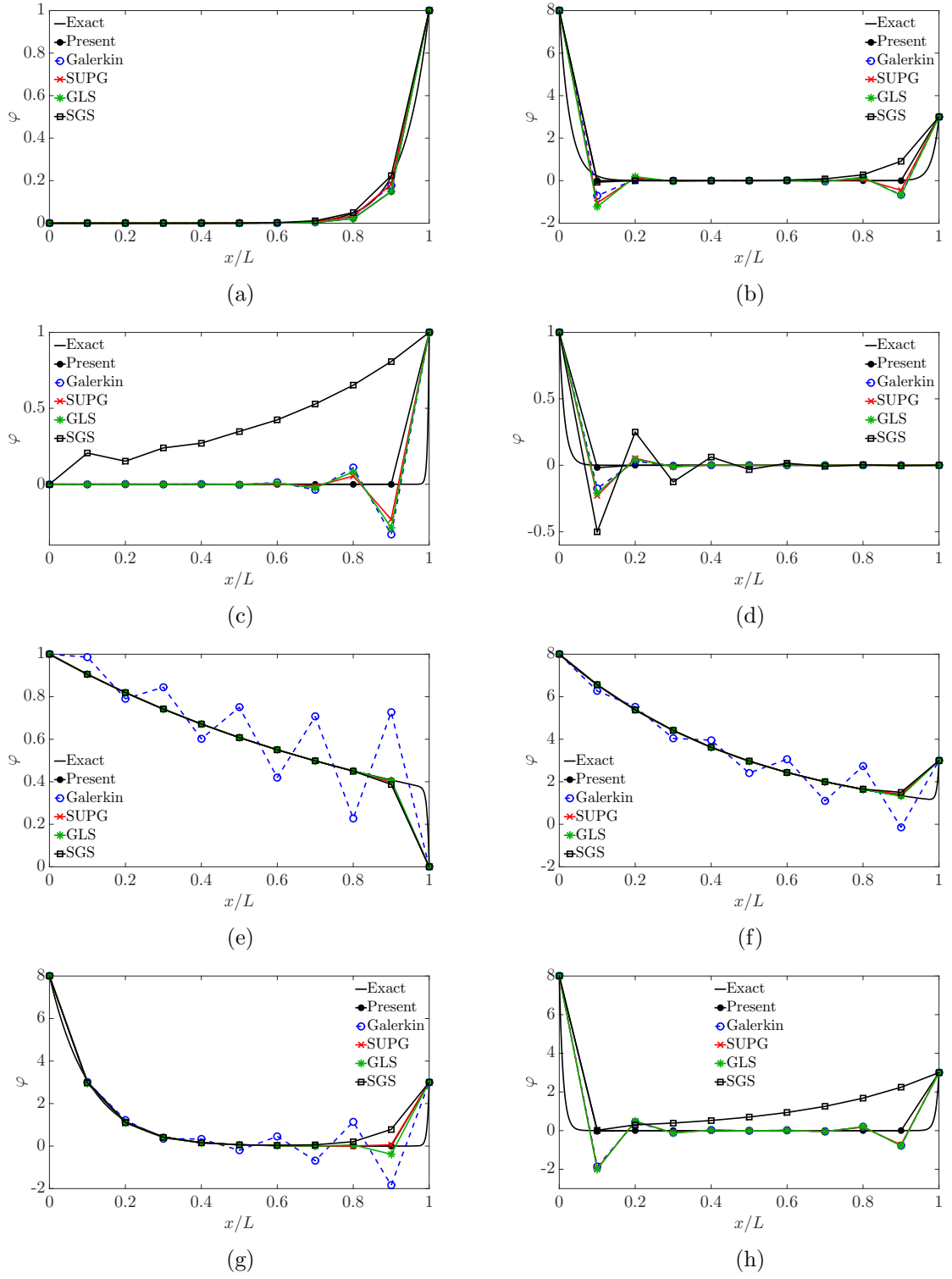


Figure 3.7: Solution of the scalar field φ of the steady CDR equation in one-dimension by setting the source term, $f = 0$: (a) $Pe = 0.1, Da = 10, (0, 1)$; (b) $Pe = 1.0, Da = 10, (8, 3)$; (c) $Pe = 10, Da = 10, (0, 1)$; (d) $Pe = 10, Da = 10, (1, 0)$; (e) $Pe = 10, Da = 0.1, (1, 0)$; (f) $Pe = 10, Da = 0.2, (8, 3)$; (g) $Pe = 10, Da = 1.0, (8, 3)$; (h) $Pe = 1.0, Da = 60, (8, 3)$.

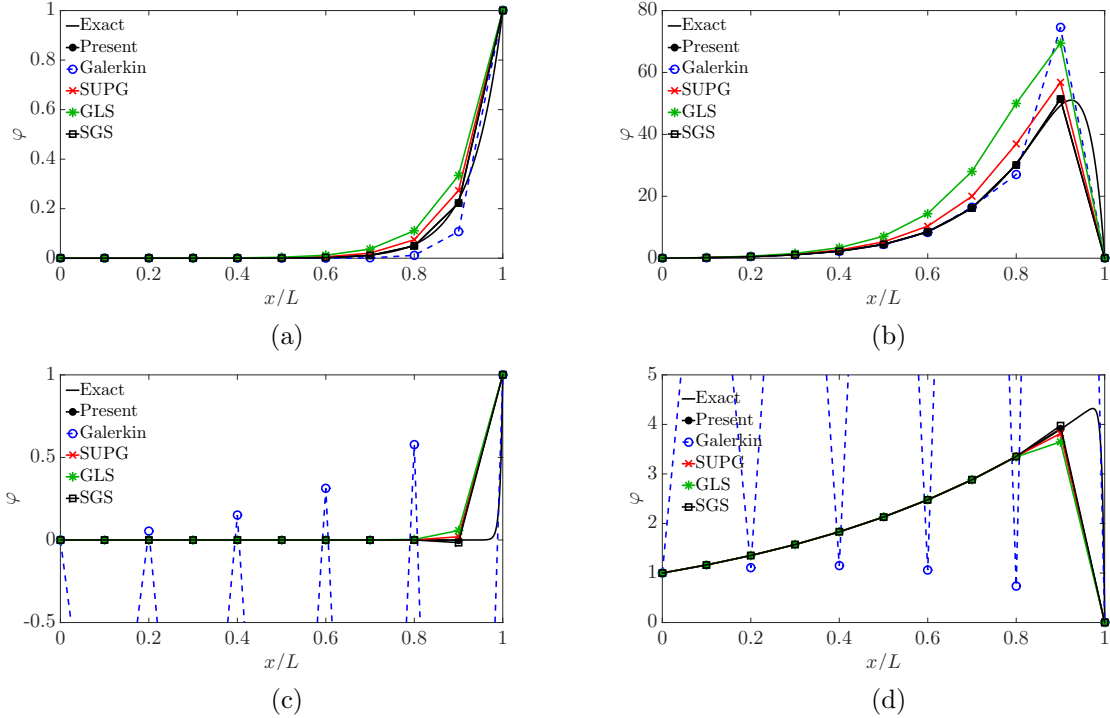


Figure 3.8: Solution of the steady CDR equation in one-dimension in the exponential regime: (a) $Pe = 1.0$, $Da = -0.4$, $f = 0$, $(0, 1)$; (b) $Pe = 1.5$, $Da = -0.5$, $f = 1$, $(0, 0)$; (c) $Pe = 9.0$, $Da = -0.15$, $f = 0$, $(0, 1)$; (d) $Pe = 9.0$, $Da = -0.15$, $f = 0$, $(1, 0)$. The Galerkin solution is very oscillatory and hence is shown partially in Figs. 3.8(c) and 3.8(d).

where $Pe = uh/2k$, $Da = sh/u$ and $\psi = sh^2/k$ and the values in brackets refer to the left and right Dirichlet boundary node values respectively.

The following key observations can be made from the steady one-dimensional study. The proposed method preserves positivity and precludes oscillations associated with the positivity and monotonicity violation. The other methods such as SUPG, GLS, and SGS lack the enforcement of positivity and local boundedness property. The PPV method behaves quite well for the propagation regime similar to the SGS method (Fig. 3.9) with minimal phase error, which is analyzed in Appendix C and D and shown in Section 3.2.1. The SGS method is excessively diffusive for high Da and Pe numbers (Figs. 3.7(c) and 3.7(h)). The Galerkin solution is very oscillatory in Figs. 3.8(c) and 3.8(d) and is partially shown.

To examine the performance of PPV method in the transient regime, the convection of two rectangular pulses is considered as the test problem for the transient CDR equation in one-dimension. The case is similar to that considered in [61]. The time integration is carried out by the Crank-Nicolson method with the nonlinear iterations via Picard fixed-point procedure. A

Chapter 3. The Positivity Preserving Variational Method

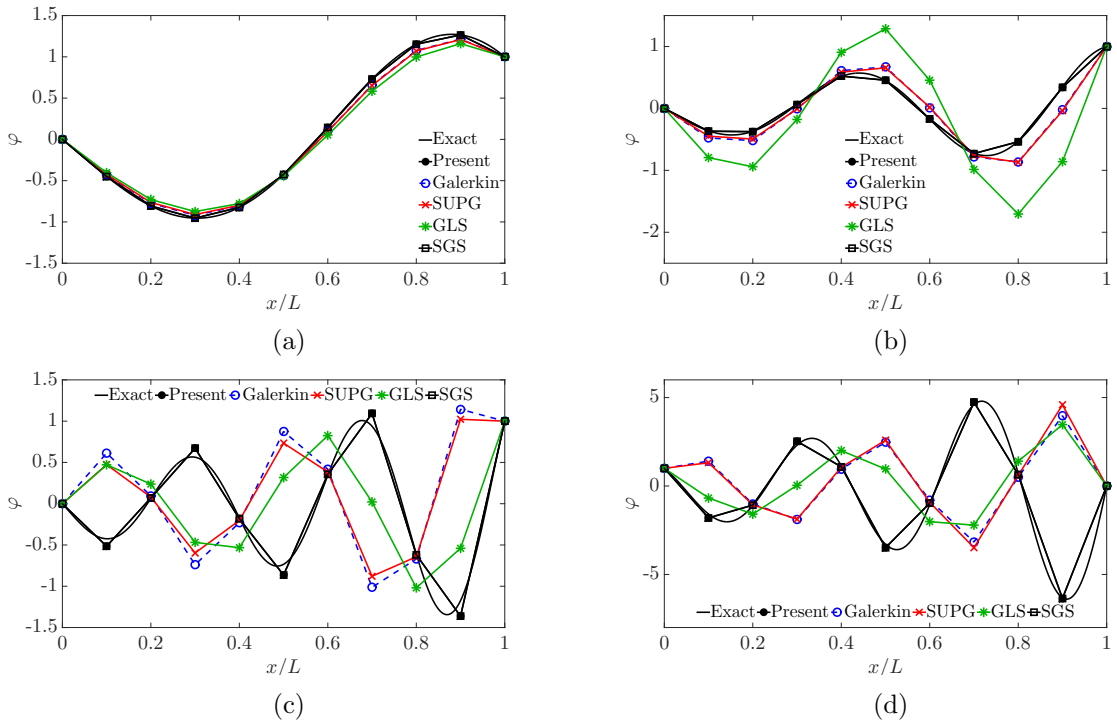


Figure 3.9: Solution of the steady CDR equation in one-dimension in the propagation regime: (a) $Pe = 0.05$, $Da = -3.0$, $f = 0$, $(0, 1)$; (b) $Pe = 0.1$, $Da = -6.0$, $f = 0$, $(0, 1)$; (c) $Pe = 0.15$, $Da = -9.0$, $f = 0$, $(0, 1)$; (d) $Pe = 0.15$, $Da = -9.0$, $f = 0$, $(1, 0)$.

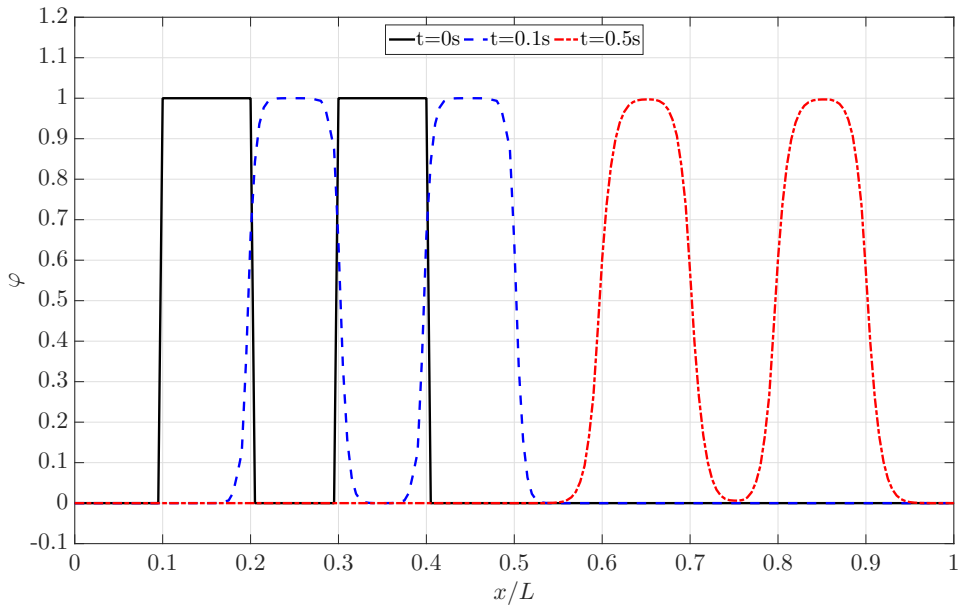


Figure 3.10: Solution of the transient CDR equation in one-dimension: Transient convection of two rectangular pulses, $u = 1$, $k = s = f = 0$.

total of 200 linear two-node elements is employed, and Δt is chosen as 0.002s with convection

velocity $u = 1$ and $k = s = f = 0$. The initial condition is

$$\varphi(x, t=0) = \begin{cases} 1, & \forall x \in [0.1, 0.2] \cup [0.3, 0.4], \\ 0, & \text{else.} \end{cases} \quad (3.84)$$

The progress of the rectangular pulse at $t = 0\text{s}$, $t = 0.1\text{s}$ and $t = 0.5\text{s}$ is shown in Fig. 3.10. Clearly, no oscillations are observed during the convection of the discontinuous rectangular pulses. The solution is smooth and the symmetry of the profile is maintained at all times.

3.4.2 Two-dimensional cases

We next consider a computational domain consisting of 20×20 and 80×80 bilinear structured quadrilateral elements for testing some two-dimensional steady-state cases. Cases are similar to those taken in [62]. Following test examples for the steady-state CDR equation in 2D are considered:

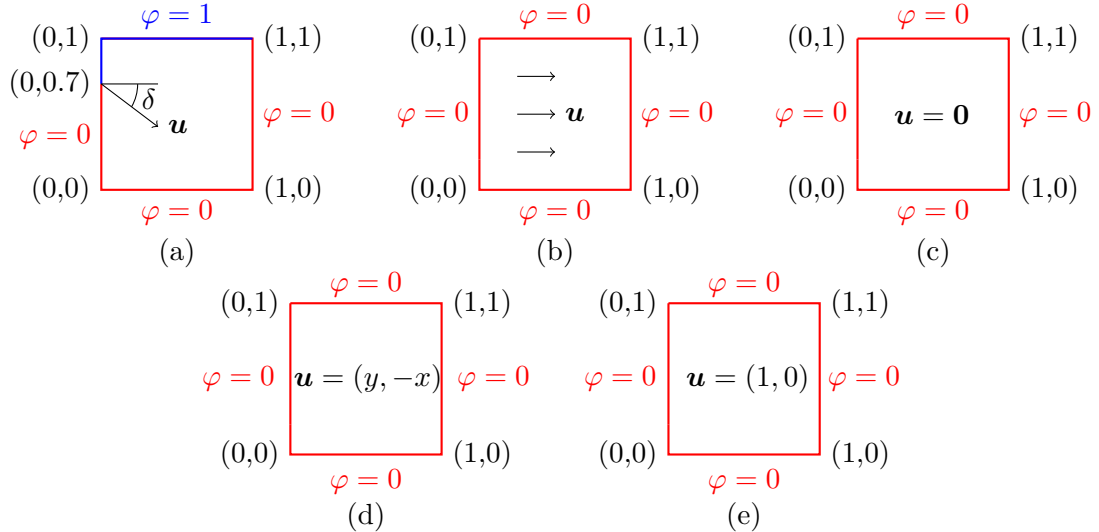


Figure 3.11: Schematic diagrams of the two-dimensional steady-state test cases: (a) convection-diffusion problem with unit skewed convection velocity, $s = 0$, $f = 0$; (b) convection-diffusion problem with constant source term, $s = 0$, $f = 1$; (c) diffusion-reaction problem with constant source term, $s = 1$, $f = 1$; (d) convection-diffusion problem with varying velocity and constant source term, $s = 0$, $f = 1$; (e) convection-diffusion problem with discontinuous source term, $s = 0$, $f(x \leq 0.5, y) = 1$, $f(x > 0.5, y) = -1$. The diffusion coefficient (k) is taken constant with a value of 10^{-8} for all the cases.

1. Convection-diffusion problem with unit convection velocity skewed to the mesh at $\delta = 0^\circ$, 30° , 45° , 60° and 90° with $|\mathbf{u}| = 1$, $k = 10^{-8}$, $s = 0$ and $f = 0$ (Fig. 3.12)

Chapter 3. The Positivity Preserving Variational Method

2. Convection-diffusion problem with constant source term. $\mathbf{u} = (1, 0)$, $k = 10^{-8}$, $s = 0$ and $f = 1$ (Fig. 3.13(a))
3. Diffusion-reaction problem with constant source term. $\mathbf{u} = (0, 0)$, $k = 10^{-8}$, $s = 1$ and $f = 1$ (Fig. 3.13(b))
4. Convection-diffusion problem with varying velocity and constant source term. $\mathbf{u} = (y, -x)$, $k = 10^{-8}$, $s = 0$ and $f = 1$ (Fig. 3.13(c))
5. Convection-diffusion with discontinuous source term. $\mathbf{u} = (1, 0)$, $k = 10^{-8}$, $s = 0$ and $f(x \leq 0.5, y) = 1, f(x > 0.5, y) = -1$ (Fig. 3.13(d))

The solution is observed to be slightly more diffusive as discussed in Remark 6. However, the internal and exponential layers are captured accurately with minimal oscillations, even the 90° skewed convection has less oscillation in the boundary. In Fig. 3.13(d), we observe some negative variation in the numerical solution for the refined case. This appears in the region where the source term $f < 0$. This shortcoming is generally manifested by all the discontinuity capturing methods which are based on the Petrov-Galerkin framework [162].

To examine the transient CDR equation in two-dimensions, pure convection of a circular bubble is simulated with a velocity at 45° with the X-axis [163, 62]. $\mathbf{u} = (0.5, 0.5)$, $k = 10^{-30}$, $s = 0$ and $f = 0$. A mesh of 300×300 was used with the Crank-Nicolson time integration method and $\Delta t = 0.005$ s. The initial condition is

$$\varphi(\mathbf{r}, t = 0) = H(R - |\mathbf{r} - \mathbf{r}^c|), \quad (3.85)$$

where $H()$ is the Heaviside function given by

$$H(y) = \frac{1 + \text{sgn}(y)}{2} = \begin{cases} 0, & y < 0, \\ 0.5, & y = 0, \\ 1, & y > 0, \end{cases} \quad (3.86)$$

where $\text{sgn}(y)$ is defined by $\frac{y}{|y|}$, \mathbf{r}^c is the center of the circular bubble $(0.5, 0.5)$, \mathbf{r} is the position vector in the computational domain and $R = 0.25$. The domain size is $[0, 3] \times [0, 3]$. The results are shown in Fig. 3.14. It can be observed that the amplitude of the circular bubble is maintained in the convection process with no observed oscillations in the solution. The solution is monotone visually and the mesh resolves the important characteristics of the solution. Table 3.2 depicts

Chapter 3. The Positivity Preserving Variational Method

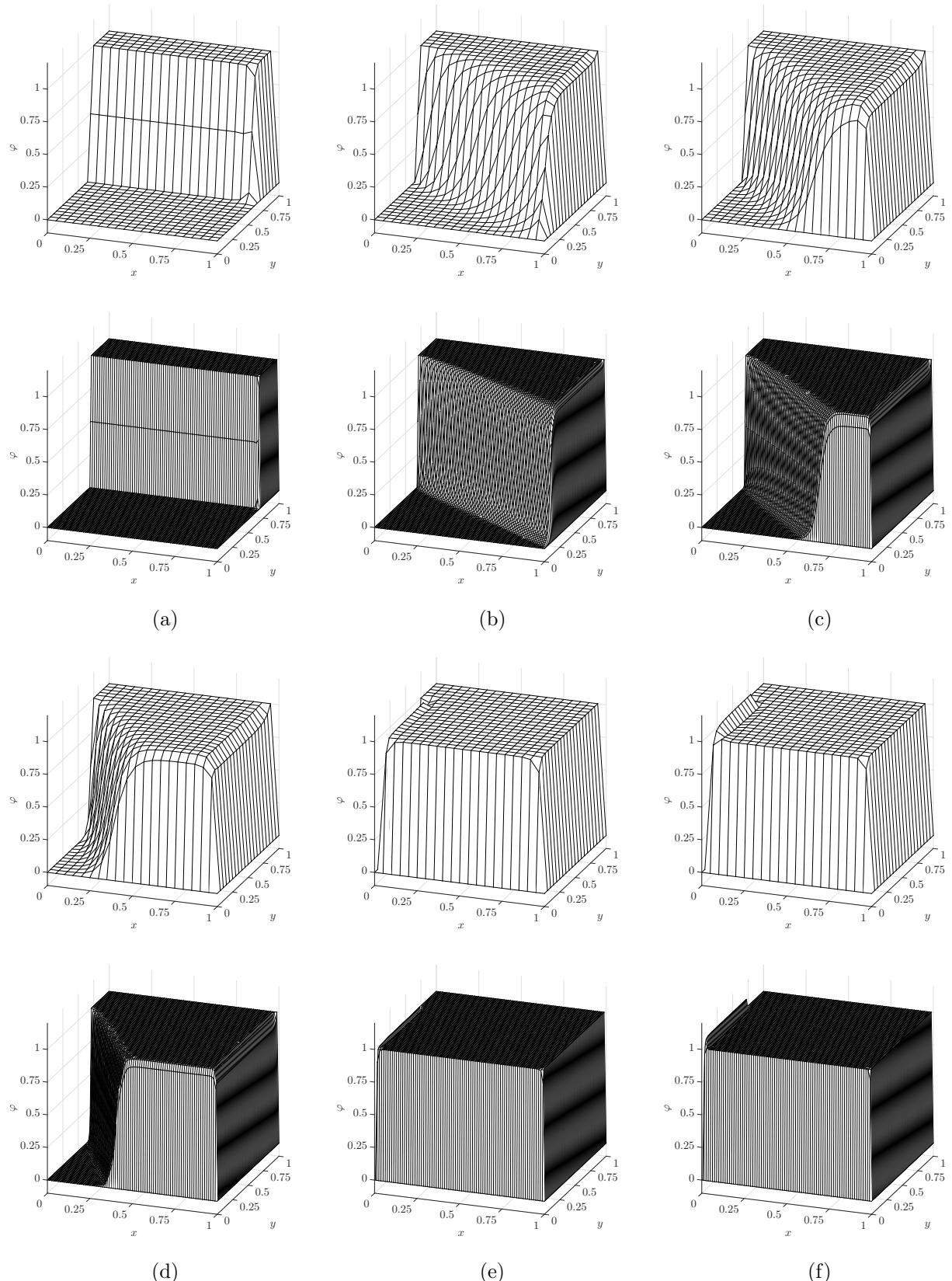


Figure 3.12: Solution of the steady-state CDR equation in two-dimensions at 20×20 and 80×80 mesh resolutions: Convection-diffusion problem with unit convection velocity skewed at- (a) 0° ; (b) 30° ; (c) 45° ; (d) 60° ; (e) 90° ; and (f) 90° (Codina [1]).

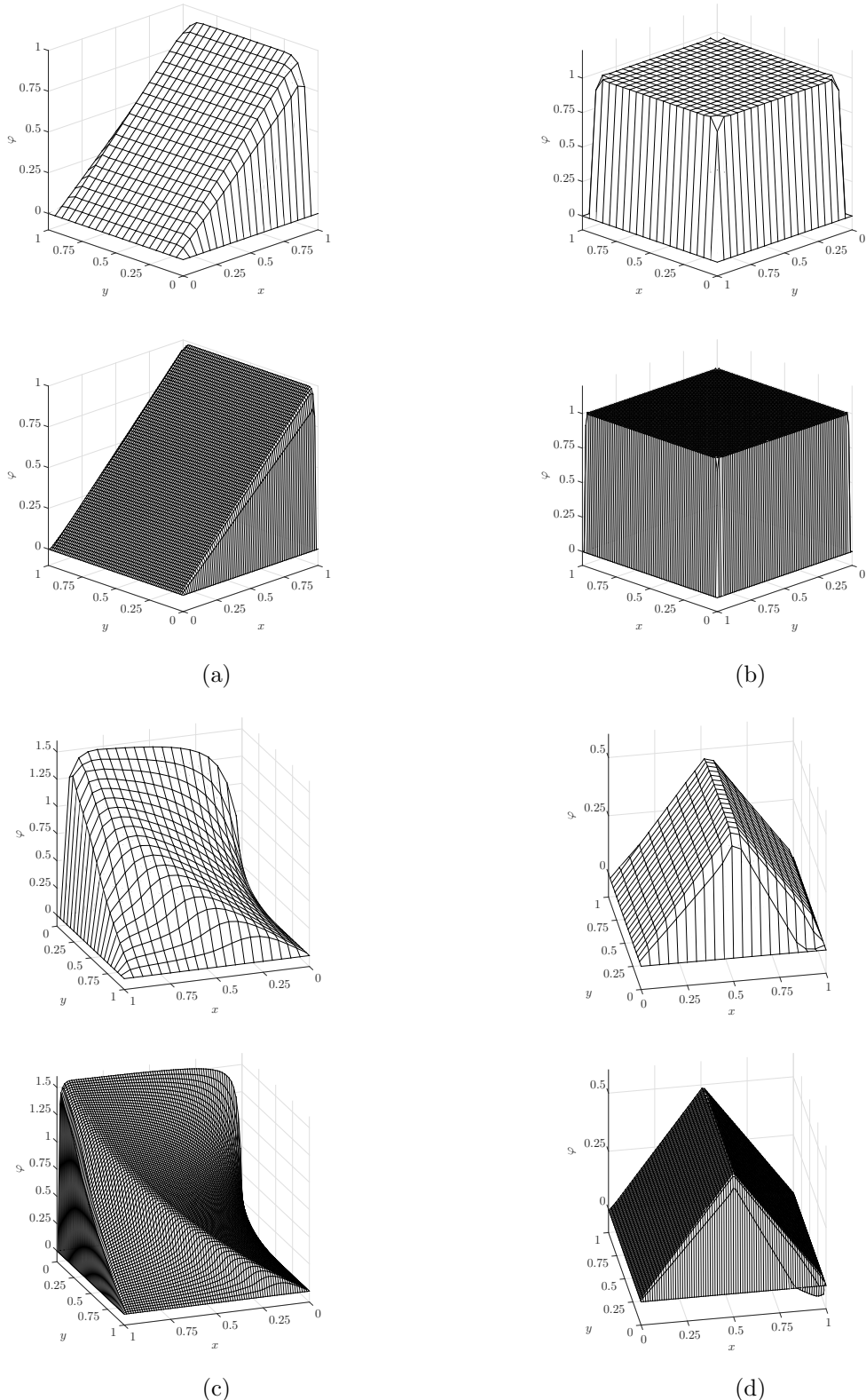


Figure 3.13: Solution of the steady-state CDR equation in two-dimensions at 20×20 and 80×80 mesh resolutions: (a) Convection-diffusion problem with constant source term; (b) Diffusion-reaction problem with constant source term; (c) Convection-diffusion problem with varying velocity and constant source term; (d) Convection-diffusion problem with discontinuous source term.

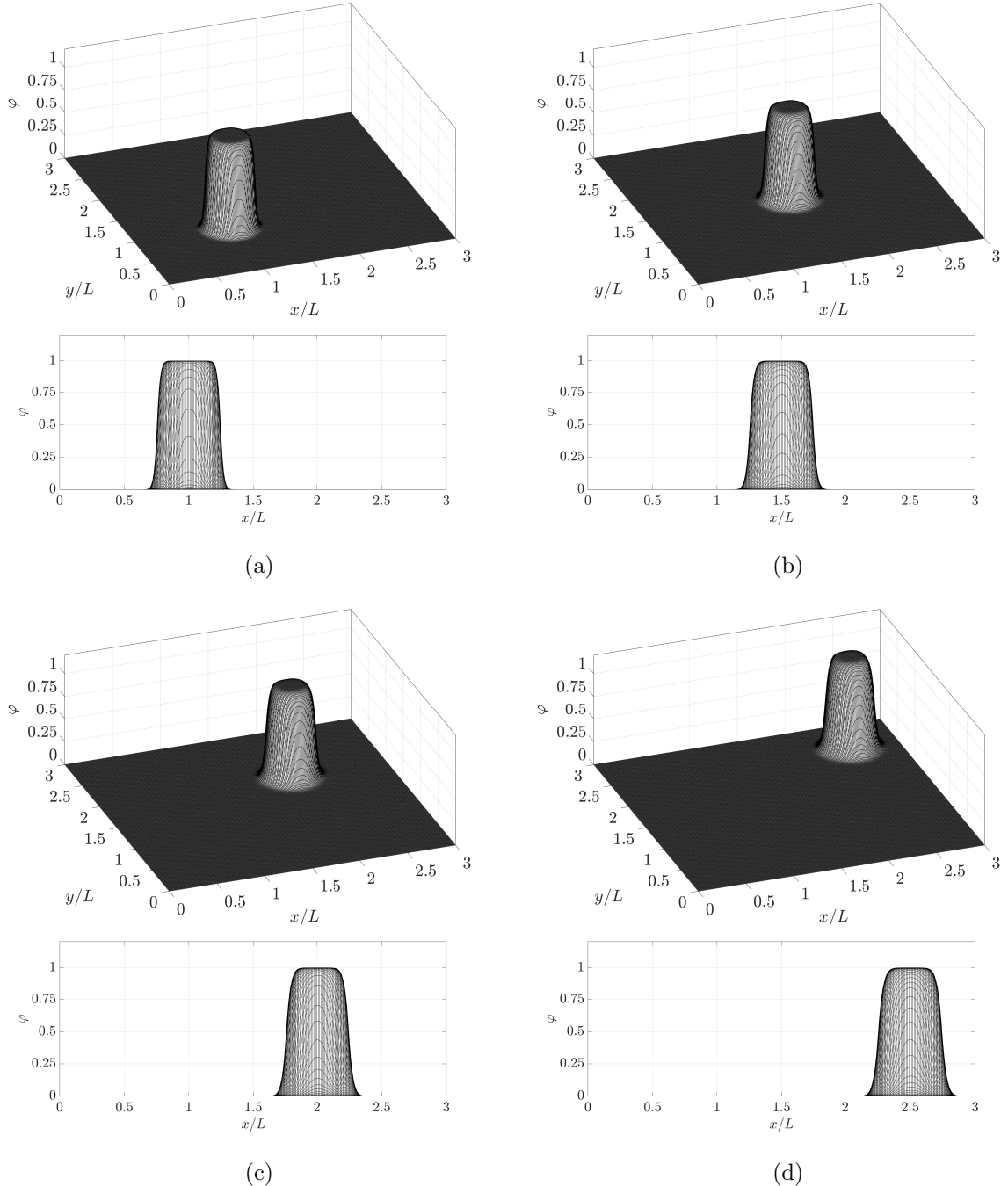


Figure 3.14: Solution of the transient CDR equation in two-dimensions: Transient convection of a circular bubble with the convection velocity at an angle of 45° with the X-axis, $k = 10^{-30}$, $s = 0$, $f = 0$ at- (a) $t = 1\text{s}$; (b) $t = 2\text{s}$, (c) $t = 3\text{s}$; (d) $t = 4\text{s}$.

Chapter 3. The Positivity Preserving Variational Method

Table 3.2: Quantification of the minimum and maximum values of the variable φ in different test cases in two-dimensions.

Case	$\max(\varphi)$	$\max(\varphi_{\text{exact}})$	$\min(\varphi)$	$\min(\varphi_{\text{exact}})$
Fig. 3.12(a) (20×20)	1.00002	1.0	-4.06514×10^{-6}	0.0
Fig. 3.12(a) (80×80)	1.00001	1.0	-3.40949×10^{-6}	0.0
Fig. 3.12(b) (20×20)	1.00165	1.0	0.0	0.0
Fig. 3.12(b) (80×80)	1.00165	1.0	-2.60600×10^{-6}	0.0
Fig. 3.12(c) (20×20)	1.00077	1.0	0.0	0.0
Fig. 3.12(c) (80×80)	1.00077	1.0	0.0	0.0
Fig. 3.12(d) (20×20)	1.00102	1.0	0.0	0.0
Fig. 3.12(d) (80×80)	1.00102	1.0	-5.67374×10^{-7}	0.0
Fig. 3.12(e) (20×20)	1.01578	1.0	0.0	0.0
Fig. 3.12(e) (80×80)	1.01634	1.0	0.0	0.0
Fig. 3.13(a) (20×20)	0.94999	0.95	0.0	0.0
Fig. 3.13(a) (80×80)	0.98749	0.9875	0.0	0.0
Fig. 3.13(b) (20×20)	1.00527	1.0	0.0	0.0
Fig. 3.13(b) (80×80)	1.00532	1.0	0.0	0.0
Fig. 3.13(c) (20×20)	1.50854	< 1.5708	0.0	0.0
Fig. 3.13(c) (80×80)	1.55723	< 1.5708	0.0	0.0
Fig. 3.13(d) (20×20)	0.50833	0.5	-0.01208	0.0
Fig. 3.13(d) (80×80)	0.50208	0.5	-0.04734	0.0
Fig. 3.14(a)	1.0	1.0	0.0	0.0
Fig. 3.14(b)	1.0	1.0	0.0	0.0
Fig. 3.14(c)	0.99999	1.0	0.0	0.0
Fig. 3.14(d)	0.99999	1.0	0.0	0.0

the comparison of the extreme values of the obtained numerical solution with that of the exact one for all the two-dimensional test cases considered. For generality, we next present some test cases in two-dimensions using unstructured and anisotropic meshes and give some insights about the performance of the proposed method.

3.4.3 Non-uniform unstructured and anisotropic meshes

To further assess the generality and robustness of the positivity preserving property, we present some numerical results for unstructured isotropic, structured anisotropic and unstructured anisotropic quadrilaterals. We consider the computational domain $\Omega = [0, 1] \times [0, 1]$ for the following three cases:

Chapter 3. The Positivity Preserving Variational Method

1. Skewed convection-diffusion problem at 60° with $|\mathbf{u}| = 1$, $k = 10^{-8}$, $s = 0$ and $f = 0$ (Fig. 3.11(a))
2. Convection-diffusion problem with constant source term with $\mathbf{u} = (1, 0)$, $k = 10^{-8}$, $s = 0$ and $f = 1$ (Fig. 3.11(b))
3. Diffusion-reaction problem with no convection with $\mathbf{u} = (0, 0)$, $k = 10^{-8}$, $s = 1$, $f = 1$ (Fig. 3.11(c))

We employ three types of meshes for the assessment:

- Mesh A: Unstructured quadrilateral in 20×20 grid (Fig. 3.15(a))
- Mesh B: Structured anisotropic quadrilateral in 10×100 grid (Fig. 3.15(b))
- Mesh C: Unstructured anisotropic quadrilateral in 20×100 grid (Fig. 3.15(c))

The meshes employed for the different cases are plotted in Figs. 3.15(a-c) while the numerical solution is superimposed for each case in the same figure. The unstructured meshes are created by perturbing the coordinates of the elements inside the domain of the structured mesh through a pseudo-random process given by

$$x_u = x_s + h_x \delta_x \text{rand}, \quad (3.87)$$

$$y_u = y_s + h_y \delta_y \text{rand}, \quad (3.88)$$

where (x_u, y_u) and (x_s, y_s) represent the nodal coordinates of the unstructured and structured meshes respectively, h_x and h_y are the mesh size of the structured mesh in x - and y -directions respectively and δ_x and δ_y are the mesh distortion parameters in the respective directions with rand representing uniformly distributed random numbers in the interval $(0, 1)$. For mesh A, we consider the mesh resolution $h_x = h_y = 1/20$ and $\delta_x = \delta_y = 0.5$ while for mesh C, we have $h_x = 1/20$, $h_y = 1/100$, $\delta_x = 0.2$ and $\delta_y = 1.0$. The plots show that the defined length scale behaves reasonably well for the cases considered herewith. It is worth pointing that high oscillations are observed for the anisotropic cases when the element length scale corresponding to Eq. (3.65) is considered. These oscillations are reduced when we use the length scale which takes into account the directionality of the wave vector (Eq. (3.66)). The comparison of the maximum and minimum values of the numerical solution with the exact solution for the cases

Chapter 3. The Positivity Preserving Variational Method

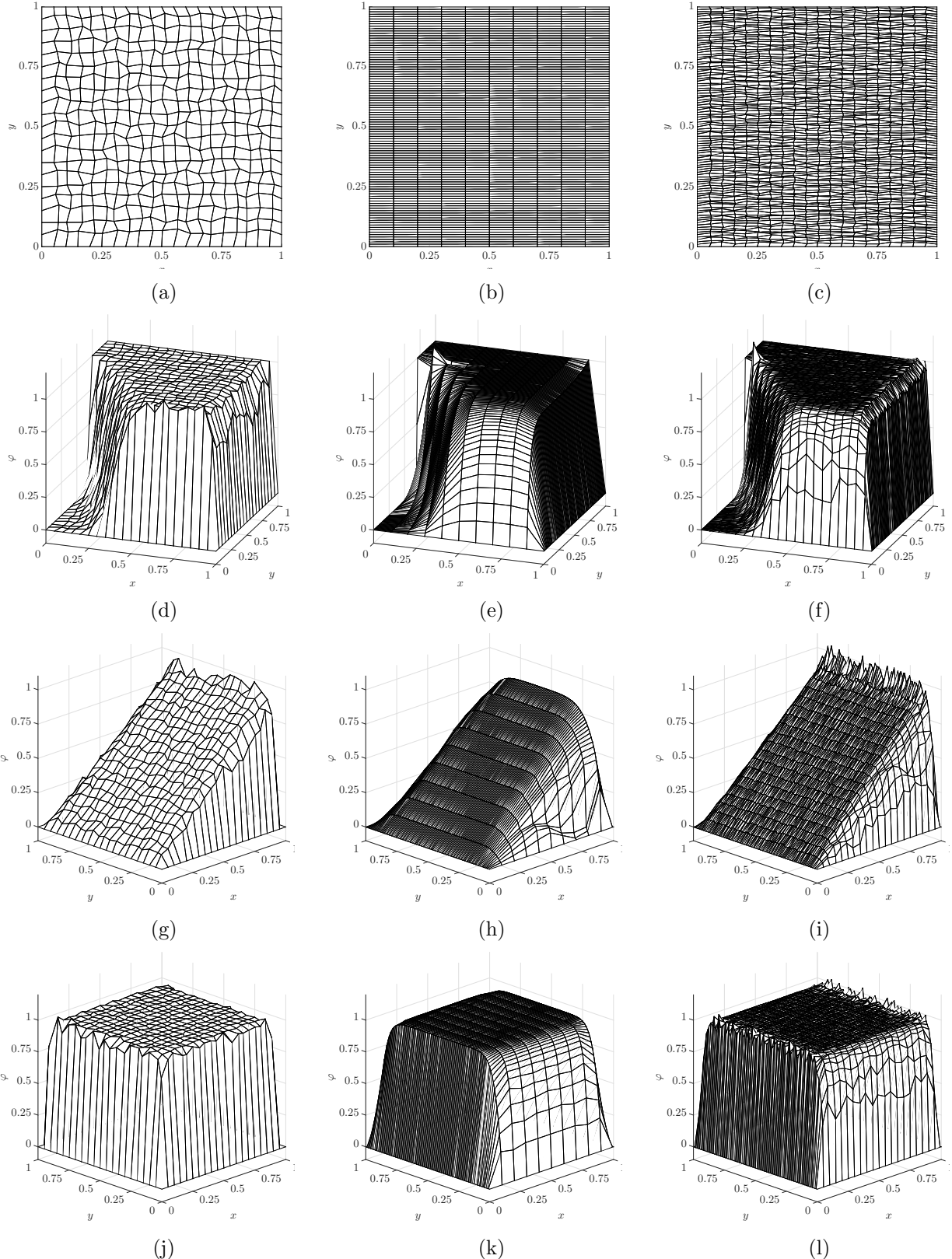


Figure 3.15: Three representative unstructured and anisotropic grids: (a) Mesh A, (b) Mesh B, (c) Mesh C. Results of the steady-state CDR equation in two-dimensions for skewed convection-diffusion problem at 60° (second row); Convection-diffusion problem with constant source term (third row); Diffusion-reaction problem (fourth row).

Chapter 3. The Positivity Preserving Variational Method

is quantified in Table 3.3. From the minimum and maximum length scales obtained by locating the direction of maximum instability [60], the range of the non-dimensional parameters namely Peclet number (Pe), Damköhler number (Da) and ψ has been summarized in Table 3.4.

Table 3.3: Quantification of the minimum and maximum values of the variable φ in different test cases in two-dimensions: Unstructured and anisotropic meshes.

Case	$\max(\varphi)$	$\max(\varphi_{\text{exact}})$	$\min(\varphi)$	$\min(\varphi_{\text{exact}})$
Fig. 3.15(d)	1.0756	1.0	0.0	0.0
Fig. 3.15(e)	1.1111	1.0	-1.1959×10^{-4}	0.0
Fig. 3.15(f)	1.1313	1.0	0.0	0.0
Fig. 3.15(g)	1.0012	< 1.0	0.0	0.0
Fig. 3.15(h)	0.8999	< 1.0	0.0	0.0
Fig. 3.15(i)	1.0787	< 1.0	0.0	0.0
Fig. 3.15(j)	1.0305	1.0	0.0	0.0
Fig. 3.15(k)	1.0	1.0	0.0	0.0
Fig. 3.15(l)	1.0728	1.0	0.0	0.0

From the tests on unstructured and anisotropic grids, we observe that the spurious oscillations

Table 3.4: The range of non-dimensional parameters: Unstructured and anisotropic meshes.

Case	$Pe = \mathbf{u} h/(2k)$	$Da = sh/ \mathbf{u} $	$\psi = sh^2/k$
Fig. 3.15(d)	$1.395 \times 10^6 - 3.875 \times 10^6$	0	0
Fig. 3.15(e)	4.33×10^6	0	0
Fig. 3.15(f)	$1.755 \times 10^6 - 2.595 \times 10^6$	0	0
Fig. 3.15(g)	$1.18 \times 10^6 - 3.895 \times 10^6$	0	0
Fig. 3.15(h)	5×10^6	0	0
Fig. 3.15(i)	$1.35 \times 10^5 - 3.01 \times 10^6$	0	0
Fig. 3.15(j)	0	∞	$1.354 \times 10^5 - 6.972 \times 10^5$
Fig. 3.15(k)	0	∞	1×10^6
Fig. 3.15(l)	0	∞	$1.648 \times 10^5 - 3.634 \times 10^5$

are reduced when the convection or the reaction effects are dominant. The internal layers in two-dimensions are captured with reasonable accuracy in the skewed convection case with unstructured quadrilaterals (Fig. 3.15(d)) while small oscillations are observed for the under-resolved and highly anisotropic meshes at the extreme values of non-dimensional parameters for the other cases. Based on these numerical experiments using anisotropic length scale and linear finite elements, the positivity behavior of the present method has been demonstrated.

3.5 Summary

To summarize, the accuracy and convergence properties of the PPV method have been systematically examined for a wide range of parameters using both one-dimensional and two-dimensional discretizations of the CDR equation. The results presented above lead to the following key characteristics of the PPV method:

- At least second-order of spatial accuracy in all the regimes of the non-dimensional parameters,
- Minimal phase error compared to the GLS and SUPG methods in the production and destruction regimes,
- Reasonable capturing of the internal and exponential layers with minimal oscillations for the test problems, and
- Generalization for non-uniform unstructured and anisotropic grids under different convection- and reaction-dominated regimes.

In the upcoming chapters, we explore the application of the PPV technique in the modeling of two-phase flows and turbulence via the Allen-Cahn and the turbulence transport equations respectively.

Chapter 4

Variational Fluid-Structure Framework

In this chapter, we review the governing equations and variational formulation for the two-phase Navier-Stokes and the structural equations, which form the fundamental laws in any fluid-structure interaction problem.

4.1 Coordinate systems

The fluid-structure formulation is described in appropriate coordinate systems to solve the governing equations for the fluid and the structure. We consider three different coordinate systems for the present study. A material domain Ω^s with material coordinates denoted by \boldsymbol{x}^s forms the reference coordinate system to represent the Lagrangian structure equation at time $t = 0$. In this domain, we follow the corresponding material point of the structure to its deformed state $\Omega^s(t)$. On the other hand, the Eulerian coordinate system is described by the spatial domain $\Omega^f(t)$ consisting of the coordinates denoted by \boldsymbol{x}^f . In the Eulerian description, the coordinates of the domain are fixed in space while we observe the change in the fluid variables in the domain. We introduce a third coordinate system with the coordinates denoted by $\boldsymbol{\chi}$ to handle the moving boundaries in the fluid-structure interaction. The fluid equations are written by selecting $\boldsymbol{\chi}$ as the reference coordinate system in what is called the arbitrary Lagrangian-Eulerian (ALE) description. The structure and the fluid-structure interface move

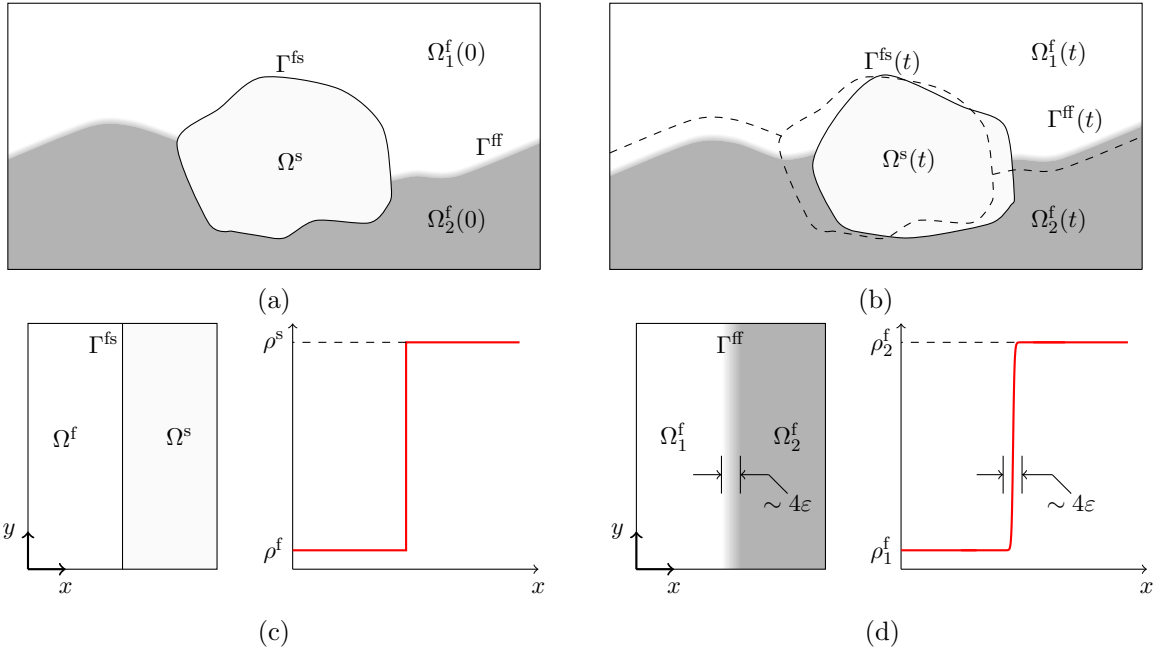


Figure 4.1: Schematic of two-phase fluid-structure interaction at (a) the initial configuration $t = 0$, and (b) some deformed configuration of the structure at time $t > 0$. $\Omega^f(0)$, Ω^s and $\Omega^f(t)$, $\Omega^s(t)$ are the fluid and the structural domains at $t = 0$ and some time $t > 0$ respectively with (c) sharp fluid-structure interface, and (d) diffused fluid-fluid interface, smeared using the internal length scale parameter ε . Γ^{fs} and Γ^{ff} denote the fluid-structure and fluid-fluid interfaces, respectively.

with the material coordinate system x^s , while the structural deformation can be realized in the fluid motion via an arbitrary movement of the fluid nodes.

4.2 The Navier-Stokes equations for two-phase flow

The two-phase flow equations are presented at the continuum level with their semi-discrete and variational formulation using the stabilized finite element framework.

4.2.1 Strong differential form

Consider a d -dimensional spatial fluid domain $\Omega^f(t) \subset \mathbb{R}^d$ with a piecewise smooth boundary $\Gamma^f(t)$. Let the boundary be decomposed into three components, the Dirichlet boundary $\Gamma_D^f(t)$, the Neumann boundary $\Gamma_H^f(t)$ and the fluid-structure boundary $\Gamma^{\text{fs}}(t)$ at time t . The domain $\Omega^f(t)$ consists of two immiscible, incompressible and Newtonian fluid phases occupying the sub-domains $\Omega_1^f(t)$ and $\Omega_2^f(t)$ with a boundary $\Gamma^{\text{ff}}(t)$ between them as shown in Fig. 4.1.

Chapter 4. Variational Fluid-Structure Framework

The governing equation for the one-fluid formulation for a viscous, incompressible and immiscible two-phase system with the boundary conditions are given as

$$\rho^f \frac{\partial \mathbf{u}^f}{\partial t} + \rho^f \mathbf{u}^f \cdot \nabla \mathbf{u}^f = \nabla \cdot \boldsymbol{\sigma}^f + \mathbf{s}^f + \mathbf{b}^f, \quad \text{on } \Omega^f(t), \quad (4.1)$$

$$\nabla \cdot \mathbf{u}^f = 0, \quad \text{on } \Omega^f(t), \quad (4.2)$$

$$\mathbf{u}^f = \mathbf{u}_D^f, \quad \forall \mathbf{x}^f \in \Gamma_D^f(t), \quad (4.3)$$

$$\boldsymbol{\sigma}^f \cdot \mathbf{n}^f = \mathbf{h}^f, \quad \forall \mathbf{x}^f \in \Gamma_H^f(t), \quad (4.4)$$

$$\mathbf{u}^f = \mathbf{u}_0^f, \quad \text{on } \Omega^f(0), \quad (4.5)$$

where \mathbf{u}^f represents the fluid velocity defined for each spatial point \mathbf{x}^f in $\Omega^f(t)$, ρ^f is the fluid density, \mathbf{s}^f denotes the surface tension singular force replaced by the continuum surface force in the diffuse-interface description, $\mathbf{b}^f = \rho^f \mathbf{g}$ is the body force applied on the fluid such as the gravitational force, with \mathbf{g} being the acceleration due to gravity. The boundary conditions at the Dirichlet and Neumann boundaries are denoted by \mathbf{u}_D^f and \mathbf{h}^f respectively, \mathbf{n}^f is the unit normal to the Neumann boundary and \mathbf{u}_0^f represents the initial velocity field at $t = 0$. The quantity $\boldsymbol{\sigma}^f$ is the Cauchy stress tensor for a Newtonian fluid, given as

$$\boldsymbol{\sigma}^f = -p \mathbf{I} + \mathbf{T}^f, \quad \mathbf{T}^f = 2\mu^f \boldsymbol{\epsilon}^f(\mathbf{u}^f), \quad \boldsymbol{\epsilon}^f(\mathbf{u}^f) = \frac{1}{2} [\nabla \mathbf{u}^f + (\nabla \mathbf{u}^f)^T], \quad (4.6)$$

where p denotes the fluid pressure, \mathbf{T}^f and $\boldsymbol{\epsilon}^f$ are the shear stress tensor and the fluid strain rate tensor respectively and μ^f denotes the dynamic viscosity of the fluid. The density and viscosity are dependent on the order parameter ϕ which evolves the fluid-fluid interface as

$$\rho^f(\phi) = \frac{1+\phi}{2} \rho_1^f + \frac{1-\phi}{2} \rho_2^f, \quad (4.7)$$

$$\mu^f(\phi) = \frac{1+\phi}{2} \mu_1^f + \frac{1-\phi}{2} \mu_2^f, \quad (4.8)$$

where ρ_i^f and μ_i^f are the density and dynamic viscosity of the i th phase of the fluid respectively.

4.2.2 Equations in the ALE framework

We write the equations in the ALE framework which combines the advantages of both the Eulerian and Lagrangian descriptions by expressing the equations in the new reference coordinates χ . Consider a one-to-one mapping function Φ^f from the referential coordinate system χ to the

spatial coordinate system \mathbf{x}^f denoted by

$$\mathbf{x}^f = \Phi^f(\chi, t), \quad (4.9)$$

and its gradient is

$$\frac{\partial \Phi^f}{\partial (\chi, t)} = \begin{pmatrix} \frac{\partial \mathbf{x}^f}{\partial \chi} & \mathbf{u}^m \\ \mathbf{0}^T & 1 \end{pmatrix}, \quad (4.10)$$

where \mathbf{u}^m is the velocity with which the spatial coordinates move with respect to the referential coordinate system χ , called the mesh velocity written as

$$\mathbf{u}^m = \left. \frac{\partial \mathbf{x}^f}{\partial t} \right|_{\chi}. \quad (4.11)$$

The material or total derivative of a function $f(\chi, t)$ in the ALE reference coordinate system can be written as

$$\frac{Df}{Dt} = \left. \frac{\partial f(\chi, t)}{\partial t} \right|_{\chi} + \left. \frac{\partial f(\mathbf{x}^f, t)}{\partial \mathbf{x}^f} \frac{\partial \mathbf{x}^f}{\partial \chi} \frac{\partial \chi}{\partial t} \right|_{\mathbf{x}^s}. \quad (4.12)$$

Considering the material derivative of the spatial coordinate \mathbf{x}^f ,

$$\mathbf{u}^f = \frac{D\mathbf{x}^f}{Dt} = \left. \frac{\partial \mathbf{x}^f(\chi, t)}{\partial t} \right|_{\chi} + \left. \frac{\partial \mathbf{x}^f}{\partial \chi} \frac{\partial \chi}{\partial t} \right|_{\mathbf{x}^s}. \quad (4.13)$$

Substituting Eqs. (4.13) and (4.11) in Eq. (4.12), we get

$$\frac{Df}{Dt} = \left. \frac{\partial f(\chi, t)}{\partial t} \right|_{\chi} + (\mathbf{u}^f - \mathbf{u}^m) \frac{\partial f(\mathbf{x}^f, t)}{\partial \mathbf{x}^f}. \quad (4.14)$$

Therefore, the one-fluid formulation in the ALE framework is obtained from Eqs. (4.14) and (4.1-4.2) as

$$\rho^f \left. \frac{\partial \mathbf{u}^f}{\partial t} \right|_{\chi} + \rho^f (\mathbf{u}^f - \mathbf{u}^m) \cdot \nabla \mathbf{u}^f = \nabla \cdot \boldsymbol{\sigma}^f + \mathbf{s}^f + \mathbf{b}^f, \quad \text{on } \Omega^f(t), \quad (4.15)$$

$$\nabla \cdot \mathbf{u}^f = 0, \quad \text{on } \Omega^f(t), \quad (4.16)$$

with the same boundary conditions as in Eqs. (4.3-4.5).

4.2.3 Semi-discrete variational form

The variational generalized- α time integration [153, 164] is employed for the temporal discretization of the flow equations. It enables a user-controlled high-frequency damping which is desirable for a coarser discretization in space and time. This is achieved by a single parameter

Chapter 4. Variational Fluid-Structure Framework

called the spectral radius ρ_∞ . Let ∂_t and Δt denote the partial derivative of a variable in time and the time step size respectively. The following expressions are employed for the temporal discretization:

$$\mathbf{u}^{f,n+1} = \mathbf{u}^{f,n} + \Delta t \partial_t \mathbf{u}^{f,n} + \gamma^f \Delta t (\partial_t \mathbf{u}^{f,n+1} - \partial_t \mathbf{u}^{f,n}), \quad (4.17)$$

$$\partial_t \mathbf{u}^{f,n+\alpha_m^f} = \partial_t \mathbf{u}^{f,n} + \alpha_m^f (\partial_t \mathbf{u}^{f,n+1} - \partial_t \mathbf{u}^{f,n}), \quad (4.18)$$

$$\mathbf{u}^{f,n+\alpha^f} = \mathbf{u}^{f,n} + \alpha^f (\mathbf{u}^{f,n+1} - \mathbf{u}^{f,n}), \quad (4.19)$$

where α^f , α_m^f and γ^f are the generalized- α parameters defined by

$$\alpha_m^f = \frac{1}{2} \left(\frac{3 - \rho_\infty}{1 + \rho_\infty} \right), \quad \alpha^f = \frac{1}{1 + \rho_\infty}, \quad \gamma^f = \frac{1}{2} + \alpha_m^f - \alpha^f. \quad (4.20)$$

Suppose $\mathcal{S}_{\mathbf{u}^f}^h$ and \mathcal{S}_p^h denote the space of trial solution such that

$$\mathcal{S}_{\mathbf{u}^f}^h = \{ \mathbf{u}_h^f \mid \mathbf{u}_h^f \in (H^1(\Omega^f(t)))^d, \mathbf{u}_h^f = \mathbf{u}_D^f \text{ on } \Gamma_D^f(t) \}, \quad (4.21)$$

$$\mathcal{S}_p^h = \{ p_h \mid p_h \in L^2(\Omega^f(t)) \}, \quad (4.22)$$

where $(H^1(\Omega^f(t)))^d$ denotes the space of square-integrable \mathbb{R}^d -valued functions with square-integrable derivatives on $\Omega^f(t)$ and $L^2(\Omega^f(t))$ is the space of the scalar-valued functions that are square-integrable on $\Omega^f(t)$. Similarly, we define $\mathcal{V}_{\psi^f}^h$ and \mathcal{V}_q^h as the space of test functions such that

$$\mathcal{V}_{\psi^f}^h = \{ \psi_h^f \mid \psi_h^f \in (H^1(\Omega^f(t)))^d, \psi_h^f = \mathbf{0} \text{ on } \Gamma_D^f(t) \}, \quad (4.23)$$

$$\mathcal{V}_q^h = \{ q_h \mid q_h \in L^2(\Omega^f(t)) \}. \quad (4.24)$$

The variational statement of the two-phase flow equations can thus be written as: find $[\mathbf{u}_h^f(t^{n+\alpha^f}), p_h(t^{n+1})] \in \mathcal{S}_{\mathbf{u}^f}^h \times \mathcal{S}_p^h$ such that $\forall [\psi_h^f, q_h] \in \mathcal{V}_{\psi^f}^h \times \mathcal{V}_q^h$,

$$\begin{aligned} & \int_{\Omega^f(t)} \rho^f(\phi) (\partial_t \mathbf{u}_h^f + (\mathbf{u}_h^f - \mathbf{u}_h^m) \cdot \nabla \mathbf{u}_h^f) \cdot \psi_h^f d\Omega + \int_{\Omega^f(t)} \boldsymbol{\sigma}_h^f : \nabla \psi_h^f d\Omega \\ & - \int_{\Omega^f(t)} \mathbf{s}\mathbf{f}_h(\phi) \cdot \psi_h^f d\Omega + \sum_{e=1}^{n_{el}} \int_{\Omega^e} \frac{\tau_m}{\rho^f(\phi)} (\rho^f(\phi) (\mathbf{u}_h^f - \mathbf{u}_h^m) \cdot \nabla \psi_h^f + \nabla q_h) \cdot \mathcal{R}_m d\Omega^e \\ & + \int_{\Omega^f(t)} q_h (\nabla \cdot \mathbf{u}_h^f) d\Omega + \sum_{e=1}^{n_{el}} \int_{\Omega^e} \nabla \cdot \psi_h^f \tau_c \rho^f(\phi) \mathcal{R}_c d\Omega^e \\ & - \sum_{e=1}^{n_{el}} \int_{\Omega^e} \tau_m \psi_h^f \cdot (\mathcal{R}_m \cdot \nabla \mathbf{u}_h^f) d\Omega^e - \sum_{e=1}^{n_{el}} \int_{\Omega^e} \frac{\nabla \psi_h^f}{\rho^f(\phi)} : (\tau_m \mathcal{R}_m \otimes \tau_m \mathcal{R}_m) d\Omega^e \\ & = \int_{\Omega^f(t)} \mathbf{b}^f(t^{n+\alpha^f}) \cdot \psi_h^f d\Omega + \int_{\Gamma_H^f} \mathbf{h}^f \cdot \psi_h^f d\Gamma, \end{aligned} \quad (4.25)$$

where the first and the second lines represent the Galerkin terms and the Petrov-Galerkin stabilization terms for the momentum equation, the third line depicts the Galerkin and the stabilization term for the continuity equation, the fourth line consists of the terms which are introduced as the approximation of the fine-scale velocity on the element interiors based on the multiscale argument [152, 165, 166] and the fifth line represents the body forces and the Neumann boundary conditions. The element-wise residuals of the momentum and the continuity equations are represented by \mathcal{R}_m and \mathcal{R}_c respectively, given by

$$\mathcal{R}_m = \rho^f \partial_t \mathbf{u}_h^f + \rho^f \mathbf{u}_h^f \cdot \nabla \mathbf{u}_h^f - \nabla \cdot \boldsymbol{\sigma}_h^f - \mathbf{s} \mathbf{f}_h - \mathbf{b}^f(t^{n+\alpha^f}), \quad (4.26)$$

$$\mathcal{R}_c = \nabla \cdot \mathbf{u}_h^f. \quad (4.27)$$

The stabilization parameters τ_m and τ_c are the least-squares metrics added to the element-level integrals in the stabilized formulation [37, 28, 167, 168] and are defined as

$$\tau_m = \left[\left(\frac{2}{\Delta t} \right)^2 + (\mathbf{u}_h^f - \mathbf{u}_h^m) \cdot \mathbf{G} (\mathbf{u}_h^f - \mathbf{u}_h^m) + C_I \left(\frac{\mu^f(\phi)}{\rho^f(\phi)} \right)^2 \mathbf{G} : \mathbf{G} \right]^{-1/2}, \quad (4.28)$$

$$\tau_c = \frac{1}{\text{tr}(\mathbf{G}) \tau_m}, \quad (4.29)$$

where C_I is a constant derived from the element-wise inverse estimates [155], \mathbf{G} is the element contravariant metric tensor, defined as

$$\mathbf{G} = \frac{\partial \boldsymbol{\xi}^T}{\partial \mathbf{x}^f} \frac{\partial \boldsymbol{\xi}}{\partial \mathbf{x}^f}, \quad (4.30)$$

where $\boldsymbol{\xi}$ are the parametric coordinates. $\text{tr}(\mathbf{G})$ is the trace of the contravariant metric tensor. This stabilization in the variational form circumvents the Babuška-Brezzi condition that is required to be satisfied by any standard mixed Galerkin method [169].

4.3 The structural equation

The structural equation is solved in the Lagrangian manner with the fluid spatial points moving according to the ALE moving mesh framework. The continuous differential equation for the structure with its variational discretization along with the boundary conditions is described in this section.

4.3.1 Strong differential form

Consider a d -dimensional structural domain $\Omega^s \subset \mathbb{R}^d$ with a piecewise smooth boundary Γ^s consisting of the material coordinates \boldsymbol{x}^s at time $t = 0$. The boundary Γ^s is divided into three disjoint sections consisting of the Dirichlet boundary Γ_D^s , the Neumann boundary Γ_H^s and the fluid-structure interface Γ^{fs} . A one-to-one mapping function $\boldsymbol{\varphi}^s(\boldsymbol{x}^s, t) : \Omega^s \rightarrow \Omega^s(t)$ is defined which denotes the position vector and maps the reference coordinates of the structure \boldsymbol{x}^s at $t = 0$ to its position in the deformed configuration $\Omega^s(t)$. Let $\boldsymbol{\eta}^s(\boldsymbol{x}^s, t)$ be the structural displacement due to the deformation. The position vector mapping is thus given by

$$\boldsymbol{\varphi}^s(\boldsymbol{x}^s, t) = \boldsymbol{\eta}^s(\boldsymbol{x}^s, t) + \boldsymbol{x}^s. \quad (4.31)$$

The velocity of the body at the deformed configuration is defined by

$$\boldsymbol{u}^s = \frac{\partial \boldsymbol{\varphi}^s}{\partial t} = \frac{\partial \boldsymbol{\eta}^s}{\partial t}, \quad \frac{\partial \boldsymbol{u}^s}{\partial t} = \frac{\partial^2 \boldsymbol{\varphi}^s}{\partial t^2} = \frac{\partial^2 \boldsymbol{\eta}^s}{\partial t^2}. \quad (4.32)$$

The structural equations can be written in the most general form as

$$\rho^s \frac{\partial^2 \boldsymbol{\varphi}^s}{\partial t^2} + \nabla \cdot \boldsymbol{\sigma}^s = \boldsymbol{b}^s, \quad \text{on } \Omega^s, \quad (4.33)$$

$$\boldsymbol{u}^s = \boldsymbol{u}_D^s, \quad \forall \boldsymbol{x}^s \in \Gamma_D^s, \quad (4.34)$$

$$\boldsymbol{\sigma}^s \cdot \mathbf{n}^s = \boldsymbol{h}^s, \quad \forall \boldsymbol{x}^s \in \Gamma_H^s, \quad (4.35)$$

$$\boldsymbol{\varphi}^s = \boldsymbol{\varphi}_0^s, \quad \text{on } \Omega^s, \quad (4.36)$$

$$\boldsymbol{u}^s = \boldsymbol{u}_0^s, \quad \text{on } \Omega^s, \quad (4.37)$$

where ρ^s , $\boldsymbol{\sigma}^s$ and \boldsymbol{b}^s denote the density, the stress tensor and the body forces acting on the structure respectively. The Dirichlet and Neumann boundary conditions on the structural velocity are denoted by \boldsymbol{u}_D^s and \boldsymbol{h}^s respectively with \mathbf{n}^s denoting the unit normal to the Neumann boundary. The initial position vector and velocity at $t = 0$ are represented by $\boldsymbol{\varphi}_0^s$ and \boldsymbol{u}_0^s respectively.

4.3.2 Semi-discrete variational form

For consistency in the discretization, the generalized- α technique is employed in discretizing the structural equation in time. The following expressions can be written in the framework:

$$\boldsymbol{\varphi}^{s,n+1} = \boldsymbol{\varphi}^{s,n} + \Delta t \mathbf{u}^{s,n} + \Delta t^2 \left(\left(\frac{1}{2} - \beta^s \right) \partial_t \mathbf{u}^{s,n} + \beta^s \partial_t \mathbf{u}^{s,n+1} \right), \quad (4.38)$$

$$\mathbf{u}^{s,n+1} = \mathbf{u}^{s,n} + \Delta t \left((1 - \gamma^s) \partial_t \mathbf{u}^{s,n} + \gamma^s \partial_t \mathbf{u}^{s,n+1} \right), \quad (4.39)$$

$$\partial_t \mathbf{u}^{s,n+\alpha_m^s} = \partial_t \mathbf{u}^{s,n} + \alpha_m^s (\partial_t \mathbf{u}^{s,n+1} - \partial_t \mathbf{u}^{s,n}), \quad (4.40)$$

$$\mathbf{u}^{n+\alpha^s} = \mathbf{u}^{s,n} + \alpha^s (\mathbf{u}^{s,n+1} - \mathbf{u}^{s,n}), \quad (4.41)$$

$$\boldsymbol{\varphi}^{n+\alpha^s} = \boldsymbol{\varphi}^{s,n} + \alpha^s (\boldsymbol{\varphi}^{s,n+1} - \boldsymbol{\varphi}^{s,n}), \quad (4.42)$$

where α^s , α_m^s , β^s and γ^s are the generalized- α parameters defined as

$$\alpha_m^s = \frac{1}{2} \left(\frac{3 - \rho_\infty}{1 + \rho_\infty} \right), \quad \alpha^s = \frac{1}{1 + \rho_\infty}, \quad \gamma^s = \frac{1}{2} + \alpha_m^s - \alpha^s, \quad \beta^s = \frac{1}{4} (1 - \alpha_m^s + \alpha^s)^2. \quad (4.43)$$

The formulation considers $\alpha^s = \alpha_m^s = \gamma^s = 0.5$ and $\beta^s = 0.25$.

Considering the space of trial solution $\mathcal{S}_{\mathbf{u}^s}^h$ and that of the test function $\mathcal{V}_{\boldsymbol{\psi}^s}^h$ which are defined as

$$\mathcal{S}_{\mathbf{u}^s}^h = \{ \mathbf{u}_h^s \mid \mathbf{u}_h^s \in (H^1(\Omega^s))^d, \mathbf{u}_h^s = \mathbf{u}_D^s \text{ on } \Gamma_D^s \}, \quad (4.44)$$

$$\mathcal{V}_{\boldsymbol{\psi}^s}^h = \{ \boldsymbol{\psi}_h^s \mid \boldsymbol{\psi}_h^s \in (H^1(\Omega^s))^d, \boldsymbol{\psi}_h^s = \mathbf{0} \text{ on } \Gamma_D^s \}, \quad (4.45)$$

the variational statement for the structural equation is given as: find $\mathbf{u}_h^s \in \mathcal{S}_{\mathbf{u}^s}^h$ such that $\forall \boldsymbol{\psi}_h^s \in \mathcal{V}_{\boldsymbol{\psi}^s}^h$,

$$\int_{\Omega^s} (\rho^s \partial_t \mathbf{u}_h^{s,n+\alpha_m^s}) \cdot \boldsymbol{\psi}_h^s d\Omega + \int_{\Omega^s} \boldsymbol{\sigma}_h^s : \nabla \boldsymbol{\psi}_h^s d\Omega = \int_{\Gamma_H^s} \mathbf{h}^s \cdot \boldsymbol{\psi}_h^s d\Gamma + \int_{\Omega^s} \mathbf{b}^s \cdot \boldsymbol{\psi}_h^s d\Omega. \quad (4.46)$$

In the present study, we consider three types of structural bodies, with increasing complexity, viz., rigid body, linear flexible body, and nonlinear multibodies. The respective simplified governing equations are described in the following sections. Note that the rigid and linear flexible body equations are solved via the generalized- α time integration while the nonlinear multibody equation is solved by a discontinuous Galerkin time integrator. Further details about this discretization can be found in [170].

4.3.2.1 Rigid body

We first consider the six degrees of freedom motion of a rigid body. Let the center of mass of the body in the reference configuration \mathbf{x}^s and the current configuration $\boldsymbol{\varphi}^s$ be \mathbf{x}_0^s and $\boldsymbol{\varphi}_0^s$ respectively and $\boldsymbol{\eta}_0^s$ denote the displacement of the center of mass due to translation of the body. Therefore, the rigid body kinematics is given by

$$\boldsymbol{\varphi}^s = \mathbf{Q}(\mathbf{x}^s - \mathbf{x}_0^s) + \boldsymbol{\varphi}_0^s = \mathbf{Q}(\mathbf{x}^s - \mathbf{x}_0^s) + \mathbf{x}_0^s + \boldsymbol{\eta}_0^s, \quad (4.47)$$

where \mathbf{Q} is a rotation matrix. Using Eqs. (4.31) and (4.47),

$$\boldsymbol{\eta}^s = (\mathbf{Q} - \mathbf{I})(\mathbf{x}^s - \mathbf{x}_0^s) + \boldsymbol{\eta}_0^s, \quad (4.48)$$

$$\frac{\partial \boldsymbol{\eta}^s}{\partial t} = \frac{\partial \mathbf{Q}}{\partial t}(\mathbf{x}^s - \mathbf{x}_0^s) + \frac{\partial \boldsymbol{\eta}_0^s}{\partial t}, \quad (4.49)$$

where \mathbf{I} is the identity matrix and Eq. (4.49) is obtained by differentiating Eq. (4.48) with respect to time. Suppose the rotational degrees of freedom for the body are given by $\boldsymbol{\theta}^s$. Equation (4.49) can be restructured in terms of the angular velocity of the body denoted by $\boldsymbol{\omega}^s = \partial \boldsymbol{\theta}^s / \partial t$ as

$$\frac{\partial \boldsymbol{\eta}^s}{\partial t} = \boldsymbol{\omega}^s \times (\boldsymbol{\varphi}^s - \boldsymbol{\varphi}_0^s) + \frac{\partial \boldsymbol{\eta}_0^s}{\partial t} \quad (4.50)$$

The rigid body equations are thus given by

$$\mathbf{M}^s \frac{\partial^2 \boldsymbol{\eta}_0^s}{\partial t^2} + \mathbf{C}_\eta \frac{\partial \boldsymbol{\eta}_0^s}{\partial t} + \mathbf{K}_\eta \boldsymbol{\eta}_0^s = \mathbf{f}^s, \text{ on } \Omega^s, \quad (4.51)$$

$$\mathbf{I}^s \frac{\partial^2 \boldsymbol{\theta}^s}{\partial t^2} + \mathbf{C}_\theta \frac{\partial \boldsymbol{\theta}^s}{\partial t} + \mathbf{K}_\theta \boldsymbol{\theta}^s = \boldsymbol{\tau}^s, \text{ on } \Omega^s, \quad (4.52)$$

where \mathbf{M}^s , \mathbf{C}_η and \mathbf{K}_η denote the mass, damping and stiffness matrices for the translational degrees of freedom respectively, \mathbf{I}^s , \mathbf{C}_θ and \mathbf{K}_θ represent the moment of inertia, damping and stiffness matrices for the rotational degrees of freedom respectively, and \mathbf{f}^s and $\boldsymbol{\tau}^s$ denote the forces and the moments applied on the body respectively.

4.3.2.2 Linear flexible body

For modeling flexible body dynamics, we consider a linear modal analysis by solving the Euler-Bernoulli beam equation. Suppose the axis of the beam is parallel to the Z -direction along which the coordinates are given by z . We solve for the lateral displacements (denoted by $\boldsymbol{\eta}^s(z, t)$) along

the beam as

$$m^s \frac{\partial^2 \boldsymbol{\eta}^s}{\partial t^2} + \frac{\partial^2}{\partial z^2} \left(EIL \frac{\partial^2 \boldsymbol{\eta}^s}{\partial z^2} \right) - PL \frac{\partial^2 \boldsymbol{\eta}^s}{\partial z^2} = \mathbf{f}^s, \quad (4.53)$$

where m^s , E , I , P , and \mathbf{f}^s denote the mass, Young's modulus, the second moment of the cross-sectional area of the beam, the applied axial tension and the externally applied force on the beam of span L respectively.

A beam under pinned-pinned condition has to satisfy the following boundary conditions at its ends

$$\boldsymbol{\eta}^s|_{z=0} = \mathbf{0}, \quad \frac{\partial^2 \boldsymbol{\eta}^s}{\partial z^2} \Big|_{z=0} = \mathbf{0}, \quad (4.54)$$

$$\boldsymbol{\eta}^s|_{z=L} = \mathbf{0}, \quad \frac{\partial^2 \boldsymbol{\eta}^s}{\partial z^2} \Big|_{z=L} = \mathbf{0}. \quad (4.55)$$

To solve Eq. (4.53), we employ a mode superposition procedure where the frequency of n th mode is given by

$$f_n = \frac{1}{2\pi} \sqrt{\frac{\frac{\pi^4}{L^3} \left(n^4 EI + \frac{n^2 PL^2}{\pi^2} \right)}{m^s}}. \quad (4.56)$$

The structural displacements are represented by the superposition of linear eigenmodes which are obtained using the eigenvalue analysis. For the current configuration, the eigenmodes are assumed to be sinusoidal so that the eigenmode shape for mode n is given by

$$S^n(z) = \sin\left(\frac{n\pi z}{L}\right). \quad (4.57)$$

Equation (4.53) can be recast into a matrix form as

$$\mathbf{M}^s \frac{\partial^2 \boldsymbol{\eta}^s}{\partial t^2} + \mathbf{K}^s \boldsymbol{\eta}^s = \mathbf{f}^s, \quad (4.58)$$

where \mathbf{M}^s and \mathbf{K}^s are the mass and stiffness matrices respectively, $\boldsymbol{\eta}^s$ is the vector of unknown displacements along the beam and \mathbf{f}^s is the vector of the force applied on the beam. Now, we project the above equation in the eigenspace with eigenmodes defined by Eq. (4.57), which transforms Eq. (4.58) to a system of linear equations with n degrees of freedom (modes) as

$$\widetilde{\mathbf{M}}^s \frac{\partial^2 \boldsymbol{\xi}^s}{\partial t^2} + \widetilde{\mathbf{K}}^s \boldsymbol{\xi}^s = \widetilde{\mathbf{f}}^s, \quad (4.59)$$

where $\widetilde{\mathbf{M}}^s = \mathbf{S}^T \mathbf{M}^s \mathbf{S}$ and $\widetilde{\mathbf{K}}^s = \mathbf{S}^T \mathbf{K}^s \mathbf{S}$ are the projected matrices on the eigenspace with \mathbf{S} being the matrix containing the eigenvectors and $\boldsymbol{\xi}^s$ being the vector of the modal responses

along the beam. The projected force vector $\tilde{\mathbf{f}}^s = \mathbf{S}^T \mathbf{f}^s$ and $\boldsymbol{\eta}^s = \mathbf{S} \boldsymbol{\xi}^s$.

4.3.2.3 Nonlinear flexible multibodies

We also consider the nonlinear flexible multibody equation to model the rigid body as well as flexible structures in a monolithic manner. The structure equation in this case is the general structural equation given by Eq. (4.33) solved on Ω_i^s , where i is the structural component of the multibody system, for example, rigid body, beam, cables, etc. The first Piola-Kirchhoff stress tensor is denoted by $\boldsymbol{\sigma}^s$ which is a function of the Cauchy-Green Lagrangian strain tensor, $\mathbf{E}(\boldsymbol{\eta}^s)$ given by $\mathbf{E}(\boldsymbol{\eta}^s) = 1/2[(\mathbf{I} + \nabla \boldsymbol{\eta}^s)^T (\mathbf{I} + \nabla \boldsymbol{\eta}^s) - \mathbf{I}]$. The structural equation for the nonlinear multibody equations is solved via discontinuous Galerkin time integration scheme, details of which are discussed in [170].

4.4 The fluid-structure interface

The coupling between the fluid and the structural equations is achieved by the velocity continuity and the equilibrium of the tractions along the fluid-structure interface. Suppose $\Gamma^{fs} = \Gamma^f(0) \cap \Gamma^s$ denotes the fluid-structure interface at $t = 0$. The interface at time t will then be denoted by $\Gamma^{fs}(t) = \varphi^s(\Gamma^{fs}, t)$. The required conditions to be satisfied at the interface can be mathematically formulated as

$$\mathbf{u}^f(\varphi^s(\mathbf{x}^s, t), t) = \mathbf{u}^s(\mathbf{x}^s, t), \quad \forall \mathbf{x}^s \in \Gamma^{fs}, \quad (4.60)$$

$$\int_{\varphi^s(\gamma, t)} \boldsymbol{\sigma}^f(\mathbf{x}^f, t) \cdot \mathbf{n}^f d\Gamma + \int_{\gamma} \boldsymbol{\sigma}^s(\mathbf{x}^s, t) \cdot \mathbf{n}^s d\Gamma = 0, \quad \forall \gamma \subset \Gamma^{fs}, \quad (4.61)$$

where \mathbf{n}^f and \mathbf{n}^s are the unit normals to the deformed fluid element $\varphi^s(\gamma, t)$ and its corresponding undeformed structural element γ respectively. Here, γ is any part of the interface Γ^{fs} in the reference configuration.

4.5 The fluid-fluid interface

In the sharp fluid-fluid interface description, the velocity continuity and the pressure-jump condition are required to be satisfied at the interface,

$$\mathbf{u}_{\Omega_1^f}^f = \mathbf{u}_{\Omega_2^f}^f, \quad \forall \mathbf{x}^f \in \Gamma^{ff}(t), \quad (4.62)$$

$$(\boldsymbol{\sigma}_{\Omega_1^f}^f - \boldsymbol{\sigma}_{\Omega_2^f}^f) \cdot \mathbf{n}_{\Gamma^{ff}} = \sigma \kappa \mathbf{n}_{\Gamma^{ff}}, \quad \forall \mathbf{x}^f \in \Gamma^{ff}(t), \quad (4.63)$$

where $(\cdot)_{\Omega_i^f}$ denotes the argument in the fluid phase i , $\mathbf{n}_{\Gamma^{ff}}$ is the normal to the fluid-fluid interface, σ is the surface tension coefficient between the two fluid phases and κ is the curvature of the interface denoted by $\kappa = -\nabla \cdot \mathbf{n}_{\Gamma^{ff}}$. The surface tension singular force in the Navier-Stokes equations (Eq. (4.1)) which models the surface tension is thus written as $\mathbf{sf} = \sigma \kappa \delta_{\Gamma^{ff}} \mathbf{n}_{\Gamma^{ff}}$, where $\delta_{\Gamma^{ff}}$ is the one-dimensional Dirac delta function given as

$$\delta_{\Gamma^{ff}} = \begin{cases} 1, & \text{for } \mathbf{x}^f \in \Gamma^{ff}(t), \\ 0, & \text{otherwise.} \end{cases} \quad (4.64)$$

The sharp-interface description based on the moving mesh framework is not trivial for complex three-dimensional fluid-fluid interfaces. Therefore, in the present formulation, we employ the diffuse fluid-fluid interface description in which the interface is assumed to have a finite thickness, $\mathcal{O}(\varepsilon)$, on which the physical properties of the two phases vary gradually based on an indicator field ϕ . The diffuse-interface description of the fluid-fluid interface recovers to the classical jump discontinuity conditions (Eqs. (4.62-4.63)) for the sharp-interface description asymptotically as $\varepsilon \rightarrow 0$ [84]. The singular force in the diffuse-interface description is replaced by a continuum surface force (CSF) [67], which depends on the order parameter (ϕ). Several forms of $\mathbf{sf}(\phi)$ have been used in the literature and are reviewed in [171, 172]. In this study, we employ the following definition:

$$\mathbf{sf}(\phi) = \sigma \varepsilon \alpha_{sf} \nabla \cdot (|\nabla \phi|^2 \mathbf{I} - \nabla \phi \otimes \nabla \phi), \quad (4.65)$$

where ε is the interface thickness parameter defined in the Allen-Cahn phase-field equation and $\alpha_{sf} = 3\sqrt{2}/4$ is a constant.

4.6 ALE mesh motion

The spatial points, $\mathbf{x}^f \in \Omega^f(t)$ can be moved within the fluid domain for an updated interface location of the fluid-structure interface by solving the following equation

$$\nabla \cdot \boldsymbol{\sigma}^m = \mathbf{0}, \quad (4.66)$$

where $\boldsymbol{\sigma}^m$ is the stress experienced by the spatial points in the fluid domain due to the strain induced by the interface deformation. Assuming that the fluid mesh behaves as a hyperelastic material, $\boldsymbol{\sigma}^m$ is written based on the Ogden model [173, 174]. Equation (4.66) solves for the fluid mesh nodal displacements $\boldsymbol{\eta}^f$, which are then used for updating the spatial nodes as

$$\boldsymbol{x}^f = \Phi^f(\boldsymbol{\chi}, t) = \boldsymbol{\chi} + \boldsymbol{\eta}^f(\boldsymbol{\chi}, t), \quad \forall \boldsymbol{x}^f \in \Omega^f(t) \text{ and } \boldsymbol{\chi} \in \Omega^f(0). \quad (4.67)$$

4.7 Summary

We reviewed the governing equations in this chapter which form the basis of the fluid-structure interaction. The key point to note is the satisfaction of the kinematic and dynamic equilibrium conditions at the fluid-structure interface which is dealt in detail in Chapter 7. We next deal with the modeling of the fluid-fluid interface in the diffuse-interface description in the two subsequent chapters.

Chapter 5

Phase-Field Formulation for Two-Phase Flows*

The interface between the two fluid phases can be modeled either by interface-tracking or interface-capturing methods. Following the advantages of the interface-capturing methods discussed in Chapter 2 and the computational complexities involved in the level-set and the volume-of-fluid techniques, we simplify our modeling of the interface by considering the phase-field methods. We choose the Allen-Cahn equation to evolve the fluid-fluid interface due to its ease in implementation compared to the higher-order Cahn-Hilliard equation. In this chapter, we develop the mathematical background involving the phase-field methods followed by the variational discretization of the Allen-Cahn equation under the positivity preserving framework. We present the coupling algorithm between the Navier-Stokes and the Allen-Cahn equations and verify as well as validate the developed two-phase fluid solver. Finally, a wave-structure interaction problem has been demonstrated for the generality of the implementation.

5.1 Background

Consider the physical domain $\Omega^f(t)$ with spatial and temporal coordinates \mathbf{x}^f and t , respectively. The phases of a two-phase fluid are indicated by a phase-indicator known as order parameter

*Parts of this chapter have been published in “V. Joshi and R.K. Jaiman, A positivity preserving and conservative variational scheme for phase-field modeling of two-phase flows, *Journal of Computational Physics*, 360, Pg. 137-166 (2018).”

$\phi(\mathbf{x}^f, t)$. The diffuse-interface description involves an interface with a finite thickness (represented by ε) where $\phi(\mathbf{x}^f, t)$ varies gradually across the interface. Under the thermodynamic arguments, the interface evolution and its dynamics are governed by the Ginzburg-Landau energy functional $\mathcal{E}(\phi)$, which can be expressed as

$$\mathcal{E}(\phi) = \int_{\Omega^f(t)} \left(\frac{\varepsilon^2}{2} |\nabla \phi|^2 + F(\phi) \right) d\Omega. \quad (5.1)$$

This energy functional consists of two components. The first term in Eq. (5.1) represents the interfacial energy depending on the gradient of the order parameter and the second term is a double-well potential function which represents the bulk energy or free energy of mixing and depends on the local value of $\phi(\mathbf{x}^f, t)$. The double-well potential function has two minima corresponding to the two stable phases. The system minimizes the functional by searching for the stable phases and thus evolving the fluid-fluid interface.

The evolution of the interface can be carried out by solving the gradient flow of the energy functional which can lead to either Cahn-Hilliard or Allen-Cahn equations. While the higher-order of the Cahn-Hilliard equation poses numerical challenges, we employ the Allen-Cahn equation in the present study which can be written as

$$\partial_t \phi = - \left(\frac{\delta \mathcal{E}(\phi)}{\delta \phi} \right). \quad (5.2)$$

Here, $\partial_t \phi$ is the partial temporal derivative of the order parameter $\phi(\mathbf{x}^f, t)$ and $F(\phi)$ is the double-well energy potential which is taken as $F(\phi) = \frac{1}{4}(\phi^2 - 1)^2$ in this study. Therefore, the two stable phases have $\phi = 1$ and $\phi = -1$ with an interface of finite thickness between them, over which ϕ varies gradually from -1 to 1 . To determine the profile of the interface at equilibrium, we minimize the energy functional by taking its variational derivative and equating it to zero. The variational derivative of the energy functional with respect to ϕ is called the chemical potential, which is given by

$$\frac{\delta \mathcal{E}}{\delta \phi} = -\varepsilon^2 \nabla^2 \phi + F'(\phi). \quad (5.3)$$

The evolution of ϕ with time tends to minimize the energy functional where the diffusive effects of $\nabla^2 \phi$ and the reactive effects of $F'(\phi)$ compete with each other. The profile of the interface at equilibrium is obtained by finding the solution of Eq. (5.3) as:

$$\phi(z) = \tanh \left(\frac{z}{\sqrt{2}\varepsilon} \right), \quad (5.4)$$

where z is the coordinate normal to the interface. The equilibrium interface thickness denoted by ε_{eqm} is the distance over which ϕ varies from -0.9 to 0.9 which can be estimated as $2\sqrt{2}\varepsilon \tanh^{-1}(0.9) = 4.164\varepsilon$.

Now, we define the constant α_{sf} which is referred in Eq. (4.65). Under equilibrium conditions and the sharp-interface limit, α_{sf} must satisfy the following condition [172]

$$\varepsilon \alpha_{\text{sf}} \int_{-\infty}^{\infty} \left(\frac{d\phi}{dz} \right)^2 dz = 1, \quad (5.5)$$

which gives $\alpha_{\text{sf}} = 3\sqrt{2}/4$ where we apply the expression of the equilibrium interface profile $\phi(z)$ given in Eq. (5.4). This gives rise to the continuum surface force expression given in Eq. (4.65).

5.2 The Allen-Cahn equation

In the present study, we consider the convective form of the Allen-Cahn (AC) equation with a Lagrange multiplier for mass conservation. In this section, the conservative Allen-Cahn equation at the continuum level is described followed by the positivity preserving and energy-stable semi-discrete variational formulation.

5.2.1 Strong differential form

Suppose $\Gamma_D^\phi(t)$ and $\Gamma_H^\phi(t)$ denote the Dirichlet and Neumann boundaries for the order parameter respectively. For improved capturing of the physical features in the solution, we employ the modified AC equation with both local and global multiplier terms in the ALE reference frame and the boundary conditions given as

$$\frac{\partial \phi}{\partial t} + (\mathbf{u}^f - \mathbf{u}^m) \cdot \nabla \phi - \gamma(\varepsilon^2 \nabla^2 \phi - F'(\phi) + \beta(t) \sqrt{F(\phi)}) = 0, \quad \text{on } \Omega^f(t), \quad (5.6)$$

$$\phi = \phi_D, \quad \forall \mathbf{x}^f \in \Gamma_D^\phi(t), \quad (5.7)$$

$$\nabla \phi \cdot \mathbf{n}^\phi = 0, \quad \forall \mathbf{x}^f \in \Gamma_H^\phi(t), \quad (5.8)$$

$$\phi = \phi_0, \quad \text{on } \Omega^f(0), \quad (5.9)$$

where \mathbf{u}^f and \mathbf{u}^m are the convection and the mesh velocities respectively and γ is a mobility parameter with units of $[T^{-1}]$ which is selected as 1 for the present study. The Dirichlet condition on the order parameter is given by ϕ_D and \mathbf{n}^ϕ is the unit outward normal to the

Neumann boundary Γ_H^ϕ , while the initial condition is denoted by ϕ_0 . The term $F'(\phi)$ denotes the derivative of $F(\phi)$ with respect to ϕ . The parameter $\beta(t)$ is the time-dependent part of the Lagrange multiplier which can be derived using the incompressible flow condition of divergence-free velocity and the given boundary conditions as

$$\beta(t) = \frac{\int_{\Omega^f(t)} F'(\phi) d\Omega}{\int_{\Omega^f(t)} \sqrt{F(\phi)} d\Omega}. \quad (5.10)$$

The Lagrange multiplier is written in such a way that for $K(\phi) = 0.5(\phi^3/3 - \phi)$ such that $K'(\phi) = \sqrt{F(\phi)}$,

$$\int_{\Omega^f(t)} K(\phi) d\Omega = \text{constant}. \quad (5.11)$$

5.2.2 Semi-discrete variational form

In this section, we write the variational formulation for the Allen-Cahn equation under the positivity preserving framework discussed in Chapter 3 to reduce the spurious oscillations in the solution of the order parameter. Solved by the Allen-Cahn equation, the variable ϕ is used to interpolate the physical properties of the fluid phases such as density and viscosity, which should always be positive. Oscillations in ϕ can lead to unbounded values which can cause the density or viscosity to be negative, thus producing unstable or unphysical results. The proposed PPV-based formulation reduces these oscillations in the solution near the region of high gradients by enforcing the positivity property of the underlying element-level matrix. Before proceeding to the presentation of the spatial PPV-based formulation, we first discretize the AC-based phase-field equation in the time domain via variational integration.

It is known that variational time integrators have the energy conserving property in comparison to Runge-Kutta time integration [175]. To enforce this property and have consistency in the temporal discretization, we employ the generalized- α time integration technique [153, 164]. Let $\partial_t \phi^{n+\alpha_m^f}$ be the derivative of ϕ with respect to time at $t^{n+\alpha^f}$. The expressions for the temporal discretization can be written as:

$$\phi^{n+1} = \phi^n + \Delta t \partial_t \phi^n + \gamma^f \Delta t (\partial_t \phi^{n+1} - \partial_t \phi^n), \quad (5.12)$$

$$\partial_t \phi^{n+\alpha_m^f} = \partial_t \phi^n + \alpha_m^f (\partial_t \phi^{n+1} - \partial_t \phi^n), \quad (5.13)$$

$$\phi^{n+\alpha^f} = \phi^n + \alpha^f(\phi^{n+1} - \phi^n), \quad (5.14)$$

where Δt is the time step size, α_m^f , α^f and γ^f are the generalized- α parameters defined in Eq. (4.20). The time discretized Allen-Cahn equation is therefore,

$$\partial_t \phi^{n+\alpha^f} + (\mathbf{u}^f - \mathbf{u}^m) \cdot \nabla \phi^{n+\alpha^f} - \varepsilon^2 \nabla^2 \phi^{n+\alpha^f} + F'(\phi^{n+\alpha^f}) - \beta(t^{n+\alpha^f}) \sqrt{F(\phi^{n+\alpha^f})} = 0. \quad (5.15)$$

For imparting the energy stability property, $F'(\phi^{n+\alpha^f})$ is written as [88]

$$F'(\phi^{n+\alpha^f}) = \frac{F(\phi^{n+1}) - F(\phi^n)}{\phi^{n+1} - \phi^n}. \quad (5.16)$$

Let $K'(\phi) = \sqrt{F(\phi)} = 0.5(\phi^2 - 1)$ be written in discretized form as

$$K'(\phi^{n+\alpha^f}) = \sqrt{F(\phi^{n+\alpha^f})} = \frac{K(\phi^{n+1}) - K(\phi^n)}{\phi^{n+1} - \phi^n} \quad (5.17)$$

The expressions in Eqs. (5.16) and (5.17) are designed to provide the energy stability property to the variational scheme. Considering the mid-point approximation of the spatial part of the Lagrange multiplier helps in simplifying the expressions in the derivation of the discrete energy law leading to an energy-stable scheme. A detailed derivation of discrete energy law has been presented in Appendix F.

Using Eq. (5.14) to replace the expression for ϕ^{n+1} in $F'(\phi^{n+\alpha^f})$ and $\sqrt{F(\phi^{n+\alpha^f})}$ and rearranging, the Allen-Cahn equation can be written in the form of convection-diffusion-reaction equation as follows:

$$\partial_t \phi^{n+\alpha^f} + \hat{\mathbf{u}} \cdot \nabla \phi^{n+\alpha^f} - \hat{k} \nabla^2 \phi^{n+\alpha^f} + \hat{s} \phi^{n+\alpha^f} - \hat{f}(t^{n+\alpha^f}) = 0, \text{ on } \Omega^f(t), \quad (5.18)$$

where $\hat{\mathbf{u}}$, \hat{k} , \hat{s} and \hat{f} are the modified convection velocity, diffusion coefficient, reaction coefficient and the source terms respectively, which are given as

$$\hat{\mathbf{u}} = \mathbf{u}^f - \mathbf{u}^m, \quad (5.19)$$

$$\hat{k} = \varepsilon^2, \quad (5.20)$$

$$\begin{aligned} \hat{s} &= \frac{1}{4} \left[\frac{(\phi^{n+\alpha^f})^2}{(\alpha^f)^3} - \left(\frac{3}{(\alpha^f)^3} - \frac{4}{(\alpha^f)^2} \right) \phi^{n+\alpha^f} \phi^n + \left(\frac{3}{(\alpha^f)^3} - \frac{8}{(\alpha^f)^2} + \frac{6}{\alpha^f} \right) (\phi^n)^2 - \frac{2}{\alpha^f} \right] \\ &\quad - \frac{\beta(t^{n+\alpha^f})}{2} \left[\frac{\phi^{n+\alpha^f}}{3(\alpha^f)^2} + \frac{1}{3} \left(-\frac{2}{(\alpha^f)^2} + \frac{3}{\alpha^f} \right) \phi^n \right], \\ \hat{f} &= -\frac{1}{4} \left[\left(-\frac{1}{(\alpha^f)^3} + \frac{4}{(\alpha^f)^2} - \frac{6}{\alpha^f} + 4 \right) (\phi^n)^3 + \left(\frac{2}{\alpha^f} - 4 \right) \phi^n \right] \end{aligned} \quad (5.21)$$

$$+ \frac{\beta(t^{n+\alpha^f})}{2} \left[\frac{1}{3} \left(\frac{1}{(\alpha^f)^2} - \frac{3}{\alpha^f} + 3 \right) (\phi^n)^2 - 1 \right]. \quad (5.22)$$

Defining the space of trial solution as \mathcal{S}_ϕ^h and that of the test function as \mathcal{V}_ϕ^h such that

$$\mathcal{S}_\phi^h = \{ \phi_h \mid \phi_h \in H^1(\Omega^f(t)), \phi_h = \phi_D \text{ on } \Gamma_D^\phi(t) \}, \quad (5.23)$$

$$\mathcal{V}_\phi^h = \{ \hat{w}_h \mid \hat{w}_h \in H^1(\Omega^f(t)), \hat{w}_h = 0 \text{ on } \Gamma_D^\phi(t) \}, \quad (5.24)$$

the variational statement for the Allen-Cahn equation is given as: find $\phi_h(\mathbf{x}^f, t^{n+\alpha^f}) \in \mathcal{S}_\phi^h$ such that $\forall \hat{w}_h \in \mathcal{V}_\phi^h$,

$$\begin{aligned} & \int_{\Omega^f(t)} \left(\hat{w}_h \partial_t \phi_h + \hat{w}_h (\hat{\mathbf{u}} \cdot \nabla \phi_h) + \nabla \hat{w}_h \cdot (\hat{k} \nabla \phi_h) + \hat{w}_h \hat{s} \phi_h - \hat{w}_h \hat{f} \right) d\Omega \\ & + \sum_{e=1}^{n_{el}} \int_{\Omega^e} \left((\hat{\mathbf{u}} \cdot \nabla \hat{w}_h) \tau (\partial_t \phi_h + \hat{\mathbf{u}} \cdot \nabla \phi_h - \nabla \cdot (\hat{k} \nabla \phi_h) + \hat{s} \phi_h - \hat{f}) \right) d\Omega^e \\ & + \sum_{e=1}^{n_{el}} \int_{\Omega^e} \chi \frac{|\mathcal{R}(\phi_h)|}{|\nabla \phi_h|} k_s^{\text{add}} \nabla \hat{w}_h \cdot \left(\frac{\hat{\mathbf{u}} \otimes \hat{\mathbf{u}}}{|\hat{\mathbf{u}}|^2} \right) \cdot \nabla \phi_h d\Omega^e \\ & + \sum_{e=1}^{n_{el}} \int_{\Omega^e} \chi \frac{|\mathcal{R}(\phi_h)|}{|\nabla \phi_h|} k_c^{\text{add}} \nabla \hat{w}_h \cdot \left(\mathbf{I} - \frac{\hat{\mathbf{u}} \otimes \hat{\mathbf{u}}}{|\hat{\mathbf{u}}|^2} \right) \cdot \nabla \phi_h d\Omega^e = 0, \end{aligned} \quad (5.25)$$

where the first line represents the Galerkin terms. The second line consists of linear stabilization terms in the form of SUPG stabilization with the stabilization parameter τ . Note that only the convective term has been taken in the weighting function, in contrast to the combined GLS-subgrid-scale methodology of PPV where we also take the reaction term. This new modification has been performed to ensure the mass conservation property in the variational form. The proof of mass conservation property of the modified PPV scheme has been derived in Appendix G. The terms in the third and fourth lines of Eq. (5.25) are the positivity preserving nonlinear stabilization terms which enforce the positivity property to the element-level matrix. The residual of the Allen-Cahn equation is given by

$$\mathcal{R}(\phi_h) = \partial_t \phi_h + \hat{\mathbf{u}} \cdot \nabla \phi_h - \nabla \cdot (\hat{k} \nabla \phi_h) + \hat{s} \phi_h - \hat{f}, \quad (5.26)$$

and the stabilization parameter τ is written as

$$\tau = \left[\left(\frac{2}{\Delta t} \right)^2 + \hat{\mathbf{u}} \cdot \mathbf{G} \hat{\mathbf{u}} + 9 \hat{k}^2 \mathbf{G} : \mathbf{G} + \hat{s}^2 \right]^{-1/2}, \quad (5.27)$$

where \mathbf{G} is the contravariant metric tensor defined in Eq. (4.30).

The details of the derivation of the added diffusions k_s^{add} , k_c^{add} and χ can be found in Chapter 3. For the current context of the AC-based phase-field equation, we have the following PPV

parameters:

$$\chi = \frac{2}{|\hat{s}|h + 2|\hat{\mathbf{u}}|}, \quad (5.28)$$

$$k_s^{\text{add}} = \max \left\{ \frac{||\hat{\mathbf{u}}| - \tau|\hat{\mathbf{u}}|\hat{s}|h}{2} - (\hat{k} + \tau|\hat{\mathbf{u}}|^2) + \frac{\hat{s}h^2}{6}, 0 \right\}, \quad (5.29)$$

$$k_c^{\text{add}} = \max \left\{ \frac{|\hat{\mathbf{u}}|h}{2} - \hat{k} + \frac{\hat{s}h^2}{6}, 0 \right\}, \quad (5.30)$$

where $|\hat{\mathbf{u}}|$ is the magnitude of the convection velocity and h is the characteristic element length which is selected as the streamline element length. In this and the subsequent chapter, we consider the coupling of the Navier-Stokes and the Allen-Cahn equations without any moving ALE meshes, i.e., $\mathbf{u}^m = \mathbf{0}$. The moving mesh and fluid-structure interaction are considered in Chapter 7 where the two-phase equations are coupled with the structural equation to get a two-phase fluid-structure interaction solver.

5.3 Partitioned iterative coupling for two-phase flows

We present a nonlinear partitioned iterative coupling between the Navier-Stokes and the Allen-Cahn equations. We start with the coupled linearized matrix of the two-phase system and then decouple it into two subsystems, viz., the Navier-Stokes solve and the Allen-Cahn solve to form a partitioned block solver.

5.3.1 Coupled linearized matrix form

Using the Newton-Raphson linearization, the coupled linearized matrix form of the two-phase system can be written as

$$[\mathbf{A}^{\text{ff}}] \{\Delta \mathbf{q}^{\text{f}}\} = \{\mathcal{R}^{\text{f}}\}, \quad (5.31)$$

where $\Delta \mathbf{q}^{\text{f}} = (\Delta \mathbf{u}^{\text{f}}, \Delta p, \Delta \phi)$ is the vector of the unknowns and \mathcal{R}^{f} is the weighted residual of the stabilized two-phase flow equations. The linearized matrix \mathbf{A}^{ff} can be expanded as

$$\mathbf{A}^{\text{ff}} = \begin{bmatrix} \mathbf{K}_{\Omega^{\text{f}}} & \mathbf{G}_{\Omega^{\text{f}}} & \mathbf{D}_{\Omega^{\text{f}}} \\ -\mathbf{G}_{\Omega^{\text{f}}}^T & \mathbf{C}_{\Omega^{\text{f}}} & \mathbf{0} \\ \mathbf{G}_{AC} & \mathbf{0} & \mathbf{K}_{AC} \end{bmatrix}, \quad (5.32)$$

where $\mathbf{K}_{\Omega^{\text{f}}}$ is the stiffness matrix of the momentum equation consisting of inertia, convection, viscous and stabilization terms, $\mathbf{G}_{\Omega^{\text{f}}}$ is the gradient operator, $\mathbf{G}_{\Omega^{\text{f}}}^T$ is the divergence operator

for the continuity equation and \mathbf{C}_{Ω^f} is the pressure-pressure stabilization term. On the other hand, \mathbf{D}_{Ω^f} contains the terms in the momentum equation having dependency on the order parameter, \mathbf{G}_{AC} consists of the velocity coupled term in the Allen-Cahn equation and \mathbf{K}_{AC} is the left-hand side stiffness matrix for the Allen-Cahn equation consisting of inertia, convection, diffusion, reaction and stabilization terms. We next decouple the above system into partitioned block components for the nonlinear partitioned iterative coupling algorithm.

5.3.2 Implementation details

The two-phase flow system in Eq. (5.32) is decoupled into two subsystems: Navier-Stokes and Allen-Cahn solves, for which the linear system of equations can be summarized as

$$\begin{bmatrix} \mathbf{K}_{\Omega^f} & \mathbf{G}_{\Omega^f} \\ -\mathbf{G}_{\Omega^f}^T & \mathbf{C}_{\Omega^f} \end{bmatrix} \begin{Bmatrix} \Delta \mathbf{u}^f \\ \Delta p \end{Bmatrix} = \begin{Bmatrix} \tilde{\mathcal{R}}_m \\ \tilde{\mathcal{R}}_c \end{Bmatrix}, \quad (5.33)$$

$$[\mathbf{K}_{AC}] \{ \Delta \phi \} = \{ \tilde{\mathcal{R}}(\phi) \}, \quad (5.34)$$

where $\tilde{\mathcal{R}}_m$, $\tilde{\mathcal{R}}_c$ and $\tilde{\mathcal{R}}(\phi)$ represent the weighted residuals of the stabilized momentum, continuity and the Allen-Cahn equations respectively. Notice that the terms forming the matrices \mathbf{D}_{Ω^f} and \mathbf{G}_{AC} do not exist after the decoupling since we decouple the equations in a partitioned iterative manner which is described below.

The algorithm of the iterative coupling between the Navier-Stokes and the Allen-Cahn equations is shown in Algorithm 1. For efficiency and robustness, we perform the implicit discretizations of the Navier-Stokes and the Allen-Cahn equations. We employ the time-splitting procedure to decouple the incompressible Navier-Stokes and Allen-Cahn updates at the discrete level. While the Navier-Stokes equations provide a predictor fluid velocity, the Allen-Cahn equation is solved to provide an updated order parameter to interpolate the density, viscosity, capillary and body forces on the Navier-Stokes side. Consider the velocity $\mathbf{u}^f(\mathbf{x}^f, t^n)$, pressure $p(\mathbf{x}^f, t^n)$ and the order parameter $\phi(\mathbf{x}^f, t^n)$ at time t^n . In the first step of the predictor-corrector iteration k , the velocity and pressure are predicted by solving the Navier-Stokes equations. In the second step, the computed fluid velocity is transferred to the Allen-Cahn equation. The convective AC equation is solved using the transferred fluid velocity to obtain an updated order parameter $\phi_{(k+1)}$ in the third step. Finally, in the fourth step, the updated order parameter is utilized in the interpolation of density $\rho^f(\phi)$, viscosity $\mu^f(\phi)$, surface tension force $\mathbf{sf}(\phi)$ and body force

Chapter 5. Phase-Field Formulation for Two-Phase Flows

$\mathbf{b}^f(\phi)$. These updated quantities are then fed into the Navier-Stokes equations in the next iteration. At the end of the nonlinear iterations when the solver has achieved the convergence criteria, the values at the next time step t^{n+1} are updated and the coupled solver is advanced in time. To our knowledge, this type of partitioned coupling has been applied to the Navier-Stokes and the Allen-Cahn equations for the first time.

Algorithm 1 Partitioned coupling of implicit Navier-Stokes and Allen-Cahn solvers

Given $\mathbf{u}^{f,0}, p^0, \phi^0$

Loop over time steps, $n = 0, 1, \dots$

Start from known variables $\mathbf{u}^{f,n}, p^n, \phi^n$

Predict the solution:

$$\mathbf{u}_{(0)}^{f,n+1} = \mathbf{u}^{f,n}$$

$$p_{(0)}^{n+1} = p^n$$

$$\phi_{(0)}^{n+1} = \phi^n$$

Loop over the nonlinear iterations, $k = 0, 1, \dots$ until convergence

[1] **Navier-Stokes Implicit Solve**

(a) Interpolate solution:

$$\mathbf{u}_{(k+1)}^{f,n+\alpha_f} = \mathbf{u}^{f,n} + \alpha^f (\mathbf{u}_{(k)}^{f,n+1} - \mathbf{u}^{f,n})$$

$$p_{(k+1)}^{n+1} = p_{(k)}^{n+1}$$

(b) Solve for $\Delta\mathbf{u}^{f,n+\alpha_f}$ and Δp^{n+1} in Eq. (5.33)

(c) Correct solution:

$$\mathbf{u}_{(k+1)}^{f,n+\alpha_f} = \mathbf{u}_{(k+1)}^{f,n+\alpha_f} + \Delta\mathbf{u}^{f,n+\alpha_f}$$

$$p_{(k+1)}^{n+1} = p_{(k+1)}^{n+1} + \Delta p^{n+1}$$

(d) Update solution:

$$\mathbf{u}_{(k+1)}^{f,n+1} = \mathbf{u}^{f,n} + \frac{1}{\alpha^f} (\mathbf{u}_{(k+1)}^{f,n+\alpha_f} - \mathbf{u}^{f,n})$$

$$p_{(k+1)}^{n+1} = p_{(k+1)}^{n+1}$$

← [4] $\phi_{(k+1)}^{n+1}$
to interpolate

$\rho^f(\phi), \mu^f(\phi)$
 $\mathbf{s}^f(\phi), \mathbf{b}^f(\phi)$

→ [2] $\mathbf{u}_{(k+1)}^{f,n+1}$

[3] **Allen-Cahn Implicit Solve**

(a) Interpolate solution:

$$\phi_{(k+1)}^{n+\alpha_f} = \phi^n + \alpha^f (\phi_{(k)}^{n+1} - \phi^n)$$

(b) Solve for $\Delta\phi^{n+\alpha_f}$ in Eq. (5.34)

(c) Correct solution:

$$\phi_{(k+1)}^{n+\alpha_f} = \phi_{(k+1)}^{n+\alpha_f} + \Delta\phi^{n+\alpha_f}$$

(d) Update solution:

$$\phi_{(k+1)}^{n+1} = \phi^n + \frac{1}{\alpha^f} (\phi_{(k+1)}^{n+\alpha_f} - \phi^n)$$

In the present investigation, we consider equal-order interpolations for all the quantities (\mathbf{u}^f, p, ϕ) for finite element discretization. At each time step, the nonlinear errors of implicit systems of the Navier-Stokes and the Allen-Chan equations are minimized by Newton-Raphson iterations. In our numerical experiments, we have found that about 2-3 nonlinear iterations are enough to obtain a reasonably converged solution. Moreover, we want to emphasize that each nonlinear iteration of the algorithm consists of just one pass through the coupled Navier-Stokes and the Allen-Cahn phase-field system. This single-pass implicit coupling, in turn, helps in reducing the computational time without compromising the accuracy and stability of the

solution. We solve the coupled equations at discrete time steps to capture the transient flow characteristics, leading to a sequence of linear system of equations. For the linear system of equations, the matrices are formed and stored using the Harwell-Boeing sparse matrix format. The linear system is solved via the generalized minimal residual (GMRES) algorithm proposed in [176], which relies on the preconditioned Krylov subspace iteration and the modified Gram-Schmidt orthogonalization. The number of matrix-vector products determines the dimension of the Krylov space from which a solution is computed. The phase-field two-phase solver relies on a hybrid parallelism for parallel computing. It employs a standard master-slave strategy for distributed memory clusters via message passing interface (MPI) based on domain decomposition strategy [177]. The parallel implementation for the two-phase solver takes the advantage of the state-of-the-art hierarchical memory and parallel architectures.

5.4 Numerical tests

In this section, we present some numerical tests to assess the scheme for the coupled Allen-Cahn and Navier-Stokes equations. In all the test cases, the location of the interface between the two phases of the fluid is evaluated by linearly interpolating the order parameter field ϕ and finding the interface where $\phi = 0$.

5.4.1 Verification of the Allen-Cahn implementation

We first verify the Allen-Cahn solver using the volume-conserved motion by curvature in two-dimensions [2]. A square computational domain $[0, 1] \times [0, 1]$ with varying element sizes is considered. Periodic boundary conditions are imposed on all the boundaries. The initial condition is given by:

$$\begin{aligned} \phi(x, y, 0) = & 1 + \tanh\left(\frac{R_1 - \sqrt{(x - 0.25)^2 + (y - 0.25)^2}}{\sqrt{2}\varepsilon}\right) \\ & + \tanh\left(\frac{R_2 - \sqrt{(x - 0.57)^2 + (y - 0.57)^2}}{\sqrt{2}\varepsilon}\right), \end{aligned} \quad (5.35)$$

where $R_1 = 0.1$ and $R_2 = 0.15$ are the radii of the two circles centered at $(0.25, 0.25)$ and $(0.57, 0.57)$, respectively. The variation of the change of the radii of the two circles is tracked and validated with the results obtained in [2] for $\varepsilon = 0.01$. The time step size in the present

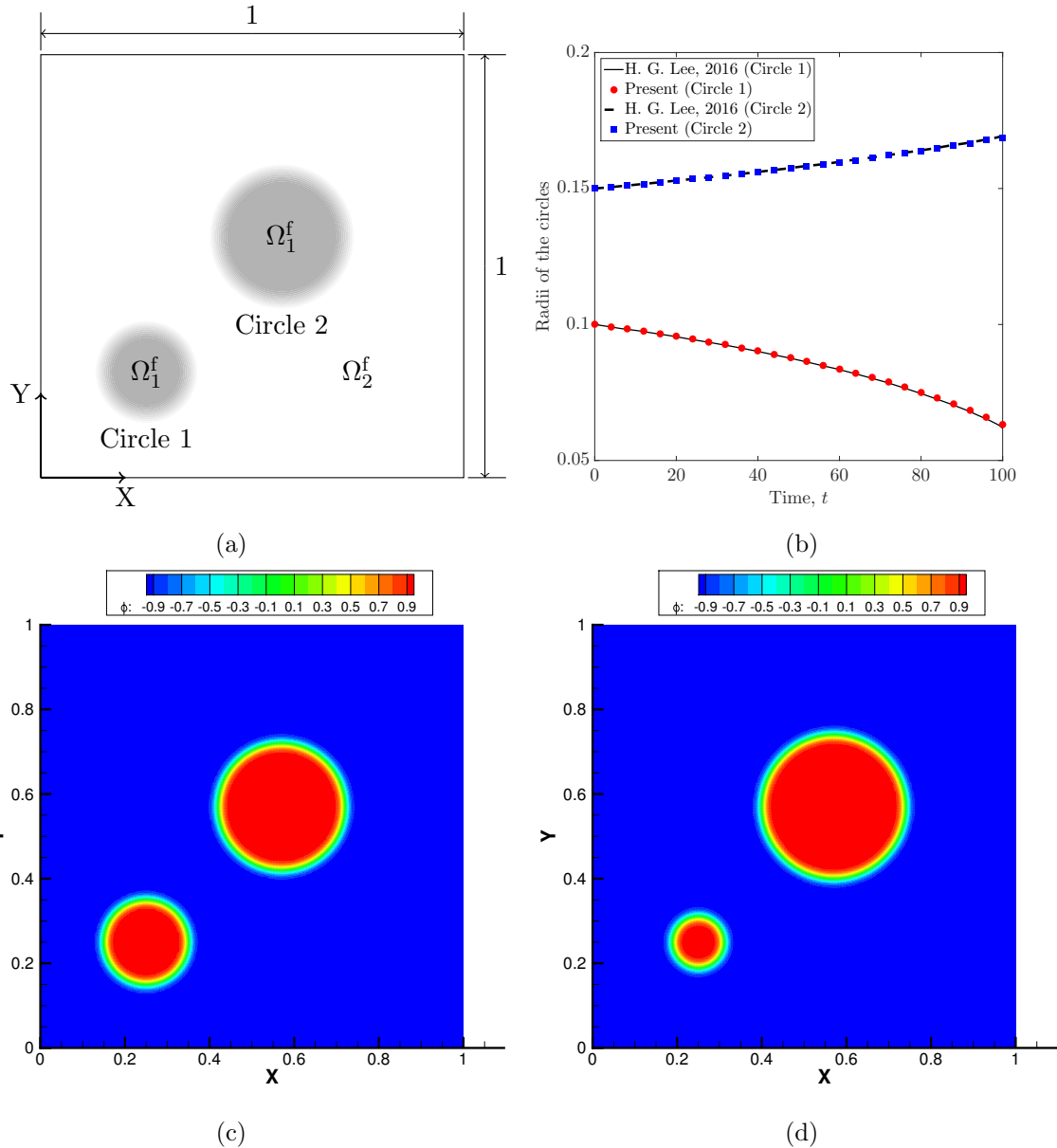


Figure 5.1: Evolution of the radii of two-dimensional circles: (a) Schematic diagram showing the computational domain, (b) Validation of the evolution of the radii of the two circles with the literature [2], and the contour plots of the order parameter ϕ at (c) $t = 0$, and (d) $t = 100$. In (a), Ω_1^f and Ω_2^f are the two phases with periodic boundary conditions imposed on all the sides.

simulation is 0.1 with the final time $t = 100$. The problem set-up with the evolution of the radii of the two circles is shown in Fig. 5.1. The results are in very close agreement with the reference.

Further analysis is carried out to quantify the appropriate number of elements required across the interface to capture the evolution of the radii. Let N_ε denote the number of elements

across the equilibrium interface thickness, $\varepsilon_{\text{eqm}} = 4.164\varepsilon$. We simulate the evolution of the radii for $N_\varepsilon \in [3, 10]$ and quantify the percentage error (e_1) in the radii at the final time $t = 100$ defined as

$$e_1 = \frac{|R_i - R_{\text{ref}}|}{R_{\text{ref}}} \times 100, \quad (5.36)$$

where R_i is the radius corresponding to different resolutions at $t = 100$ and R_{ref} is the radius obtained for $N_\varepsilon = 10$ at $t = 100$. The results are summarized in Table 5.1. It can be observed that for circle 2 (the large circle), $N_\varepsilon > 3$ is sufficient for getting the solution within 1% error while for circle 1, $N_\varepsilon > 6$ is required to obtain results with similar accuracy. The reason is the different curvature of the two circles. With the decreasing radius of circle 1, its curvature increases and more number of elements are needed to sufficiently capture its interface.

Table 5.1: Percentage error in the final radii of the two circles for different mesh resolutions.

$N_\varepsilon \rightarrow$	3	4	5	6	7	8
Circle 1	10.39	5.29	3.26	1.54	0.91	0.58
Circle 2	1.28	0.60	0.36	0.20	0.15	0.02

To understand the behavior of the solver under spatial and temporal refinements, we evaluate the L^2 error of the solution over the whole domain at $t = 50$ by decreasing element and time step sizes. The L^2 error is calculated as:

$$e_2 = \frac{\|\Phi - \Phi_{\text{ref}}\|_2}{\|\Phi_{\text{ref}}\|_2}, \quad (5.37)$$

where Φ is the vector of the solution of order parameter ϕ at the final time $t = 50$ over the whole domain for the respective refinement, Φ_{ref} is the vector of the solution of the finest resolution and $\|\cdot\|_2$ is the L^2 norm. The spatial refinement is carried out uniformly by decreasing the element size from $h = 1/72$ until $h = 1/2304$. The finest grid $h = 1/2304$ is selected as the reference solution for evaluating the error norm. For the temporal refinement, we take $\Delta t = 0.4$ and decrease it by a factor of 2 until $\Delta t = 0.025$. The solution corresponding to $\Delta t = 3.90625 \times 10^{-4}$ is taken as the reference solution.

The mesh and temporal convergence results are plotted in Fig. 5.2. Both the spatial and temporal convergence trends confirm the second-order accuracy of our implementation. The order of temporal convergence is second-order due to the nonlinear energy-stable properties which are imparted by the mid-point approximation in the discretization. The second-order of

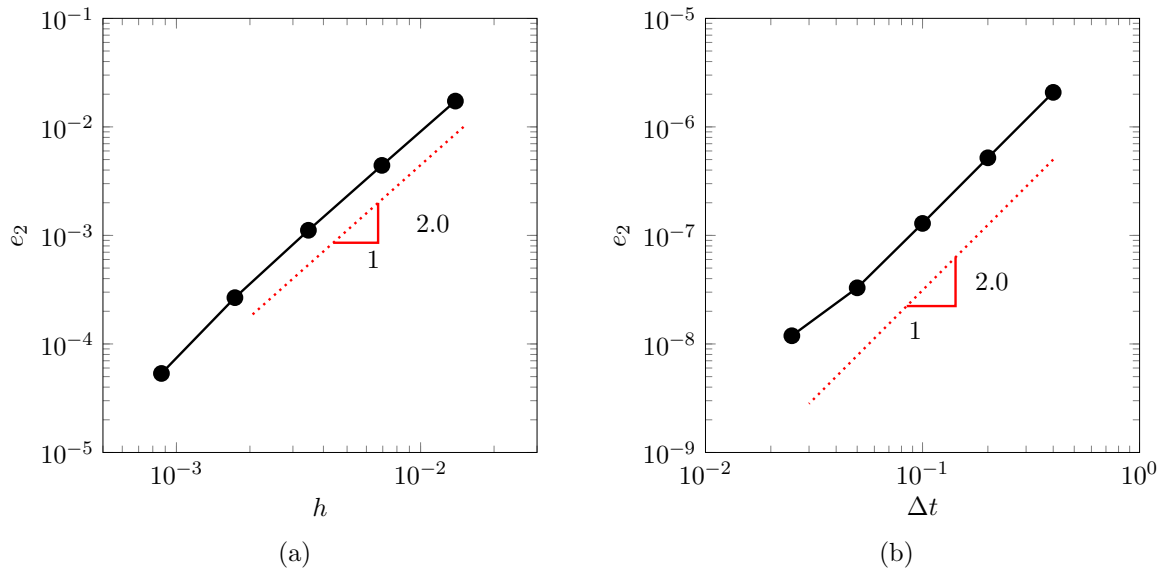


Figure 5.2: Convergence study for the present method through dependence of non-dimensionalized L^2 error (e_2) as a function of: (a) uniform mesh refinement h , and (b) uniform temporal refinement Δt .

temporal accuracy is analytically proved in Appendix H by evaluating the truncation error of the temporally discretized AC equation.

Finally, to analyze the conservation of mass or the order parameter ϕ , we quantify the percentage change in ϕ over the time with respect to the initial value. For this particular example, the mass loss is approximately $5.4577 \times 10^{-5} \%$. Note that the mass conservation depends on the tolerance of the linear GMRES solver as well as the nonlinear tolerance. A linear tolerance of 10^{-15} and the nonlinear tolerance of 10^{-4} are chosen for this example. Within this limit, it can be deduced that the mass is reasonably conserved for the variational finite element scheme.

5.4.2 Laplace-Young law

To verify the coupling between the Allen-Cahn and the incompressible Navier-Stokes equations at high-density ratio, we consider a simple test problem of Laplace-Young law. The law states that the pressure difference (Δp) across the interface of a static bubble in a two-phase fluid system is equivalent to the ratio of the surface tension (σ) and the radius of curvature (R) of the bubble,

$$\Delta p = p_{\text{in}} - p_{\text{out}} = \frac{\sigma}{R}. \quad (5.38)$$

In the equilibrium state, the velocity vanishes $\mathbf{u}^f = \mathbf{0}$ and the pressure gradient balances the surface tension force, i.e.,

$$\nabla p = \sigma \varepsilon \frac{3\sqrt{2}}{4} \nabla \cdot (|\nabla \phi|^2 \mathbf{I} - \nabla \phi \otimes \nabla \phi). \quad (5.39)$$

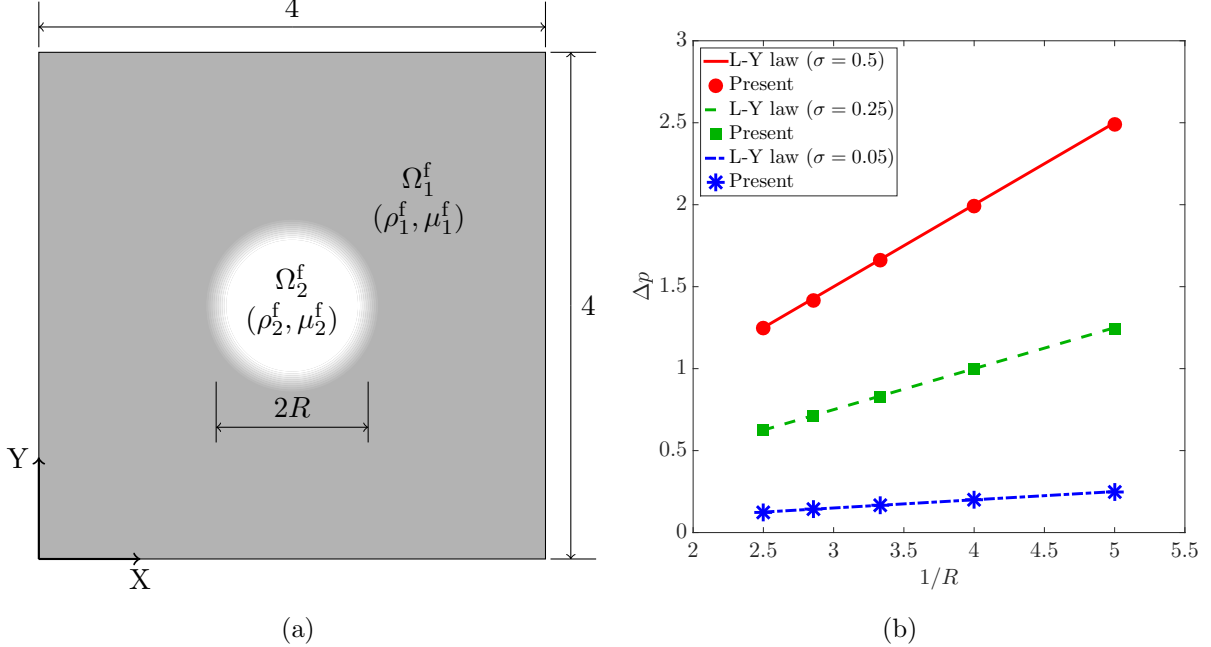


Figure 5.3: Laplace-Young law: (a) Schematic diagram showing the computational domain, (b) Comparison of the pressure difference across the interface in a static bubble obtained from the simulation with the Laplace-Young law. In (a), Ω_1^f and Ω_2^f are the two fluid phases with densities $\rho_1^f = 1000$ and $\rho_2^f = 1$, viscosities $\mu_1^f = 10$, $\mu_2^f = 0.1$ and acceleration due to gravity $\mathbf{g} = (0, 0, 0)$ and all the boundaries have periodic boundary condition.

The density and dynamic viscosity of the two fluids are taken as $\rho_1^f = 1000$, $\rho_2^f = 1$, $\mu_1^f = 10$ and $\mu_2^f = 0.1$. In the numerical tests, we consider a domain size $\Omega^f = [0, 4] \times [0, 4]$ with uniform structured mesh of grid size $1/200$ with different radii of the bubble (0.2, 0.25, 0.3, 0.35 and 0.4 units) and three surface tensions (0.5, 0.25 and 0.05 units). Periodic boundary conditions are applied on all the boundaries. The initial condition is given by:

$$\phi(x, y, 0) = -\tanh\left(\frac{R - \sqrt{(x - x_c)^2 + (y - y_c)^2}}{\sqrt{2}\varepsilon}\right), \quad (5.40)$$

where R is the radius of the bubble with its centre at $(x_c, y_c) = (2, 2)$. The interface thickness parameter is $\varepsilon = 0.01$. The time step size is taken as $\Delta t = 0.01$ s and the pressure difference is measured after 5000 time steps. The schematic of the computational domain and the represen-

tative results are shown in Fig. 5.3. The pressure difference in Fig. 5.3(b) shows good agreement with the Laplace-Young law. This demonstrates the coupling between the Allen-Cahn and the Navier-Stokes equations for high-density ratio.

5.4.3 Sloshing tank problem

To further assess the phase-field solver, we now present a standard sloshing tank problem. A rectangular computational domain $\Omega^f \in [0, 1] \times [0, 1.5]$ is considered for the simulation. It is discretized with different resolutions characterized by the number of elements in the equilibrium interface thickness denoted by N_ε . Varying densities and viscosities of the two fluid phases as $\rho_1^f = 1000$, $\rho_2^f = 1$, $\mu_1^f = 1$, $\mu_2^f = 0.01$ and $\mathbf{g} = (0, -1, 0)$ will also test the ability of the solver to handle high-density and viscosity ratios. The capillary effects due to surface tension have been neglected in this test case. The initial condition is defined as:

$$\phi(x, y, 0) = -\tanh\left(\frac{y - (1.01 + 0.1\sin((x - 0.5)\pi))}{\sqrt{2}\varepsilon}\right). \quad (5.41)$$

A slip boundary condition is set along the walls and a Dirichlet boundary condition is prescribed at the top boundary as $p = 0$. The problem set-up is given in Fig. 5.4(a) with the contour plot of ϕ of the initial condition in Fig. 5.4(b). To have a detailed analysis of the problem, we perform a series of experiments to assess: (a) the effectiveness of the PPV technique, (b) appropriate number of elements (N_ε) required in the equilibrium interface thickness, (c) proper value of Δt to obtain results with sufficient accuracy, and (d) the effect of ε on the two-phase flow solution. The quantification of error in the following analysis is carried out by evaluating the L^2 error (e_3) defined by

$$e_3 = \frac{\|\Phi - \Phi_{\text{ref}}\|_2}{\|\Phi_{\text{ref}}\|_2}, \quad (5.42)$$

where Φ is the temporal solution of the interface elevation at the left boundary, Φ_{ref} is the solution of the finest resolution associated with the respective study and $\|\cdot\|_2$ is the L^2 norm.

5.4.3.1 Effectiveness of the PPV technique

First, we emphasize the advantage of using the PPV-based technique for the phase-field equation. In the convection- and reaction-dominated regions, the linear stabilized variational formulation results in oscillations near the regions with high gradients, which can result in un-

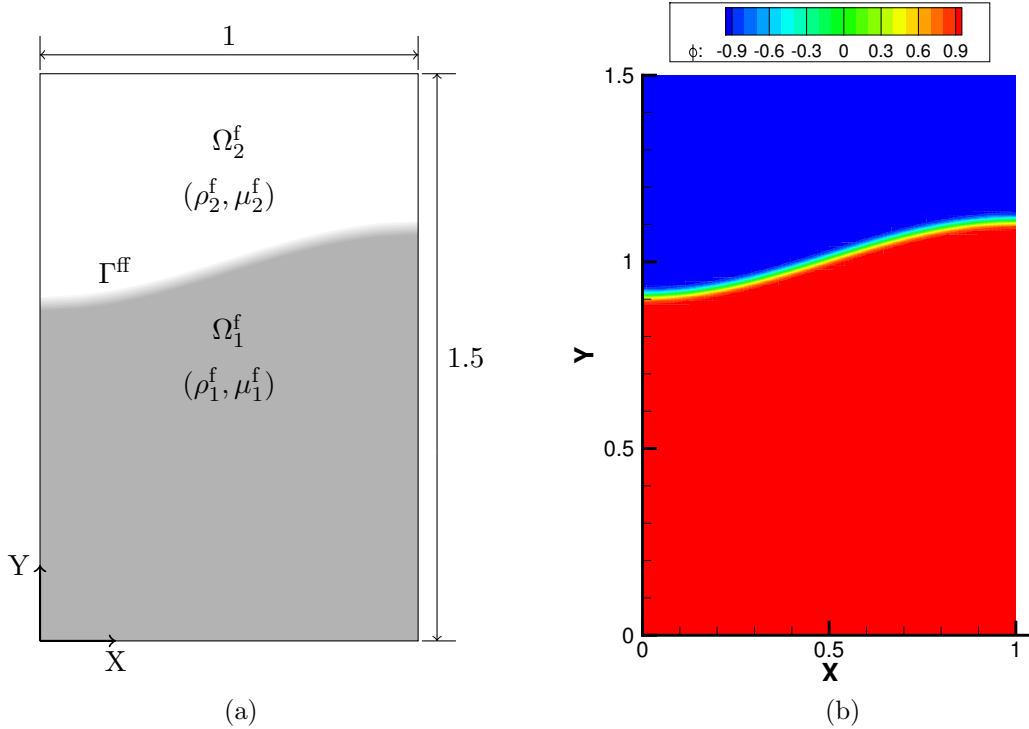


Figure 5.4: Sloshing in a rectangular tank: (a) Schematic diagram showing the computational domain, (b) Contour plot of the order parameter ϕ at $t = 0$. In (a), Ω_1^f and Ω_2^f are the two fluid phases with densities $\rho_1^f = 1000$ and $\rho_2^f = 1$, viscosities $\mu_1^f = 1$, $\mu_2^f = 0.01$ and acceleration due to gravity $\mathbf{g} = (0, -1, 0)$ and the walls of the tank have slip boundary condition with $p = 0$ at the upper boundary.

bounded solution. However, the order parameter ϕ solved by the Allen-Cahn equation needs to be bounded at all times to ensure that positive values of density and viscosity are transferred to the Navier-Stokes equations. The present variational technique detects the regions of high gradients depending on the residual of the equation and adds diffusion to those regions to eliminate such oscillations. To demonstrate the effect of the PPV technique to the present

Table 5.2: Bounds in the solution of interface evolution at the left boundary with and without PPV consideration.

N_ε	min(ϕ)		max(ϕ)	
	non-PPV	PPV	non-PPV	PPV
3	-1.0544	-1.0	1.0154	0.9999
4	-1.0065	-1.0	1.0023	0.9999

problem, we simulate two test cases: (a) with nonlinear PPV stabilization terms and (b) without nonlinear PPV terms. Here, the parameters $\Delta t = 0.001$, $\varepsilon = 0.01$ with $N_\varepsilon = 3$ and $N_\varepsilon = 4$ are considered for the numerical experiments. The minimum and maximum values of the solu-

tion of the interface evolution at the left boundary are evaluated to quantify the bounds of the numerical solution. The values are summarized in Table 5.2. From the table, it is evident that

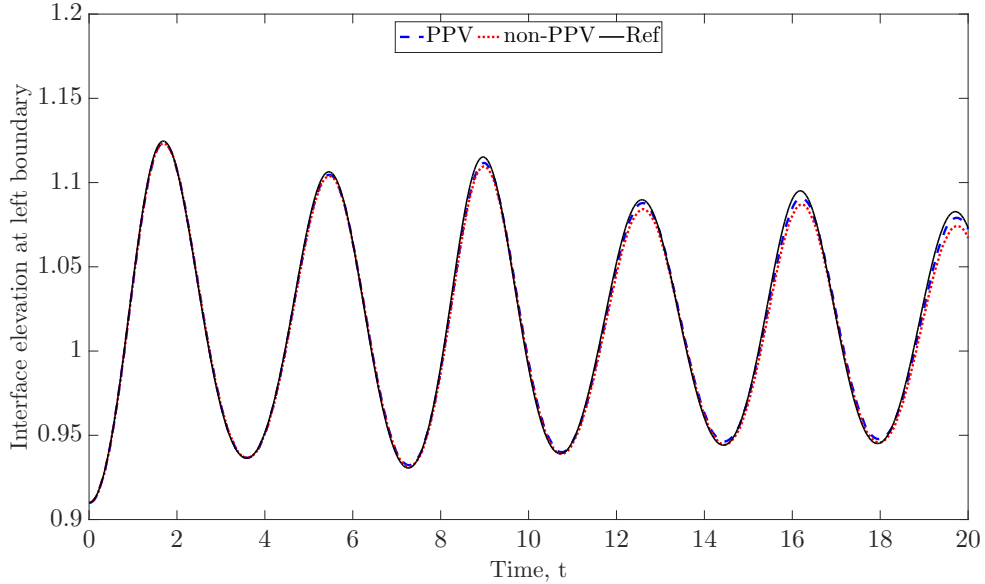


Figure 5.5: Sloshing tank problem: Effect of using the PPV technique on the evolution of the interface. $\varepsilon = 0.01$, $\Delta t = 0.001$ and $N_\varepsilon = 3$. The reference solution is obtained at $N_\varepsilon = 8$.

the current formulation reduces the oscillations and preserves the boundedness and positivity of the phase-field solution. The solution obtained is also compared in Fig. 5.5 for $N_\varepsilon = 3$. The reference solution is the solution for $N_\varepsilon = 8$, $\Delta t = 0.001$ and $\varepsilon = 0.01$. The percentage error for the non-PPV-based solution is 0.3548% and that for the PPV-based solution is 0.1905%. For the case when the nonlinear PPV terms are not present, the solution is unbounded. However, for evaluating the density and viscosity values, we chop off the values larger than 1 and smaller than -1 to get physical values for the density and viscosity. We observe from Fig. 5.5 that this chopping leads to less accurate solution compared to the reference solution, while the PPV-based solution is more accurate.

5.4.3.2 Effect of the number of elements in the equilibrium interfacial thickness (N_ε)

We systematically perform mesh convergence studies to quantify the sufficient resolution needed to obtain accurate solution. The mesh resolution is characterized by N_ε . Figure 5.6 shows the evolution of the interface at the left boundary of the domain with different N_ε with fixed $\varepsilon = 0.01$

and $\Delta t = 0.001$. The error is quantified in Table 5.3 with the reference solution taken as that with $N_\varepsilon = 8$. We conclude that N_ε of 4 or 5 is sufficient to capture the interface. Increasing

Table 5.3: Error (e_3) in the solution for different N_ε .

$N_\varepsilon \rightarrow$	3	4	5	6
$e_3 (\times 10^{-3})$	2.491	1.094	0.564	0.208

N_ε gives more accurate solution however the difference is very small. Therefore, N_ε of 4 or 5 seems to be a good compromise between accuracy and computational cost.

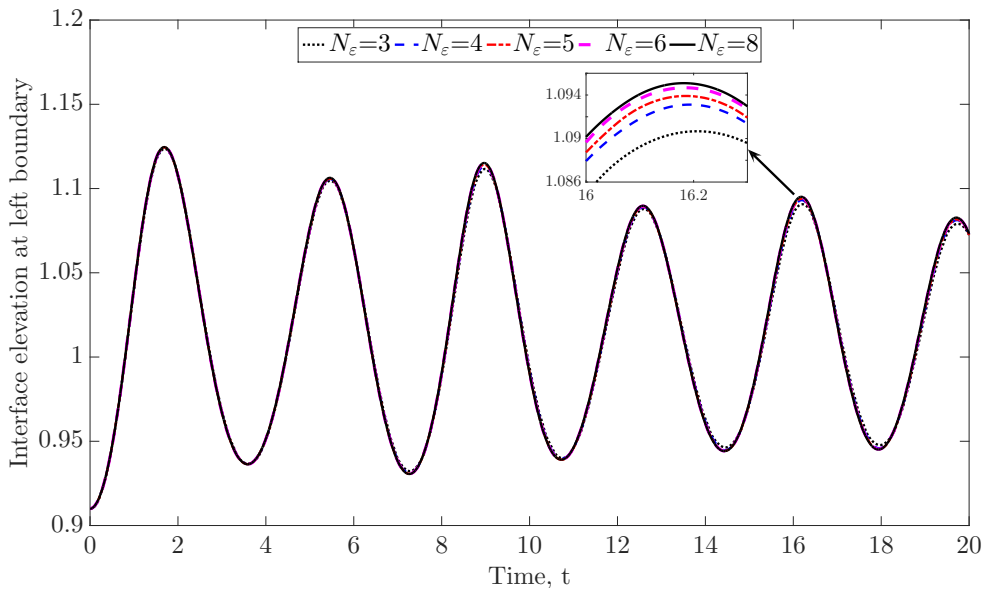


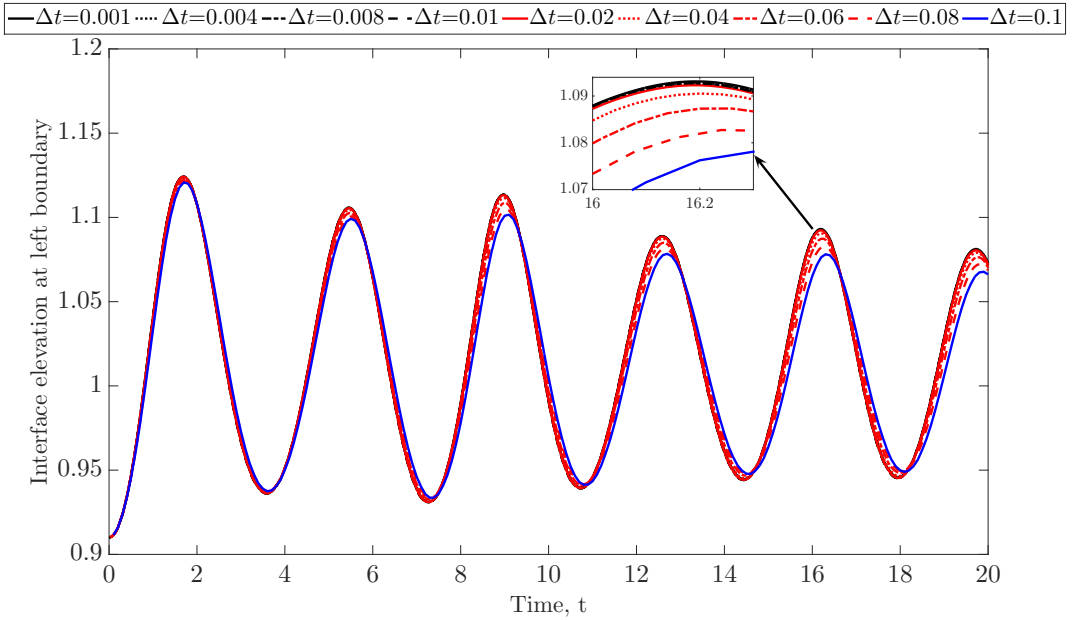
Figure 5.6: Sloshing tank problem: Effect of N_ε on the evolution of the interface. $\varepsilon = 0.01$ and $\Delta t = 0.001$ are kept constant.

5.4.3.3 Effect of the time step size (Δt)

To observe the effect of Δt on the solution, we plot the time convergence plot in Fig. 5.7 with $N_\varepsilon = 4$ and $\varepsilon = 0.01$. Varying time steps between 0.1 and 0.001 are chosen. The plot shows that the difference in the solution is noticeable till $\Delta t = 0.01$, after which further reduction in the time step size has little effect on the accuracy of the solution. The error is shown in Table 5.4 with solution at $\Delta t = 0.001$ as the reference solution.

Table 5.4: Error (e_3) in the solution for different Δt .

$\Delta t \rightarrow$	0.1	0.08	0.06	0.04	0.02	0.01	0.008	0.004
$e_3 (\times 10^{-3})$	10.839	6.959	3.759	1.418	0.457	0.478	0.474	0.324


 Figure 5.7: Sloshing tank problem: Effect of Δt on the evolution of the interface. $\varepsilon = 0.01$ and $N_\varepsilon = 4$ are kept constant.

5.4.3.4 Effect of the interfacial thickness parameter (ε)

The parameter ε represents the thickness of the interface. The limit $\varepsilon \rightarrow 0$ gives the sharp-interface limit. Although decreasing ε will indeed give more accurate representation of the interface, it will increase the computational cost due to the requirement of large number of elements in the equilibrium interfacial thickness region. Figure 5.8 shows the evolution of the interface for different ε values with fixed $\Delta t = 0.01$ and $N_\varepsilon = 4$. The error is quantified in Table 5.5 with the solution at $\varepsilon = 0.005$ taken as the reference solution. A selection of $\varepsilon = 0.01$ is a good compromise between the accuracy and the cost of computation. Finally, we compare and

 Table 5.5: Error (e_3) in the solution for different ε .

$\varepsilon \rightarrow$	0.02	0.01
$e_3 (\times 10^{-3})$	5.469	1.269

validate the results obtained from the current simulation considering $N_\varepsilon = 4$, $\Delta t = 0.01$ and $\varepsilon = 0.01$ with those obtained using extended finite element method (XFEM) in [3]. The method

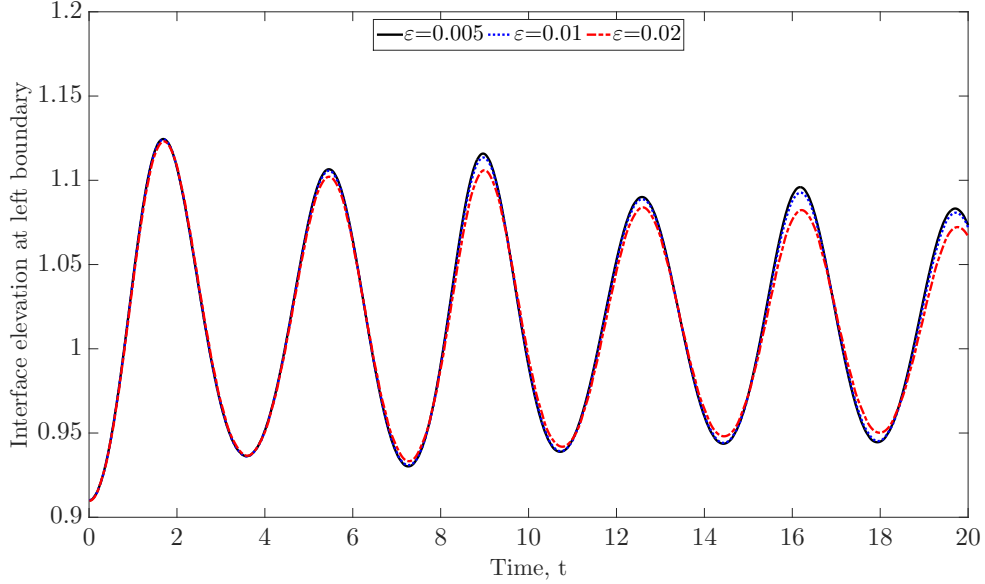


Figure 5.8: Sloshing tank problem: Effect of ε on the evolution of the interface. $\Delta t = 0.01$ and $N_\varepsilon = 4$ are kept constant.

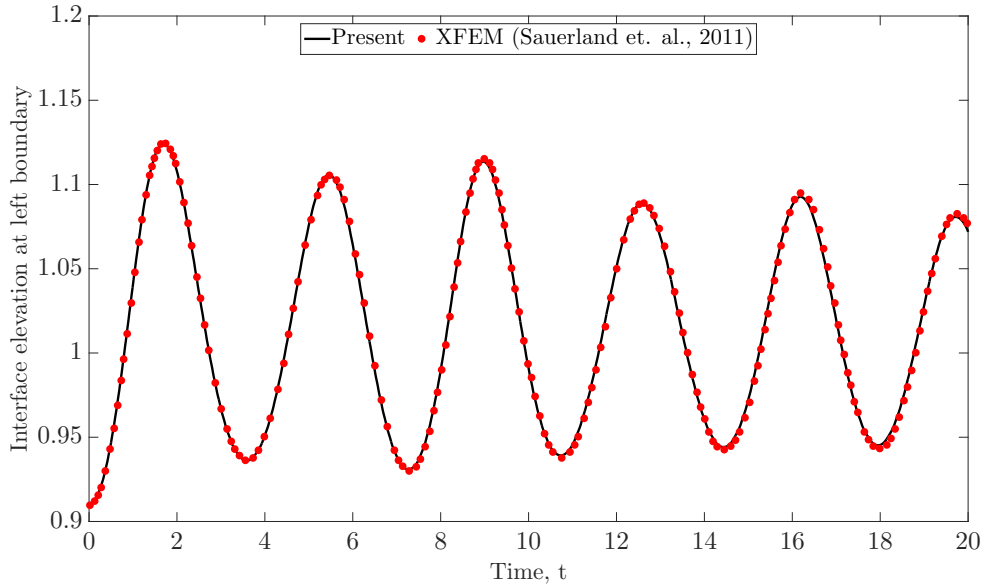


Figure 5.9: Comparison of the solution considering $N_\varepsilon = 4$, $\Delta t = 0.01$ and $\varepsilon = 0.01$ with XFEM-based level set approach in [3].

in [3] employs a local enrichment of the pressure interpolation shape functions and solves the level-set equation to capture the interface with reinitialization procedure. The present method is much simpler to implement without performing any reinitialization or geometric reconstruction. From Fig. 5.9, we observe that sufficiently accurate results can be obtained by applying the diffuse-interface approach. Furthermore, the proposed algorithm consisting of single-pass

implicit partitioned coupling discussed in Section 5.3.2 helps to reduce the computational time without compromising the accuracy and the stability of the solution. For demonstrating the ability of the solver to handle the topological changes of the fluid-fluid interface, we next simulate the two- and three-dimensional dam-break problems for unstructured meshes.

5.4.4 Two-dimensional dam-break problem

In this section, we present the two-dimensional dam-break problem to assess the ability of the solver to handle breaking and merging of air-water interface in a representative two-phase flow problem. A rectangular computational domain $[0, 0.584] \times [0, 0.438]$ shown in Fig. 5.10(a) is considered for the present study. A water column of size 0.146×0.292 units is placed at the left boundary of the domain at time $t = 0$. The initial condition is given by:

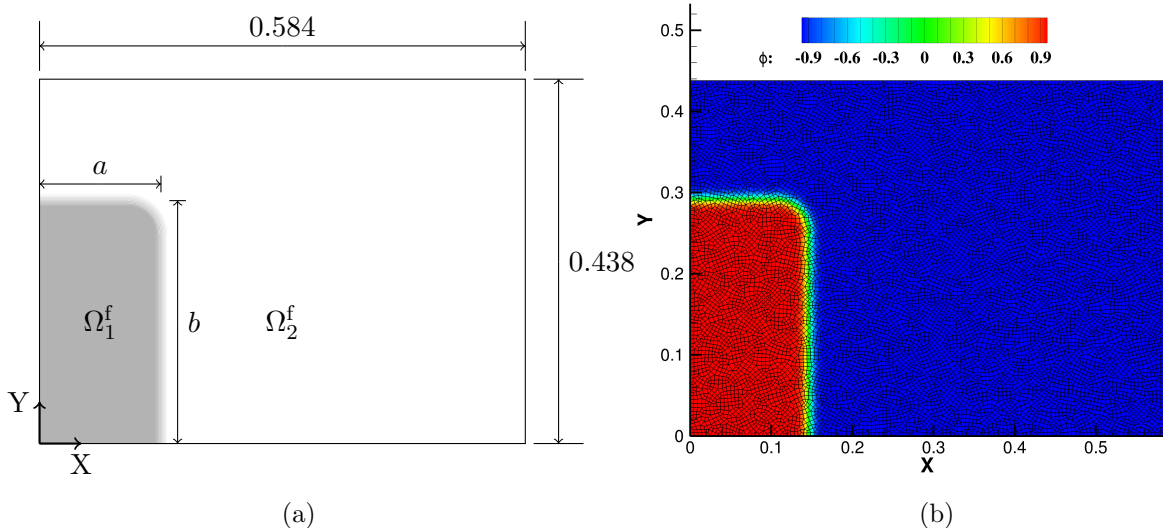


Figure 5.10: Two-dimensional dam-break problem: (a) schematic diagram showing the computational domain, and (b) the contour plot of the order parameter ϕ at $t = 0$. In (a), Ω_1^f and Ω_2^f are the two phases with $\rho_1^f = 1000$, $\rho_2^f = 1$, $\mu_1^f = 10^{-3}$ and $\mu_2^f = 10^{-5}$ and acceleration due to gravity is taken as $\mathbf{g} = (0, -9.81, 0)$.

$$\phi(x, y, 0) = \begin{cases} -\tanh\left(\frac{y - b}{\sqrt{2}\varepsilon}\right), & \text{for } x \leq (a - r), y \geq (b - r), \\ -\tanh\left(\frac{x - a}{\sqrt{2}\varepsilon}\right), & \text{for } x > (a - r), y < (b - r), \\ \tanh\left(\frac{r - \sqrt{(x - (a - r))^2 + (y - (b - r))^2}}{\sqrt{2}\varepsilon}\right), & \text{for } x \geq (a - r), y \geq (b - r), \\ 1, & \text{elsewhere,} \end{cases} \quad (5.43)$$

where $a = 0.146$, $b = 0.292$ and $r = 0.04$ are the width, height and the radius of the curve of the water column respectively, $\phi = 1$ and $\phi = -1$ correspond to the order parameter on Ω_1^f and Ω_2^f respectively. A non-uniform mesh consisting of about 13,500 nodes and 13,300 four-node quadrilaterals is employed for the study. The interfacial thickness parameter ε is selected as 0.005. The total computational time for simulating 1000 time steps with step size of $\Delta t = 0.001$ is about 0.453 hour on 4 CPUs. The interface location at the left and bottom

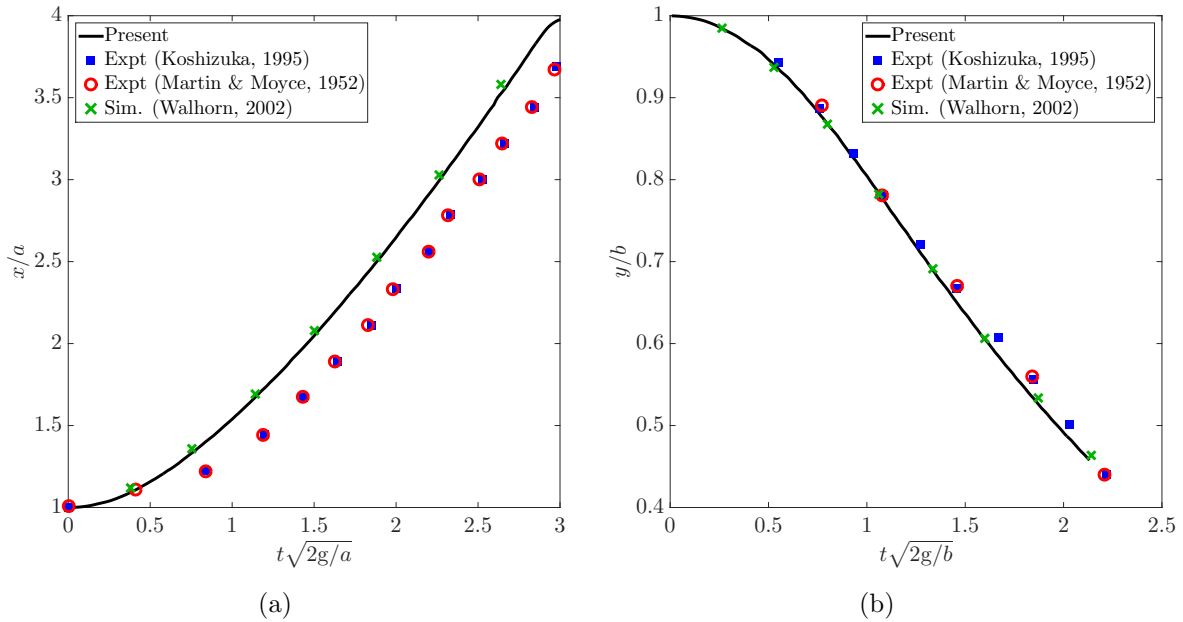


Figure 5.11: Two-dimensional dam-break problem: temporal evolution of non-dimensional water column (a) width and (b) height.

boundaries are tracked as a function of time for the validation with experiments [178, 179] and the interface-tracking simulation [180]. The temporal variation of the interface location based on the non-dimensional water column width/height is compared with the results from the literature in Fig. 5.11 whereby a good agreement can be seen. The evolution of the height of the water column is quantified very well. However, the expansion of the water column (in width) in the experiment is slower than what is predicted from the simulation. As discussed in [3], this delay can be attributed to the time required to remove the partition, which holds the water column to its initial profile in the experiment.

The profiles of the interface evolution are shown in Fig. 5.12. It is in good agreement with the profiles obtained in the literature. Some variations can be found which may be due to the closed domain condition in the numerical study.

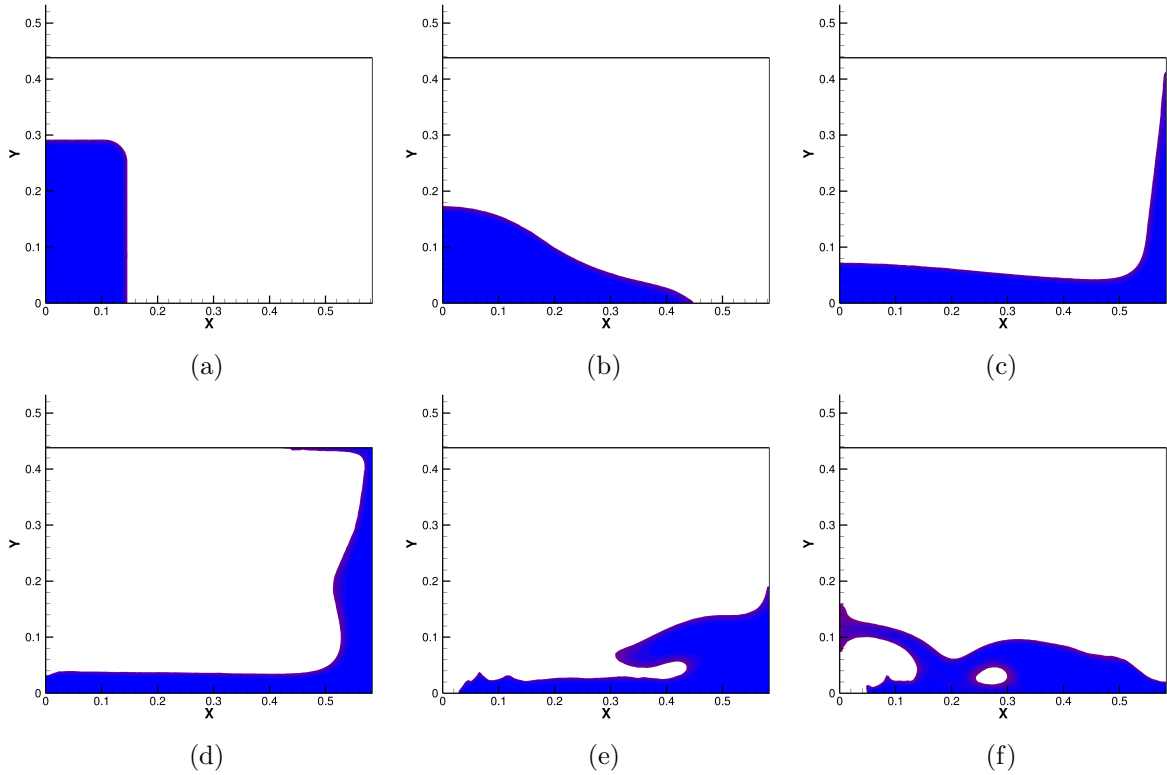


Figure 5.12: Interface profiles for two-dimensional dam-break problem: (a) $t = 0.0$, (b) $t = 0.2$, (c) $t = 0.4$, (d) $t = 0.6$, (e) $t = 0.8$ and (f) $t = 1.0$. The profile shown depicts the contour of the order parameter cutoff below 0, i.e., it only shows the domain consisting water.

5.4.5 Three-dimensional dam-break with obstacle

To further assess the phase-field solver, we simulate the three-dimensional dam-break problem with a rectangular obstacle. The computational domain is a cuboid of size $L \times B \times H$, with $L = 3.22$, $B = 1$ and $H = 1$ and a water column of size $L_w \times B_w \times H_w$, where $L_w = 1.228$, $B_w = 1$ and $H_w = 0.55$. The rectangular cuboid obstacle is of size $l \times b \times h$, where $l = 0.161$, $b = 0.403$ and $h = 0.161$. The dimensions of the domain are given in Fig. 5.13. To extract the pressure for comparison with the experiment, we introduce two probes at the following locations (with respect to the axis orientation given in Fig. 5.13):

- $(2.3955, 0.021, -0.5255)$: Pressure value (P1)
- $(2.3955, 0.061, -0.5255)$: Pressure value (P2)

The notation in the parentheses is the name of the probe used in the experiment of Maritime Research Institute Netherlands (MARIN) [181, 182]. To obtain the variation in the water

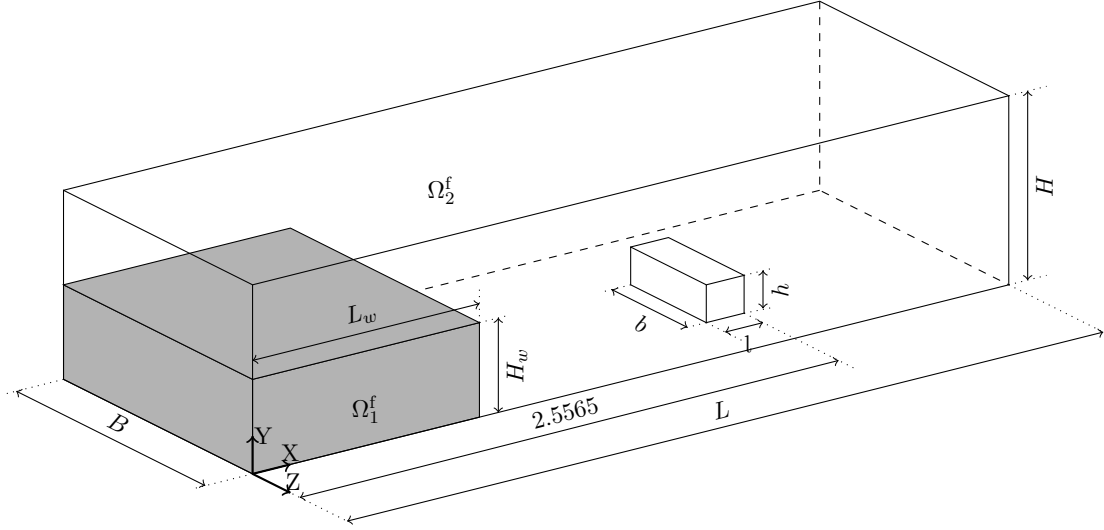


Figure 5.13: Schematic diagram showing the computational domain for three-dimensional dam-break with obstacle. Ω_1^f and Ω_2^f are the two phases with $\rho_1^f = 1000$, $\rho_2^f = 1.225$, $\mu_1^f = 1.002 \times 10^{-3}$ and $\mu_2^f = 1.983 \times 10^{-5}$, acceleration due to gravity is taken as $\mathbf{g} = (0, -9.81, 0)$ and slip boundary condition is imposed on all the boundaries.

level (i.e., the air-water interface), the height of the water is tracked at two locations, viz., $(X, Z) = (2.724, -0.5)$ and $(X, Z) = (2.228, -0.5)$ corresponding to H1 and H2 probes of the experiment, respectively. The data of the experiment is taken from [183]. The computational

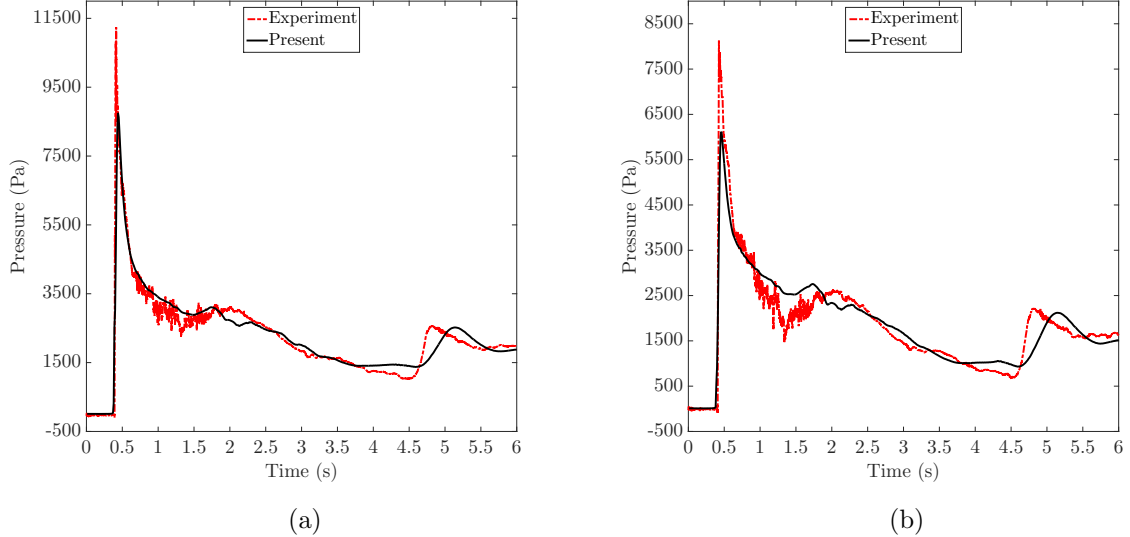


Figure 5.14: Three-dimensional dam-break problem: temporal evolution of the pressure at the probe points: (a) P1 and (b) P2.

domain is discretized into 430,000 nodes with 2.5 million tetrahedral elements. The interfacial thickness parameter is chosen as $\varepsilon = 0.02$. The total computational time for the simulation of

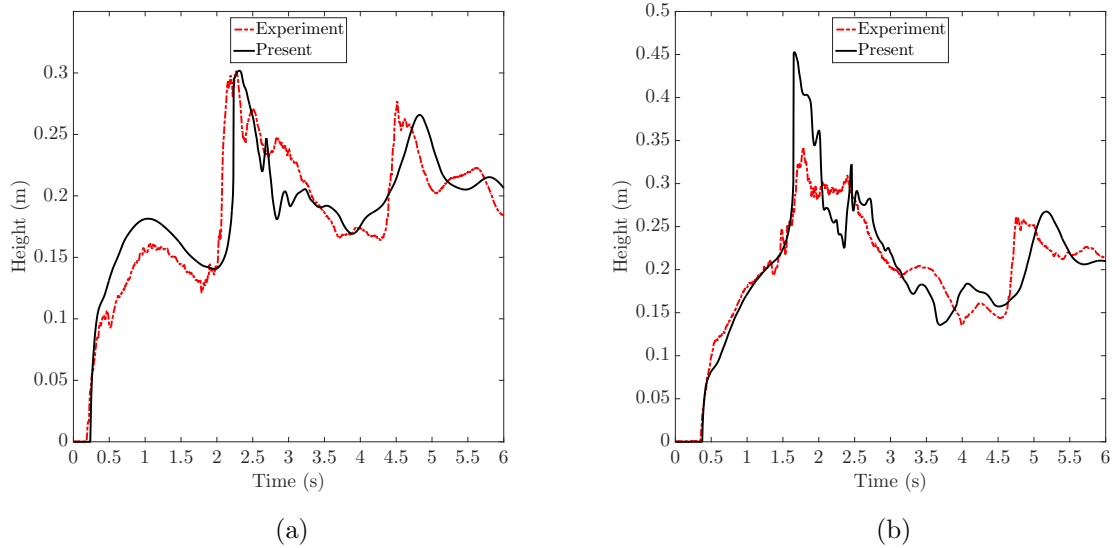


Figure 5.15: Three-dimensional dam-break problem: temporal evolution of the height at the probe points: (a) H1 and (b) H2.

1200 time steps with $\Delta t = 0.005$ is 2.2 hours on 24 CPUs. The comparison between the results obtained from the present simulation and the experiment is depicted in Figs. 5.14 and 5.15. The change in the iso-contours of water ($\phi > 0$) have been plotted in Fig. 5.16 which shows a good qualitative agreement with the results from the literature [184, 185, 182]. These tests confirm the ability of the solver to capture the air-water interface with topological changes. After assessing the present formulation for the Allen-Cahn equation and its coupling with the Navier-Stokes equations, we next demonstrate its application to a wave-structure interaction problem.

5.5 Application to wave-structure interaction

Before we consider the phase-field two-phase solver for a wave run-up problem, we first briefly present a background theory of ocean waves. Propagation of free-surface waves is a very complex phenomenon due to the irregular nature of the waves and nonlinear effects. It is very challenging to develop an extensive mathematical formulation to predict this phenomenon. The simplest model is the linear or first-order wave theory where it is assumed that the fluid is incompressible, inviscid and irrotational, density is uniform throughout the fluid, waves are planar and monochromatic. Nonlinear boundary conditions at the free-surface are linearized to

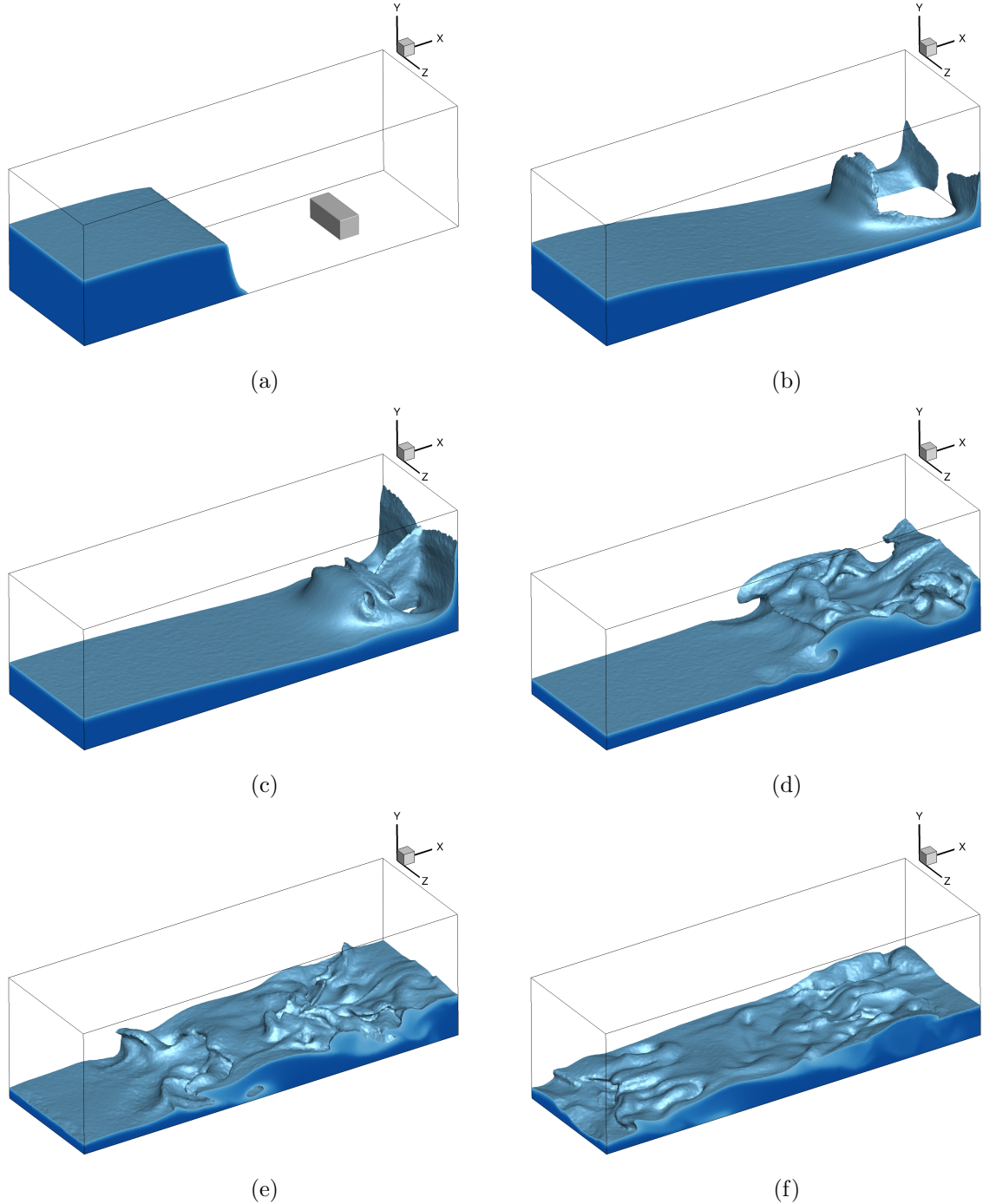


Figure 5.16: Three-dimensional dam-break problem: temporal evolution of the iso-contours of water ($\phi > 0$) at time: (a) 0.125s, (b) 0.75s, (c) 1.125s, (d) 2s, (e) 2.5s and (f) 3s.

further simplify the model [21, 22]. A more accurate model involving the nonlinearities of the wave phenomenon is the second-order Stokes wave theory developed in [186]. The notations used in the description of the wave theory are shown in Fig. 5.17. Apart from the notations shown, T is the time period of the wave, $\omega = 2\pi/T$ is the angular frequency and $k = 2\pi/\lambda$ is

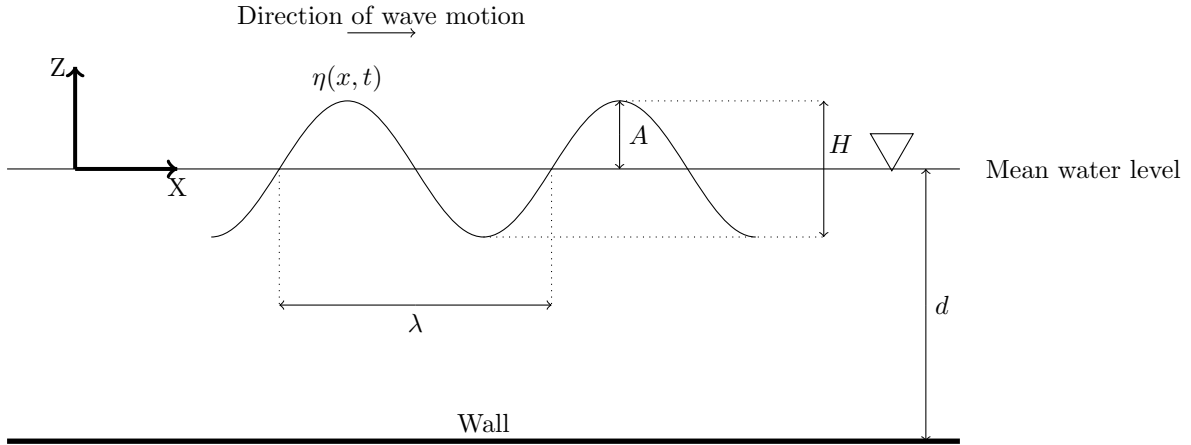


Figure 5.17: Notations and coordinate system in the description of the second-order Stokes wave theory: $\eta(x, t)$ is the profile of the free-surface, d is the water depth, A is the amplitude of the wave, $H = 2A$ is the height of the wave and λ is the wavelength.

the wave number. We summarize the results obtained by the second-order Stokes wave theory.

The free-surface profile of the wave is given as

$$\eta(x, t) = \frac{H}{2} \cos(kx - \omega t) + \frac{\pi H^2}{8\lambda} \frac{(\cosh(kd))(2 + \cosh(2kd))}{\sinh^3(kd)} \cos[2(kx - \omega t)]. \quad (5.44)$$

The horizontal and vertical components of the velocity to generate the above profile can be derived as

$$u(x, z, t) = \frac{Hgk}{2\omega} \frac{\cosh[k(d+z)]}{\cosh(kd)} \cos(kx - \omega t) + \frac{3H^2\omega k}{16} \frac{\cosh[2k(d+z)]}{\sinh^4(kd)} \cos[2(kx - \omega t)], \quad (5.45)$$

$$w(x, z, t) = \frac{Hgk}{2\omega} \frac{\sinh[k(d+z)]}{\cosh(kd)} \sin(kx - \omega t) + \frac{3H^2\omega k}{16} \frac{\sinh[2k(d+z)]}{\sinh^4(kd)} \sin[2(kx - \omega t)]. \quad (5.46)$$

With the description of the second-order Stokes waves, we set up a numerical wave tank to demonstrate the wave run-up problem across a vertical truncated cylinder. The vertical truncated cylinder is one of the most common structural members in many offshore structures, e.g., gravity-based structures, semi-submersibles, and tension-leg platforms. The wave run-up on a submerged structure is measured by the run-up ratio, R/A defined as the ratio of the highest free-surface elevation of the fluid (water in this case) at the front-face of the cylinder to the amplitude of the incident incoming wave. The run-up depends on two important non-dimensional parameters: the wave steepness, kA and the wave scattering parameter, ka , which are given by

$$kA = \frac{2\pi A}{\lambda}, \quad (5.47)$$

$$ka = \frac{2\pi a}{\lambda}, \quad (5.48)$$

where A is the amplitude of the incident wave, a and λ denote the radius of the cylinder and the wavelength of the incoming wave, respectively. If the steepness of the incoming wave is increased (kA is increased) or if the cross-sectional width of the structure is increased (ka is increased) leading to more resistance to the flow, the run-up ratio increases. The quantification of the run-up ratio with kA and ka is of a particular interest in ocean engineering. Some of the experimental and numerical works dealing with the run-up ratio of different cross-sectional structures are discussed in [4, 187].

For the present demonstration, we consider a truncated circular cylinder as the structure being impinged by the incoming waves. We keep the parameter ka constant and quantify the run-up on the cylinder by varying kA values. The computational setup is similar to that employed in [187] and its schematic is shown in Fig. 5.18. The size of the computational

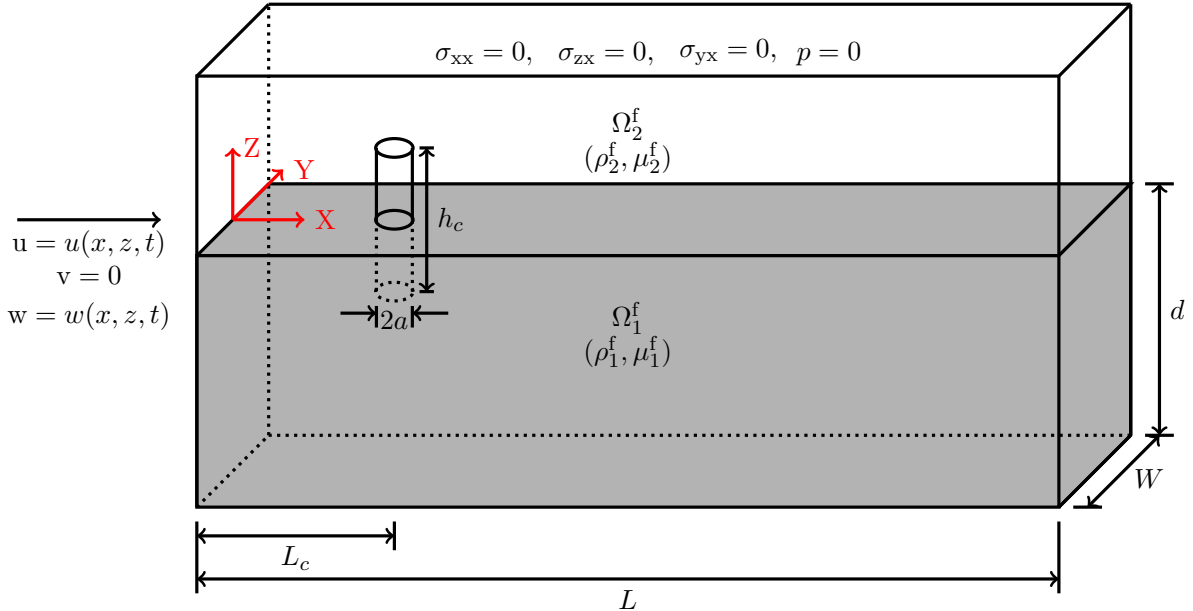


Figure 5.18: A schematic of the wave-structure problem. The computational setup and boundary conditions are shown for the Navier-Stokes equations. Here, $\mathbf{u}^f = (u, v, w)$ denotes the components of the fluid velocity which are given by Eqs. (5.45) and (5.46) with $v = 0$. Stress-free boundary condition with zero pressure is given at the top surface of the wave tank. Slip boundary condition is imposed at the X-Z plane at $y = -1$ and $y = 1$. All other boundaries have the no-slip condition. Moreover, zero Neumann boundary condition is imposed for the order parameter ϕ on all the boundaries.

domain is $24\text{m} \times 2\text{m} \times 2\text{m}$, i.e., $L = 24\text{m}$ and $W = 2\text{m}$. The depth of the water is $d = 1.2\text{m}$ and the draft of the submerged cylinder is 0.4m . The diameter of the cylinder is $2a = 0.2\text{m}$

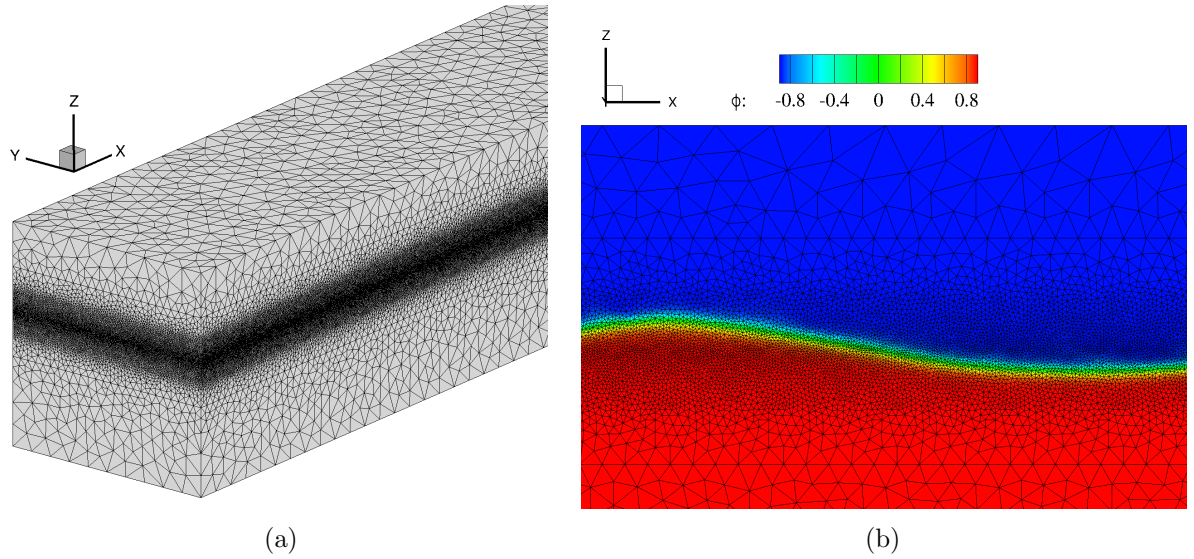


Figure 5.19: Three-dimensional computational mesh and contours of order parameter for the run-up problem: (a) refined interfacial region with unstructured finite element mesh, (b) contour plot of order parameter ϕ superimposed with the unstructured mesh.

and its total height is $h_c = 0.8\text{m}$. The center of the cylinder is at a distance of $L_c = 3.6\text{m}$ from the left boundary. The boundary conditions employed in the simulation are as follows: velocity inlet according to Eqs. (5.45) and (5.46) to simulate Stokes waves at the left boundary, the stress-free boundary condition with zero pressure at the top boundary and slip boundary condition at the two sides at $y = -1\text{m}$ and $y = 1\text{m}$. All other boundaries (bottom and right) satisfy the no-slip boundary condition. The order parameter ϕ is initialized with the interface at $z = 0\text{m}$ with Ω_1^f phase depicting water ($\rho_1^f = 1000, \mu_1^f = 1.002 \times 10^{-3}$) and Ω_2^f representing air ($\rho_2^f = 1.225, \mu_2^f = 1.983 \times 10^{-5}$). The interface thickness parameter for the Allen-Cahn solver is taken as $\varepsilon = 0.02$. Initial numerical tests suggested that employing a much sharper interface by taking smaller ε does not affect the solution for this wave-structure interaction problem. The time-step size is taken as $\Delta t = 0.0025$ with the total number of time steps as 5000. The capillary effects due to the surface tension have been neglected for the modeling of the free-surface waves.

Based on the experimental campaign in [4], we select the ka value of 0.208 which gives a wavelength of $\lambda = 3.0208\text{m}$. For the Stokes waves, the time period is a function of wavelength as $\lambda = \frac{gT^2}{2\pi} \tanh\left(\frac{2\pi d}{\lambda}\right)$, which gives $T = 1.40045\text{s}$. We vary the kA values by changing the amplitude of the wave and quantify the run-up ratio R/A for the truncated cylinder. An unstructured

finite element mesh is constructed for the numerical wave tank via open-source mesh generator [188]. A gradually coarsening mesh from mesh size $\delta = 0.01$ at $z = 0$ to $\delta = 0.02$ is used to capture the interface region from $z = -0.2$ to $z = 0.2$. This resolution also ensures that at least 4 number of elements fall under the equilibrium interfacial region to capture the interface properties accurately. Furthermore, the resolution of the mesh is increased to a value of $\delta = 0.01$ enveloping the cylinder. The total number of grid nodes in the mesh are around 5.6 million with approximately 34 million tetrahedral unstructured elements. The mesh is depicted in Fig. 5.19. The simulations are performed using 600 CPU cores with the MPI parallelism. The total time taken to complete the 5000 time steps is approximately 6.5 hours with approximately 5 seconds to complete a minimum of 3 nonlinear iterations in a time step.

The free-surface wave elevation is recorded in time at two locations- one at $x = 2\text{m}$ and the other at $x = 3.5\text{m}$ (the front-face of the cylinder). The wave elevation is determined by linearly interpolating the order parameter and considering the interface where $\phi = 0$. The wave amplitude is calculated as the amplitude of the first harmonic of the free-surface elevation of the incident wave at the first probe point at $x = 2\text{m}$ by taking the Fourier transform of the elevation η as $A = A(\omega_1)$, where ω_1 is the first harmonic frequency of the incident wave. The wave run-up on the front-face of the cylinder at $x = 3.5\text{m}$ is calculated as the mean of the maximum amplitude from each wave cycle as $R = \frac{1}{M} \sum_{n=1}^M \eta_n$, where η_n is the peak amplitude of the free-surface elevation η at $x = 3.5\text{m}$ of the nth wave cycle and M is the total number of wave cycles which is equal to 5 in this case. The wave run-up ratio is evaluated as the ratio

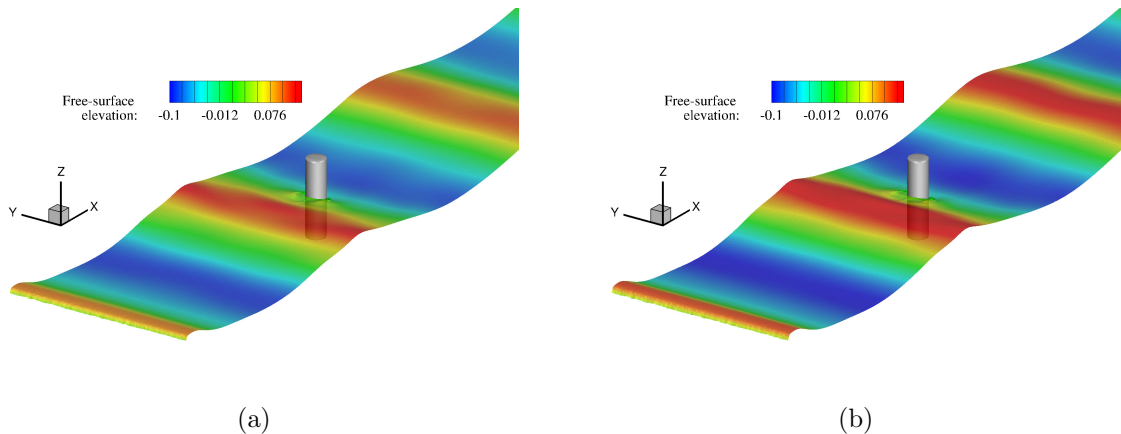


Figure 5.20: Water wave run-up on a truncated cylinder: Snapshots of iso-contours $\phi = 0$ colored by the free-surface elevation for two representative wave steepness parameters at $t/T = 8.926$: (a) $kA = 0.1837$, and (b) $kA = 0.2146$.

of the wave run-up R on the front-face of the cylinder and the incident wave amplitude A . All the post-processing is performed in the time interval $t/T \in [4, 9]$ to exclude any initial transient solutions. The data is post-processed in a similar manner as the experimental campaign [4].

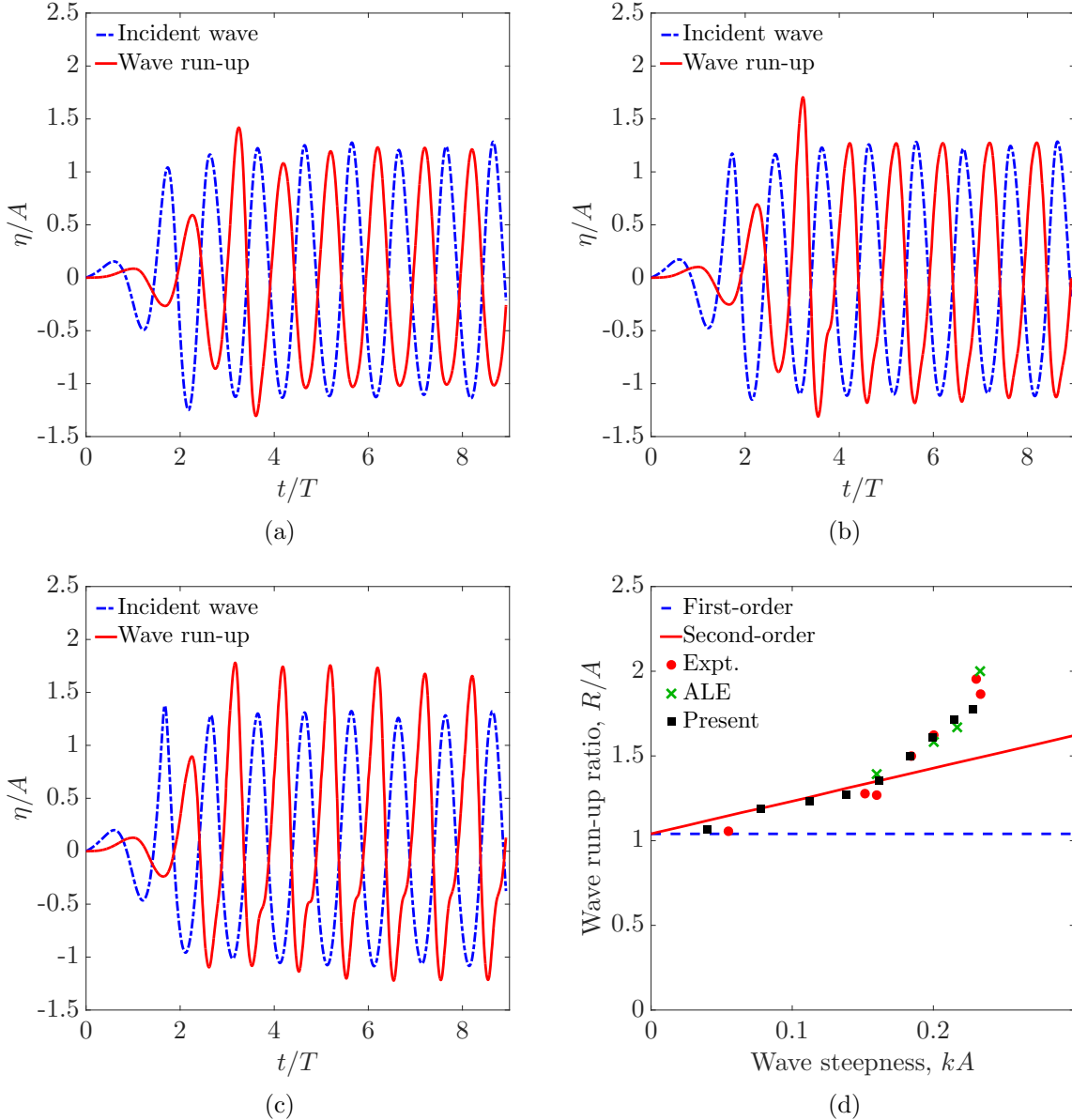


Figure 5.21: Water wave run-up on a truncated cylinder: Time histories of the free-surface elevations at the probe locations for three representative wave steepness parameters: (a) $kA = 0.0779$, (b) 0.1381, (c) 0.2146, and (d) comparison of the wave run-up ratio with the results from the literature at $ka = 0.208$: The first- and second-order results are from frequency domain potential theory, the experimental results are from the campaign in [4] and the ALE results are from the free-surface ALE solver in [5]. Time and free-surface elevation are non-dimensionalized by time period T and wave amplitude A respectively.

We simulate cases for a range of $kA \in [0.04, 0.2282]$. The iso-contours of the free-surface at

$\phi = 0$ colored by the free-surface elevation are plotted in Fig. 5.20 for two different kA values at $t/T = 8.926$. The time history of the incident wave and run-up for different kA values is plotted in Fig. 5.21(a-c). We observe a secondary kink in the wave run-up at high kA values in the figures similar to the findings in the literature. The wave run-up ratio is compared with the results from the literature in Fig. 5.21(d). Our results are in good agreement with the theoretical estimates and the experimental measurements.

5.6 Summary

In this chapter, we applied the positivity preserving framework to the phase-field modeling of two-phase flows via the Allen-Cahn equation. The salient features of the formulation are:

- A stable and efficient nonlinear partitioned coupling of the Navier-Stokes and the Allen-Cahn equations involving fluid phases with high-density ratio,
- Improved mass conservation and energy stability properties by considering the mid-point temporal approximations for the derivative of the double-well potential and the Lagrange multiplier,
- Provably second-order accuracy of the spatial and temporal discretizations for the Allen-Cahn equation,
- Direct implementation of the phase-field equation without relying on operator splitting,
- Reduction in oscillations in the solution due to the positivity property,
- Optimal number of finite elements in the equilibrium interfacial region $\sim 4 - 5$, and
- Capability of the solver to handle topological changes in the fluid-fluid interface (breaking and merging).

Chapter 6

Mesh Adaptive Procedure for Phase-Field Formulation*

Following the improvement of the solution in solving the Allen-Cahn equation using the positivity preserving variational method in Chapter 5, we further try to improve the accuracy in the solution by employing a nonlinear procedure to adapt the two-dimensional mesh along the fluid-fluid interface based on the residual estimates of the Allen-Cahn equation. The adaptive procedure is based on the newest vertex bisection algorithm which avoids the memory intensive storage of the hierarchical tree-type data structure for refinement/coarsening. This adaptive procedure is discussed in the present chapter. Assessment of the algorithm is conducted via numerical tests followed by a demonstration on the dam-break problem.

6.1 Adaptive variational Allen-Cahn procedure

In this section, we present a nonlinear adaptive partitioned procedure for implicitly discretized Navier-Stokes and Allen-Cahn equations. We start with defining some of the errors used to quantify the solution obtained by solving the Navier-Stokes, the Allen-Cahn equations and the errors corresponding to the adaptive algorithm. Let the vector containing the increments of velocity and pressure in the linearized matrix of the Navier-Stokes equations (Eq. (5.33)) be

*Parts of this chapter have been published in “V. Joshi and R.K. Jaiman, An adaptive variational procedure for the conservative and positivity preserving Allen-Cahn phase-field model, *Journal of Computational Physics*, 366, Pg. 478-504 (2018).”

denoted by $\Delta\mathbf{X}$ and the vector of the respective updated quantities at $t_{(k)}^{n+1}$ be represented as $\mathbf{X}_{(k)}^{n+1}$, k being the nonlinear iteration index. We define the error in solving the Navier-Stokes equations as

$$e_{NS} = \frac{\|\Delta\mathbf{X}\|}{\|\mathbf{X}_{(k)}^{n+1}\|}. \quad (6.1)$$

Similarly, for the linearized matrix form of the Allen-Cahn equation (Eq. (5.34)), the numerical error in solving the Allen-Cahn equation can be written as

$$e_{AC} = \frac{\|\Delta\phi\|}{\|\phi_{(k)}^{n+1}\|}. \quad (6.2)$$

These error expressions are utilized for the convergence criteria of the nonlinear iterations.

The goal of the proposed procedure is the reduction of the nonlinear errors while solving the Navier-Stokes and the Allen-Cahn equations along with the reduction of the error indicator due to adaptivity. Since the underlying equations involved in the phase-field formulation are inherently nonlinear, the nonlinear convergence plays a crucial role in the conservation and accuracy of the solution. The errors introduced due to the mesh refinement/coarsening also impact the solution accuracy. Therefore, the primary goal of the proposed algorithm is to reduce the errors introduced due to mesh adaptivity within a tolerance limit followed by the reduction in the nonlinear errors of the underlying equations. This will be elaborated in the subsequent sections.

6.1.1 Residual error estimates for the conservative Allen-Cahn equation

The Galerkin variational formulation of the Navier-Stokes and the Allen-Cahn equations is simply the differential operator multiplied by the weighting function and integrated by parts as appropriate, which tends to minimize the residual of the equations in a chosen set of weighting functions. When the solution of the underlying differential equation is smooth, as measured relative to the differential equation on the given mesh, the variational error tends to be small at convergence. If the solution exhibits oscillations near sharp gradients due to dominant convection and reaction effects on an under-resolved mesh, the residual of the equation has a significantly large value. This residual needs to be minimized to obtain an accurate and close-

Chapter 6. Mesh Adaptive Procedure for Phase-Field Formulation

to-converged solution, defined by the user-defined tolerance limit. Therefore, the mesh has to be refined in those areas to capture the sharp gradients in the solution. This suggests using the residual of the differential equation as an indicator of the error for the adaptive mesh procedure.

For the quantification of the error on which our adaptive procedure will be based, the residual error estimates are derived for the Galerkin discretization of the Allen-Cahn equation. Consider the domain $\Omega^f(t)$ which consists of elements Ω_e , chosen such that $\Omega^f(t) = \cup_{e=1}^{n_{el}} \Omega_e$ and $\emptyset = \cap_{e=1}^{n_{el}} \Omega_e$ where n_{el} is the number of elements. Let Γ be the Lipschitz continuous boundary of the domain $\Omega^f(t)$, Γ_D and Γ_N be the Dirichlet and Neumann boundaries of $\Omega^f(t)$ respectively such that $\Gamma = \Gamma_D \cup \Gamma_N$. Furthermore, let \mathcal{E} denote the set of edges for all the elements in the domain, \mathcal{E}_Γ , \mathcal{E}_{Γ_D} and \mathcal{E}_{Γ_N} be the set of edges on the boundary Γ , Γ_D and Γ_N respectively. Consider \mathcal{E}_{Ω_e} to be the set of edges of an element Ω_e and \mathcal{E}_Ω be the set of all the interior edges of $\Omega^f(t)$. The Galerkin terms of Eq. (5.25) can be written after integration by parts as

$$\begin{aligned} & \int_{\Omega^f(t)} \hat{w}_h \partial_t \phi_h d\Omega + \int_{\Omega^f(t)} \hat{w}_h (\hat{\mathbf{u}} \cdot \nabla \phi_h) d\Omega + \int_{\Omega^f(t)} \nabla \hat{w}_h \cdot (\hat{k} \nabla \phi_h) d\Omega + \int_{\Omega^f(t)} \hat{w}_h \hat{s} \phi_h d\Omega \\ & - \int_{\Omega^f(t)} \hat{w}_h \hat{f} d\Omega = \sum_{e=1}^{n_{el}} \int_{\Omega_e} \hat{w}_h \mathcal{R}_{\Omega_e}(\phi_h) d\Omega_e + \sum_{E \in \mathcal{E}} \int_E \hat{w}_h \mathcal{R}_E(\phi_h) dE, \end{aligned} \quad (6.3)$$

where \mathcal{R}_{Ω_e} and \mathcal{R}_E are the element and edge-based residuals, given as,

$$\mathcal{R}_{\Omega_e} = \partial_t \phi_h + \hat{\mathbf{u}} \cdot \nabla \phi_h - \hat{k} \nabla^2 \phi_h + \hat{s} \phi_h - \hat{f}, \quad (6.4)$$

$$\mathcal{R}_E = \begin{cases} -\mathbb{J}_E(\mathbf{n}_E \cdot \hat{k} \nabla \phi_h), & \text{if } E \in \mathcal{E}_\Omega, \\ -\mathbf{n}_E \cdot \hat{k} \nabla \phi_h, & \text{if } E \in \mathcal{E}_{\Gamma_N}, \\ 0, & \text{if } E \in \mathcal{E}_{\Gamma_D}, \end{cases} \quad (6.5)$$

where $\mathbb{J}_E(\cdot)$ is the jump of the argument across the element edge E and \mathbf{n}_E is the normal to the edge E .

After some algebraic manipulations and using inequalities (see Appendix I for detailed steps), we establish the expression for the error estimate as

$$\|\phi - \phi_h\| \leq c^* \left\{ \sum_{e=1}^{n_{el}} h_{\Omega_e}^2 \|\mathcal{R}_{\Omega_e}\|_{\Omega_e}^2 + \sum_{E \in \mathcal{E}} h_E \|\mathcal{R}_E\|_E^2 \right\}^{1/2} \|\hat{w}\|_{H^1(\Omega^f(t))}, \quad (6.6)$$

where h_{Ω_e} is the diameter of the element Ω_e , h_E is the length of the edge E and c^* is some arbitrary constant.

$$\|\phi - \phi_h\| \leq c^* \left\{ \sum_{e=1}^{n_{el}} h_{\Omega_e}^2 \|\mathcal{R}_{\Omega_e}\|_{\Omega_e}^2 + \sum_{e=1}^{n_{el}} \sum_{E \in \mathcal{E}_{\Omega_e} \cap \mathcal{E}} h_E \|\mathcal{R}_E\|_E^2 \right\}^{1/2} \|\hat{w}\|_{H^1(\Omega^f(t))}. \quad (6.7)$$

Let η_{Ω_e} denote the error indicator of the triangular element Ω_e on the mesh. The error estimate can be recast as

$$\|\phi - \phi_h\| \leq \eta = \left(\sum_{e=1}^{n_{el}} \eta_{\Omega_e}^2 \right)^{1/2}, \quad (6.8)$$

$$\eta_{\Omega_e}^2 = h_{\Omega_e}^2 \|\mathcal{R}_{\Omega_e}\|_{\Omega_e}^2 + \sum_{E \in \mathcal{E}_{\Omega_e} \cap \mathcal{E}} h_E \|\mathcal{R}_E\|_E^2, \quad (6.9)$$

where η is the error estimate and η_{Ω_e} is the error indicator for the element Ω_e .

6.1.2 The adaptive algorithm

Given the error indicators for each element η_{Ω_e} calculated from the error estimates of the Allen-Cahn equation, we employ the newest vertex bisection algorithm [189] for the mesh adaptivity. The algorithm first marks the elements and the edges based on the error indicators and then proceeds to refine or coarsen the elements. The marking of the elements for refinement is carried out by the Dörfler criterion [190], which finds the minimum set of elements Ω^M such that

$$\theta \sum_{\Omega_e \in \Omega} \eta_{\Omega_e}^2 \leq \sum_{\Omega_e \in \Omega^M} \eta_{\Omega_e}^2, \quad (6.10)$$

for a user-defined $\theta \in (0, 1)$. This criterion, therefore, selects the elements for refinement which have a large contribution to the error estimate. A schematic for the refinement algorithm is shown in Fig. 6.1. Suppose the element ABC is selected for refinement. The edges of the

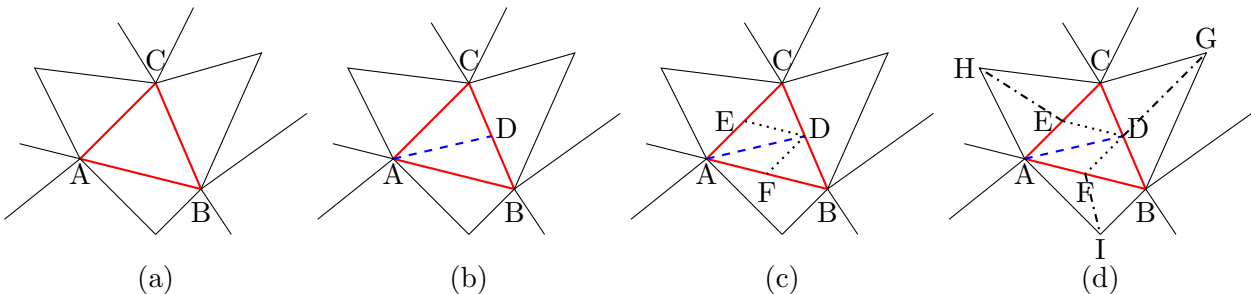


Figure 6.1: A schematic of the newest vertex bisection algorithm for refinement: (a) marked element for refinement, (b) bisection of the largest edge, (c) bisection of the other marked edges, (d) inclusion of more elements to remove hanging nodes.

element (AB, BC, and CA) are then marked for refinement. The bisection algorithm starts

with the largest edge among the marked edges (BC) by addition of a new node (D), followed by the bisection of the other edges (AB and AC). At this point, a new array is created which indicates the nodes which are added by bisection (can be coarsened) or which belong to the initial grid (cannot be coarsened). This simplifies the implementation of the algorithm since we do not need a tree-type data structure containing the information about the parent and children elements. Once the marked edges are refined, there would be some hanging nodes (D, E, and F in Fig. 6.1(c)). Some extra elements are then created to avoid these hanging nodes (Fig. 6.1(d)). This completes the refining algorithm for a particular element. A similar bisection process is carried out for all the marked elements. Once all the marked elements are refined, the algorithm proceeds to solve the underlying equation on the updated refined mesh. The interpolation of the variables while refining is carried out by setting the value of the newest added node equal to the half of the sum of the values at the nodes of the two extremes of the corresponding edge, for example, in Fig. 6.1(b), the value of a variable at D will be half the sum of its values at B and C.

Based on the residual error indicators, the elements with small errors can be coarsened using the node-based coarsening algorithm in a similar way with the help of the created array containing the information about the added nodes by bisection. Certain nodes are marked which are considered to be “good” for coarsening to ensure that the conformity of the mesh is not compromised. Nodes are then removed based on the Dörfler criterion with θ_c as the user-defined coarsening parameter. Details about the coarsening algorithm can be found in [115].

6.1.3 The nonlinear adaptive variational partitioned (NAVP) procedure

We now present the procedure for the partitioned iterative coupling of the incompressible Navier-Stokes and the Allen-Cahn equations. Within a predictor-corrector process, implicit time discretizations are adopted for efficiency and robustness of the partitioned coupling. Non-linear iterations are employed to minimize the partitioning errors between the two differential equations.

The proposed procedure for the coupled Navier-Stokes and Allen-Cahn solver is summarized in Algorithm 2. Consider the velocity $\mathbf{u}^{f,n}$, pressure p^n and the order parameter ϕ^n given at

Algorithm 2 Nonlinear adaptive variational partitioned (NAVP) procedure for implicit Navier-Stokes and Allen-Cahn solvers

```

1: Given  $\mathbf{u}^{f,0}$ ,  $p^0$ ,  $\phi^0$  on  $\mathcal{T}^0$ 
2: Loop over time steps,  $n = 0, 1, \dots$ 
3: Start from known variables  $\mathbf{u}^{f,n}$ ,  $p^n$ ,  $\phi^n$  on  $\mathcal{T}^n$ 
4: Predict the solution on  $\mathcal{T}_{(0)}^{n+1} = \mathcal{T}^n$ :
5:    $\mathbf{u}_{(0)}^{f,n+1} = \mathbf{u}^{f,n}$ 
6:    $p_{(0)}^{n+1} = p^n$ 
7:    $\phi_{(0)}^{n+1} = \phi^n$ 
8: Loop over the nonlinear iterations,  $k = 0, 1, \dots, nIterMax$  until convergence
9:   Solve Navier-Stokes equations for updated values of  $\mathbf{u}_{(k)}^{f,n+1}$  and  $p_{(k)}^{n+1}$  on  $\mathcal{T}_{(k)}^{n+1}$  and
   evaluate  $e_{NS}$ 
10:  Solve Allen-Cahn equation for updated values of  $\phi_{(k)}^{n+1}$  on  $\mathcal{T}_{(k)}^{n+1}$  and evaluate  $e_{AC}$ 
11:  Evaluate the error estimator  $\eta$ 
12:  if ( $e_{NS} \leq tol_{NS}$ ) and ( $e_{AC} \leq tol_{AC}$ ) and ( $\eta \leq tol_R$ ) then
13:    refine = 0; coarsen = 1; break = 1
14:  elseif ( $e_{NS} > tol_{NS}$ ) and ( $e_{AC} > tol_{AC}$ ) and ( $\eta \leq tol_R$ ) then
15:    refine = 0; coarsen = 0
16:  elseif ( $\eta > tol_R$ ) then
17:    refine = 1; coarsen = 0
18:  elseif ( $k = nIterMax$ ) then
19:    refine = 0; coarsen = 1; break = 1
20:  endif
21:  if ( $n_{el} > nElemMax$ ) and (  $k = 1$  or  $k = nIterMax$  ) then
22:    refine = 0; coarsen = 1
23:  elseif ( $n_{el} > nElemMax$ ) and ( $k \neq 1$ ) and ( $break \neq 1$ ) then
24:    refine = 0; coarsen = 0
25:  endif
26:  if (coarsen = 1) then
27:    coarsen the mesh
28:  endif
29:  if (refine = 1) then
30:    refine the mesh
31:  endif
32:  Satisfy boundary conditions on the new mesh  $\mathcal{T}_{(k+1)}^{n+1}$ 
33:  if (break = 1) then
34:    break the nonlinear iteration loop
35:  endif
36: Copy the solution of current time step to previous time step on  $\mathcal{T}_{(k+1)}^{n+1}$ 

```

the discretized points at time t^n on a grid \mathcal{T}^n (line 3). The variables are predicted for the next time step before the start of the nonlinear iterations to $\mathbf{u}_{(0)}^{f,n+1}$, $p_{(0)}^{n+1}$ and $\phi_{(0)}^{n+1}$ (lines 4-7). In the first step of a nonlinear iteration k , the Navier-Stokes equations are solved using Eq. (5.33) and the velocity and pressure values at $n + 1$ are updated. The error corresponding

to the Navier-Stokes equations e_{NS} is also evaluated at this step. The updated velocity is then transferred to the Allen-Cahn solver which solves Eq. (5.34) and updates the order parameter $\phi_{(k)}^{n+1}$. e_{AC} is also evaluated for the error in solving the Allen-Cahn equation. Then, the error estimator η is computed using Eqs. (6.8) and (6.9). At this step, the convergence criterion is checked based on which it is decided if the mesh is to be coarsened/refined (lines 12-20). The tolerances for the convergence criteria are set by the user, whereby tol_{NS} , tol_{AC} and tol_R denote the tolerances for the Navier-Stokes, the Allen-Cahn equations, and the error estimator, respectively. The convergence criteria are constructed such that the mesh will be coarsened only at the last nonlinear iteration and it will be refined until the criteria for tol_R is satisfied. In the procedure, while $nIterMax$ denotes the maximum number of nonlinear iterations specified by the user, $nElemMax$ represents the number of maximum elements that can exist on the domain. We coarsen the grid if the number of elements n_{el} exceeds this limit (lines 21-25). This ensures that there is no refining/coarsening in the intermediate nonlinear iterations to capture the nonlinearities of the underlying equations. Based on the outcome of the convergence criteria, the mesh is refined/coarsened (lines 26-31) after which the boundary conditions on the new mesh $\mathcal{T}_{(k+1)}^{n+1}$ are satisfied. In the end of the nonlinear iterations, the solver updates the variables and proceeds to the next time step.

While satisfying the convergence criteria, the primary objective is to reduce the residual errors due to the adaptive algorithm or the error indicator η , for which the mesh will be refined. Once the refinement criterion is satisfied, the solver will tend to reduce the individual errors corresponding to the Navier-Stokes and the Allen-Cahn equations by iterating through the nonlinear iterations while maintaining the same mesh resolution. This captures the nonlinearities and maintains the convergence properties of the underlying equations. Based on the proposed algorithmic procedure, we next present the numerical tests of increasing complexity to assess the effectiveness of the partitioned adaptive scheme.

6.2 Convergence and performance study

In this section, we perform numerical tests to assess the adaptive procedure via standalone tests for the Allen-Cahn equation and liquid sloshing in a tank for the coupled Navier-Stokes and Allen-Cahn system.

6.2.1 Spinodal decomposition in a complex curved geometry

In this section, we demonstrate our adaptive phase-field finite element formulation for the spinodal decomposition in a complicated curved domain. The motivation of this test is to demonstrate the generality and the energy stability of our method based on the unstructured grid and the body-fitted formulation for complex geometric boundaries for two-phase transport found in numerous micro-fluidics and oil/gas applications.

We take the complex geometry as a spiral curve made from semicircles of increasing radius, which is given as:

$$c(r, \theta) = (r\cos(\theta), r\sin(\theta)), \quad (6.11)$$

where $\theta \in [0, 5\pi]$ and r is the radius of the semicircle which varies as $0.5 + (n - 1)0.5$ with $n = 1, 2, 3, 4, 5$ corresponding to the intervals $[0, \pi], [\pi, 2\pi], [2\pi, 3\pi], [3\pi, 4\pi]$ and $[4\pi, 5\pi]$ respectively with center of the semicircle alternatively varying between $(0, 0)$ and $(0.5, 0)$ with the intervals. The width of the curve is 0.5. The computational domain with an unstructured triangular mesh discretization is shown in Fig. 6.2. The initial condition of the order parameter is considered

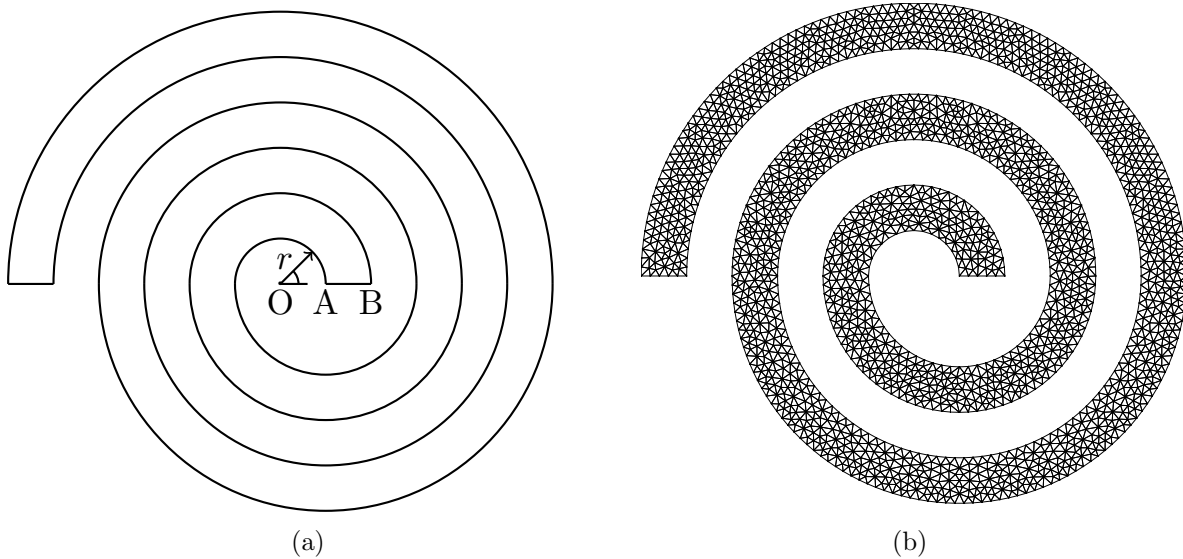


Figure 6.2: Spinodal decomposition in a spiral domain: (a) schematic diagram showing the computational domain and (b) initial triangular mesh at $t = 0$. In (a), the coordinates of O, A and B are $(0, 0)$, $(0.5, 0)$ and $(1, 0)$ respectively and r denotes the radius of the spiral curve varying with angle θ as given in Eq. (6.11).

as

$$\phi(x, y, 0) = 0.1\text{rand}, \quad (6.12)$$

where rand are the random values from the uniform distribution in the interval $[-1, 1]$. The interface thickness parameter is $\varepsilon = 0.01$. With $\Delta t = 0.01$, the simulation is run for 10000 time steps. The user-defined convergence tolerances are selected as $tol_{NS} = tol_{AC} = 5 \times 10^{-4}$ and $tol_R = 10^{-2}$. The refining and coarsening parameters are $\theta = 0.5$ and $\theta_c = 0.05$, respectively. The random initial condition falls under the chemical spinodal region of the double-well potential curve which has a higher free energy compared to the equilibrium phases. This leads to a phase separation due to the spinodal decomposition which tends to minimize the free energy functional. We track the variation in the discrete free energy given by Eq. (F.9) through the spinodal decomposition process in Fig. 6.3. The energy functional at time t^n is given by

$$E(\phi^n) = \int_{\Omega^f(t)} \left(\frac{1}{2} (\varepsilon^2 + \chi \frac{|\mathcal{R}(\phi_h)|}{|\nabla \phi_h|} k_c^{\text{add}}) |\nabla \phi^n|^2 + F(\phi^n) \right) d\Omega. \quad (6.13)$$

The trend clearly depicts the decreasing energy with a large gradient flow at the initial phase

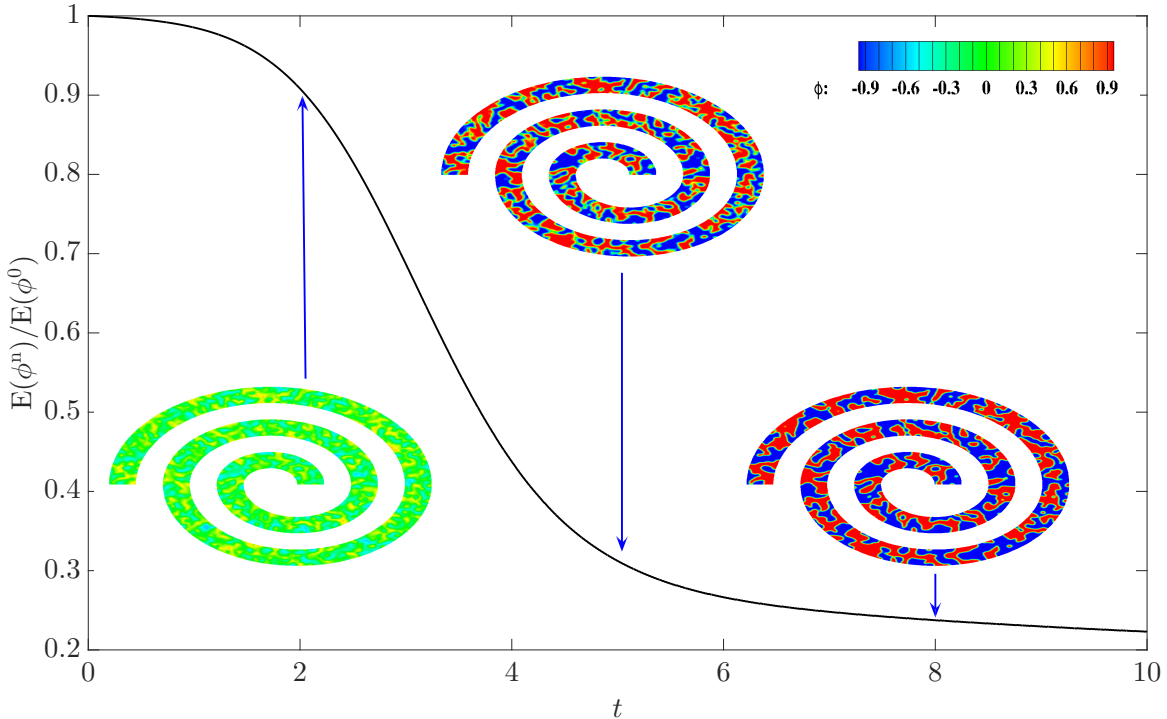


Figure 6.3: Decay of the total discrete energy with time for the spinodal decomposition in a spiral domain. The contours of the order parameter are shown at different time instances $t \in [2, 5, 8]$. The total energy decreases with time making the scheme energy stable.

separation region while the rate of decrease becomes slower as the coarsening of the phases begin. The adaptive mesh at $t = 100$ of the computational domain with the contours of the order parameter are depicted in Fig. 6.4.

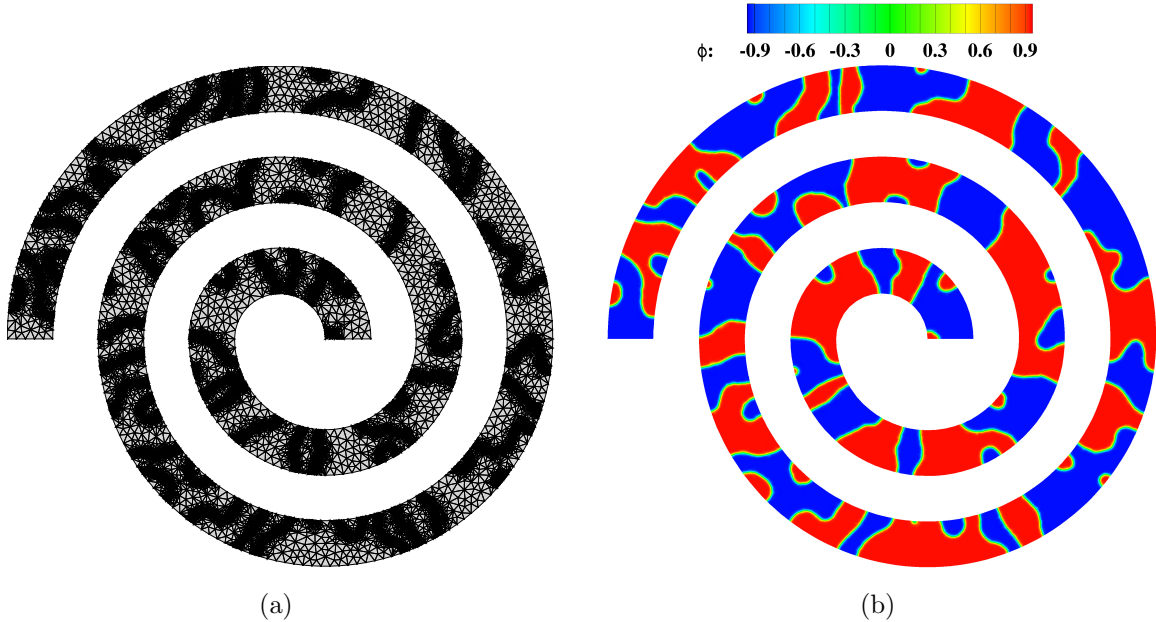


Figure 6.4: Solution of the spinodal decomposition in a spiral domain at $t = 100$: (a) the adapted mesh and (b) the contours of the order parameter ϕ .

6.2.2 Volume conserved motion by curvature

We next illustrate the effectiveness of the standalone Allen-Cahn solver for the conservation of volume (or mass) of the order parameter ϕ . The computational domain with the initial condition are the same as that in Section 5.4.1. The interface thickness parameter is chosen as $\varepsilon = 0.005$ with the error tolerances as $tol_{NS} = tol_{AC} = 5 \times 10^{-4}$ and $tol_R = 3 \times 10^{-4}$. The refining and coarsening parameters are $\theta = 0.5$ and $\theta_c = 0.05$ respectively. The mesh is refined iteratively along the initial profile of the order parameter based on the gradients of the initial condition before the start of the time loop. The time step size in the present simulation is 0.4 with the final time $t = 400$. The evolution of the adaptive mesh of the two circles is shown in Fig. 6.5(a-b). The variation of the radii is compared with the literature in Fig. 6.5(c). The results are in very close agreement with the reference. The variation of the total mass of the order parameter as a function of time is also shown in Fig. 6.5(d). The mass of the order

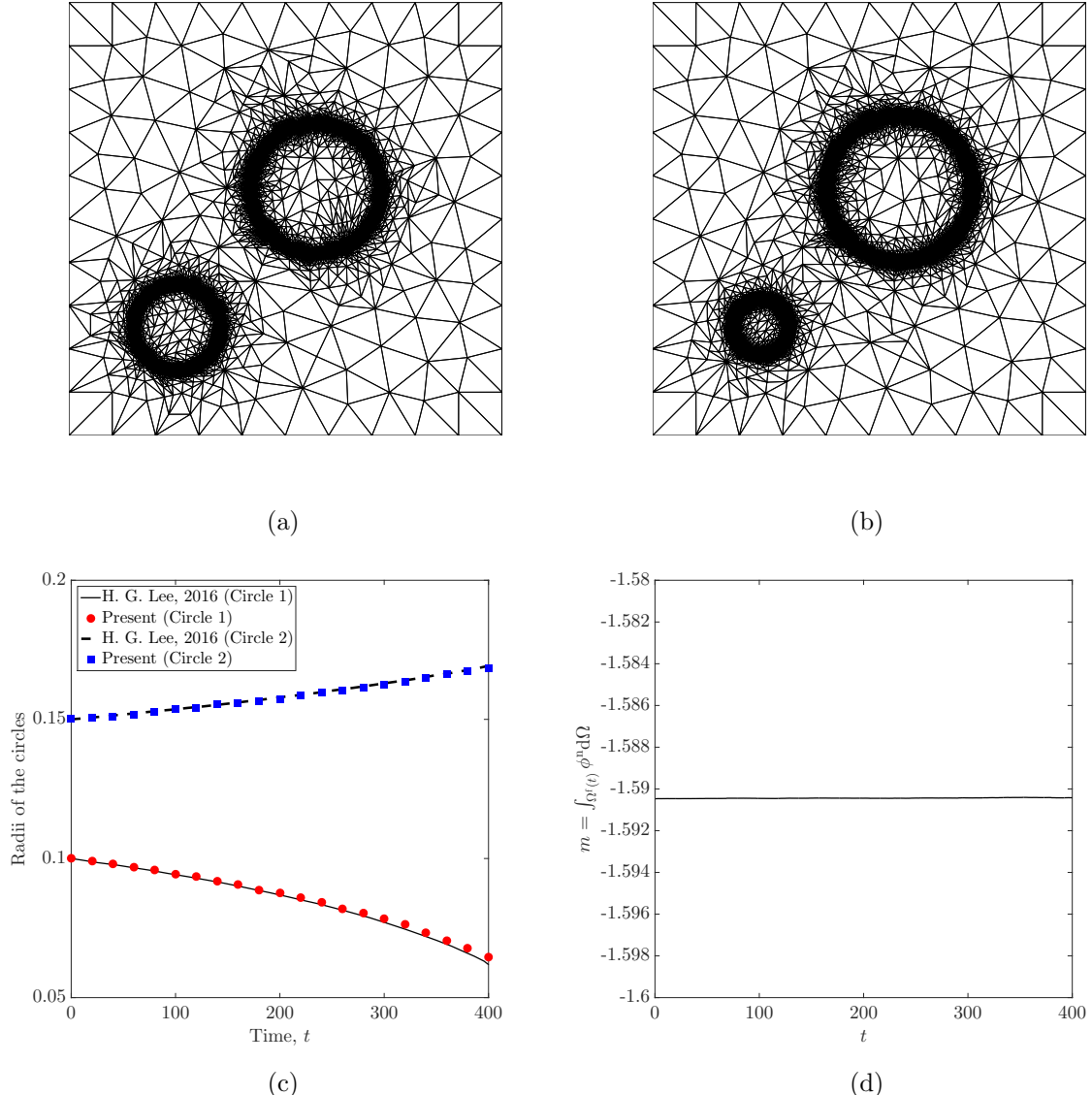


Figure 6.5: Assessment of volume conservation during the interface evolution according to mean curvature flow: the adaptive mesh at (a) $t = 0$, (b) $t = 400$, (c) validation of the evolution of the radii of the two circles with the literature [2], and (d) the variation of the total mass of the order parameter ϕ with time.

parameter at a particular time step t^n is defined as:

$$m = \int_{\Omega^f(t)} \phi^n d\Omega. \quad (6.14)$$

Quantitatively, the fraction of the change in mass over the total time and the initial mass is evaluated as 3.2066×10^{-5} ($\approx 0.003\%$).

6.2.3 Liquid sloshing in a tank

In this section, we study the results of the numerical tests conducted for a liquid sloshing tank problem. A rectangular domain $\Omega^f \in [0, 1] \times [0, 1.5]$ is discretized with three-node triangles of varying sizes for the simulation. The physical parameters such as density, viscosity, and acceleration due to gravity with the computational domain including the initial condition are the same as that in Section 5.4.3.

Each test case is set up on an initial grid of element size Δx . The mesh is refined iteratively along the initial profile of the order parameter based on the gradients of the initial condition before the start of the time loop. To have a detailed analysis of the problem, we perform a series of experiments to assess some of the measured quantities such as mass conservation, the number of degrees of freedom, the computational cost (elapsed time), the error in solving the Allen-Cahn equation (e_{AC}) and the residual error for the adaptive procedure (η). The mass of the order parameter is computed using Eq. (6.14). The number of degrees of freedom at a time t^n is the total number of element nodes of the mesh in the last nonlinear iteration of the time step. The cumulative elapsed time is the cumulative time taken by the solver to complete a time step on 1 CPU. The simulation is run for 5 cycles of the oscillation of the interface inside the tank with a time period of $T_{oscill} = 3.6s$. All the tests are simulated in 4 core Intel Xeon 3.50GHz \times 1 CPU with 16GB memory. Furthermore, no bounds on the maximum number of elements are considered for the sloshing tank problem, i.e., lines 21-25 of the Algorithm 2 are neglected. The refinement and coarsening parameters are selected as $\theta = 0.5$ and $\theta_c = 0.05$ respectively for all the cases.

6.2.3.1 Background mesh convergence

Since the error estimates for the adaptive procedure are evaluated only for the Allen-Cahn equation, we need to have a sufficiently refined background mesh to capture the flow physics of the Navier-Stokes equations such as the high gradients in the velocity contours near the interface region. Therefore, a systematic mesh convergence study for the background mesh is performed for $\varepsilon = 0.01$ by considering the initial background mesh of different size $\Delta x \in [0.02, 0.16]$. The interface elevation at the left boundary throughout the simulation is recorded in Fig. 6.6. The

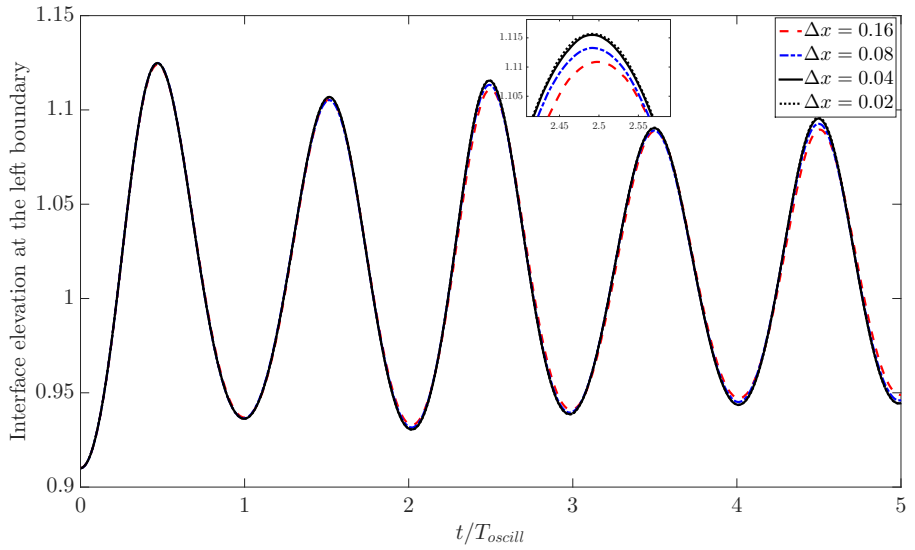


Figure 6.6: Background mesh convergence for the sloshing tank problem: evolution of the interface at the left boundary with $\varepsilon = 0.01$ and different background mesh sizes.

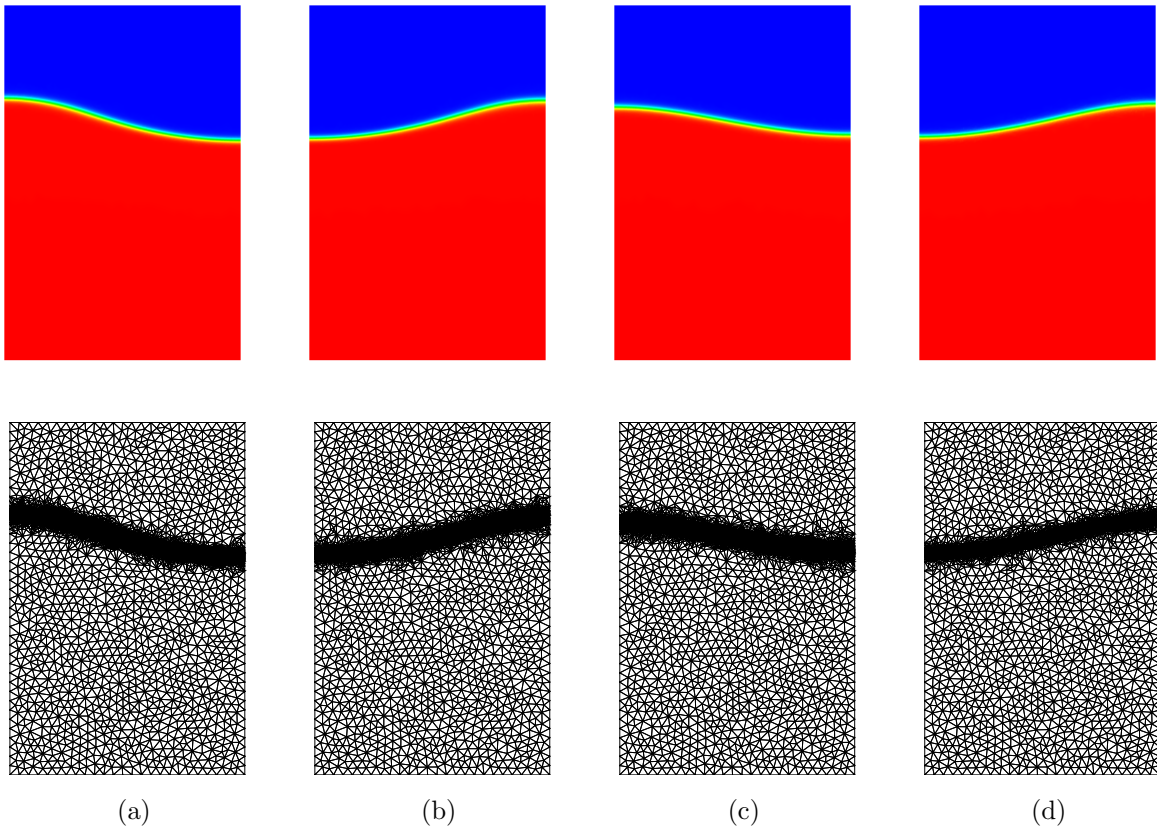


Figure 6.7: Contours of the order parameter ϕ (top) and the adaptive mesh (bottom) for the sloshing tank problem with background mesh $\Delta x = 0.04$ and $\varepsilon = 0.01$ at t/T_{oscill} : (a) 0.55, (b) 1.94, (c) 3.6 and (d) 5.

error is quantified as:

$$e_{bg} = \frac{\|\Phi - \Phi_{ref}\|_2}{\|\Phi_{ref}\|_2}, \quad (6.15)$$

where Φ is the temporal solution of the interface elevation at the left boundary for different background meshes and Φ_{ref} is the finest mesh solution of the interface elevation ($\Delta x = 0.02$). It is observed that the percentage error in e_{bg} for $\Delta x = 0.16, 0.08$ and 0.04 is 0.32% , 0.12% and 0.023% respectively. Similar error variation is obtained for $\varepsilon = 0.005$ considering $\Delta x \in [0.01, 0.08]$ with error percentage as 0.14% , 0.17% and 0.007% for $\Delta x = 0.08, 0.04$ and 0.02 respectively with $\Delta x = 0.01$ as the reference mesh. We choose $\Delta x = 0.04$ as the background mesh for further studies. The evolution of the adaptive grid with the contours of the order parameter ϕ at four instances corresponding to the extreme amplitudes of the sloshing is shown in Fig. 6.7.

6.2.3.2 Assessment of the nonlinear adaptive variational partitioned (NAVP) procedure

In this section, we examine the effectiveness of the NAVP procedure on the mass conservation of ϕ , the variation of residual error η and the computational cost (degrees of freedom and elapsed time). Figure 6.8 shows the variation of the measured quantities with time on an adaptive grid employing the NAVP procedure ($\Delta x = 0.04$) and a non-adaptive grid with $\Delta x = 0.01$. The interfacial thickness parameter ε is selected as 0.01 . The tolerances are set to $tol_{NS} = tol_{AC} = 5 \times 10^{-4}$ and $tol_R = 10^{-3}$. It is observed that error in mass conservation is reduced for the adaptive grid compared to the non-adaptive Eulerian fixed grid by around 3 times (Fig. 6.8(a)).

The error in the mass conservation is evaluated as

$$e_{mass} = \frac{m_{t=0} - m}{m_{t=0}}, \quad (6.16)$$

where m is defined by Eq. (6.14) and $m_{t=0}$ is the mass at $t = 0$. This is the consequence of increased density of elements near the interfacial region which helps to capture the interface more accurately. The increase in the density of elements near the interfacial region leads to reduced residual error η compared to the non-adaptive method (Fig. 6.8(b)). The computational cost has been quantified as the variation of the number of degrees of freedom with non-dimensional time and the cumulative elapsed time of the simulation in Fig. 6.8(c-d). The adaptive procedure

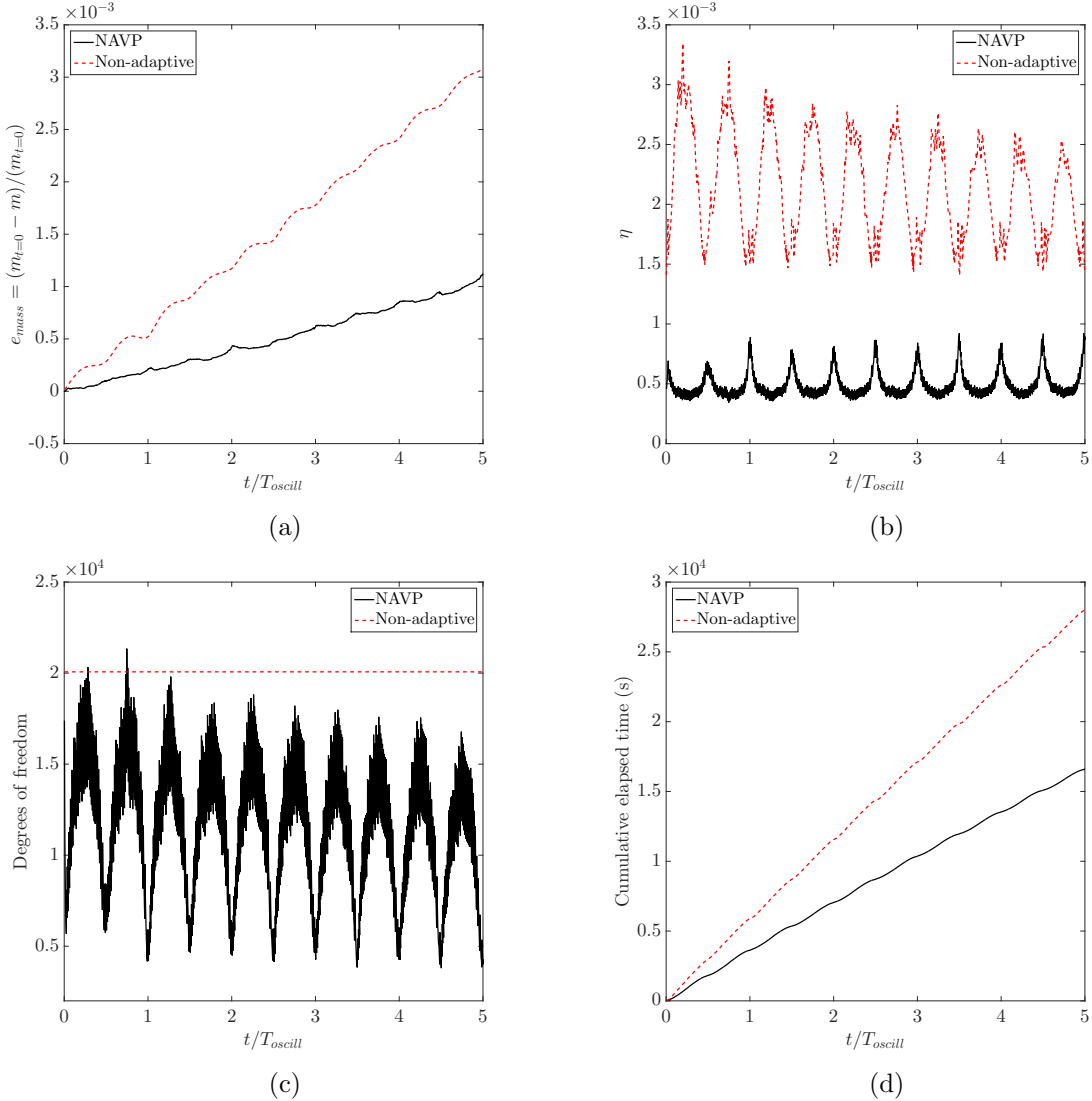


Figure 6.8: Variation of the measured quantities with time in the sloshing tank problem: (a) the error in mass conservation evaluated using Eq. (6.16), (b) the residual error η , (c) the number of degrees of freedom or unknowns, and (d) the cumulative elapsed time.

reduces the number of degrees of freedom, which leads to a lesser elapsed time for the simulation.

6.2.3.3 Advantage of the PPV technique

To observe the effect of the addition of the positivity preserving nonlinear terms in Eq. (5.25), we compare the extreme values of the order parameter ϕ at $t/T_{\text{oscill}} = 5$ for the adaptive method with and without the PPV terms. The setup is the same as that of Section 6.2.3.2. The bounds of the solution of ϕ are summarized in Table 6.1. It can be observed that the

Table 6.1: Bounds of the solution of interface evolution over the whole domain for different techniques.

Method	$\min(\phi)$	$\max(\phi)$
Adaptive (no PPV)	-1.00044	1.00027
NAVP	-1.0	1.0

solution remains bounded when the nonlinear positivity preserving terms are incorporated in the formulation. However, the difference is very minor in the sloshing tank problem, it may be higher for different problems due to the restriction criterion for the number of elements in the algorithm. These nonlinear PPV terms provide a necessary stabilization in highly convection- and reaction-dominated flows.

6.2.3.4 Relationship between tol_R and ε

In this section, we briefly discuss the relationship between the tolerance set for the residual error η (tol_R) and the interfacial thickness parameter ε . We measure the total mass loss, the average number of degrees of freedom and the average error in solving the Allen-Cahn equation (\bar{e}_{AC}). The total mass loss is evaluated using Eq. (6.16) with m taking the mass at final time $t/T_{oscill} = 5$. The variation of these measured quantities with tol_R is plotted in Fig. 6.9. Some

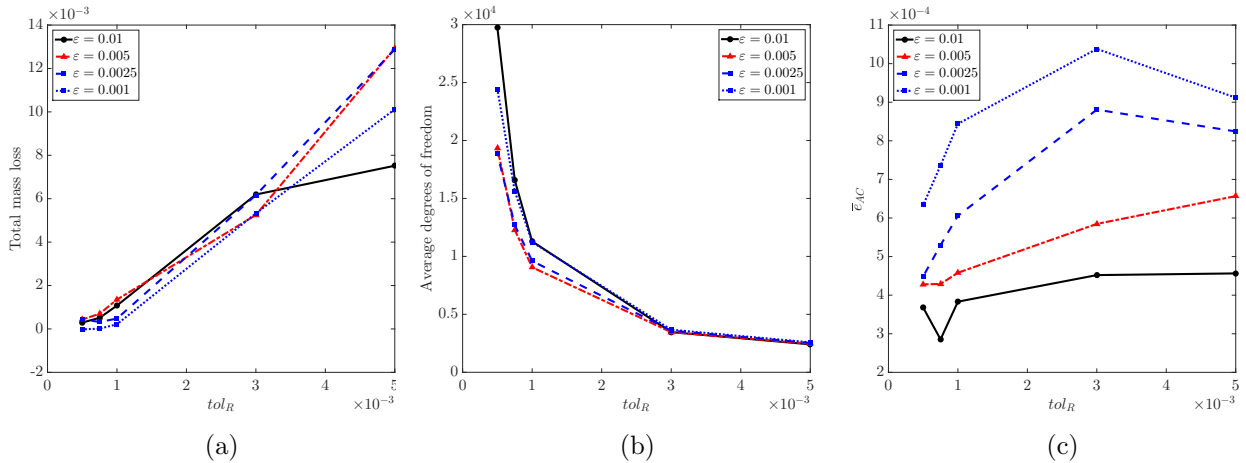


Figure 6.9: Variation of the measured quantities with tol_R in the sloshing tank problem: (a) the total mass loss, (b) the average number of degrees of freedom and (c) the average error in solving the Allen-Cahn equation (\bar{e}_{AC}).

of the observations are as follows. First, the total mass loss is higher for low ε when large tol_R is chosen as the convergence criteria for η , while it reduces as the tolerance is tightened.

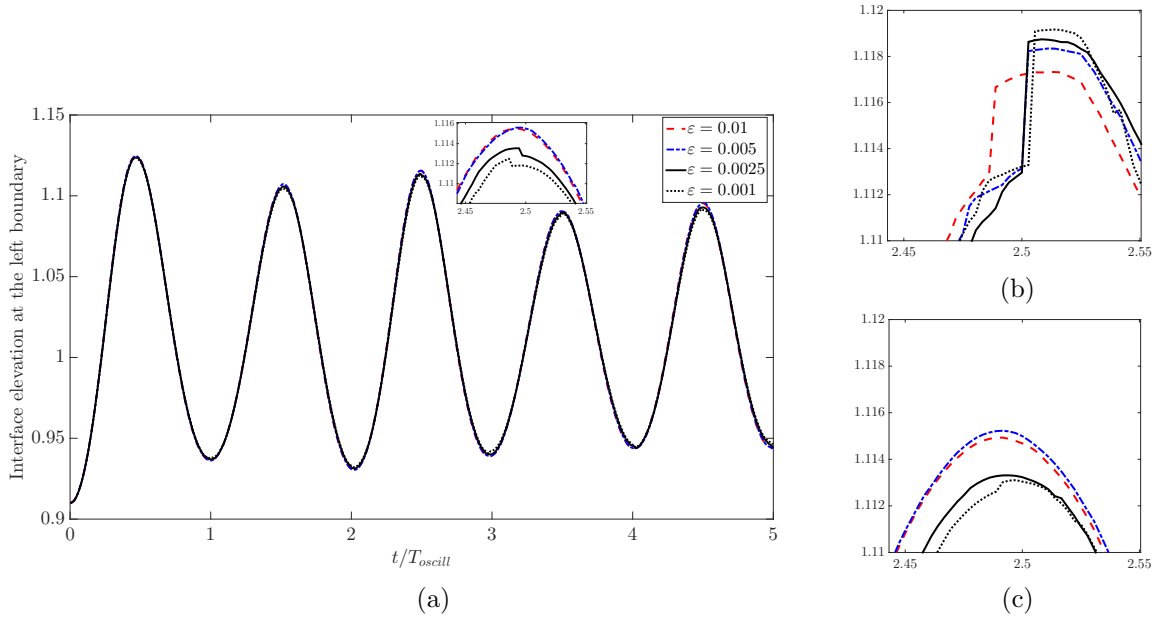


Figure 6.10: Variation of the interface at the left boundary in the sloshing tank problem: (a) $tol_R = 1 \times 10^{-3}$, (b) $tol_R = 5 \times 10^{-3}$ and (c) $tol_R = 5 \times 10^{-4}$.

Second, the average number of unknowns to be solved decreases with ε as tol_R becomes smaller. Third, the average error in solving the Allen-Cahn equation is much higher for lower ε at high tol_R . These observations seem to suggest that selecting a smaller ε value for large tol_R does not improve the solution. This is evident from the time history of the surface elevation at the left boundary for varying ε and tol_R in Fig. 6.10. Figure 6.10(a) shows the variation of the free-surface elevation for $tol_R = 1 \times 10^{-3}$, while Figs. 6.10(b) and (c) depict the close-up view of the same plot for $tol_R = 5 \times 10^{-3}$ and $tol_R = 5 \times 10^{-4}$ respectively. It can be seen that for higher tol_R , all values of ε have a kink in the plot. This kink is due to excessive coarsening near the interface area because of high tol_R . Consequently, the error \bar{e}_{AC} is higher because the given tol_R is not enough to capture the crucial interface physics. As the tolerance tol_R is tightened, lower ε values tend to approach the converged solution. Therefore, the selection of ε is directly dependent on the convergence criteria for tol_R . In order to exploit the benefits of lower computational cost, less error and good mass conservation properties, the tolerance tol_R has to be reduced for small ε values. In the next section, we present the results corresponding to $\varepsilon = 0.005$ and 0.0025 with $tol_R = 5 \times 10^{-4}$.

6.2.3.5 Role of the interfacial thickness parameter ε

The effect of reducing the interfacial thickness parameter ε is studied by conducting the numerical tests with $tol_{NS} = tol_{AC} = tol_R = 5 \times 10^{-4}$ for all the cases. The variation of mass, degrees of freedom and the residual error with t/T_{oscill} is plotted in Fig. 6.11. It is observed that

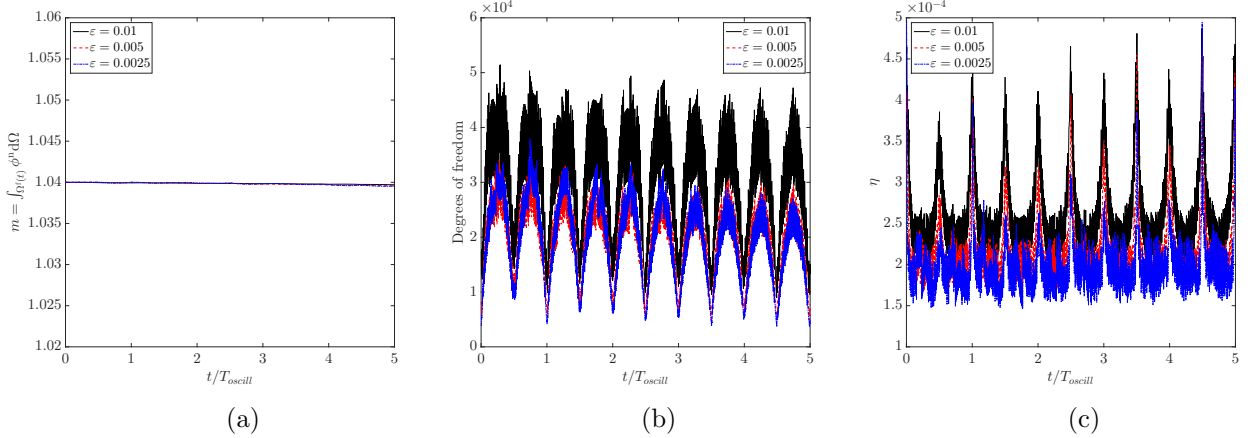


Figure 6.11: Variation of the measured quantities with time in the sloshing tank problem for varying interface thickness parameter ε : (a) mass evaluated using Eq. (6.14), (b) degrees of freedom or unknowns, and (c) residual error indicator η .

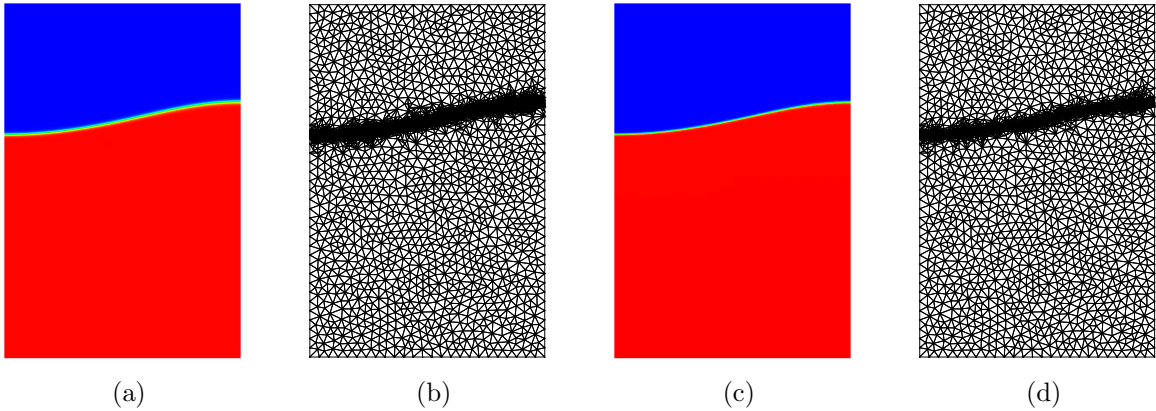


Figure 6.12: Contours of the order parameter ϕ (a and c) and the adaptive mesh (b and d) for the sloshing tank problem at $t/T_{oscill} = 5$ for: $\varepsilon = 0.005$ (a and b), and $\varepsilon = 0.0025$ (c and d).

reduction in the ε leads to lesser degrees of freedom for the same tol_R . Therefore, the benefit of the adaptivity is noticeable while using lower interface thickness parameter since the degrees of freedom would increase with lesser ε for a fixed Eulerian grid. Moreover, the residual error η also gets reduced with a decrease in ε . The contours of the order parameter and the respective mesh for $\varepsilon = 0.005$ and 0.0025 at $t/T_{oscill} = 5$ are shown in Fig. 6.12. This completes the

assessment of the proposed NAVP procedure. In the next section, we demonstrate the NAVP procedure for a classical dam-break problem.

6.3 Application to dam-break problem

We consider the two-dimensional dam-break problem to demonstrate the adaptive properties of the proposed NAVP procedure. In this widely studied problem of dam-break flow, there is a sudden collapse of a rectangular column of fluid onto a horizontal surface. This problem involves a large unsteady deformation of air-water interface and characterizes the dynamics associated with gravity and viscosity effects. The computational domain with the boundary and initial

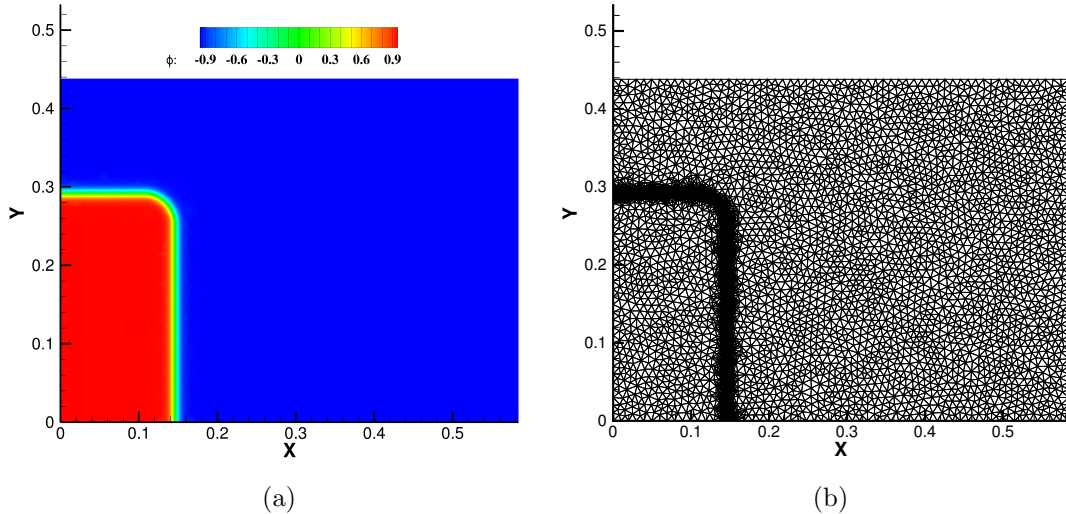


Figure 6.13: Two-dimensional dam-break problem: (a) the contour plot of the order parameter ϕ at $t = 0$, and (b) the initial refined mesh at $t = 0$.

conditions are the same as in Section 5.4.4. The contour of the order parameter with the adaptive initial mesh are shown in Fig. 6.13. A non-uniform triangular unstructured mesh with background mesh size $\Delta x = 0.01$ is employed for the demonstration. The interfacial thickness parameter ε is selected as 0.005. The tolerances are set as $tol_{NS} = tol_{AC} = 1 \times 10^{-4}$ and $tol_R = 5 \times 10^{-4}$. A restriction of the maximum number of elements is kept in the convergence criteria as 25000. The interface location at the left and bottom boundaries are tracked with time for the validation with experiments [178, 179] and the interface-tracking simulation of [180]. In Fig. 6.14, the temporal variation of the interface location based on the non-dimensional water column width/height is compared with the results from the literature. A good agreement is

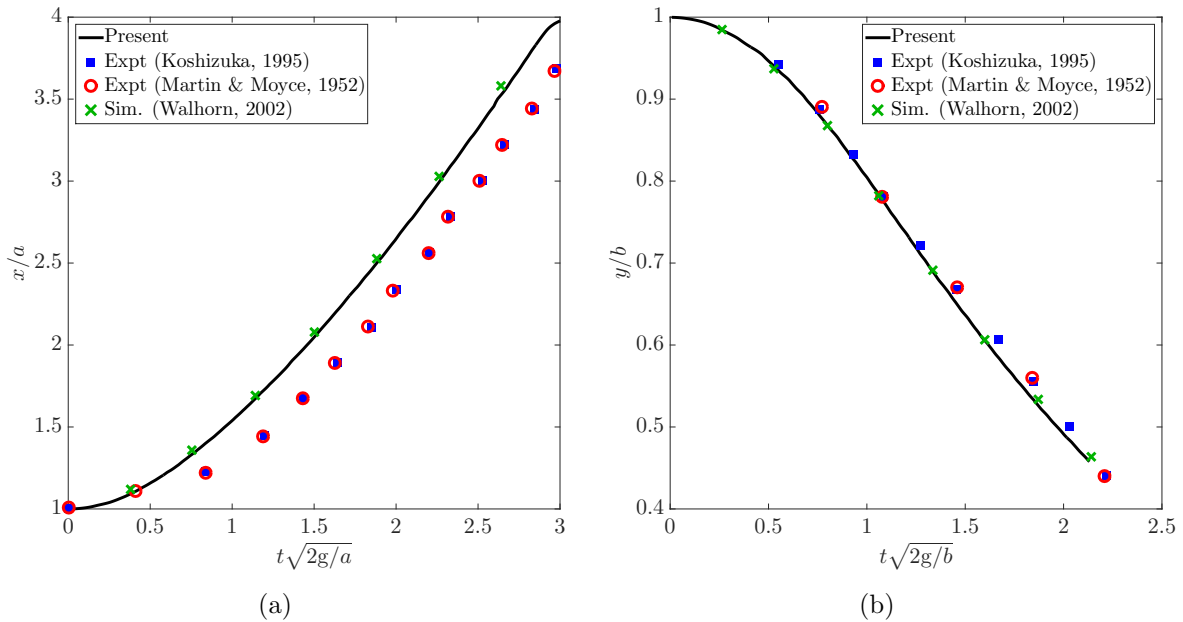


Figure 6.14: Two-dimensional dam-break problem: temporal evolution of non-dimensional water column (a) width and (b) height. The results from the present method are in good agreement with the literature.

found for our NAVP procedure based on the Navier-Stokes and the Allen-Cahn equations. The contours of the order parameter ϕ and the evolving mesh are depicted in Fig. 6.15 at $t\sqrt{(2g/a)} \in [2.32, 11.60]$. In terms of the computational cost, the average number of degrees of freedom for the adaptive simulation is 15,000 which yields an average η of 3.36×10^{-3} compared to the non-adaptive grid with degrees of freedom 21,355 with an average η of 7.57×10^{-3} . This shows the decrease in the residual error indicators in the adaptive grid with lesser degrees of freedom, thus reducing the computational cost.

6.4 Summary

We explored the improvement in the solution of the two-phase flows resulting from the mesh adaptivity in this chapter. Some of the benefits of employing the presented adaptive variational procedure are:

- Improvement in mass conservation by three times compared to non-adaptive meshes,
 - Reduction in the computational time by 40%,

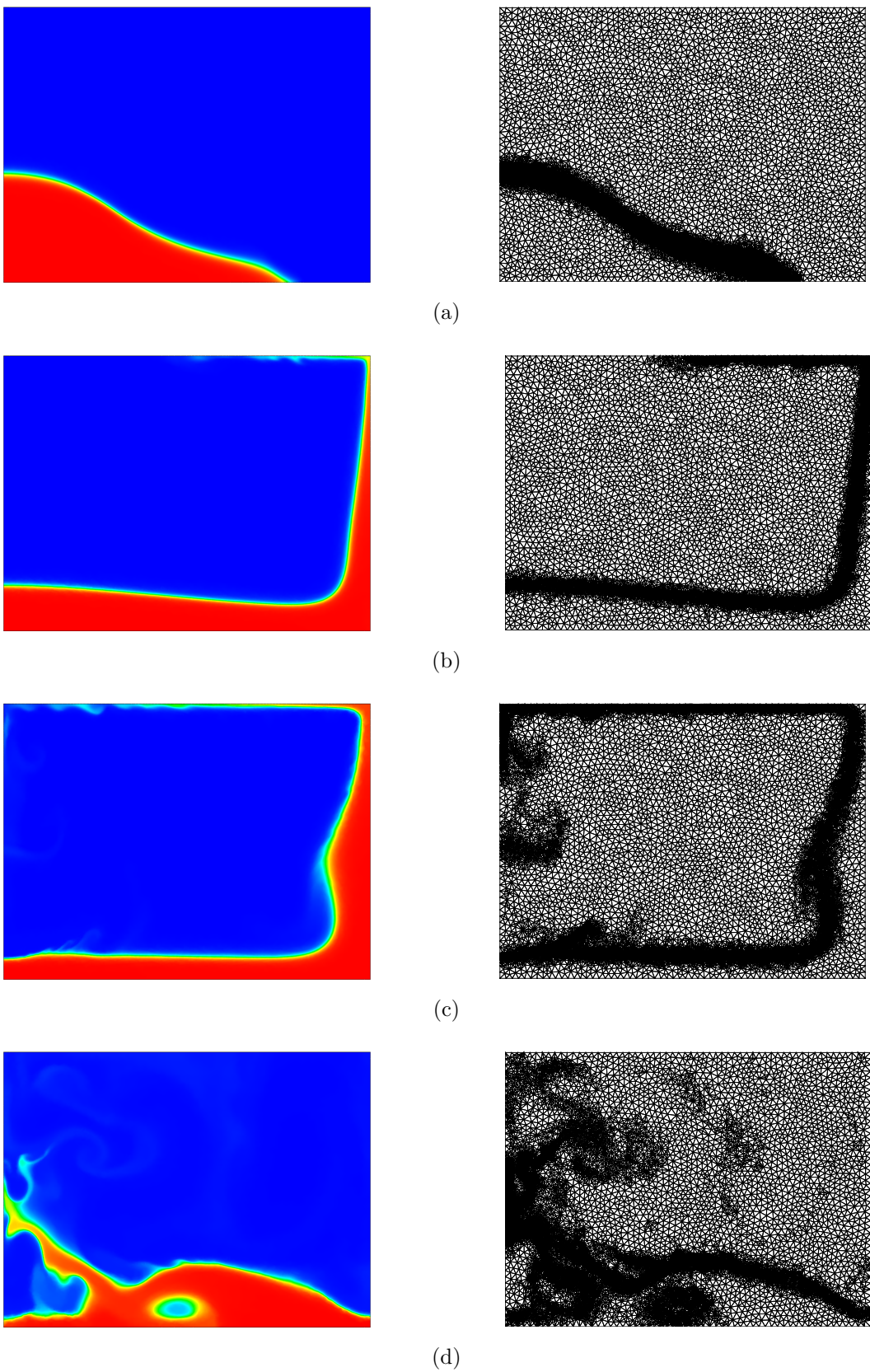


Figure 6.15: Contours of the order parameter ϕ (left) and the adaptive mesh (right) for the dam-break problem at $t\sqrt{(2g/a)}$: (a) 2.32, (b) 4.64, (c) 9.96 and (d) 11.60.

Chapter 6. Mesh Adaptive Procedure for Phase-Field Formulation

- Reduction in the residual error of the Allen-Cahn equation, and
- Simplified data structures to handle the adaptive algorithm.

The unique feature of the presented procedure is its generality in the sense that it can be extended to three-dimensions, whereby the variational formulation poses no restriction with respect to the extension. This was demonstrated by three-dimensional simulations in Chapter 5. However, some effort has to be put in to extend the adaptive algorithm of refining through bisection and coarsening to three-dimensions. This can be considered as an extension of the present study in the future. Since we have established the framework to model the two-phases, we next discuss the coupling of the structural equations with the two-phase fluid system.

Chapter 7

Two-Phase Fluid-Structure Interaction*

With the variational formulation established for the two-phase flow and the structural equations, the coupling between the Navier-Stokes (flow) and the Allen-Cahn (phase indicator) equations is extended to include the structural deformation for the two-phase fluid-structure interaction problems in this chapter. We first discuss the partitioned coupling between the three blocks, viz., the fluid, the phase indicator, and the structure. This is followed by standard benchmarks of heave and rotational motion of a rigid circular cylinder and a rectangular barge respectively. Finally, we demonstrate the current two-phase FSI solver for vortex-induced vibration of an offshore riser with an internal two-phase flow.

7.1 The nonlinear partitioned iterative FSI coupling

In this section, we discuss the partitioned iterative coupling for the two-phase FSI system. We begin with the coupled linearized matrix form and discuss the quasi-Newton updates that are carried out to correct the fluid forces on the structure. Then, the algorithm for the coupling is presented for the block-type partitioned system.

*Parts of this chapter have been published in “V. Joshi and R.K. Jaiman, A hybrid variational Allen-Cahn/ALE scheme for the coupled analysis of two-phase fluid-structure interaction, *International Journal for Numerical Methods in Engineering*, (Under review) (2018).”

7.1.1 Coupled linearized matrix form

We present the coupled linearized matrix form of the variationally discretized two-phase fluid-structure equations for non-overlapping decomposition of the fluid and structure domains. Corresponding to the domain decomposition, the set of degrees of freedom (DOFs) is decomposed into the interior DOFs for the two-phase fluid-structure system and the fluid-structure interface DOFs for the Dirichlet-to-Neumann (DtN) mapping. Using the Newton-Raphson type of linearization, the coupled two-phase fluid-structure system with the DtN mapping along the fluid-structure interface can be expressed as

$$\begin{bmatrix} \mathbf{A}^{ss} & \mathbf{0} & \mathbf{0} & \mathbf{A}^{Is} \\ \mathbf{A}^{sI} & \mathbf{I} & \mathbf{0} & \mathbf{0} \\ \mathbf{0} & \mathbf{A}^{If} & \mathbf{A}^{ff} & \mathbf{0} \\ \mathbf{0} & \mathbf{0} & \mathbf{A}^{fl} & \mathbf{I} \end{bmatrix} \begin{Bmatrix} \Delta\boldsymbol{\eta}^s \\ \Delta\boldsymbol{\eta}^I \\ \Delta\mathbf{q}^f \\ \Delta\mathbf{f}^I \end{Bmatrix} = \begin{Bmatrix} \mathcal{R}^s \\ \mathcal{R}_D^I \\ \mathcal{R}^f \\ \mathcal{R}_N^I \end{Bmatrix}, \quad (7.1)$$

where $\Delta\boldsymbol{\eta}^s$ denotes the increment in the structural displacement, $\Delta\boldsymbol{\eta}^I$ and $\Delta\mathbf{f}^I$ represent the increments in the displacement and the forces along the fluid-structure interface. The increment in the unknowns associated with the two-phase fluid domain is denoted by $\Delta\mathbf{q}^f = (\Delta\mathbf{u}^f, \Delta p, \Delta\phi)$. On the right hand side, \mathcal{R}^s and \mathcal{R}^f represent the weighted residuals of the structural and stabilized two-phase flow equations respectively, whereas \mathcal{R}_D^I and \mathcal{R}_N^I denote the residuals corresponding to the imbalances during the enforcement of the kinematic (Dirichlet) condition (Eq. (4.60)) and the dynamic (Neumann) condition (Eq. (4.61)) at the fluid-structure interface respectively.

The block matrices on the left-hand side can be described as follows. \mathbf{A}^{ss} represents the matrix consisting of the mass, damping and stiffness matrices of the structural equation for the non-interface structural DOFs and \mathbf{A}^{Is} is the transformation to obtain the structural force vector from the fluid-structure interface. \mathbf{A}^{sI} maps the structural displacements to the fluid-structure interface which satisfies the Dirichlet kinematic condition with \mathbf{I} being an identity matrix. \mathbf{A}^{fl} transfers the fluid forces to the fluid-structure interface to satisfy the Neumann dynamic equilibrium condition. \mathbf{A}^{If} associates the ALE mapping of the fluid spatial points and \mathbf{A}^{ff} consists of the stabilized terms for the Navier-Stokes and the Allen-Cahn equations (Eq. (5.32)).

The idea behind the nonlinear iterative force correction (NIFC) procedure is to construct the

Chapter 7. Two-Phase Fluid-Structure Interaction

cross-coupling effect of strong fluid-structure interaction along the interface without forming the off-diagonal Jacobian term (\mathbf{A}^{Is} in Eq. (7.1)) via nonlinear iterations. The correction relies on an input-output relationship between the structural displacement and the force transfer at each nonlinear iteration. The input-output feedback process can also be considered as a nonlinear generalization of the steepest descent method to transform a divergent fixed-point iteration to a stable and convergent update of the approximate forces associated with the interface degrees of freedom [191]. Unlike the brute-force iterations in the strongly coupled FSI which lead to severe numerical instabilities for low structure-to-fluid mass ratios, the NIFC procedure provides a desired stability to the partitioned fluid-structure coupling, without the explicit evaluation of the off-diagonal Jacobian term. As derived in [191], the idea of partitioning is to eliminate the off-diagonal term \mathbf{A}^{Is} to facilitate the staggered sequential updates for strongly coupled fluid-structure system. Through static condensation, Eq. (7.1) can be written as

$$\begin{bmatrix} \mathbf{A}^{ss} & \mathbf{0} & \mathbf{0} & \mathbf{0} \\ \mathbf{A}^{sI} & \mathbf{I} & \mathbf{0} & \mathbf{0} \\ \mathbf{0} & \mathbf{A}^{If} & \mathbf{A}^{ff} & \mathbf{0} \\ \mathbf{0} & \mathbf{0} & \mathbf{0} & \mathbf{A}^{II} \end{bmatrix} \begin{Bmatrix} \Delta\boldsymbol{\eta}^s \\ \Delta\boldsymbol{\eta}^I \\ \Delta\mathbf{q}^f \\ \Delta\mathbf{f}^I \end{Bmatrix} = \begin{Bmatrix} \mathcal{R}^s \\ \mathcal{R}_D^I \\ \mathcal{R}^f \\ \tilde{\mathcal{R}}_N^I \end{Bmatrix}. \quad (7.2)$$

In the nonlinear interface force correction, we form the iterative scheme of the following matrix-vector product form

$$\Delta\mathbf{f}^I = (\mathbf{A}^{II})^{-1} \tilde{\mathcal{R}}_N^I, \quad (7.3)$$

where $(\mathbf{A}^{II})^{-1}$ is not constructed explicitly. Instead, the force correction vector $\Delta\mathbf{f}^I$ at the nonlinear iteration (subiteration) k can be constructed by successive matrix-vector products. This process essentially provides the control for the interface fluid force $\mathbf{f}^I = \int_{\Gamma^{fs}} \boldsymbol{\sigma}^f \cdot \mathbf{n}^f d\Gamma$ to stabilize strong fluid-structure interaction at low structure-to-fluid mass ratio. The scheme proceeds in a similar fashion as the predictor-corrector schemes by constructing the iterative interface force correction at each iteration. Let the error in the interface fluid force between the initial and first nonlinear iteration be $\Delta\mathbf{E}_{(0)}^I = \mathbf{f}_{(1)}^I - \mathbf{f}_{(0)}^I$. Similarly, the force at the iteration $k + 1$ is given by

$$\mathbf{f}_{(k+1)}^I = \mathbf{f}_{(k)}^I + \Delta\mathbf{f}_{(k)}^I = \mathbf{f}_{(k)}^I + [(\mathbf{A}^{II})^{-1} \tilde{\mathcal{R}}_N^I]_{(k)}. \quad (7.4)$$

For the iterative correction of the fluid forces, a power method is considered for the above matrix problem. We assume an iteration matrix \mathbf{M} which is diagonalizable in such a way that

Chapter 7. Two-Phase Fluid-Structure Interaction

$\mathbf{M}\mathbf{v}_{(k)} = \lambda_{(k)}\mathbf{v}_{(k)}$ for each k and eigenvalues $\lambda_{(k)}$ are distinct and nonzero with the corresponding eigenvectors $\mathbf{v}_{(k)}$. The correction to the forces is then constructed with the aid of the error vector $\Delta\mathbf{E}_{(0)}^I$ as

$$\mathbf{f}_{(k+1)}^I = \mathbf{f}_{(k)}^I + \mathbf{M}^k \Delta\mathbf{E}_{(0)}^I, \quad (7.5)$$

which can be written in terms of successive estimates as

$$\mathbf{f}_{(k+1)}^I = \mathbf{f}_{(0)}^I + \sum_{i=0}^k \mathbf{M}^i \Delta\mathbf{E}_{(0)}^I, \quad \text{for } k = 1, 2, \dots \quad (7.6)$$

The error vectors $\Delta\mathbf{E}_{(k)}^I$ can then be expressed in terms of the eigenvalues and eigenvectors λ and \mathbf{v} respectively to obtain a sequence of transformation for the force vector $\mathbf{f}_{(k+1)}^I$ similar to the Aitken's iterated Δ^2 process [191].

This interface force correction can also be interpreted as a quasi-Newton update

$$\Delta\mathbf{f}_{(k+1)}^I = \Delta\mathbf{f}_{(k)}^I + \Lambda_{(k)} \Delta\mathbf{E}_{(0)}^I, \quad (7.7)$$

where $\Delta\mathbf{f}_{(k+1)}^I = \mathbf{f}_{(k+1)}^I - \mathbf{f}_{(k)}^I$, $\Delta\mathbf{f}_{(k)}^I = \mathbf{f}_{(k)}^I - \mathbf{f}_{(k-1)}^I$ and $\Lambda_{(k)} = (\mathbf{M}^k - \mathbf{M}^{k-1})$ is an $n \times n$ matrix. There are three possible alternatives for the matrix $\Lambda_{(k)}$, namely, scalar, diagonal and full matrix. We consider $\Lambda_{(k)} = \alpha_{(k)} \mathbf{I}$ for the iterative quasi-Newton update, which can be considered as a minimal residual iteration method when $(\mathbf{y}, \Delta\mathbf{f}_{(k+1)}^I) = 0$ for some \mathbf{y} , where (\cdot, \cdot) denotes the standard inner product. Thus, we have

$$(\mathbf{y}, \Delta\mathbf{f}_{(k+1)}^I) = (\mathbf{y}, \Delta\mathbf{f}_{(k)}^I) + \alpha_{(k)} (\mathbf{y}, \Delta\mathbf{E}_{(0)}^I) = 0, \quad (7.8)$$

$$\implies \alpha_{(k)} = -\frac{(\mathbf{y}, \Delta\mathbf{f}_{(k)}^I)}{(\mathbf{y}, \Delta\mathbf{E}_{(0)}^I)}. \quad (7.9)$$

It can be observed that the choice of $\mathbf{y} = \Delta\mathbf{E}_{(0)}^I$ minimizes $\|\Delta\mathbf{f}_{(k+1)}^I\|$ and this type of iterative procedure is similar to the minimal residual method [192, 193].

7.1.2 Implementation details

The two-phase flow system in Eq. (5.32) is decoupled into two subsystems: Navier-Stokes and Allen-Cahn solves, for which the linear system of equations is summarized in Eqs. (5.33-5.34). Using a Newton-Raphson technique, the resulting two-phase flow variables and the ALE mesh displacement coming from the finite element discretization are evaluated by solving the linear system of equations via the generalized minimal residual (GMRES) algorithm proposed in [176].

Chapter 7. Two-Phase Fluid-Structure Interaction

To form the linear matrix system, we only construct the required matrix-vector products of each block matrix for the GMRES algorithm, instead of constructing the left-hand side matrix explicitly.

The algorithm for the partitioned iterative coupling of the implicit two-phase fluid-structure interaction solver is presented in Algorithm 3. It consists of seven steps in a nonlinear iteration

Algorithm 3 Partitioned coupling of implicit two-phase fluid-structure interaction solver

Given $\mathbf{u}^{f,0}$, p^0 , ϕ^0 , $\boldsymbol{\eta}^{s,0}$

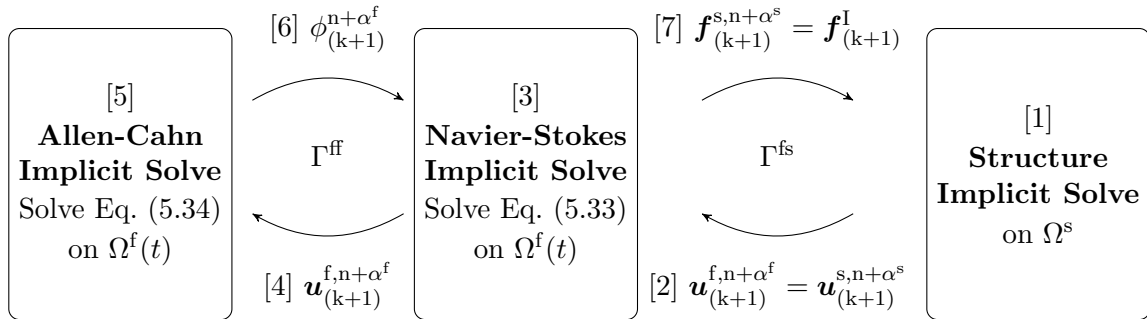
Loop over time steps, $n = 0, 1, \dots$

Start from known variables $\mathbf{u}^{f,n}$, p^n , ϕ^n , $\boldsymbol{\eta}^{s,n}$

Predict the solution:

$$\mathbf{u}_{(0)}^{f,n+1} = \mathbf{u}^{f,n}; \quad p_{(0)}^{n+1} = p^n; \quad \phi_{(0)}^{n+1} = \phi^n; \quad \boldsymbol{\eta}_{(0)}^{s,n+1} = \boldsymbol{\eta}^{s,n}$$

Loop over the nonlinear iterations, $k = 0, 1, \dots$ until convergence



for the exchange of data between the different blocks of the solver. In a typical nonlinear iteration k , the first step involves the solution of the structural equation to get the updated structural displacements $\boldsymbol{\eta}_{(k+1)}^{s,n+1}$. These displacements are transferred to the Navier-Stokes solve by satisfying the ALE compatibility condition at the fluid-structure interface Γ^{fs} in the second step. This is accomplished as follows: let the updated mesh displacement be denoted by $\boldsymbol{\eta}_{(k+1)}^{m,n+1}$. This mesh displacement is equated to the structural displacement at the interface Γ^{fs} to prevent any overlaps between the fluid and the structural domains,

$$\boldsymbol{\eta}_{(k+1)}^{m,n+1} = \boldsymbol{\eta}_{(k+1)}^{s,n+1}, \text{ on } \Gamma^{fs}. \quad (7.10)$$

Moreover, the conservation property between the moving elements in the fluid domain is satisfied by equating the fluid velocity to the mesh velocity at the interface, i.e.,

$$\mathbf{u}_{(k+1)}^{f,n+\alpha^f} = \mathbf{u}_{(k+1)}^{m,n+\alpha^f}, \text{ on } \Gamma^{fs}, \quad (7.11)$$

where the mesh velocity is written as,

$$\boldsymbol{u}_{(k+1)}^{m,n+\alpha^f} = \frac{\boldsymbol{\eta}_{(k+1)}^{m,n+1} - \boldsymbol{\eta}_{(k+1)}^{m,n}}{\Delta t} = \boldsymbol{u}_{(k+1)}^{s,n+\alpha^s} \text{ on } \Gamma^{fs}. \quad (7.12)$$

This ensures that the no-slip condition is satisfied at the fluid-structure interface (Eq. (4.60)). The mesh displacement for each spatial point $\boldsymbol{x}^f \in \Omega^f(t)$ is obtained by modeling the fluid mesh as a hyper-elastic material in equilibrium (Eq. 4.66), and is modeled by the Ogden model [173, 174]. The mesh velocity for the spatial points $\boldsymbol{x}^f \in \Omega^f(t)$ is then evaluated using the first equality in Eq. (7.12). The convection velocity is adjusted by subtracting the mesh velocity $\boldsymbol{u}_{(k+1)}^{m,n+\alpha^f}$ from the fluid velocity $\boldsymbol{u}_{(k+1)}^{f,n+\alpha^f}$ and transferred to the Navier-Stokes solve. In the third step, the Navier-Stokes equations are solved in the ALE reference coordinate system (Eq. (5.33)), thus solving for updated velocity $\boldsymbol{u}_{(k+1)}^{f,n+1}$ and pressure $p_{(k+1)}^{n+1}$. This updated fluid velocity with the mesh velocity (to obtain the adjusted convection velocity) is then transferred to the Allen-Cahn solve in the fourth step. The Allen-Cahn equation (Eq. (5.34)) is solved to evolve the fluid-fluid interface Γ^{ff} in the updated mesh configuration in the fifth step. The physical properties of the fluid such as its density, viscosity, and surface tension are then updated with the help of the updated order parameter values $\phi_{(k+1)}^{n+1}$ in the sixth step. With the help of all the updated fluid variables, the hydrodynamic forces on the fluid-structure interface Γ^{fs} is evaluated by integrating the stress tensor over the structural surface. The force corrected by the NIFC [191, 194] procedure, $\boldsymbol{f}_{(k+1)}^I$ at the fluid-structure interface is equated with the structural force in the final step, thus satisfying the dynamic equilibrium (Eq. (4.61)) at the fluid-structure interface,

$$\boldsymbol{f}_{(k+1)}^{s,n+\alpha^s} = \boldsymbol{f}_{(k+1)}^I \text{ on } \Gamma^{fs}. \quad (7.13)$$

7.1.3 General remarks

The exact surface tracking of the fluid-structure interface via the ALE technique along with the interface-capturing phase-field technique for the fluid-fluid interface renders the formulation hybrid. While the phase-field model approximates the interface by a smeared surface using the internal length scale parameter, the present Allen-Cahn based phase-field formulation is derived from the thermodynamic arguments and has a theoretical basis in the minimization of the Ginzburg-Landau energy functional. Unlike the level-set and volume-of-fluid techniques, the

interface evolution by the phase-field description simplifies the formulation by avoiding any re-initialization or geometric reconstruction of the interface. Furthermore, the PPV formulation to solve the nonlinear Allen-Cahn equation helps to establish the positivity condition nonlinearly at the local element matrix level resulting in the positivity preserving and monotone scheme, which has been shown in Section 3.2.2.1.

The ability of the solver to handle low structure-to-fluid mass ratio can be attributed to the NIFC procedure based on quasi-Newton updates. Further details about the NIFC formulation can be found in [191, 194]. The above-mentioned characteristics of the proposed partitioned coupling between the two-phase fluid and the structure lead to a robust and stable formulation. Moreover, the partitioned-block type feature of the solver leads to flexibility and ease in its implementation to the existing variational solvers. These desirable features of the proposed formulation are analyzed and assessed through various numerical tests in the next section.

7.2 Numerical tests

In this section, we present some numerical tests to assess the coupling between the two-phase Allen-Cahn based solver and the structural solver. To accomplish this, we perform the decay tests by examining the interaction of the free-surface with a rigid circular cylinder under translation and a rectangular barge under pure rotation.

7.2.1 Heave decay test under translation

We herein consider the free heave motion of a circular cylinder at the free-surface of water. The schematic of the computational domain, $\Omega \in [0, 90D] \times [0, 14.6D] \times [0, 17D]$ considered in this study is shown in Fig. 7.1, where a circular cylinder of diameter $D = 0.1524\text{m}$ is placed initially at an offset of $0.167D$ from the free-surface of water. The density of the cylinder is half that of the denser fluid, i.e., $\rho^s = 500$, $\rho_1^f = 1000$ and $\rho_2^f = 1.2$. The dynamic viscosities of the two phases are $\mu_1^f = 10^{-3}$ and $\mu_2^f = 1.8 \times 10^{-5}$. The acceleration due to gravity is $\mathbf{g} = (0, -9.81, 0)$. Apart from the high density ratio between the two phases, $\rho^* = \rho_1^f / \rho_2^f = 833.3$, a low structure-to-fluid density ratio ($\rho^s / \rho_1^f = 0.5$) based on the denser fluid has been chosen. The initial

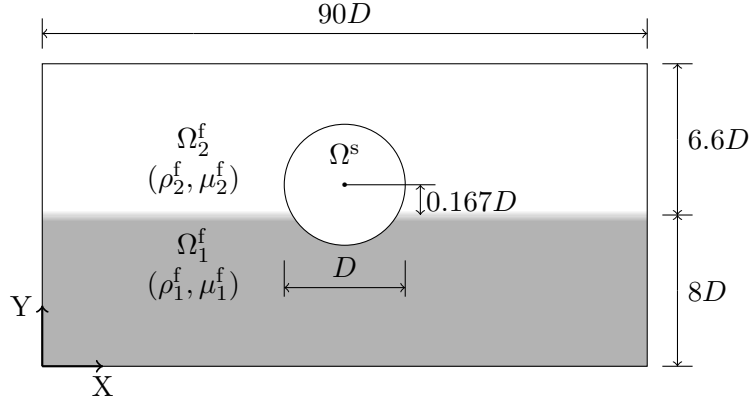


Figure 7.1: Schematic of the decay response of a cylinder of diameter D under gravity in the X - Y cross-section. The computational domain extends a distance of $17D$ in the Z -direction.

condition for the order parameter is given as

$$\phi(x, y, 0) = -\tanh\left(\frac{y}{\sqrt{2}\varepsilon}\right). \quad (7.14)$$

We have employed the hybrid RANS/LES model discussed in Chapter 8 for modeling the turbulent effects. The Reynolds number is defined based on the maximum velocity achieved by the cylinder and its diameter with respect to the denser fluid, i.e., $Re = \rho_1^f U_{cyl} D / \mu_1^f \approx 30,000$.

A typical computational mesh prepared for the decay test is shown in Fig. 7.2. A boundary layer covers the structural cylinder with the first layer at a distance from the cylindrical surface such as to maintain $y^+ \sim 1$ (Fig. 7.2(b)). Moreover, a refined mesh consisting of a cylinder with radius $3.3D$ is constructed around the boundary layer region to capture the vortices produced due to the heave motion at the free-surface (Fig. 7.2(a)). To capture the air-water interface accurately, the interfacial region is refined in accordance with the suggestions in Section 5.4.3.2 such that at least 4 elements lie in the equilibrium interface region. Therefore, the employment of a sharper fluid-fluid interface (smaller ε) leads to a more refined mesh, assuming the interfacial region is sufficiently captured by the refinement. **The mesh consists of 72,604 number of nodes with 144,566 triangular elements in the two-dimensional plane perpendicular to the axis of the cylinder.** The mesh is then extruded in the Z -direction consisting of 7 layers. The no-slip boundary condition is satisfied at the cylindrical surface while the slip boundary condition is set on all other boundaries.

We first present the convergence studies for which we considered the two-dimensional domain for the current case. For the temporal convergence, a time step of $\Delta t = 2 \times 10^{-2}$ is decreased

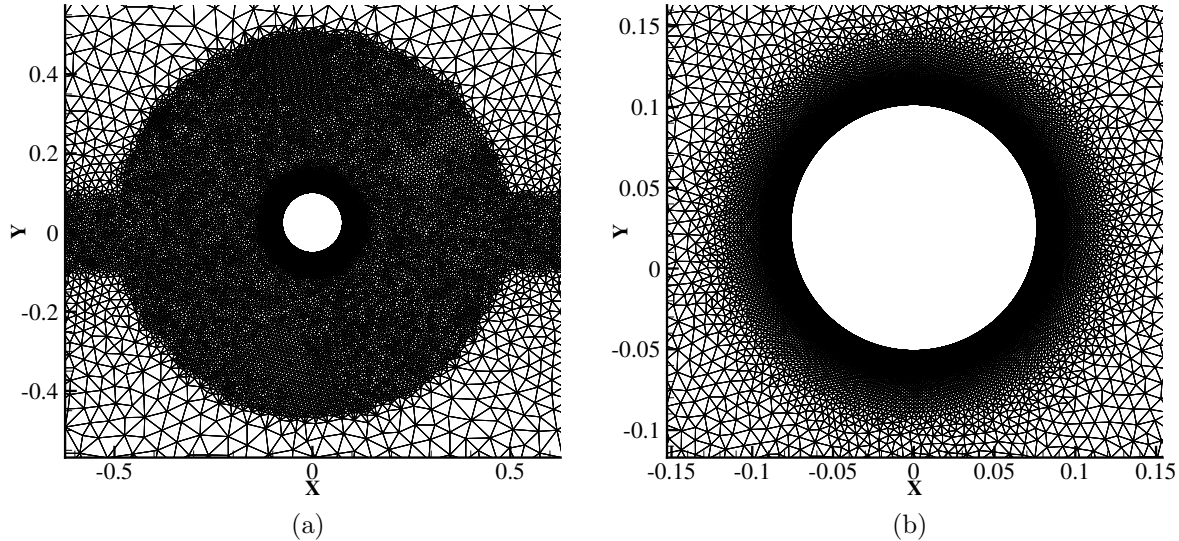


Figure 7.2: Mesh employed for the decay response of a cylinder interacting with the free-surface: (a) the refined mesh around the cylinder to capture the flow vortices near the structure, and (b) the boundary layer mesh around the cylinder with $y^+ \sim 1$ for hybrid RANS/LES modeling.

by a factor of 2 till $\Delta t = 6.25 \times 10^{-4}$. The interfacial thickness parameter is selected as $\varepsilon = 0.01$ for the study. The decaying heave motion of the cylinder under different time steps is plotted in Fig. 7.3(a). A non-dimensional error for quantifying the convergence is established which is defined as

$$e_1 = \frac{\|\boldsymbol{\eta} - \boldsymbol{\eta}_{\text{ref}}\|_2}{\|\boldsymbol{\eta}_{\text{ref}}\|_2}, \quad (7.15)$$

where $\boldsymbol{\eta}$ represents the temporal evolution of the heave motion of the cylinder for corresponding time step, $\boldsymbol{\eta}_{\text{ref}}$ is the heave motion evolution with time for the finest time step ($\Delta t = 6.25 \times 10^{-4}$) and $\|\cdot\|_2$ is the standard Euclidean L^2 norm. Figure 7.3(b) shows the plot for the error e_1 with the time step size Δt , which gives a temporal convergence of 1.6.

The spatial convergence is studied based on the interface thickness parameter ε . Three values of the parameter were selected, viz., $\varepsilon \in [0.02, 0.01, 0.005]$. In accordance with the suggestion of 4 number of elements in the interfacial region, smaller ε leads to a more refined mesh. The mesh for $\varepsilon = 0.02, 0.01$ and 0.005 consists of 35,954 (71,300 elements), 72,604 (144,566 elements), and 205,094 (409,494 elements) nodes, respectively. The heave motion is shown in Fig. 7.4 for different values of ε . We observe a minor difference in the response of the cylinder interacting with the free-surface. Therefore, based on the convergence studies, we select the interface thickness parameter of $\varepsilon = 0.01$ and a time step of $\Delta t = 0.0025$ for further

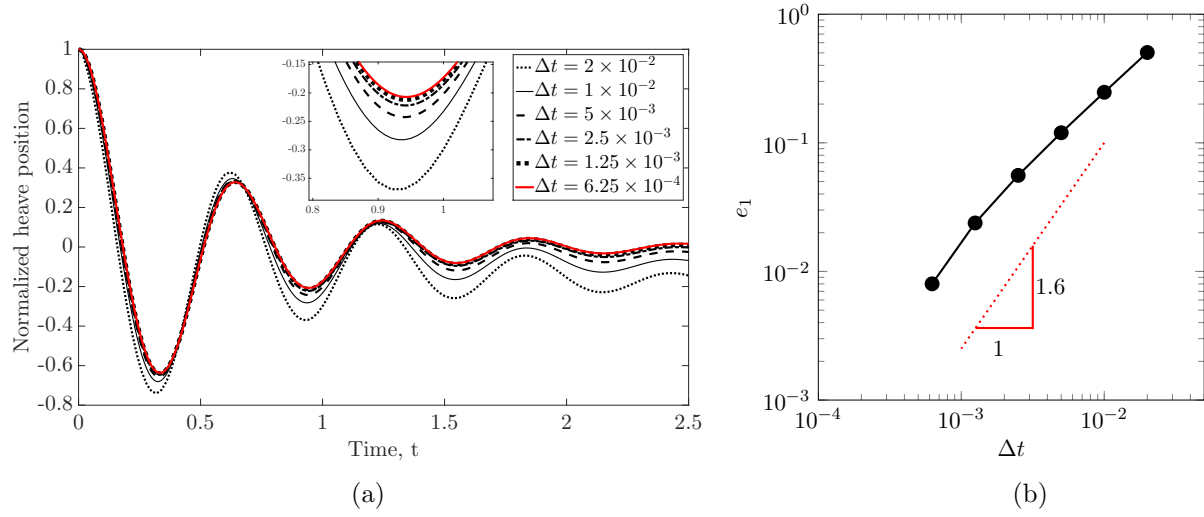


Figure 7.3: Temporal convergence study for the decay test of a circular cylinder: (a) heave motion employing temporal refinement, and (b) the dependence of non-dimensionalized L^2 error (e_1) as a function of uniform temporal refinement Δt .

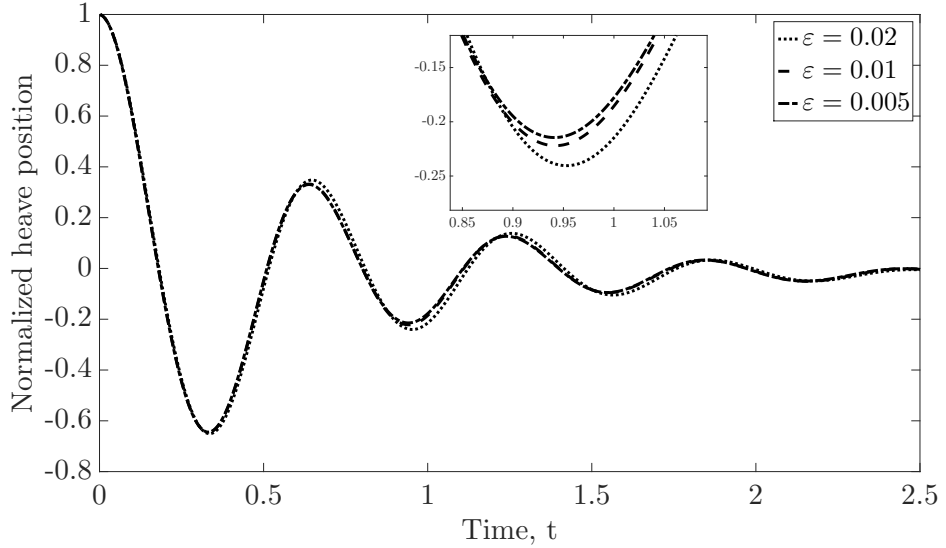


Figure 7.4: Dependence of spatial grid convergence on the interfacial thickness parameter ε for the decay test of a circular cylinder at free-surface.

assessment.

In what follows, we perform the three-dimensional computation of the fluid-structure interaction problem with the selected spatial and temporal convergence parameters for validation with the experiment [6] and the simulation [7]. The three-dimensional mesh consists of 580,000 nodes with 1.01 million six-node wedge elements. The simulation is carried out with 48 processors which took a total computational time of 11.63 hours. The solver performed 4 nonlinear

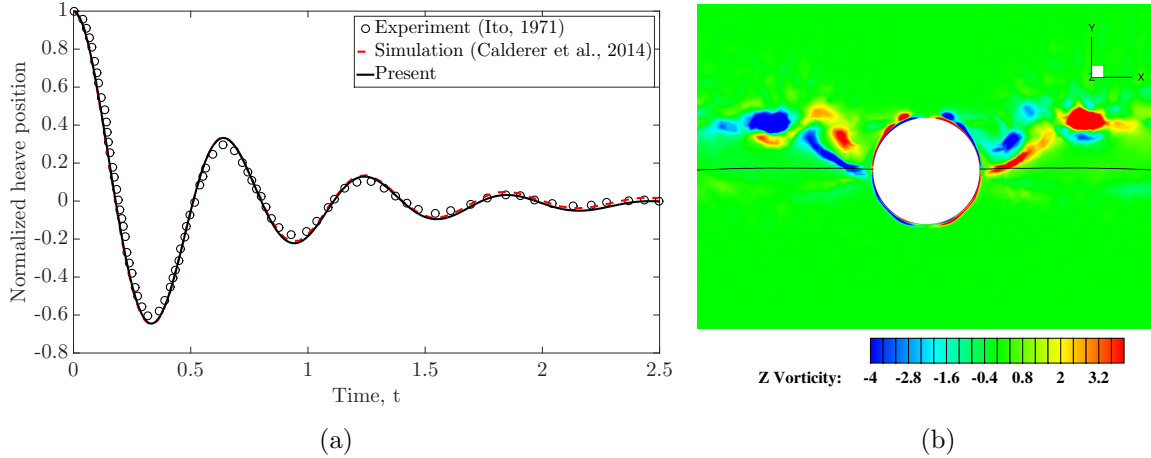


Figure 7.5: Decay test of a circular cylinder under translation along the free-surface: (a) validation of the heave motion of the cylinder at the free-surface with the experimental [6] and simulation [7] studies, and (b) Z -vorticity contours around the cylinder at $t = 1.5$ s with the free-surface indicated at $\phi = 0$.

iterations to achieve a nonlinear convergence tolerance of 5×10^{-4} . The results of the evolution of the heave of the cylinder are shown in Fig. 7.5(a) where we find a very good agreement with the literature. The Z -vorticity contours with the interface shown at $\phi = 0$ are depicted in Fig. 7.5(b). A finer grid surrounding the cylinder can increase the resolution of the vortices around the cylinder.

7.2.2 Decay test under rotation along free-surface

For further validation and robustness assessment, we consider the pure rotation of a rectangular barge of length $L = 0.3$, height $H = 0.2$ and width $W = 3L$ at the free-surface of water. The computational domain $\Omega \in [0, 58.3L] \times [0, 6.3L] \times [0, 3L]$ with the barge inclined at an angle of $\theta = 15^\circ$ from the free-surface level is shown in Fig. 7.6(a). The center of gravity of the barge is at the free-surface level with its mass moment of inertia and the rotational damping matrices respectively as

$$\mathbf{I}^s = \begin{bmatrix} 0 & 0 & 0 \\ 0 & 0 & 0 \\ 0 & 0 & 0.236 \end{bmatrix} \text{kg} \cdot \text{m}^2, \quad \mathbf{C}_\theta = \begin{bmatrix} 0 & 0 & 0 \\ 0 & 0 & 0 \\ 0 & 0 & 0.275 \end{bmatrix} \text{kg} \cdot \frac{\text{m}^2}{\text{s}}. \quad (7.16)$$

The physical properties of the fluid domain are $\rho_1^f = 1000$, $\rho_2^f = 1.2$, $\mu_1^f = 10^{-3}$, $\mu_2^f = 1.8 \times 10^{-5}$ and $\mathbf{g} = (0, -9.81, 0)$. The initial condition for the order parameter is given as

$$\phi(x, y, 0) = -\tanh\left(\frac{y}{\sqrt{2}\varepsilon}\right). \quad (7.17)$$

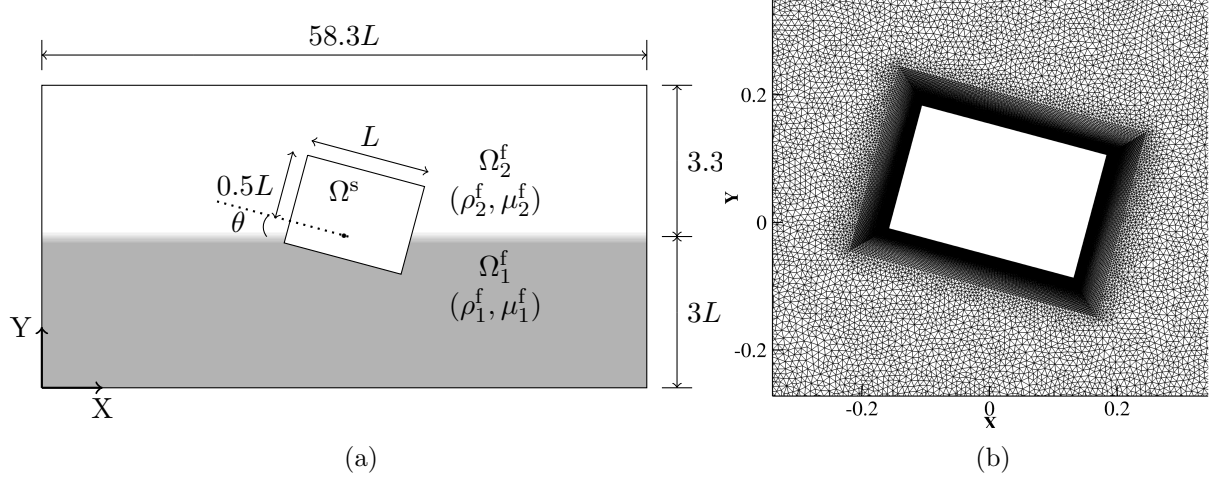


Figure 7.6: Rotation of a rectangular barge under gravity: (a) schematic of the computational setup of a barge of length $L = 0.3$, height $H = 0.2$ and width $W = 3L$ in the X - Y cross-section, and (b) zoom-in view of the computational mesh near the barge with boundary layer. The computational domain extends a distance of $3L$ in the Z direction.

The Reynolds number is defined based on the maximum velocity achieved by the upper corner of the barge and its length, with respect to the denser fluid, i.e., $Re = \rho_1^f U_{corner} L / \mu_1^f \approx 99,500$. The computational mesh employed for the simulation, shown in Fig. 7.6(b), is constructed with similar characteristics as the mesh in Section 7.2.1. A boundary layer envelops the rectangular barge with a refined mesh to capture the vortices produced at the free-surface. Moreover, the evolution in the free-surface is captured by a refined region around the fluid-fluid interface. The mesh extrudes in the Z -direction and consists of 10 layers.

With the converged spatial and temporal parameters, we validate the rotational response of the rectangular barge with that of the experiment [8] and the computational data [7]. The mesh consists of 1,025,684 nodes with 1,856,930 six-node wedge elements. The simulation is carried out by 72 processors with a computational time of 22.2 hours. On an average, the solver performed 4 nonlinear iterations to achieve a nonlinear convergence tolerance of 5×10^{-4} . The rotational motion is plotted in Fig. 7.7(a) where we observe a good agreement with the available results in the literature. The Z -vorticity contours are shown in Fig. 7.7(b) at $t = 1.4$ s. This concludes the validation and convergence studies for the coupled FSI two-phase solver. We next demonstrate a practical problem of a uniform flow across a flexible pipeline with internal two-phase flow.

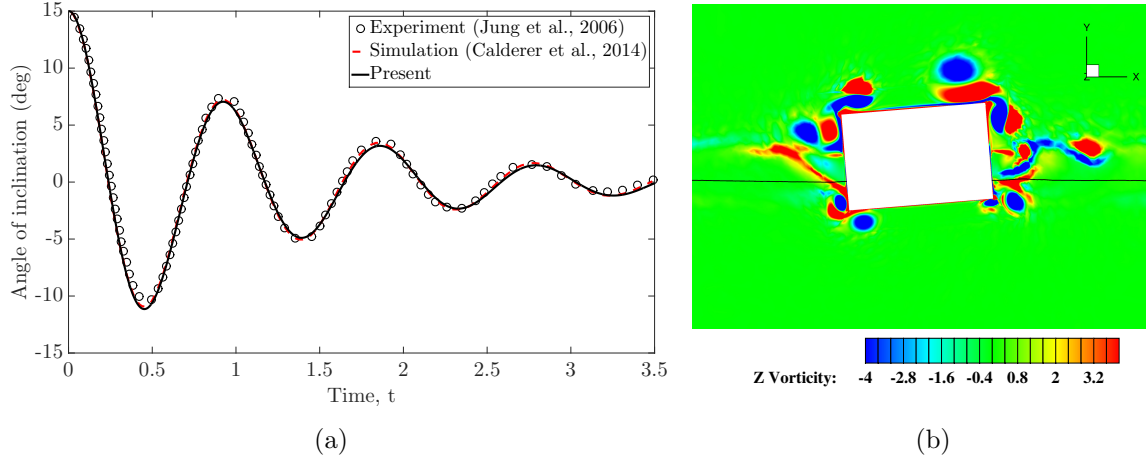


Figure 7.7: Decay test under rotation: (a) validation of the rotational motion of the rectangular barge at the free-surface with the experimental [8] and simulation [7] studies, and (b) Z -vorticity contours around the barge at $t = 1.4$ s with the free-surface indicated at $\phi = 0$.

7.3 Application to flexible riser FSI with internal two-phase flow

We next demonstrate the capability of the developed phase-field FSI solver in handling a practical problem of a riser with an internal two-phase flow and exposed to external uniform current flow. A typical schematic for the problem is shown in Fig. 7.8. The riser has an outer diameter of D and span of $L = 20D$. The inflow and outflow boundaries are at a distance of $10D$ and $30D$ from the center of the riser respectively. The side walls are equidistant from the riser center at $15D$ on either side. The outer surface of the riser is exposed to a uniform inflow current of $\mathbf{u}^f = (U_\infty, 0, 0)$. The no-slip boundary condition is satisfied at the outer surface of the riser. All other boundaries are slip boundaries except the outflow where the stress-free condition is satisfied. The fluid domain exposed to the external part of the riser is denoted by Ω_1^f . The interior of the riser has internal diameter $2r_2$ with an initial concentric profile for the two phases with the interface at a radius of r_1 from the riser axis separating the two phases Ω_2^f and Ω_1^f . A prescribed profile for the Z -velocity is imposed at the inlet of the riser for the internal flow, while the stress-free condition is satisfied at the outlet of the internal flow. The velocity is such that no-slip condition is satisfied at the internal surface of the riser. We consider the profile of the velocity for a co-annular, laminar and fully developed flow regime consisting of immiscible

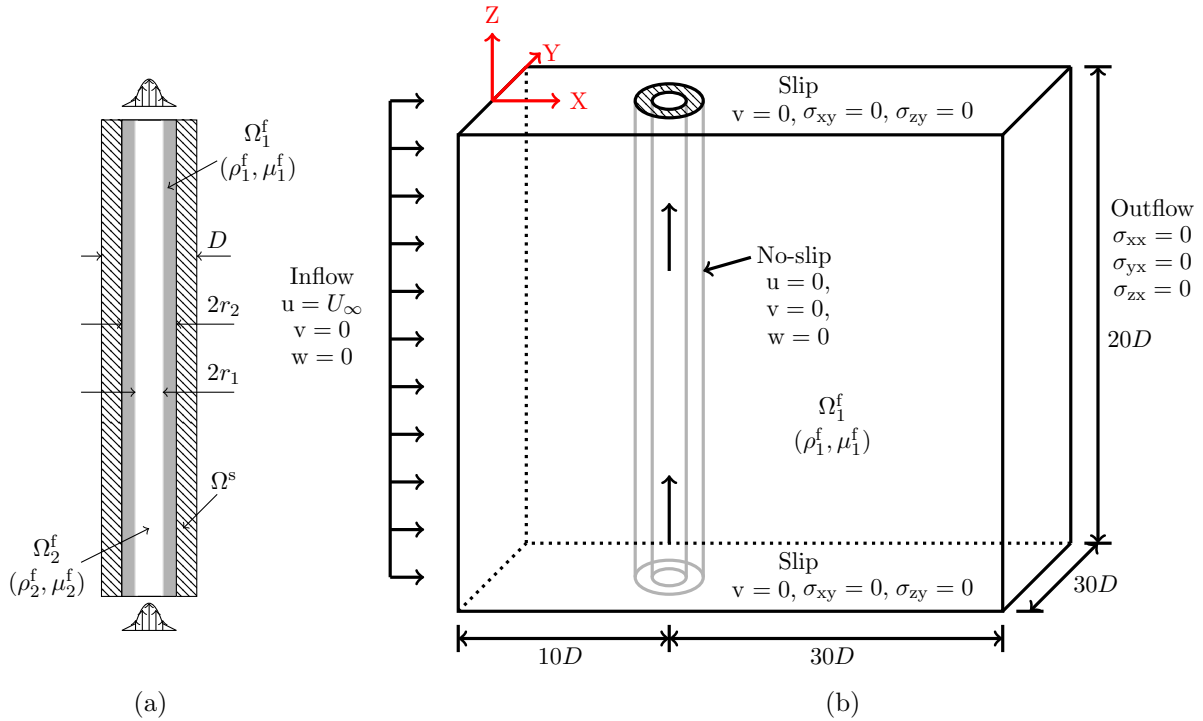


Figure 7.8: Schematic of the uniform flow past a flexible riser with an internal two-phase flow: (a) the $X - Z$ cross-section of the flexible riser with the internal flow velocity profile at the inlet and outlet of the pipe, and (b) the computational setup and boundary conditions employed for the demonstration. Here, $\mathbf{u}^f = (u, v, w)$ denotes the components of the fluid velocity and the hatched area shows the flexible structure (riser).

Newtonian fluids, given by [195]

$$\mathbf{u}^f = (0, 0, w), \quad (7.18)$$

$$w(R) = \begin{cases} \frac{C[1 - (r^*)^2 + \mu^*((r^*)^2 - R^2)]}{(r^*)^{n+3}(\mu^* - 1) + 1}, & 0 \leq R \leq r^*, \\ \frac{C[1 - R^2]}{(r^*)^{n+3}(\mu^* - 1) + 1}, & r^* \leq R \leq 1, \end{cases} \quad (7.19)$$

where $R = \sqrt{x^2 + y^2}/r_2$, $r^* = r_1/r_2$, $\mu^* = \mu_1^f/\mu_2^f$ and $C = (n+3)/2$, where $n = 1$ for a circular tube. The physical parameters employed for the demonstration are $r_1 = 0.2$, $r_2 = 0.4$ and $\mathbf{g} = (0, 0, 0)$. The initial condition for the order parameter is given as

$$\phi(x, y, 0) = \begin{cases} \tanh\left(\frac{\sqrt{x^2 + y^2} - r_1}{\sqrt{2}\varepsilon}\right), & \sqrt{x^2 + y^2} \leq r_2, \\ 1, & \text{elsewhere.} \end{cases} \quad (7.20)$$

In the present demonstration, we employ a linear flexible body solver for solving the structural equation. The Euler-Bernoulli beam equation is solved in the eigenspace with the struc-

Chapter 7. Two-Phase Fluid-Structure Interaction

Table 7.1: Non-dimensional parameters for the two cases considered for the present study.

Cases	Re	m^*	ρ^*	μ^*	U_r	P^*	EI^*	ρ^s/ρ^f
Case 1	100	2.89	100	100	5	0.34	5872.8	6.68
Case 2	1000	2.89	100	100	5	0.34	5872.8	6.68

tural displacement represented as a linear combination of the eigenmodes. This analysis has been explained in Section 4.3.2.2. Following the notations from Section 4.3.2.2, the non-dimensional parameters for the VIV of the riser with the internal flow are defined as follows:

$$\begin{aligned} Re &= \frac{\rho_1^f U_\infty D}{\mu_1^f} = \frac{\rho_2^f U_\infty D}{\mu_2^f}, & m^* &= \frac{m^s}{\pi D^2 L \rho_1^f / 4}, & \rho^* &= \frac{\rho_1^f}{\rho_2^f}, & \mu^* &= \frac{\mu_1^f}{\mu_2^f}, \\ U_r &= \frac{U_\infty}{f_1 D}, & P^* &= \frac{P}{\rho_1^f U_\infty^2 D^2}, & EI^* &= \frac{EI}{\rho_1^f U_\infty^2 D^4}, \end{aligned} \quad (7.21)$$

where Re , m^* , ρ^* , μ^* , U_r , P^* and EI^* denote the non-dimensional quantities, viz., Reynolds number, mass ratio, density ratio, viscosity ratio, reduced velocity, axial tension and flexural rigidity of the riser modeled as a beam. Here, f_1 denotes the frequency of the first eigenmode calculated by Eq. (4.56). We consider two cases with different Reynolds number in the present demonstration. The non-dimensional numbers related to the cases are shown in Table 7.1.

The computational mesh for the demonstration is depicted in Fig. 7.9. The mesh is divided

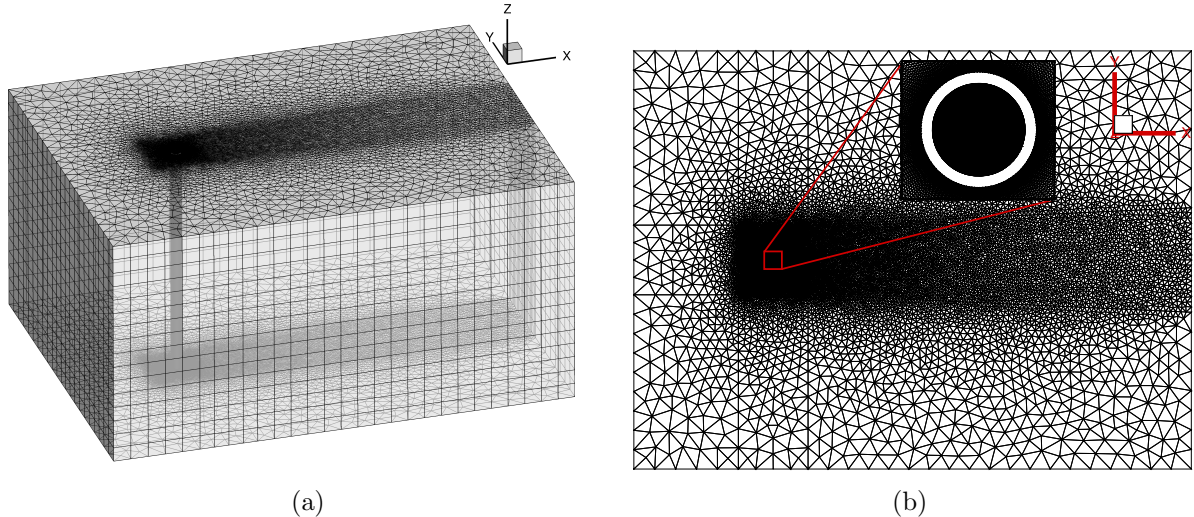


Figure 7.9: Computational mesh for the VIV of a riser with an internal two-phase flow: (a) three-dimensional view of the mesh, and (b) two-dimensional cross-section of the mesh with refined wake region behind the riser and refined internal region of the riser to capture the interface between the two phases in the internal flow accurately.

into two parts: external and internal. The external mesh consists of the fluid domain external to

the riser. A two-dimensional cross-section is shown in Fig. 7.9(b) where we find a refined wake region to capture the flow structures. This external mesh is extruded in the third dimension consisting of 130 layers so that mesh element size in the spanwise direction is $\sim 0.15D$. Figure 7.9(a) only shows some of the layers for clarity. The internal mesh comprises of the internal volume of the riser. It is much more refined than the external region to capture the two-phase interface and is extruded 500 layers in the third dimension. The complete three-dimensional mesh contains 5.14 million grid points with 10.08 million six-node wedge elements. The solver performed 4 – 5 nonlinear iterations to achieve a nonlinear convergence tolerance of 5×10^{-4} .

In the following subsections, we provide a brief physical insight on the response of the riser for the two cases and the effect of the external flow VIV on the internal flow regime. As the reduced velocity for the two cases lies within the “lock-in” range, we expect the maximum amplitude to be of the order of the riser diameter. We also shed some light on the response wave patterns and their frequencies. Further parametric studies need to be conducted to thoroughly understand the physics of this complex coupled problem, which is beyond the scope of the present work.

7.3.1 Amplitude response and flow patterns

The amplitude of the riser is found maximum at the mid-point along its span and has been plotted in Fig. 7.10 for the two Reynolds number cases. Cases 1 and 2 are simulated for a non-dimensional time tU_∞/D of 90 and 50 respectively so that at least 4 cycles of VIV are captured. The temporal variation of the response amplitude along the riser in the cross-flow and in-line directions are shown in Figs. 7.11 and 7.12 for Cases 1 and 2 respectively. We observe a standing wave pattern along the riser from the plots. Furthermore, a spectral analysis of the amplitude response at $z/L = 0.5$ reveals a single non-dimensional frequency (fU_∞/D) of 0.1709 in the cross-flow and 0.3662 in the in-line directions for Case 1, indicating the lock-in phenomenon. On the other hand, the in-line oscillation in Case 2 shows a multi-modal response comprising of fU_∞/D as 0.1953 and 0.3662 and the cross-flow vibration indicates a single frequency response with $fU_\infty/D = 0.1709$.

The flow contours of the Z -vorticity along the riser span with the visualization of the internal flow via the order parameter ϕ are shown in Fig. 7.13 for Case 1 and Fig. 7.14 for Case 2. The

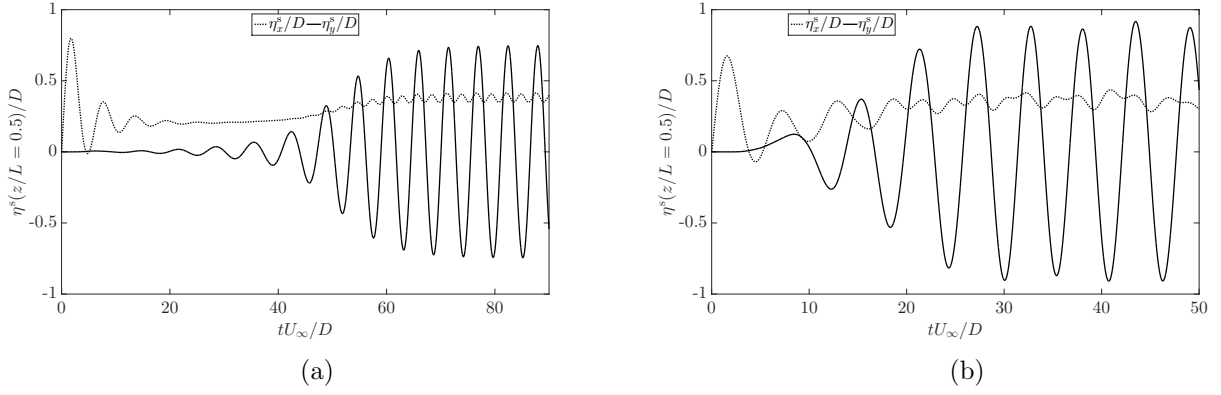


Figure 7.10: The response amplitude at the mid-point of the riser ($z/L = 0.5$) exposed to external uniform flow with internal two-phase flow: (a) Case 1 ($Re = 100$), and (b) Case 2 ($Re = 1000$).

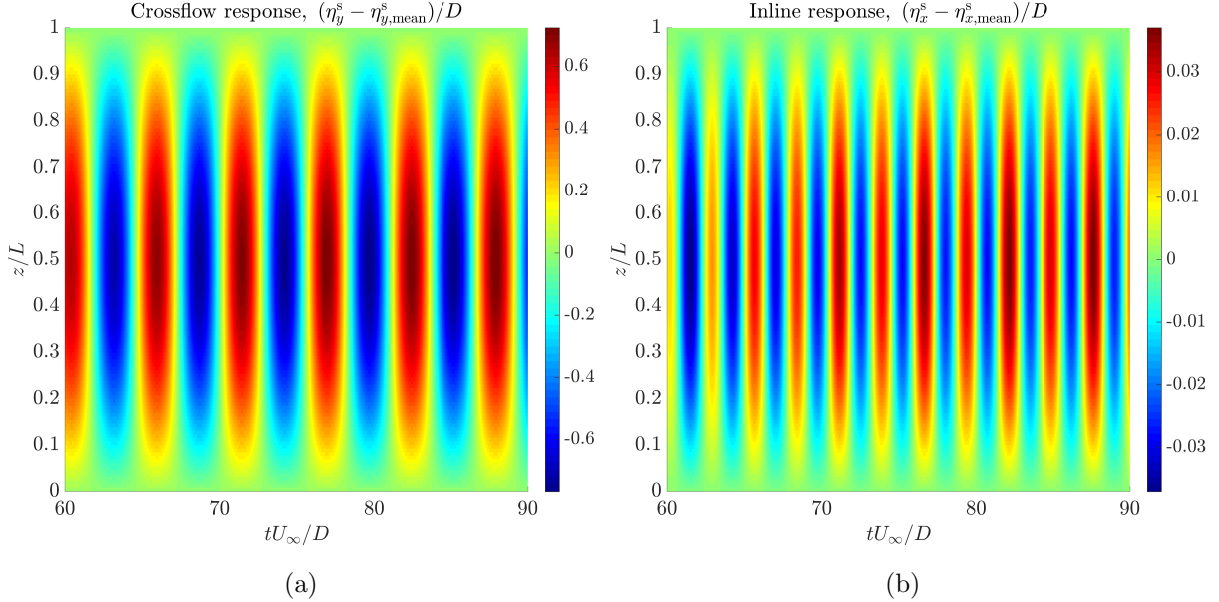


Figure 7.11: Response amplitudes of the riser along the span with non-dimensional time tU_∞/D for Case 1: (a) cross-flow, and (b) in-line.

irregularity in the vortex patterns suggests the onset of turbulent wake for Case 2. It is found that the topological changes in the fluid-fluid interface are captured qualitatively in the current two-phase FSI simulation. The change in the internal flow pattern from co-annular regime to bubble/slug flow pattern can be observed due to the vibrating riser.

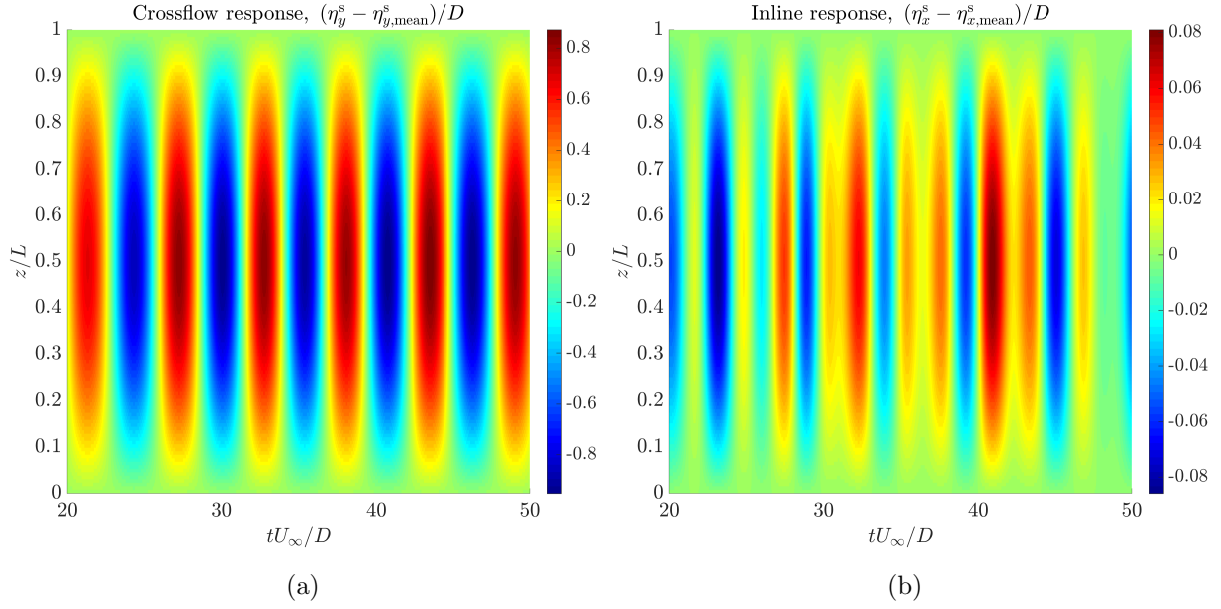


Figure 7.12: Response amplitudes of the riser along the span with non-dimensional time tU_∞/D for Case 2: (a) cross-flow, and (b) in-line.

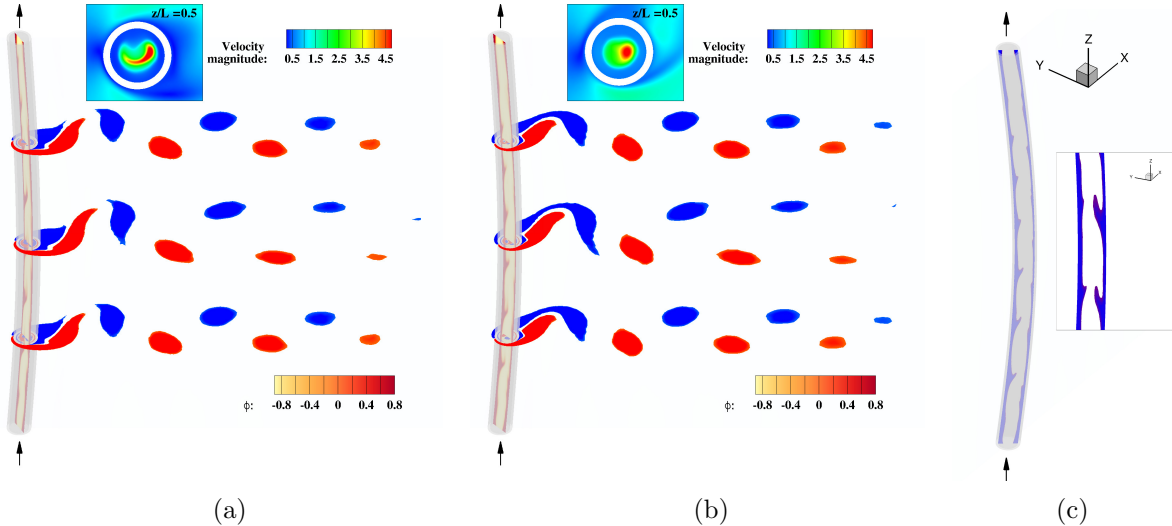


Figure 7.13: Contour plots for the VIV of a riser at $Re = 100$ with internal two-phase flow at tU_∞/D : (a) 80, (b) 90 and (c) the internal flow along the riser. The Z -vorticity contours are shown at three cross-sections along the riser, viz., $z/L \in [0.25, 0.5, 0.75]$ and are colored with red for positive vorticity and blue for negative vorticity. The inset figure provides the velocity magnitude at the mid-section of the riser. The interior two-phase flow of the riser is visualized by the contours of order parameter $\phi > 0$ at an arbitrary plane passing through the axis of the deformed riser.

7.3.2 Relationship between VIV and internal flow patterns

To investigate the effect of the VIV on the internal fluid flow and vice-versa, we simulate

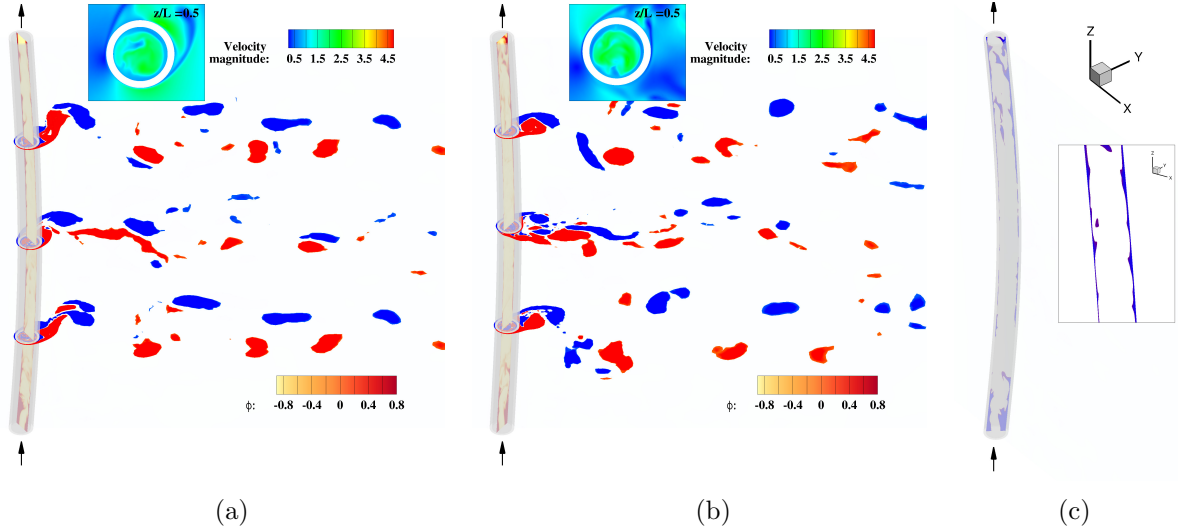


Figure 7.14: Contour plots for the VIV of a riser at $Re = 1000$ with internal two-phase flow at tU_∞/D : (a) 40, (b) 50 and (c) the internal flow along the riser. The Z -vorticity contours are shown at three cross-sections along the riser, viz., $z/L \in [0.25, 0.5, 0.75]$ and are colored with red for positive vorticity and blue for negative vorticity. The inset figure provides the velocity magnitude at the mid-section of the riser. The interior two-phase flow of the riser is visualized by the contours of order parameter $\phi > 0$ at an arbitrary plane passing through the axis of the deformed riser.

the VIV problem of the riser without the internal flow, i.e., a solid riser with the same non-dimensional parameters considered for Case 1. Results show an insignificant difference in the vibrational amplitude along the riser. It can be inferred that the internal flow has negligible or no effect on the VIV response of the riser for the parameters considered in the study. This may be due to the dominant effect of the external flow on VIV compared to the inertia of the internal fluid. On the other hand, the effect of the VIV on the internal flow is evident from the flow contours in Figs. 7.13(c) and 7.14(c). It is observed that the co-annular initial two-phase flow pattern is transitioning into an elongated bubble/slug flow pattern. This type of flow pattern prediction through a fully-coupled two-phase FSI can be advantageous to improve multiphase flow assurance. A rigorous parametric study is required to quantify the variation of the structural parameters, reduced velocity and the mass ratio on the internal flow regimes, which forms a topic for future study.

7.4 Summary

We presented the FSI coupling for dealing with the two-phase flows in this chapter by considering the fluid-structure interface as Lagrangian and evolving the fluid-fluid interface based on the Allen-Cahn equation written in the ALE referential coordinates. Furthermore, the issue of getting an ill-conditioned matrix due to low structure-to-fluid mass ratio is resolved by a nonlinear iterative force correction procedure. The key takeaways about the capability of the two-phase FSI solver developed in this chapter are:

- Ability to handle high density and viscosity ratios,
- Stable solution at low structure-to-fluid mass ratios,
- Almost second-order of temporal accuracy for the FSI simulations, and
- Flexibility and ease of implementation due to the partitioned block-type coupling.

This concludes the numerical development for the fundamental two-phase FSI problem. In the next chapter, we look into the hybrid RANS/LES turbulence modeling for high Reynolds number flows where we extend the developed PPV technique to the turbulence transport equation.

Chapter 8

PPV based Hybrid RANS/LES

Turbulence Application*

In this chapter, we extend the positivity preserving variational formulation presented in Chapter 3 to the turbulence transport equation. The closure problem of the turbulence modeling in the Navier-Stokes equations is discussed along with the variational formulation. Uniform single-phase flow across a rigid cylinder at Reynolds numbers of 3,900 and 140,000 are considered for the validation. Finally, the vortex-induced vibration of an offshore riser at Reynolds number of 4,000 is studied by employing the presented formulation.

8.1 Background

Offshore systems usually operate at high Reynolds number regime, thus necessitating the need to model the turbulent effects in the computational simulations. In the present work, a hybrid RANS/LES type of turbulence modeling is employed which combines the advantages of both the RANS and LES in decreasing the computational mesh refinement. This is carried out by the delayed detached eddy simulation (DDES). The Navier-Stokes equations can be written after

*Parts of this chapter have been published in “V. Joshi and R.K. Jaiman, A variationally bounded scheme for delayed detached eddy simulation: Application to vortex-induced vibration of offshore riser, *Computers and Fluids*, 157, Pg. 84-111 (2017).”

Reynolds averaging as

$$\rho^f \frac{\partial \mathbf{u}^f}{\partial t} + \rho^f \mathbf{u}^f \cdot \nabla \mathbf{u}^f = \nabla \cdot \boldsymbol{\sigma}^f + \nabla \cdot \boldsymbol{\sigma}^{ddes} + \mathbf{s}^f + \mathbf{b}^f, \quad \text{on } \Omega^f(t), \quad (8.1)$$

$$\nabla \cdot \mathbf{u}^f = 0, \quad \text{on } \Omega^f(t), \quad (8.2)$$

where all the primitive variables (fluid velocity and pressure) are Reynolds averaged and $\boldsymbol{\sigma}^{ddes}$ is the turbulent stress tensor given by $\boldsymbol{\sigma}^{ddes} = \mu_T^f (\nabla \mathbf{u}^f + (\nabla \mathbf{u}^f)^T)$, with μ_T^f representing the turbulent dynamic viscosity. The closure problem for computing the turbulent dynamic viscosity is resolved by solving the Spalart-Allmaras one-equation turbulence model for the turbulent kinematic viscosity, $\nu_T^f = \mu_T^f / \rho^f$ which is discussed in the following section.

8.2 Turbulence transport equation

In this section, we discuss the differential form of the closure equation for the turbulence model and review the weak form based on the PPV technique.

8.2.1 Strong differential form

Consider the physical domain $\Omega^f(t)$ with the spatial and temporal coordinates denoted by \mathbf{x}^f and t respectively. The Spalart-Allmaras one-equation solves for the eddy viscosity $\tilde{\nu}$ from which the turbulent kinematic viscosity can be computed as

$$\nu_T^f = \tilde{\nu} f_{v1}, \quad f_{v1} = \frac{\tilde{\chi}^3}{\tilde{\chi}^3 + c_{v1}^3}, \quad \tilde{\chi} = \frac{\tilde{\nu}}{\nu^f}, \quad (8.3)$$

where $\nu^f = \mu^f / \rho^f$ is the molecular kinematic viscosity of the fluid. Suppose $\Gamma_D^{\tilde{\nu}}(t)$ and $\Gamma_H^{\tilde{\nu}}(t)$ denote the Dirichlet and Neumann boundaries for the eddy viscosity respectively. The turbulence transport equation in the ALE framework is then given as,

$$\frac{\partial \tilde{\nu}}{\partial t} \Big|_{\mathbf{x}} + (\mathbf{u}^f - \mathbf{u}^m) \cdot \nabla \tilde{\nu} = P - D + \frac{1}{\tilde{\sigma}} [\nabla \cdot ((\nu^f + \tilde{\nu}) \nabla \tilde{\nu}) + c_{b2} (\nabla \tilde{\nu})^2], \quad \text{on } \Omega^f(t), \quad (8.4)$$

$$\tilde{\nu} = \tilde{\nu}_D, \quad \forall \mathbf{x}^f \in \Gamma_D^{\tilde{\nu}}(t), \quad (8.5)$$

$$\nabla \tilde{\nu} \cdot \mathbf{n}^{\tilde{\nu}} = \tilde{\nu}_H, \quad \forall \mathbf{x}^f \in \Gamma_H^{\tilde{\nu}}(t), \quad (8.6)$$

$$\tilde{\nu} = \tilde{\nu}_0, \quad \text{on } \Omega^f(0), \quad (8.7)$$

where $P = c_{b1}\tilde{S}\tilde{\nu}$ and $D = c_{w1}f_w(\tilde{\nu}/\tilde{d})^2$ are the production and destruction terms, $\tilde{S} = S + (\tilde{\nu}/(\kappa^2\tilde{d}^2)f_{v2}$, S being the magnitude of vorticity, c_{b1} , c_{b2} , $\tilde{\sigma}$, κ , c_{w1} and c_{v1} are the constants defined for the turbulence model in [196], $\tilde{d} = d - f_d \max(0, d - C_{DES}\Delta)$, d is the distance to the closest wall, C_{DES} is the DES coefficient and Δ is based on the largest dimension of the grid element. The quantity f_d is given by $f_d = 1 - \tanh([Ar_d]^p)$, which is designed to be 1 in the LES region and the constants $A = 8$ and $p = 3$. The quantity r_d is defined as: $r_d = \tilde{\nu}/(\sqrt{u_{i,j}u_{i,j}}\kappa^2d^2)$, where $u_{i,j}$ is the velocity gradient and κ is the Kármán constant. Setting $f_d = 0$ yields RANS setting ($\tilde{d} = d$) and when $f_d = 1$, $\tilde{d} = \min(d, C_{DES}\Delta)$ which corresponds to the DES model. The empirical constant C_{DES} was calibrated to 0.65. The value of \tilde{S} is limited using the method given in [125] to avoid numerical problems. In Eqs. (8.5-8.7), $\tilde{\nu}_D$ and $\tilde{\nu}_H$ denote the Dirichlet and Neumann conditions on the eddy viscosity respectively, $\mathbf{n}^\tilde{\nu}$ denotes the unit normal to the Neumann boundary and $\tilde{\nu}_0$ represents the initial condition for the eddy viscosity.

8.2.2 Semi-discrete variational form

In this section, we write the variational formulation for the turbulence transport equation under the positivity preserving framework discussed in Chapter 3 to reduce the spurious oscillations in the solution corresponding to the eddy viscosity. Before proceeding to the presentation of the spatial PPV-based variational formulation, we first discretize the equation in the time domain via generalized- α time integration [153, 164]. Let $\partial_t\tilde{\nu}^{n+\alpha_m^f}$ be the derivative of $\tilde{\nu}$ with respect to time at $t^{n+\alpha^f}$. The expressions for the temporal discretization can be written as:

$$\tilde{\nu}^{n+1} = \tilde{\nu}^n + \Delta t \partial_t \tilde{\nu}^n + \gamma^f \Delta t (\partial_t \tilde{\nu}^{n+1} - \partial_t \tilde{\nu}^n), \quad (8.8)$$

$$\partial_t \tilde{\nu}^{n+\alpha_m^f} = \partial_t \tilde{\nu}^n + \alpha_m^f (\partial_t \tilde{\nu}^{n+1} - \partial_t \tilde{\nu}^n), \quad (8.9)$$

$$\tilde{\nu}^{n+\alpha^f} = \tilde{\nu}^n + \alpha^f (\tilde{\nu}^{n+1} - \tilde{\nu}^n), \quad (8.10)$$

where Δt is the time step size, α_m^f , α^f and γ^f are the generalized- α parameters defined in Eq. (4.20). The time discretized turbulence transport equation is therefore,

$$\begin{aligned} & \partial_t \tilde{\nu}^{n+\alpha_m^f} + (\mathbf{u}^f - \mathbf{u}^m) \cdot \nabla \tilde{\nu}^{n+\alpha^f} - c_{b1}\tilde{S}\tilde{\nu}^{n+\alpha^f} + c_{w1}f_w \frac{(\tilde{\nu}^{n+\alpha^f})^2}{\tilde{d}^2} \\ & - \frac{c_{b2}}{\tilde{\sigma}} (\nabla \tilde{\nu}^{n+\alpha^f})^2 - \frac{1}{\tilde{\sigma}} \nabla \cdot (\nu^f + \tilde{\nu}^{n+\alpha^f}) \nabla \tilde{\nu}^{n+\alpha^f} = 0. \end{aligned} \quad (8.11)$$

Chapter 8. PPV based Hybrid RANS/LES Turbulence Application

Equation (8.11) can be written in the form of convection-diffusion-reaction equation as follows:

$$\partial_t \tilde{\nu}^{n+\alpha_m^f} + \tilde{\mathbf{u}} \cdot \nabla \tilde{\nu}^{n+\alpha^f} - \nabla \cdot (\tilde{k} \nabla \tilde{\nu}^{n+\alpha^f}) + \tilde{s} \tilde{\nu}^{n+\alpha^f} = 0, \quad \text{on } \Omega^f(t), \quad (8.12)$$

where $\tilde{\mathbf{u}}$, \tilde{k} and \tilde{s} are the modified convection velocity, diffusion coefficient and reaction coefficient respectively, which are given as

$$\tilde{\mathbf{u}} = \mathbf{u}^f - \mathbf{u}^m - \frac{c_{b2}}{\tilde{\sigma}} \nabla \tilde{\nu}^{n+\alpha^f}, \quad \tilde{k} = \frac{1}{\tilde{\sigma}} (\nu^f + \tilde{\nu}^{n+\alpha^f}), \quad \tilde{s} = -c_{b1} \tilde{S} + c_{w1} f_w \frac{\tilde{\nu}^{n+\alpha^f}}{\tilde{d}^2}. \quad (8.13)$$

Defining the space of trial solution as $\mathcal{S}_{\tilde{\nu}}^h$ and that of the test function as $\mathcal{V}_{\tilde{\nu}}^h$ such that

$$\mathcal{S}_{\tilde{\nu}}^h = \{\tilde{\nu}_h \mid \tilde{\nu}_h \in H^1(\Omega^f(t)), \tilde{\nu}_h = \tilde{\nu}_D \text{ on } \Gamma_D^{\tilde{\nu}}(t)\}, \quad (8.14)$$

$$\mathcal{V}_{\tilde{\nu}}^h = \{\tilde{w}_h \mid \tilde{w}_h \in H^1(\Omega^f(t)), \tilde{w}_h = 0 \text{ on } \Gamma_D^{\tilde{\nu}}(t)\}, \quad (8.15)$$

the variational statement for the turbulence transport equation is given as: find $\tilde{\nu}_h(\mathbf{x}^f, t^{n+\alpha^f}) \in \mathcal{S}_{\tilde{\nu}}^h$ such that $\forall \tilde{w}_h \in \mathcal{V}_{\tilde{\nu}}^h$,

$$\begin{aligned} & \int_{\Omega^f(t)} \left(\tilde{w}_h \partial_t \tilde{\nu}_h + \tilde{w}_h (\tilde{\mathbf{u}} \cdot \nabla \tilde{\nu}_h) + \nabla \tilde{w}_h \cdot (\tilde{k} \nabla \tilde{\nu}_h) + \tilde{w}_h \tilde{s} \tilde{\nu}_h \right) d\Omega \\ & + \sum_{e=1}^{n_{el}} \int_{\Omega^e} \left((\tilde{\mathbf{u}} \cdot \nabla \tilde{w}_h + |\tilde{s}| \tilde{w}_h) \tau_t (\partial_t \tilde{\nu}_h + \tilde{\mathbf{u}} \cdot \nabla \tilde{\nu}_h - \nabla \cdot (\tilde{k} \nabla \tilde{\nu}_h) + \tilde{s} \tilde{\nu}_h) \right) d\Omega^e \\ & + \sum_{e=1}^{n_{el}} \int_{\Omega^e} \chi \frac{|\mathcal{R}(\tilde{\nu}_h)|}{|\nabla \tilde{\nu}_h|} k_s^{\text{add}} \nabla \tilde{w}_h \cdot \left(\frac{\tilde{\mathbf{u}} \otimes \tilde{\mathbf{u}}}{|\tilde{\mathbf{u}}|^2} \right) \cdot \nabla \tilde{\nu}_h d\Omega^e \\ & + \sum_{e=1}^{n_{el}} \int_{\Omega^e} \chi \frac{|\mathcal{R}(\tilde{\nu}_h)|}{|\nabla \tilde{\nu}_h|} k_c^{\text{add}} \nabla \tilde{w}_h \cdot \left(\mathbf{I} - \frac{\tilde{\mathbf{u}} \otimes \tilde{\mathbf{u}}}{|\tilde{\mathbf{u}}|^2} \right) \cdot \nabla \tilde{\nu}_h d\Omega^e = \int_{\Gamma_H^{\tilde{\nu}}(t)} \tilde{w}_h \tilde{\nu}_H d\Gamma, \end{aligned} \quad (8.16)$$

where the terms in the first line correspond to the Galerkin terms, the second line consists of the linear stabilization terms which convert the method to Galerkin/least-squares when $\tilde{s} > 0$ and to subgrid-scale when $\tilde{s} < 0$, thus maintaining the phase of the exact solution. Similar to the flow equations, the weighting function related to the diffusion coefficient is neglected here since the values are very small because of bi/trilinear finite element space considered in the present study. Terms in the fourth and fifth lines are the nonlinear stabilization terms in the streamline and crosswind directions while the term in the right-hand side of the equation is the Neumann boundary condition. The residual of the transport equation is given by

$$\mathcal{R}(\tilde{\nu}_h) = \partial_t \tilde{\nu}_h + \tilde{\mathbf{u}} \cdot \nabla \tilde{\nu}_h - \nabla \cdot (\tilde{k} \nabla \tilde{\nu}_h) + \tilde{s} \tilde{\nu}_h. \quad (8.17)$$

The linear stabilization parameter τ_t is given by:

$$\tau_t = \left[\left(\frac{2}{\Delta t} \right)^2 + \tilde{\mathbf{u}} \cdot \mathbf{G} \tilde{\mathbf{u}} + C_I \tilde{k}^2 \mathbf{G} : \mathbf{G} + \tilde{s}^2 \right]^{-1/2}, \quad (8.18)$$

where C_I and \mathbf{G} are the constant obtained from the inverse estimate and the contravariant tensor defined in Eq. (4.30).

The PPV parameters for the current context of the turbulence transport equation are given as:

$$\chi = \frac{2}{|\tilde{s}|h + 2|\tilde{\mathbf{u}}|}, \quad (8.19)$$

$$k_s^{\text{add}} = \max \left\{ \frac{||\tilde{\mathbf{u}}| - \tau_t |\tilde{\mathbf{u}}| \tilde{s} + \tau_t |\tilde{\mathbf{u}}| |\tilde{s}| |h|}{2} - (\tilde{k} + \tau_t |\tilde{\mathbf{u}}|^2) + \frac{(\tilde{s} + \tau_t \tilde{s} |\tilde{s}|) h^2}{6}, 0 \right\}, \quad (8.20)$$

$$k_c^{\text{add}} = \max \left\{ \frac{||\tilde{\mathbf{u}}| + \tau_t |\tilde{\mathbf{u}}| |\tilde{s}| |h|}{2} - \tilde{k} + \frac{(\tilde{s} + \tau_t \tilde{s} |\tilde{s}|) h^2}{6}, 0 \right\}, \quad (8.21)$$

where $|\tilde{\mathbf{u}}|$ is the magnitude of the convection velocity of the transport equation. The characteristic element length h is selected as the streamline element length.

The PPV method has been shown to preserve the positivity and boundedness of the numerical solution as well as deal with the negative reaction coefficients quite effectively in the different regimes. The method will, however, produce subgrid-scale-like solutions in the production regime which are inherently oscillatory in the propagation region. The eddy viscosity will be negative in this regime; we adopt a clipping of the solution in that situation. This need for clipping is due to the modeling deficiency of the phenomenological turbulence equation to obtain a stable and convergent solution. We apply the method to the conventional S-A turbulence model without any modifications to the model equations but using the nonlinear finite element stabilization strategy. We next discuss the numerical studies conducted for the flow across a circular cylinder at high Reynolds numbers and then demonstrate the turbulent FSI solver for the flexible riser VIV.

8.3 Flow across circular cylinder at Re=3,900 and Re=140,000

Before we study the VIV of a long flexible riser, we first validate the application of the positivity preserving method to the DDES turbulence model for a stationary circular cylinder at subcritical

Reynolds numbers.

8.3.1 Mesh characteristics

We validate the application of the PPV method in the S-A model against the experimental data and computational simulations for the uniform flow across a stationary circular cylinder at $Re = 3,900$ (laminar separation) and $Re = 140,000$ (turbulent separation). It is known that the success of DES depends on the quality of the mesh and the isotropic element size in the region where LES mode of the model is to be activated. The grid we adopted for our study is similar to that used in [13]. The schematic of the computational domain is depicted in Fig. 8.1. The diameter of the stationary circular cylinder is denoted by D . The distances of the

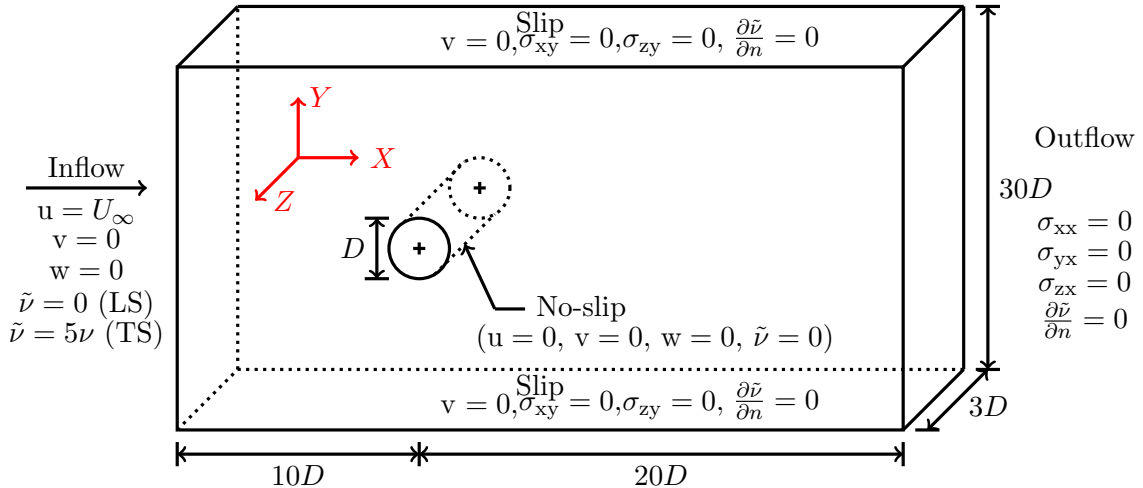


Figure 8.1: A schematic of the flow past a three-dimensional circular cylinder at high Reynolds number. The computational setup and boundary conditions are shown for the Navier-Stokes and DDES equations. Here, $\mathbf{u}^f = (u, v, w)$ denotes the components of the fluid velocity, LS and TS denote the laminar separation and turbulent separation cases respectively.

inlet and outlet boundaries from the center of the cylinder are $10D$ and $20D$ respectively. The side walls are equidistant from the center of the cylinder. The distance between the side walls is $30D$, which corresponds to a blockage of 3.3% . No-slip boundary condition with $\tilde{\nu} = 0$ is imposed on the wall of the cylinder with slip conditions at the side walls. A periodic boundary condition is applied along the Z -axis. The freestream velocity at the inlet boundary is along the X -axis with $\tilde{\nu} = 0$ for the laminar separation case and $\tilde{\nu} = 5\nu$ for $Re = 140,000$, where ν is the molecular viscosity of the fluid. The span of the cylinder should be long enough to capture the three-dimensional turbulence structures. The axis of the cylinder is parallel to the

Z -axis with a spanwise width of $3D$ in the present simulation. A non-zero initial condition for the eddy viscosity ($\tilde{\nu} = 5\nu$) is imposed. A uniform flow field is used as an initial condition and the transition period is taken up to $tU_\infty/D = 100$. All the statistical results are evaluated from $tU_\infty/D = 100 - 250$ for $Re = 140,000$ case and from $tU_\infty/D = 100 - 450$ for $Re = 3,900$ case. This ensures capturing of about 70 vortex shedding cycles at $Re = 3,900$ and 45 shedding cycles at $Re = 140,000$.

The three-dimensional computational domain is discretized by unstructured finite element mesh which consists of 1,457,595 grid nodes and 1,421,820 eight-node brick elements. The boundary layer thickness is $0.25D$, with the stretching ratio, $\Delta y_{j+1}/\Delta y_j$ of 1.25 and the number of divisions in the wall-normal direction is 37 which gives a distance of the first grid point of $1.623 \times 10^{-5}D$ from the cylinder wall giving $y^+ \approx 0.12$ for $Re = 140,000$ and $y^+ \approx 0.004$ for $Re = 3,900$. We have followed the guidelines given in [197] for making the mesh in an open-source mesh generator [188]. The grid then varies isotropically in the LES focus region. The spanwise grid size, Δz is $0.05D$ dividing the spanwise length of $3D$ into 60 layers. This process ensures the isotropic property of the elements in the LES focus region of the mesh. The time

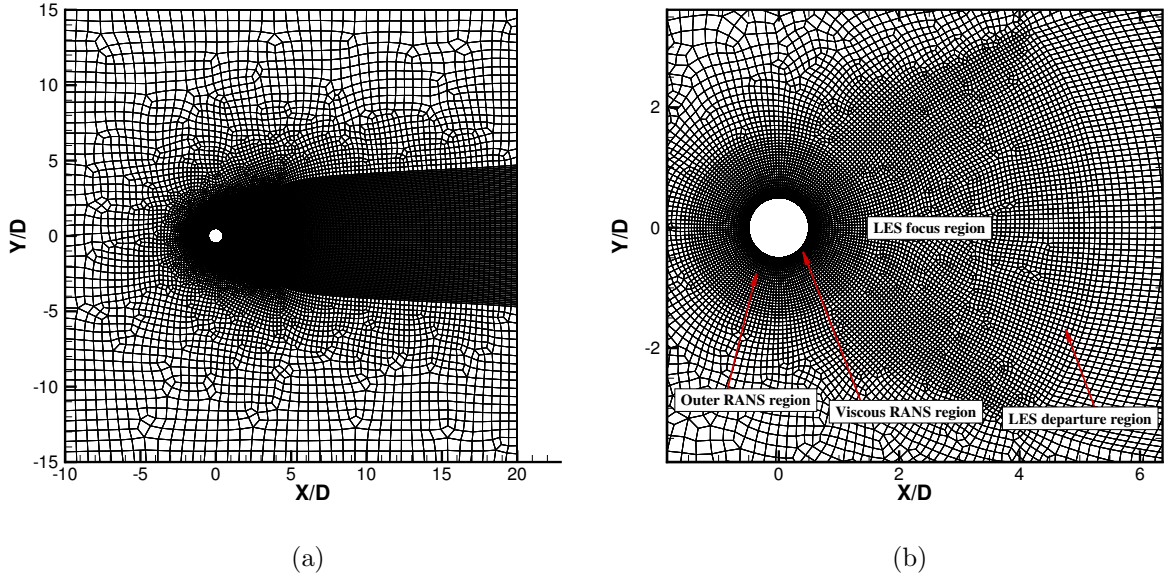


Figure 8.2: Mesh characteristics for the flow past a circular cylinder: (a) mesh in the full computational domain in the cross-sectional X - Y plane, (b) various mesh regions around the cylinder for the well-designed DES mesh. While the elements in the LES focus region are isotropic and well resolved for capturing the wake dynamics, the viscous RANS region maintains $y^+ < 1$ close to the cylinder surface.

step size, Δt is selected as 0.05 to maintain the Courant number, Co defined by $|\mathbf{u}^f| \Delta t / \Delta \leq 1$ in the LES focus region, where Δ is the largest dimension of the grid element. The details of the mesh and the various flow regions are given in Figs. 8.2(a) and 8.2(b) respectively.

8.3.2 Hydrodynamic coefficients

The hydrodynamic parameters obtained from the DDES at $Re = 3,900$ and $Re = 140,000$ are compared against the experimental results and the numerical simulations in Tables 8.1 and 8.2, respectively. The turbulent separation case can be implemented in an experiment by making the boundary layer turbulent before separation by tripping. Instead, the compared experimental values are from experiments at very high Reynolds number [11]. We observe that the various quantities such as the mean drag coefficient (\bar{C}_D), root mean square of the lift coefficient (C_L^{rms}), Strouhal frequency (St), length of the recirculation bubble (L_r/D) and the base pressure coefficient (C_{pb}) of the stationary cylinder are in good agreement with the compared results. L_r/D is the measured length from the base of the cylinder to the point of null mean streamline velocity along the centerline behind the cylinder. The fluid loads on the

Table 8.1: Comparison of the hydrodynamic parameters pertaining to the flow across a circular stationary cylinder at $Re = 3,900$ (Laminar Separation).

Study	\bar{C}_D	C_L^{rms}	St	L_r/D	$-C_{pb}$
Present	1.0069	0.1715	0.2075	1.462	0.8998
DES [198]	1.0246	0.1897	0.2166	1.4909	-
Experiment [9, 199, 200]	0.99 ± 0.05	-	0.215 ± 0.005	1.4 ± 0.1	0.88 ± 0.05

Table 8.2: Comparison of the hydrodynamic parameters pertaining to the flow across a circular stationary cylinder at $Re = 140,000$ (Turbulent Separation).

Study	\bar{C}_D	C_L^{rms}	St	L_r/D	$-C_{pb}$
Present	0.5782	0.0957	0.2930	1.113	0.6991
DES (TS1) [13]	0.57	0.08	0.30	1.1	0.65
DES (TS2) [13]	0.59	0.06	0.31	1.2	0.67
Experiment [201]	0.59	-	0.29	-	0.72
Experiment [11]	0.62-0.74	-	0.27	-	0.5-0.9

cylinder are evaluated by integrating the surface traction taking into account the first layer of

elements on the cylindrical surface. The instantaneous force coefficients are defined as

$$C_L = \frac{1}{\frac{1}{2}\rho^f U_\infty^2 D} \int_{\Gamma} (\boldsymbol{\sigma}^f \cdot \mathbf{n}) \cdot \mathbf{n}_y d\Gamma, \quad (8.22)$$

$$C_D = \frac{1}{\frac{1}{2}\rho^f U_\infty^2 D} \int_{\Gamma} (\boldsymbol{\sigma}^f \cdot \mathbf{n}) \cdot \mathbf{n}_x d\Gamma, \quad (8.23)$$

where \mathbf{n}_x and \mathbf{n}_y are the Cartesian components of the unit normal \mathbf{n} to the cylindrical surface and $\boldsymbol{\sigma}^f$ is the fluid stress tensor with Γ being the surface boundary of the cylinder. The pressure coefficient is defined as

$$C_p = \frac{p - p_\infty}{\frac{1}{2}\rho^f U_\infty^2}, \quad (8.24)$$

where p and p_∞ are the pressure at the concerned point and pressure at far-field respectively. The base pressure coefficient (C_{pb}) is obtained by replacing p with the base pressure of the cylinder.

The time histories of the hydrodynamic force coefficients and the frequency spectrum of the lift coefficient are depicted in Figs. 8.3 and 8.4 respectively. Comparison of the mean

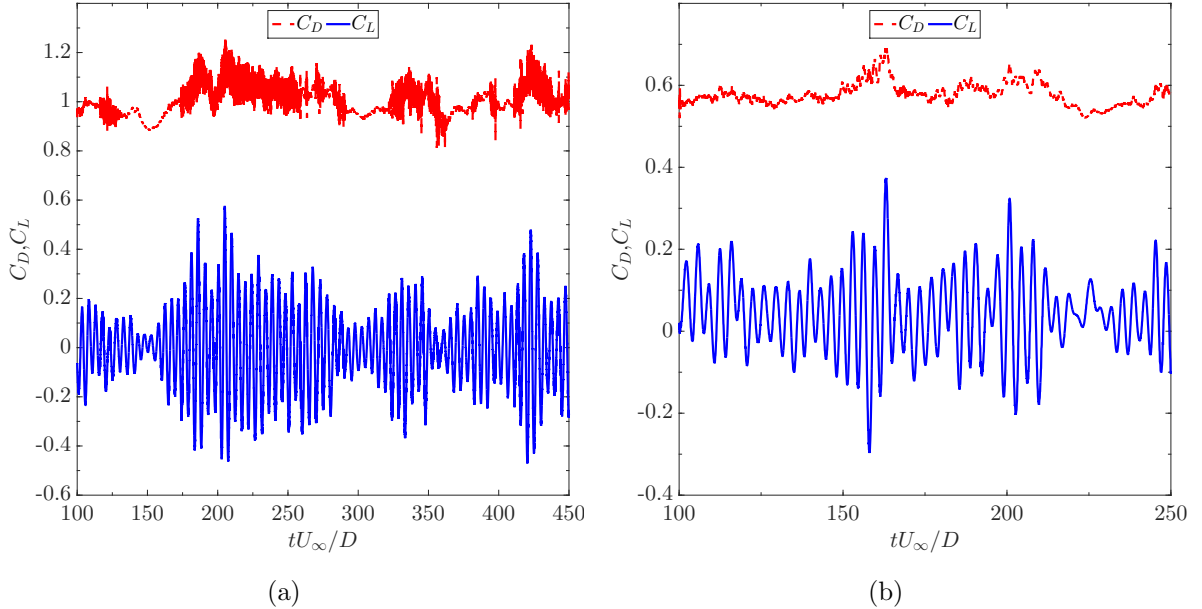


Figure 8.3: Time histories of the hydrodynamic force coefficients for the flow past a circular stationary cylinder at two subcritical Reynolds numbers: (a) $Re = 3,900$, and (b) $Re = 140,000$.

pressure coefficient with the angle around the circumference of the cylinder is shown in Fig. 8.5. A good agreement is observed for both the Reynolds number cases. In Fig. 8.5(a), the role of the positivity preserving method on the pressure coefficient along the circumference of

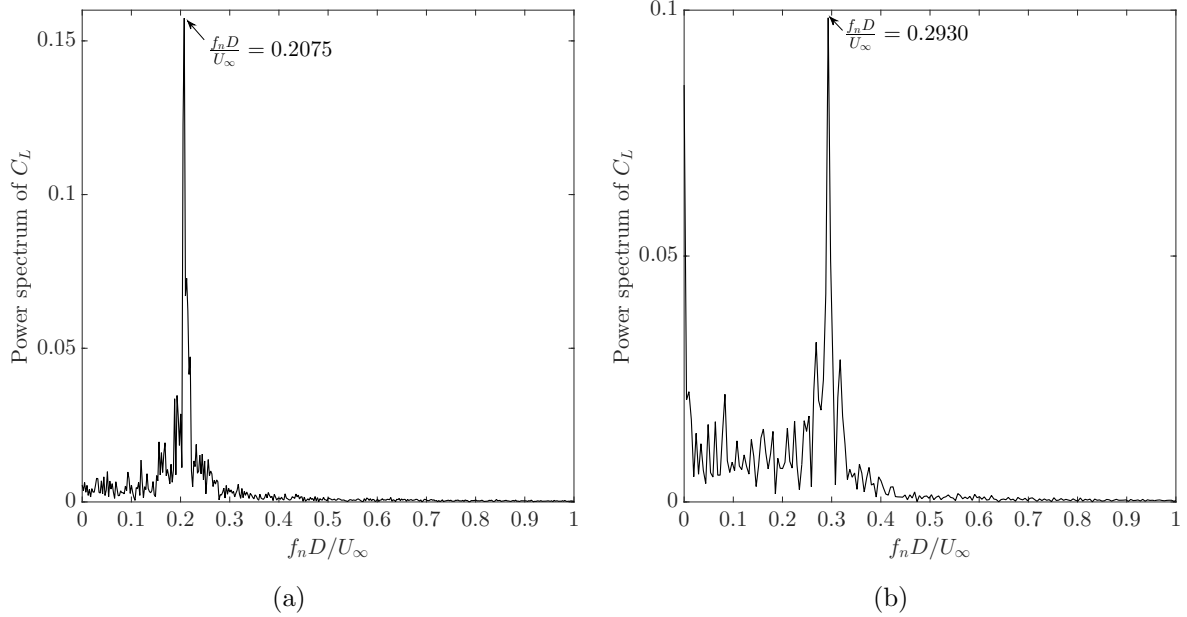


Figure 8.4: Spectrum of the lift coefficient C_L for the stationary circular cylinder at: (a) $Re = 3,900$, (b) $Re = 140,000$.

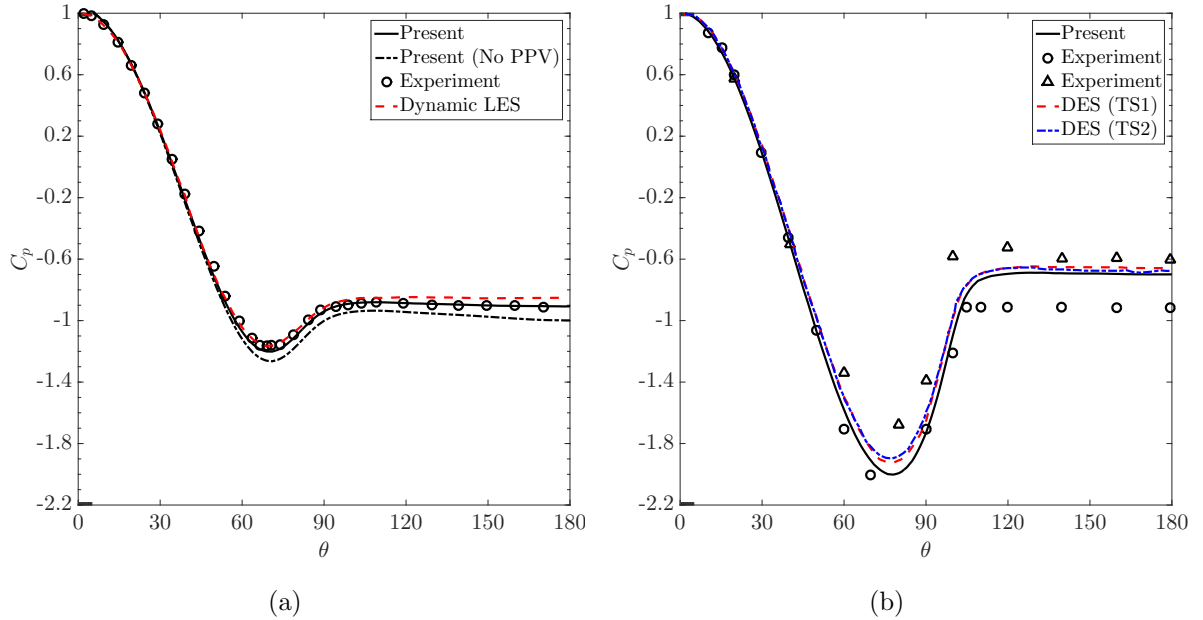


Figure 8.5: Flow past a stationary circular cylinder: Variation of C_p along the circumference with angle θ at (a) $Re = 3,900$: (—) Present simulation, (- -) Present (no PPV method), (○) Experiment [9], (---) Dynamic LES [10]; (b) $Re = 140,000$: (—) Present simulation, (○) Experiment at $Re = 8.5 \times 10^6$ [11], (△) Experiment at $Re = 7.6 \times 10^6$ [12], (---) DES [13], (- · -) DES [13]. Here the angle $\theta = 0$ denotes the stagnation point.

the cylinder is also illustrated. It is observed that the absence of the PPV treatment does not lead to a good prediction of the pressure distribution C_p in the leeward side of the cylinder.

This suggests that the nonlinear stabilization based on the PPV method is crucial to capture the high-gradients in the shear layer dominated regions in the near-wake region of the cylinder. Moreover, over-predicted values of the hydrodynamic coefficients are obtained when only the GLS-based stabilized method is employed for the DDES transport equation. This study confirms the effectiveness and the need of the PPV treatment for the turbulence transport equation based on the SA-DDES model.

8.3.3 Flow visualization

The turbulent wake details of the complex three-dimensional fluid flow around the cylinder for $Re = 3,900$ and $Re = 140,000$ are visible in Figs. 8.6(a) and 8.6(c) respectively. The vortex structures are depicted in the figure using the Q -criterion at the iso-surface of 0.25 colored by the normalized freestream velocity. The expected narrower wake and the shifting of turbulent separation point down to further back of the cylinder for $Re = 140,000$ is clearly visible. We can observe the large rolls of spanwise vorticity with the streamwise ribs connecting the rolls through the braid region in Figs. 8.6(b) and 8.6(d). The braid region consists of more fine eddies and small turbulent structures which depicts the resolution of smaller scales in the turbulence modeling. As it is well known, turbulence is a multiscale phenomenon with energy being generated by the large-sized eddies. These large eddies then lose this energy by the vortex stretching mechanism and disintegrate into smaller eddies, losing the energy to the molecular viscosity, known as the energy cascade. Unsteady RANS equation does not resolve these smaller eddies which leads to its ineffectiveness in turbulent simulations while DDES acts as LES-type in the separated flow region behind the cylinder and captures these crucial fluctuations. In the inertial range of the cascade, the slope of the energy spectrum with the wavenumber/frequency remains constant at $-5/3$ obeying the Kolmogorov's rule. Figs. 8.7(a) and 8.7(b) depict such spectrum of the transverse velocity fluctuations at the downstream locations along the centerline of the cylinder wake at $Re = 3,900$ and $Re = 140,000$ respectively.

8.3.4 Comparison of flow statistics

The behavior of the mean streamwise and transverse velocities at different locations in the wake of the cylinder at $Re = 3,900$ is shown in Fig. 8.8. We consider two experimental and two

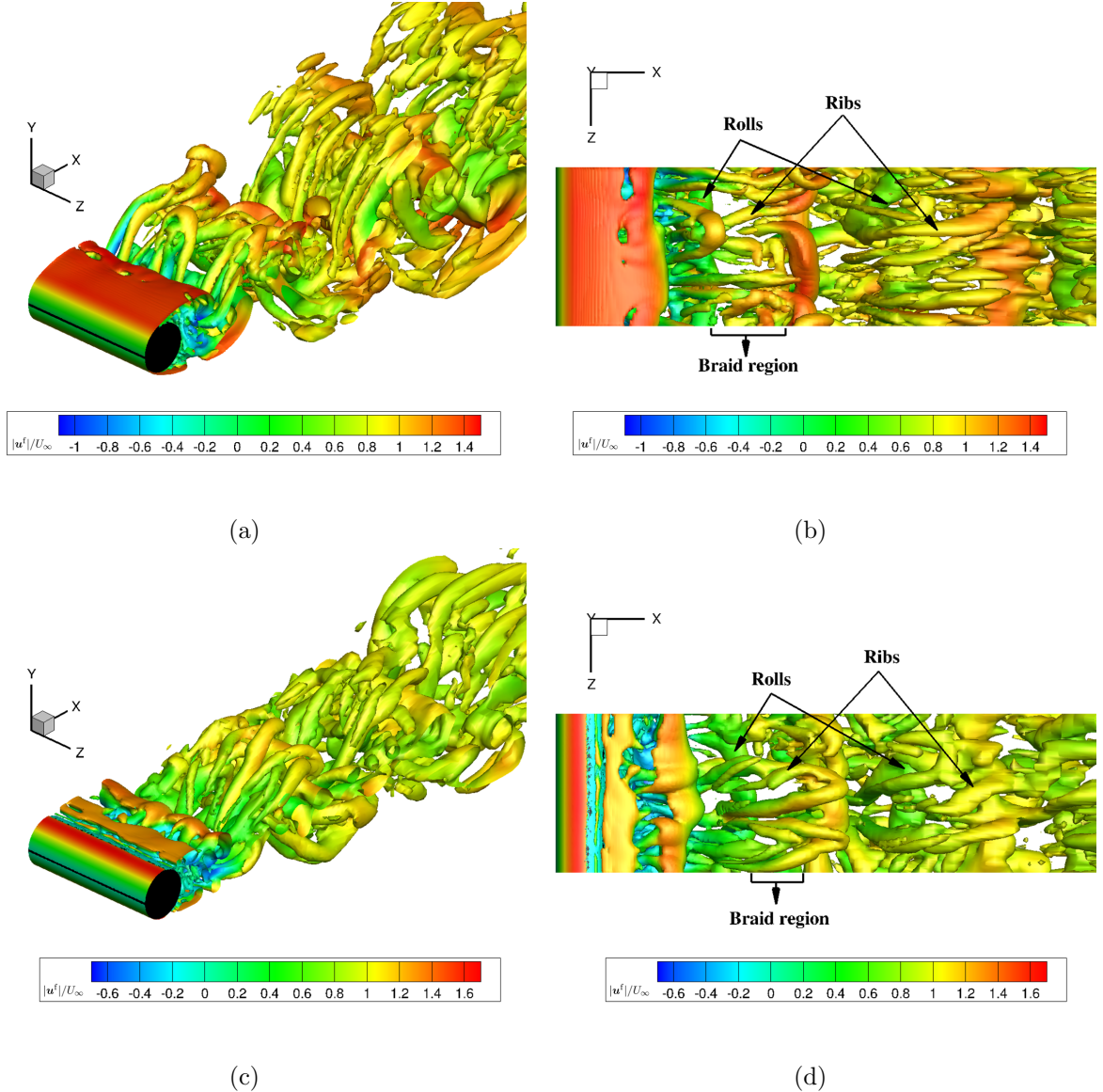


Figure 8.6: Flow past a stationary circular cylinder at subcritical Reynolds numbers: Vortical wake structures of iso-surfaces of $Q^+ = 0.25$ colored by $|u^f|/U_\infty$ at $tU_\infty/D = 150$: Three-dimensional view at (a) $Re = 3,900$ and (c) $Re = 140,000$. Top-view- The rolls with the braid region consisting of small-scale structures and the ribs can be observed at (b) $Re = 3,900$ and (d) $Re = 140,000$.

numerical simulation results for comparison in Fig. 8.8, namely LES at $Re = 3,900$ using (i) sixth-order compact centered difference incompressible Navier-Stokes solver for aspect ratio of $L/D = \pi D$ and $961 \times 960 \times 48$ points [14], (ii) Galerkin B-Spline method having a dynamic Smagorinsky subgrid-scale model with a grid consisting of $205 \times 185 \times 48$ points with a spanwise length of πD [15], and the PIV experiments at $Re = 3,900$ by [14] with aspect ratio of cylinder, $L/D = 20$ and by [16] with spanwise length of $21D$ with photographs taken at a frequency of 6

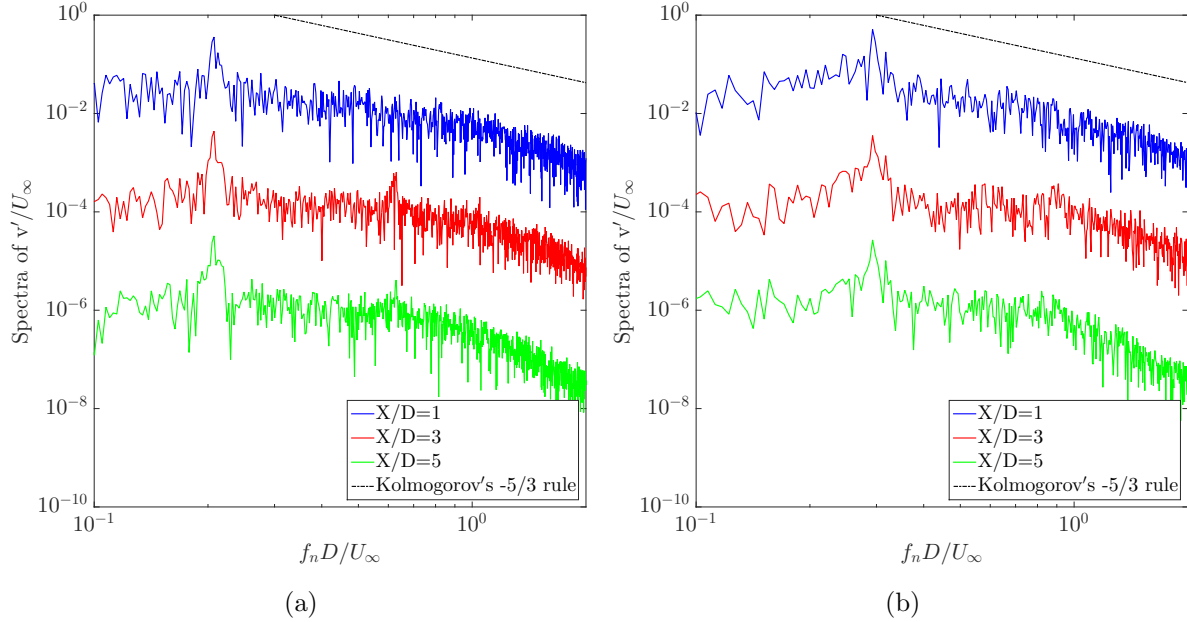


Figure 8.7: Flow past a stationary circular cylinder: Spectra of the transverse velocity and the Kolmogorov's rule at (a) $Re = 3,900$, (b) $Re = 140,000$.

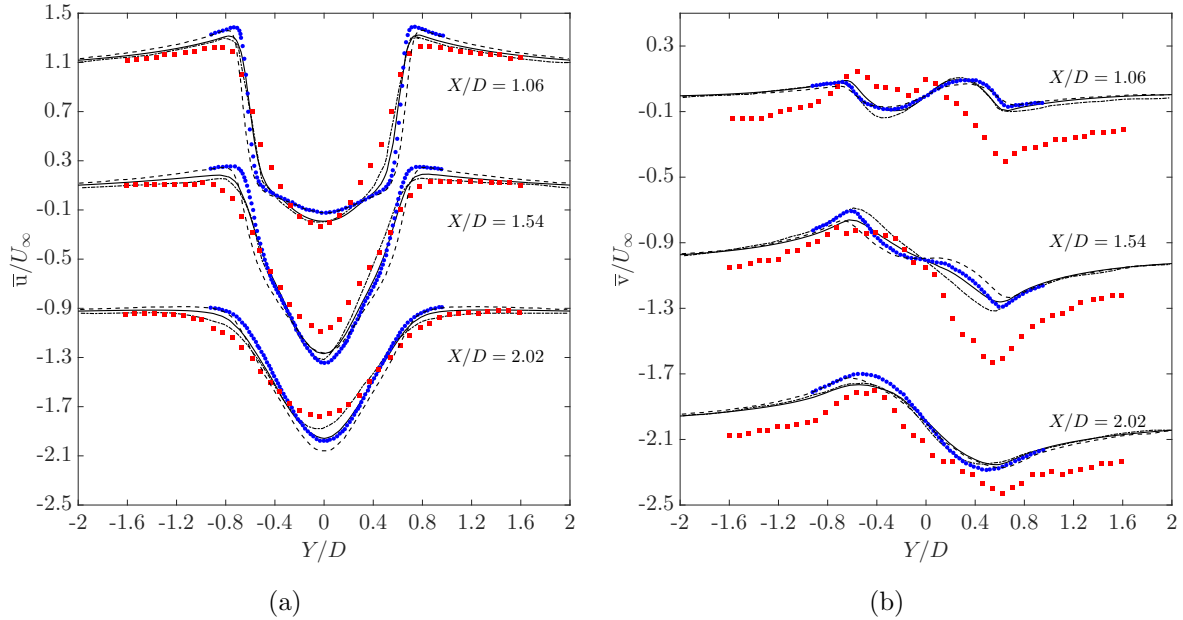


Figure 8.8: Mean velocity at three locations in the wake of the stationary circular cylinder at $Re = 3,900$: (a) Streamwise velocity; (b) Transverse velocity. (—) Present simulation, (---) LES [14], (···) B-Spline simulation [15], (●) PIV experiment [14], (■) Experiment [16].

Hz containing 29 vortex shedding cycles. It can be inferred from the results that at $Re = 3,900$, the turbulent characteristics of the flow are successfully captured by the current mesh resolution.

After studying and validating the PPV-based turbulent formulation for a stationary cylin-

der at high Reynolds number, we now present a numerical demonstration of vortex-induced vibrations along an offshore riser at $Re = 4,000$ and compare the results with the experimental data.

8.4 VIV of an offshore riser

Understanding the flow dynamics of a flexible offshore riser is a complex problem since vortex shedding can excite several modes of the riser, which makes the dynamic response to be multi-modal and multi-frequency. In this study, we have made an attempt to understand the response of the flexible riser while comparing the results with that of the experiment [135] at Reynolds number of $Re = 4,000$. We first validate the flexible riser using the experimental data for the case with an incoming uniform current of 0.2 m/s (case no. 1103 in [135]). All the plotted values are non-dimensionalized with respect to the riser diameter D and the incoming flow velocity U_∞ .

8.4.1 Key fluid-structure parameters

The riser is modeled using the governing equation of a uniform beam subjected to a tension P neglecting the damping and shear effects (as shown in Fig. 8.9(a)). We use the modal analysis to predict the displacement of the flexible long riser for which the description can be found in Section 4.3.2.2. The non-dimensional parameters used for the simulation are:

$$Re = \frac{\rho^f U_\infty D}{\mu^f} = 4000, \quad m^* = \frac{m^s}{\pi D^2 L \rho^f / 4} = 2.23, \quad U_r = \frac{U_\infty}{f_1 D} = 5.6, \quad (8.25)$$

$$EI^* = \frac{EI}{\rho^f U_\infty^2 D^4} = 2.1158 \times 10^7, \quad P^* = \frac{P}{\rho^f U_\infty^2 D^2} = 5.10625 \times 10^4, \quad (8.26)$$

where Re , m^* , U_r , EI^* and P^* are the non-dimensional quantities, viz., Reynolds number, mass ratio, nominal reduced velocity, flexural rigidity and axial tension respectively. The nominal reduced velocity is evaluated at the first modal natural frequency of the structure f_1 .

8.4.2 Mesh characteristics

We validate the flexible riser model and the response characteristics against the experimental data for the uniform flow across the riser at the Reynolds number, $Re = 4000$. The schematic

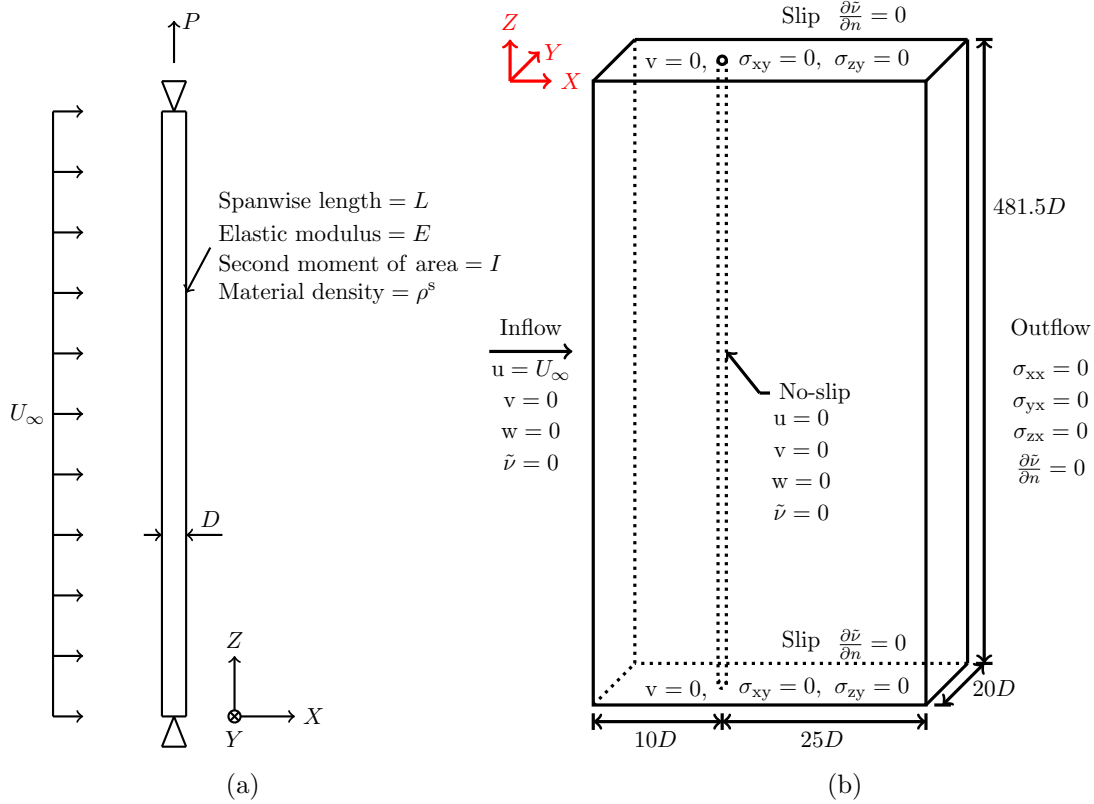


Figure 8.9: A long flexible riser model in uniform current flow along the Z -axis: (a) Pinned-pinned tensioned riser with uniform flow, (b) Sketch to illustrate the computational setup and boundary conditions for the PPV-based DDES on flow past a flexible riser. Here, $\mathbf{u}^f = (u, v, w)$ denotes the fluid velocity components. Consistent with the experimental measurement, a tensioned beam with the pinned at both ends and free to oscillate in the IL (X) and CF (Y) directions is employed in the numerical simulation.

of the computational domain is depicted in Fig. 8.9(b). The distances of the inlet and outlet boundaries from the center of the riser are $10D$ and $25D$ respectively. The side walls are equidistant from the center of the riser with a distance of $10D$ on each side corresponding to a blockage of 5%. No-slip boundary condition with $\tilde{v} = 0$ is imposed at the riser wall with slip conditions at the side-wall planes and planes perpendicular to the axis of the riser. The freestream velocity at the inlet boundary is along the X -axis with $\tilde{v} = 0$. The riser is $481.5D$ in the spanwise direction (along the Z -axis).

The requirement for obtaining an economical solution for a large-scale problem (e.g. flexible riser VIV) is to determine the minimum number of degrees of freedom to describe the flow characteristics and loads with sufficient accuracy. The resolution of the boundary layer, near-and far-wake regions are some of the challenges. The computational domain is discretized by unstructured finite element mesh with a relatively coarser grid in the $X-Y$ plane compared

to the mesh employed in Section 8.3.1 to maintain a reasonable level of boundary layer and wake resolution. The discretization in the direction parallel to the riser axis is varied in the simulation for the mesh convergence study. The mesh characteristics are summarized in Table 8.3. The number of divisions along the circumference of the riser cross-section is taken as 160

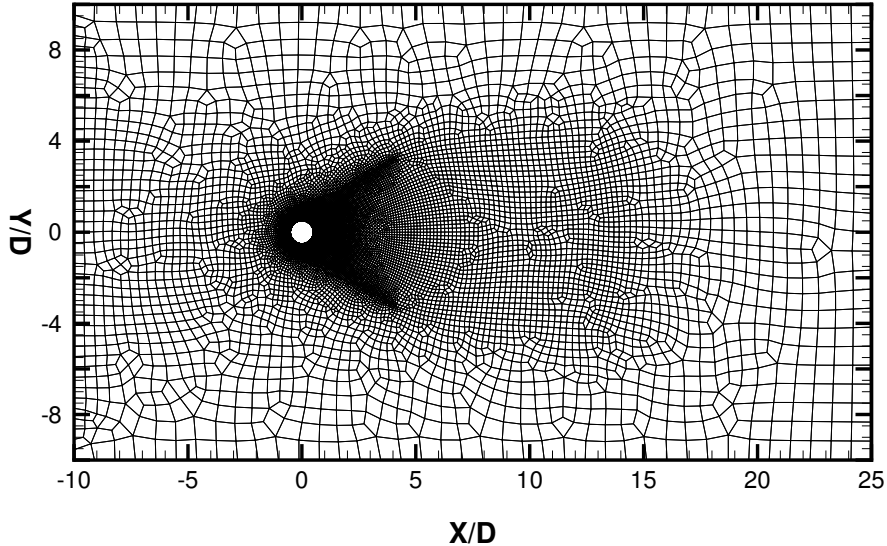


Figure 8.10: Uniform flow past a long flexible riser model: Two-dimensional mesh in the X - Y plane employed in the computation of flexible riser VIV. This mesh is extruded in the third dimension to obtain the three-dimensional mesh.

Table 8.3: Mesh details for flexible riser with $L/D = 481.5$ in a uniform current flow at $Re = 4000$.

Mesh	Number of nodes	Number of elements	Spanwise layers
M1	3,247,155	3,200,800	200
M2	6,478,155	6,401,600	400
M3	12,940,155	12,803,200	800

for all the cases. The boundary layer thickness of $0.25D$, with the stretching ratio, $\Delta y_{j+1}/\Delta y_j$ of 1.15 and the number of divisions in the wall-normal direction are selected such that $y^+ < 1$. A representative two-dimensional layer of the grid for the problem is shown in Fig. 8.10. The non-dimensional time step size, $\Delta t U_\infty / D$ is selected as 0.1.

8.4.3 Amplitude response

The time histories of the amplitude response of the position $z/L = 0.55$ of the riser are shown in Fig. 8.11 for the finest mesh M3. The simulation was run till a non-dimensionalized time of $tU_\infty/D = 800$ which consisted of 8000 time steps during the simulation. However, we have

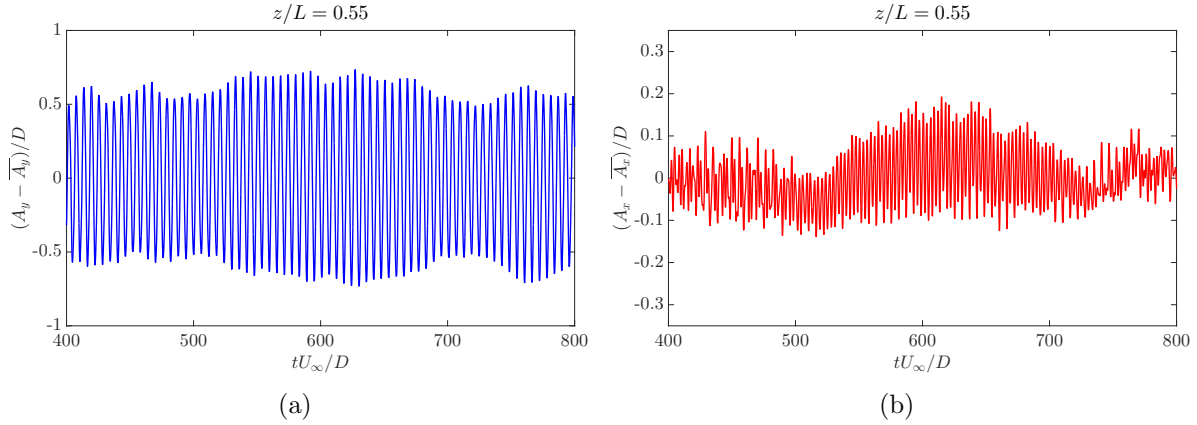


Figure 8.11: Uniform current flow past a flexible riser model $L/D = 481.5$ at $(Re, m^*, U_r) = (4000, 2.23, 5.6)$: Dependence of riser response at $z/L = 0.55$ with spanwise resolution for 800 layers: (a) cross-flow response and (b) in-line response.

shown the statistics for $tU_\infty/D \in [400, 800]$ to avoid any initial transient effects. It is observed that the response has a large variation in the in-line direction in meshes M1 and M2 but it reduces in M3. However, the cross-flow amplitude maintains a similar trend across the different mesh resolutions.

Figure 8.12 shows the comparison of the root mean square values of the in-line and cross-flow amplitude along the riser for the three meshes employed in the study. The notations used in the figures are given as follows: A_x and A_y are the displacement amplitude values at a point along the riser while \bar{A}_x and \bar{A}_y represent the temporal mean values of the in-line and cross-flow displacements at a particular spanwise location, respectively. The root mean square values of the amplitude are given by:

$$A_{x,\text{rms}} = \sqrt{\frac{1}{N} \sum_{i=1}^N (A_{x,i} - \bar{A}_x)^2}, \quad A_{y,\text{rms}} = \sqrt{\frac{1}{N} \sum_{i=1}^N (A_{y,i} - \bar{A}_y)^2}, \quad (8.27)$$

where N denotes the number of samples taken which is 4000 in this case. While the simulated cross-flow amplitude is in good agreement with the experimental measurement, as shown in Fig. 8.12, there is some over-prediction of the in-line response $A_{x,\text{rms}}/D$. The difference in

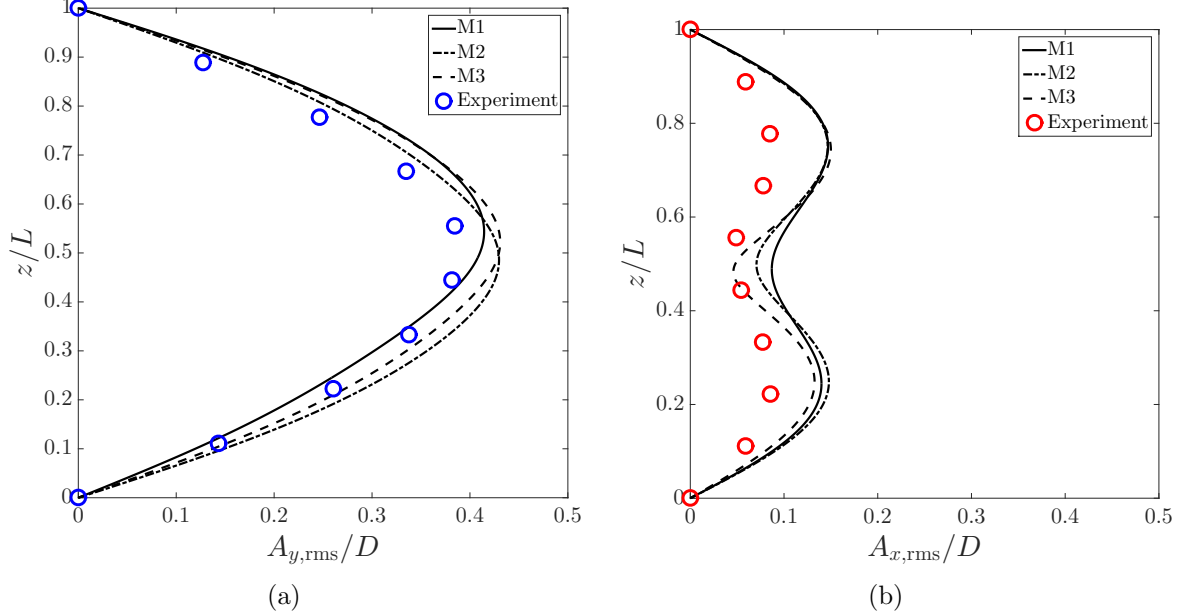


Figure 8.12: Uniform current flow past a flexible riser model $L/D = 481.5$ at $(Re, m^*, U_r) = (4000, 2.23, 5.6)$: Variation of the root mean square amplitude along the span of the riser for different employed meshes: (a) Cross-flow amplitude; (b) In-line amplitude. The first mode (fundamental) response for the CF and the second mode for the IL can be seen.

the peak in-line displacement between the numerical and experimental measurements is $< 15\%$ with respect to the total peak rms amplitude A/D , where $A = \sqrt{(A_{x,\text{rms}}^2 + A_{y,\text{rms}}^2)}$. Owing to a sensitive and chaotic-like response of the in-line amplitude, the absolute difference between the numerical and experimental measurements is up to $\sim 55\%$ around the peak location. As clearly evident in Fig. 8.11 (b), the in-line amplitude is quite aperiodic and non-stationary over the long time window of $tU_\infty/D \in [400, 800]$, whereas the cross-flow amplitude exhibits a relatively regular and stationary response. Due to such sensitivity, small numerical and experimental uncertainties in complex physical phenomena (e.g., the lock-in range and boundary-layer separation) can lead to a large impact on the in-line response and the drag force. From a practical viewpoint, the in-line response is several factors smaller than the cross-flow amplitude, thus a good estimate of the cross-flow response is generally sufficient for the riser fatigue study. Nonetheless, there is a need for further study to understand the role of the effects of variable tension on the lock-in range and the roughness effect on the laminar flow separation over the riser surface. As the performance of the mesh M3 is the best among the different types of meshes considered, we present the results corresponding to the mesh M3.

The riser response envelope in a uniform current flow is illustrated in Fig. 8.13. It can be

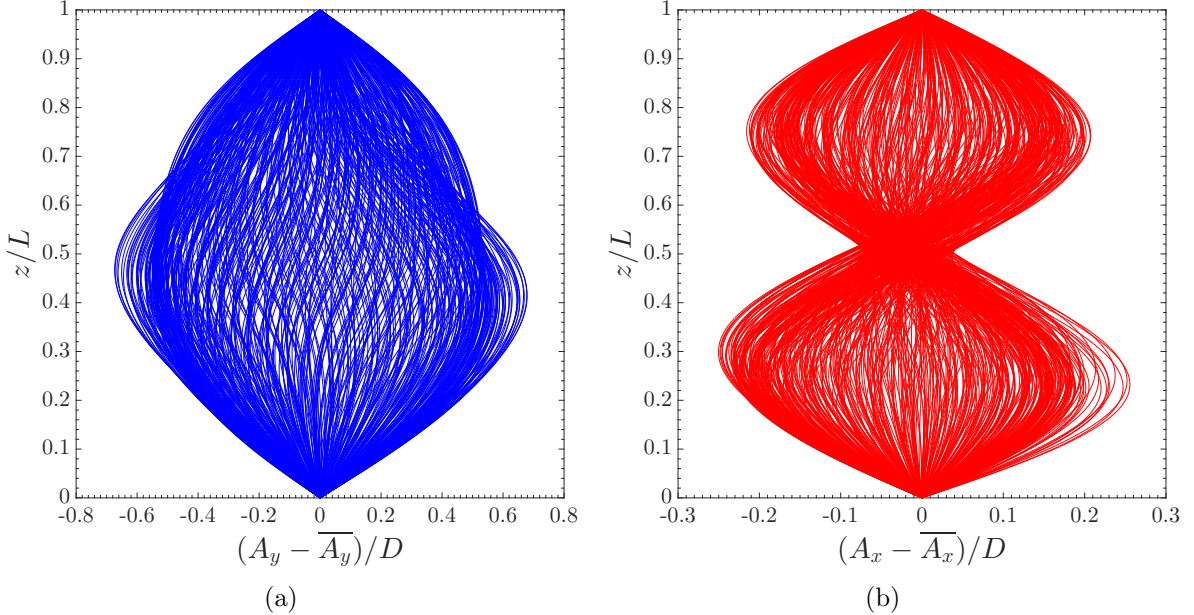


Figure 8.13: Riser response envelope with spanwise resolution of 800 layers for uniform current flow past a flexible riser model at $(Re, m^*, U_r) = (4000, 2.23, 5.6)$: (a) Cross-flow and (b) In-line directions. The riser is vibrating in the fundamental mode in the CF and the second mode for the IL directions.

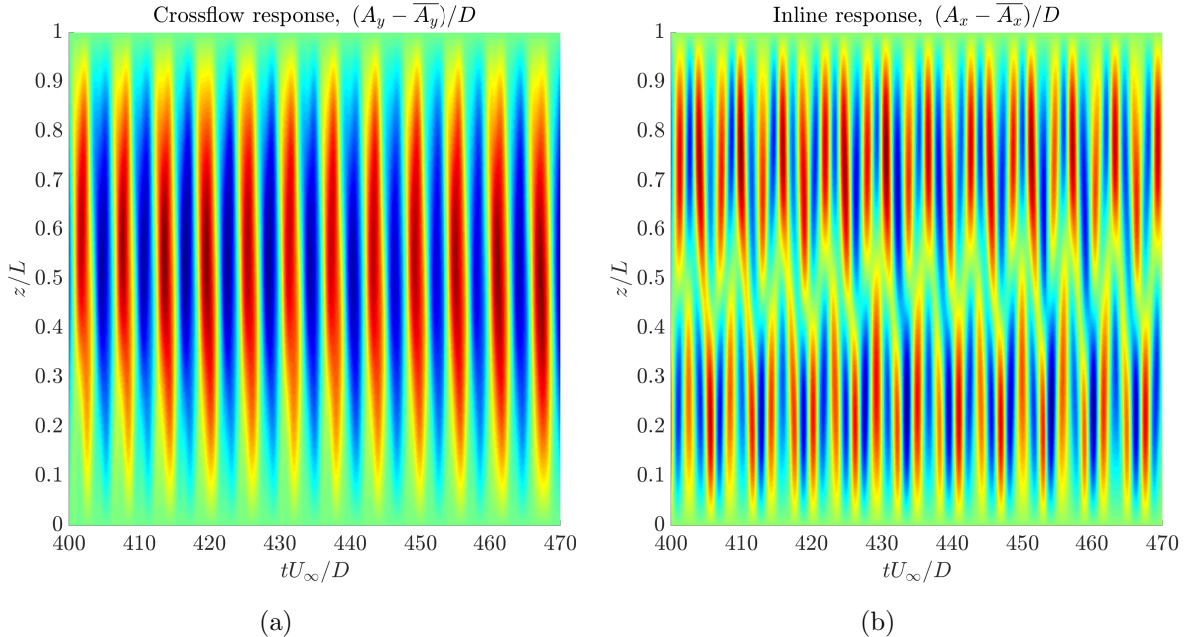


Figure 8.14: Standing wave response of flexible riser VIV with spanwise resolution of 800 layers for uniform current flow past a flexible riser model at $(Re, m^*, U_r) = (4000, 2.23, 5.6)$: (a) Cross-flow and (b) In-line directions. While the CF resonant response is at the fundamental mode, the IL wave response has a second mode pattern.

inferred that the riser vibrates with a dominated second mode in the in-line (IL) direction and the first mode in the cross-flow (CF) direction. Since the amplitudes of vibration are coupled to the flow physics and the hydrodynamic forces, we observe this phenomenon. Generally, the dominant frequency of the in-line vibration is twice that of cross-flow vibration for the flow across the cylinder. This is reflected in the dominant response modes of the riser. The riser response along the riser span is plotted as a function of time in Fig. 8.14.

We can observe the twice frequency in the in-line response as compared to the cross-flow response. We also notice the standing wave pattern to the response of the riser. This agrees with the recent observation made in [202] that a pure standing wave response is manifested by a single mode.

It was further discussed in [203] that for in-line and cross-flow standing wave response, one observes alternating regions of conditions which are favorable and unfavorable for VIV. This can be seen if we consider the equations of the standing waves as follows:

$$A_y(z, t) = A_1 \sin\left(\frac{2\pi z}{\lambda}\right) \sin(\omega t), \quad A_x(z, t) = A_2 \sin\left(\frac{4\pi z}{\lambda}\right) \sin(2\omega t + \phi), \quad (8.28)$$

where λ and ω are the wavelength and frequency of the waves, respectively. The standing wave pattern represents the sloshing of energy from kinetic to potential along the riser system. If we plot the trajectories of locations along the riser z -direction with the help of the equations above, we get clockwise trajectory (unfavorable for VIV) for one half and counter-clockwise trajectory (favorable for VIV) on the other half of the riser. Here, the clockwise and counter-clockwise directions are with reference to the direction of the in-line motion with that of the flow direction at the cross-flow extremes, meaning that counter-clockwise will be motion at cross-flow extreme against the incoming flow and vice-versa. This behavior of alternating trajectory has been observed in the present simulation which is consistent with the observed standing waves. A detailed understanding of these alternating orbital trajectories is provided in [204].

8.4.4 Spectral analysis of response amplitude

Due to the observation of alternating trajectories along the riser and also in time, we will focus on two time windows for the subsequent analyses: $tU_\infty/D \in [400, 470]$ where the lower part of the riser ($0 < z/L < 0.5$) is undergoing favorable VIV trajectory and $tU_\infty/D \in [600, 670]$ where the

upper part ($0.5 < z/L < 1$) has a counter-clockwise trajectory to the incoming flow. Spectral analysis of the vibration amplitude provides an insight into the dominant frequencies in the vibration. Figures 8.15 and 8.16 depict the frequencies along the different locations of the riser with the orbital trajectories for the time window of $tU_\infty/D \in [400, 470]$ and $tU_\infty/D \in [600, 670]$ respectively. We make the following observations. First, for every location along the riser, we observe a dominant non-dimensional frequency (fD/U_∞) of 0.166 for the cross-flow vibration and 0.342 for the in-line vibration. Therefore, the in-line vibrational frequency is twice that of the cross-flow frequency. Moreover, the values of the frequencies are much closer to the experimental value than the numerical results of [145]. Second, for the cross-flow vibration, in almost all the cases, we observe the second and third modes with a frequency of 0.342 and 0.508 respectively. Third, analyzing the in-line vibration spectra, higher modes having a frequency twice that of the dominant frequency are found for most of the locations along the riser. Furthermore, a frequency of 1.5 times the dominant frequency is also observed.

8.4.5 Trajectory along the riser

Figures 8.15 and 8.16 also show the orbital trajectories at various locations along the riser. As expected, we observe the figure-8 configuration for most of the locations. For the time window [400, 470], we notice that the trajectory of the riser is clockwise on the top of figure-8 at locations $z/L \in [0.55, 0.88]$ while it is counter-clockwise for $z/L \in [0.11, 0.44]$. This trajectory configuration is reversed in the time window [600, 670] in which the riser has a counter-clockwise trajectory for $z/L \in [0.55, 0.88]$ and clockwise on the other locations. These transitions along the riser and with time are also observed in the experiment [135] and are consistent with the standing wave response discussion in Section 8.4.3. Furthermore, in the experiment, this shift in the direction of the trajectory is observed throughout the time for which the experiment is conducted. The numerical simulation could capture just one cycle of such shift due to the time constraint of the computation. A comparison of the trajectories between the experiment and the simulation is shown in Fig. 8.17. The trajectories at $z/L = 0.44$ and $z/L = 0.55$ are found to be more erratic than other locations since they act as the transition region from clockwise to counter-clockwise or vice-versa of the orbital trajectories along the riser for a given time window. The amplitude in the cross-flow direction is found to be much larger than that in the in-line

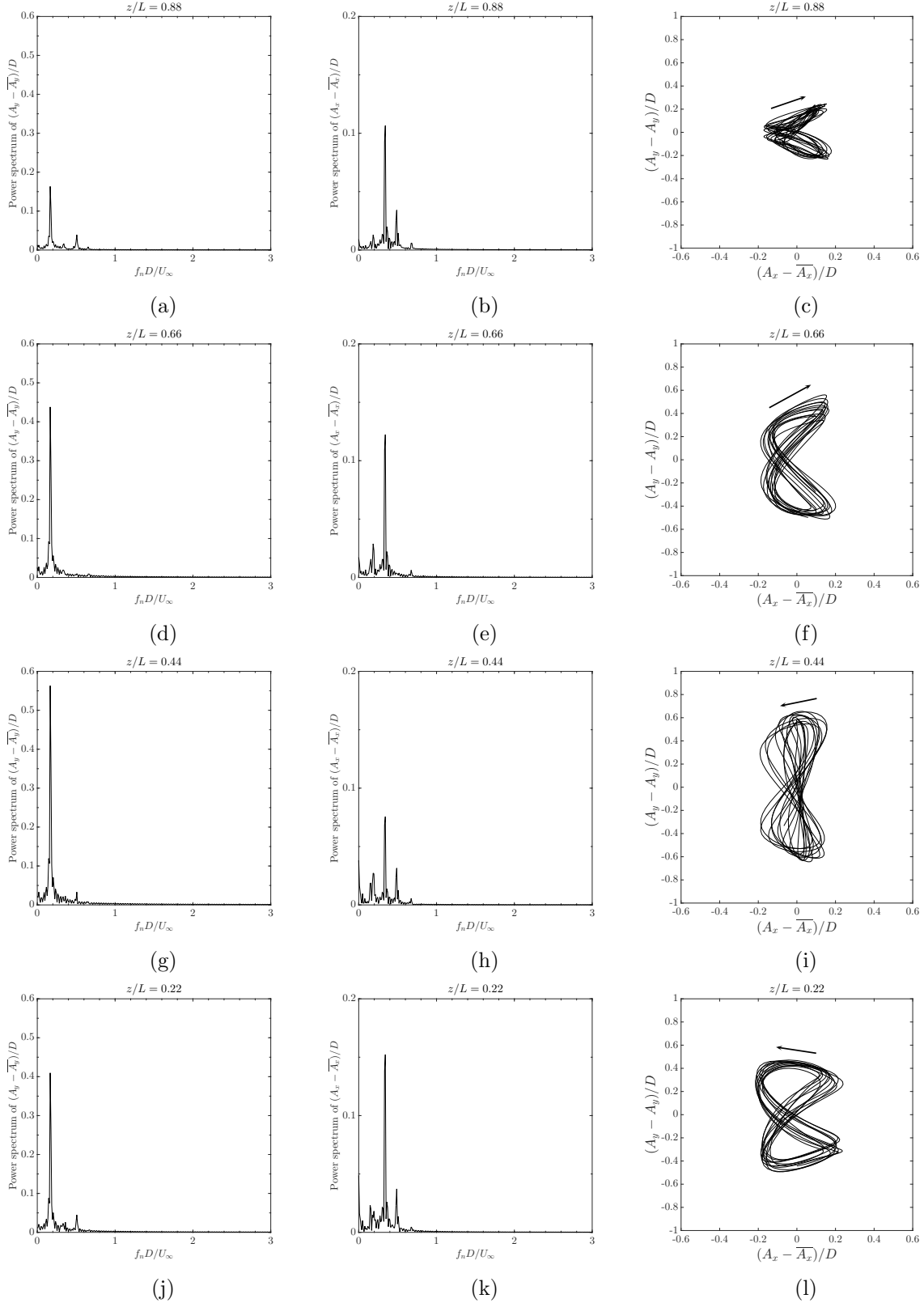


Figure 8.15: Oscillation frequencies and orbital trajectory at different locations $z/L \in [0.22, 0.88]$ along the span of the riser in the time window $tU_\infty/D \in [400, 470]$. The horizontal row corresponds to the same location of the riser with the first and second column giving the power spectra of cross-flow and in-line amplitudes respectively.

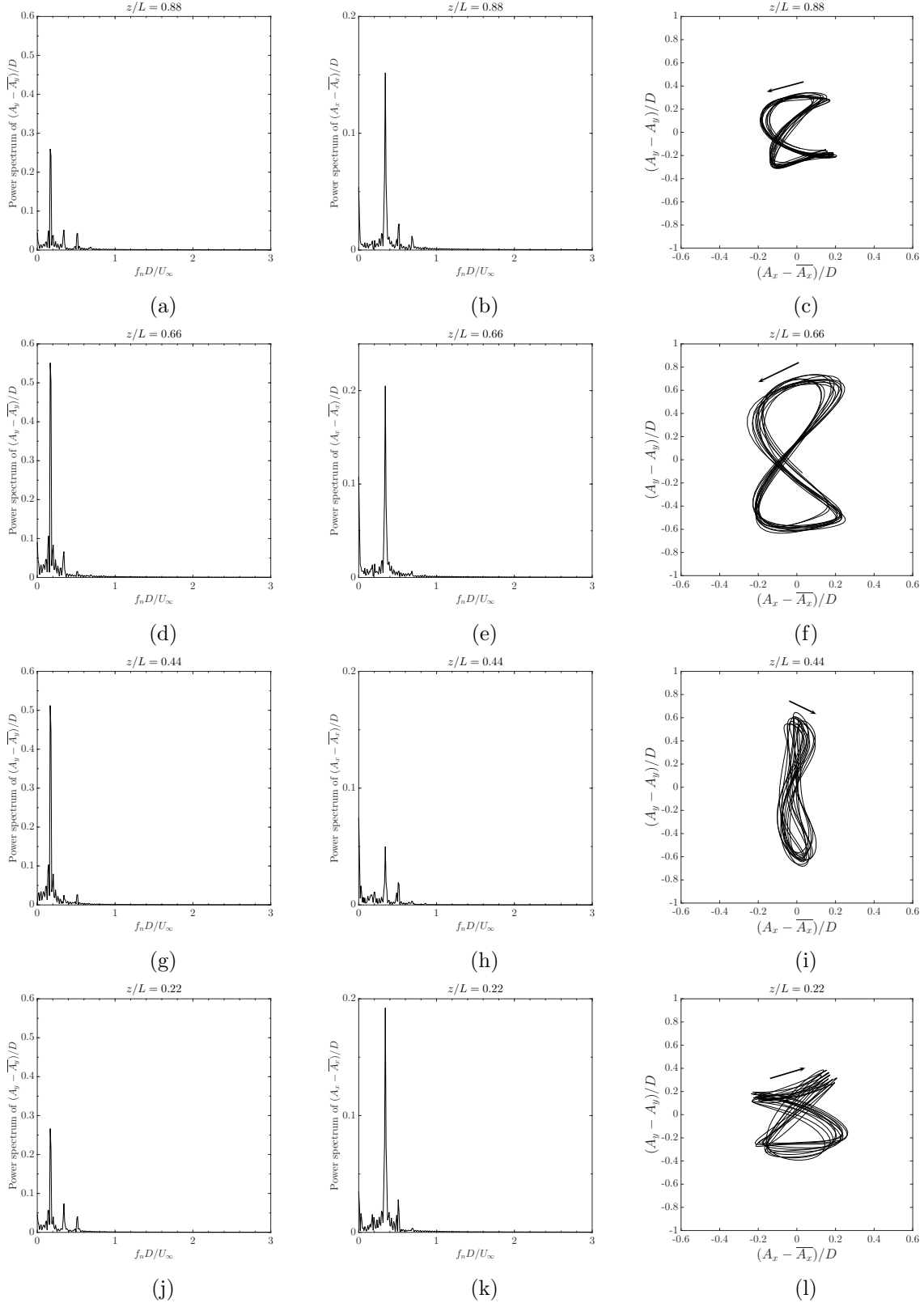


Figure 8.16: Oscillation frequencies and orbital trajectory at different locations $z/L \in [0.22, 0.88]$ along the span of the riser in the time window $tU_\infty/D \in [600, 670]$. The horizontal row corresponds to the same location of the riser with the first and second column giving the power spectra of cross-flow and in-line amplitudes respectively.

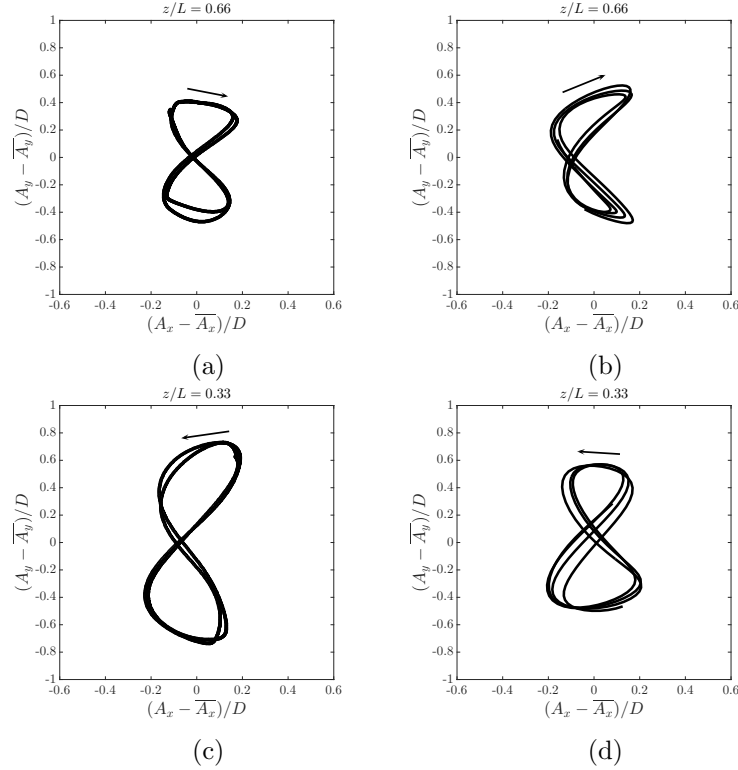


Figure 8.17: Orbital trajectory at different locations along the span of the riser ($Re, m^*, U_r = (4000, 2.23, 5.6)$): Comparison of experimental trajectory (left column) with the simulation in the time window $tU_\infty/D \in [440, 460]$ (right column)

direction [132]. The figure-8 motions tend to have a preferred direction of trajectory in which the cylinder would move upstream (counter-clockwise) at the extreme transverse vibrations [133]. This is observed in the current simulation in which the counter-clockwise pattern in the trajectory is observed when we have very large transverse amplitudes. In other words, the counter-clockwise pattern is associated with positive energy transfer from the surrounding fluid to the flexible riser, while the clockwise motion provides a damping to the vibrating riser.

8.4.6 Flow visualization

Figure 8.18 depicts the contours of different variables along the riser at $tU_\infty/D = 460$ and $tU_\infty/D = 650$ respectively. We plot the vibration amplitude along the riser with the spanwise Z -vorticity patterns at various locations along the riser ($z/L \in [0.11, 0.88]$). We observe that the amplitude response of the riser is higher at the bottom side in Fig. 8.18(a) since the lower side of the riser is undergoing the counter-clockwise trajectory in this case. This type of trajectory is opposed to the incoming flow which in turn produces more shear as the fluid does net work

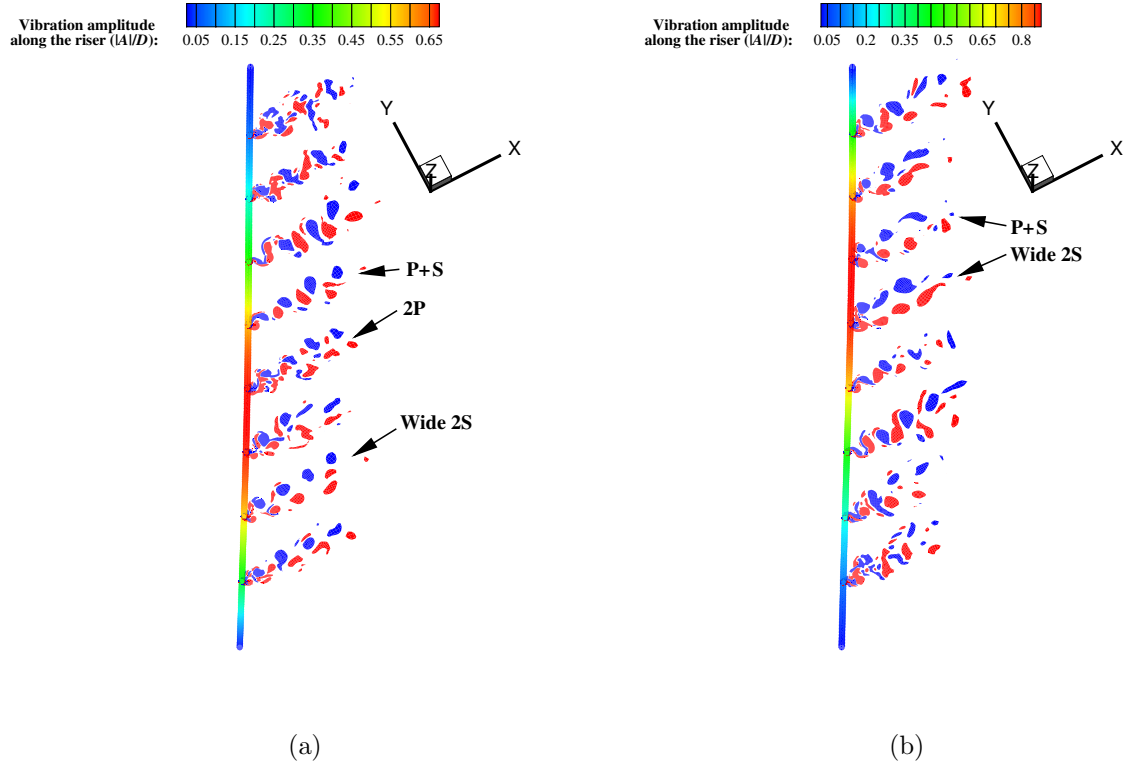


Figure 8.18: Flow visualization along the flexible riser undergoing VIV at $(Re, m^*, U_r) = (4000, 2.23, 5.6)$: Vibration amplitude along the riser with Z -vorticity contours in various sections- red and blue color indicate the positive and negative vorticity respectively: (a) $tU_\infty/D = 460$ and (b) $tU_\infty/D = 650$. The vorticity contours are plotted for different locations along the riser corresponding to $z/L \in [0.11, 0.88]$.

on the structure [205]. While the reverse is observed for $tU_\infty/D = 650$ in Fig. 8.18(b) where we have counter-clockwise trajectory on the upper part of the riser. The vortex pattern is however much complex. We can observe the 2S mode of vortex shedding in most of the locations and a wider 2S with two rows configuration near the locations where large vibration amplitude is found. At some of the places, a 2P vortex mode is also observed. Further analysis is required to better assess the vortex dynamics in detail.

8.5 Summary

A practical application of the vortex-induced vibration along an offshore riser is demonstrated in the present chapter via the PPV-based hybrid RANS/LES turbulence modeling. Some of the key observations about the VIV of a riser are as follows:

- For $Re = 4,000$, $m^* = 2.26$ and $U_r = 5.6$, the riser response is under dual resonance, i.e.,

the in-line frequency of vibration is twice that of the cross-flow vibration,

- Higher modal frequencies are observed in the spectra of the response amplitude, thus making it a multi-frequency response,
- Alternating trajectories are observed along the span of the riser and also in time, consistent with the observations in the experiment, and
- Complex vortex pattern is noticed consisting of 2S, wider 2S and 2P modes of vortex shedding patterns.

With a basic understanding of uniform flow across an offshore riser, we next demonstrate the capability of the solver to simulate a coupled drilling vessel-riser system which is subjected to incoming ocean waves and current.

Chapter 9

Application to Coupled Vessel Riser System*

This chapter discusses the application of the coupled two-phase FSI solver to the ship hydrodynamics and the coupled drillship-riser system. The computational domain and the non-dimensional fluid-structure parameters are presented which characterize the physical problem with some of the findings from the computations are highlighted.

9.1 Flow across a Wigley hull

We start with a simple case of a parabolic Wigley hull. The hull geometry is given by the formula,

$$y = 0.5B \left(1 - 4 \left(\frac{x}{L} \right)^2 \right) \left(1 - \left(\frac{z}{D} \right)^2 \right), \quad (9.1)$$

$$-0.5L \geq x \geq 0.5L, \quad (9.2)$$

$$-D \geq z \geq 0, \quad (9.3)$$

where $L = 4\text{m}$, $B = 0.4\text{m}$ and $D = 0.25\text{m}$ are the length, beam and draft of the hull respectively. The computational domain size is $16\text{m} \times 4.1\text{m} \times 3\text{m}$ with the initial free-surface position at $z =$

*Parts of this chapter have been published in “V. Joshi, P.S. Gurugubelli, Y.Z. Law, R.K. Jaiman and P.F.B. Adaikalaraj, A 3D coupled fluid-flexible multibody solver for offshore vessel-riser system, *Proceedings of the 37th International Conference on Ocean, Offshore and Arctic Engineering*, OMAE2018-78281, Madrid, Spain (2018).”

Chapter 9. Application to Coupled Vessel Riser System

0m, shown in Fig. 9.1. The depth of water is set at 2m. We study the wave pattern on the hull at

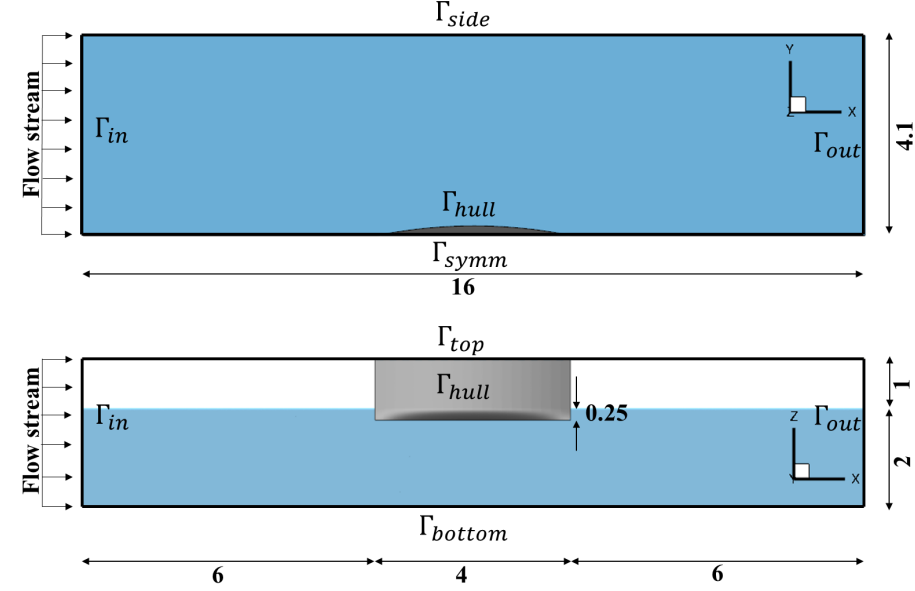


Figure 9.1: Schematic of the Wigley hull with the computational domain. Γ_{in} and Γ_{out} denote the inlet and outlet boundaries with freestream velocity at Γ_{in} . Slip boundary conditions are satisfied on the boundaries including Γ_{side} , Γ_{bottom} , Γ_{top} and Γ_{symm} . No-slip condition is imposed on the hull surface Γ_{hull} .

two Froude numbers $Fr = U_\infty / \sqrt{|\mathbf{g}|L}$, viz., 0.25 and 0.316, where U_∞ is the freestream velocity of the incoming flow and $\mathbf{g} = (0, 0, -9.81)$ is the acceleration due to gravity. The densities and dynamic viscosities of the two phases are $\rho_1^f = 1000$, $\mu_1^f = 10^{-3}$, $\rho_2^f = 1$ and $\mu_2^f = 10^{-5}$. A Dirichlet condition of the freestream velocity is imposed at the inlet boundary Γ_{in} and a stress-free Neumann condition is satisfied at the outlet boundary Γ_{out} . The surface of the Wigley hull Γ_{hull} satisfies the no-slip condition, and all other boundaries have slip boundaries. Notice that the simulation is carried out considering one-half surface of the hull as the hull geometry is symmetric along the $X - Z$ plane.

Three types of unstructured mesh resolutions are considered for the study. The details about the mesh are summarized in Table 9.1 and a typical mesh corresponding to Mesh 2 is depicted in Fig. 9.2. The mesh consists of four-node tetrahedron elements and is constructed such that a refined region is maintained along the free-surface to capture the fluid-fluid interface.

We compare the wave profiles along the hull with the experimental results [146] for the two Froude numbers in Fig. 9.3 where we find a good agreement with the experimental data. In the figure, η denotes the elevation of the free-surface along the surface of the Wigley hull. We

Chapter 9. Application to Coupled Vessel Riser System

Table 9.1: Different mesh resolutions for flow across a Wigley hull.

Mesh name	No. of nodes	No. of elements
Mesh 1	379,024	2,250,442
Mesh 2	2,413,022	14,737,877
Mesh 3	4,595,360	28,200,396

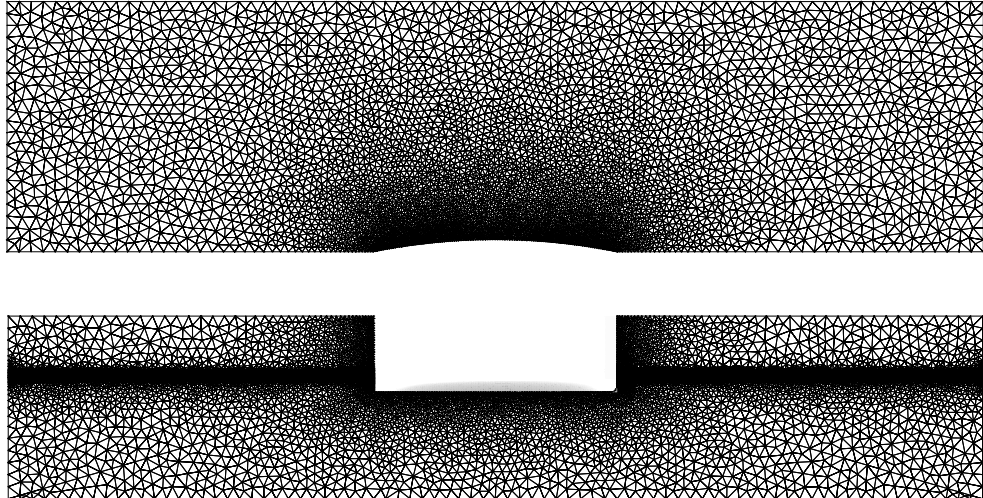


Figure 9.2: Computational Mesh 2 for the flow across a Wigley hull with the top and side view. The mesh consists of half of the Wigley hull with symmetric boundary condition.

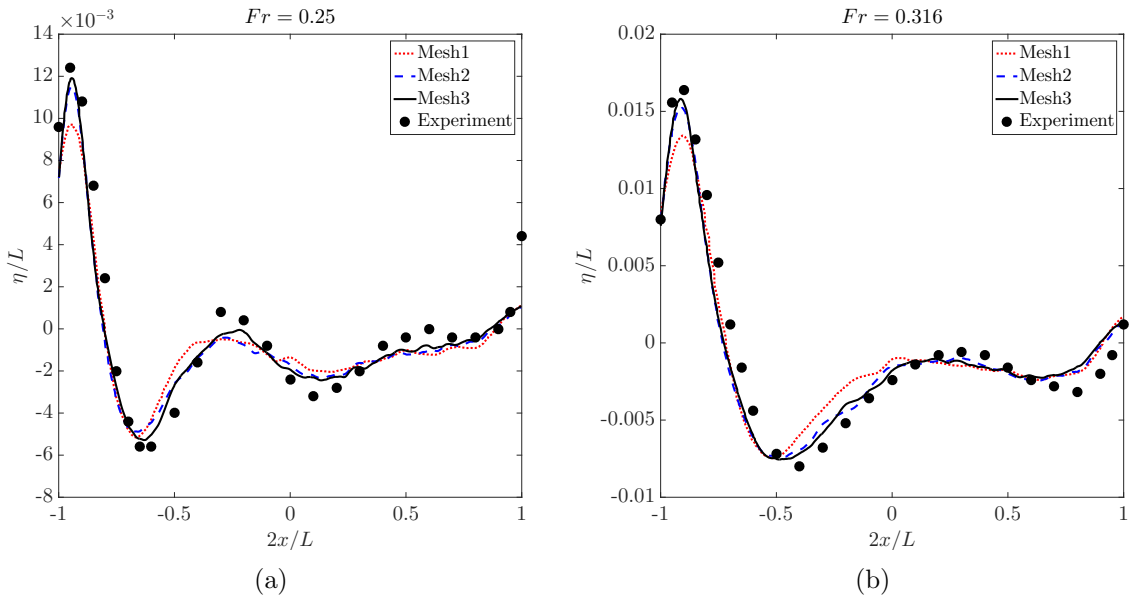


Figure 9.3: Wave profile elevation along the Wigley hull: comparison between the experimental data and numerical results at (a) $Fr = 0.25$ and (b) $Fr = 0.316$.

also provide the contours of the free-surface colored by the wave elevation in Fig. 9.4 where we observe the formation of the Kelvin waves near the downstream of the hull. Since the hull

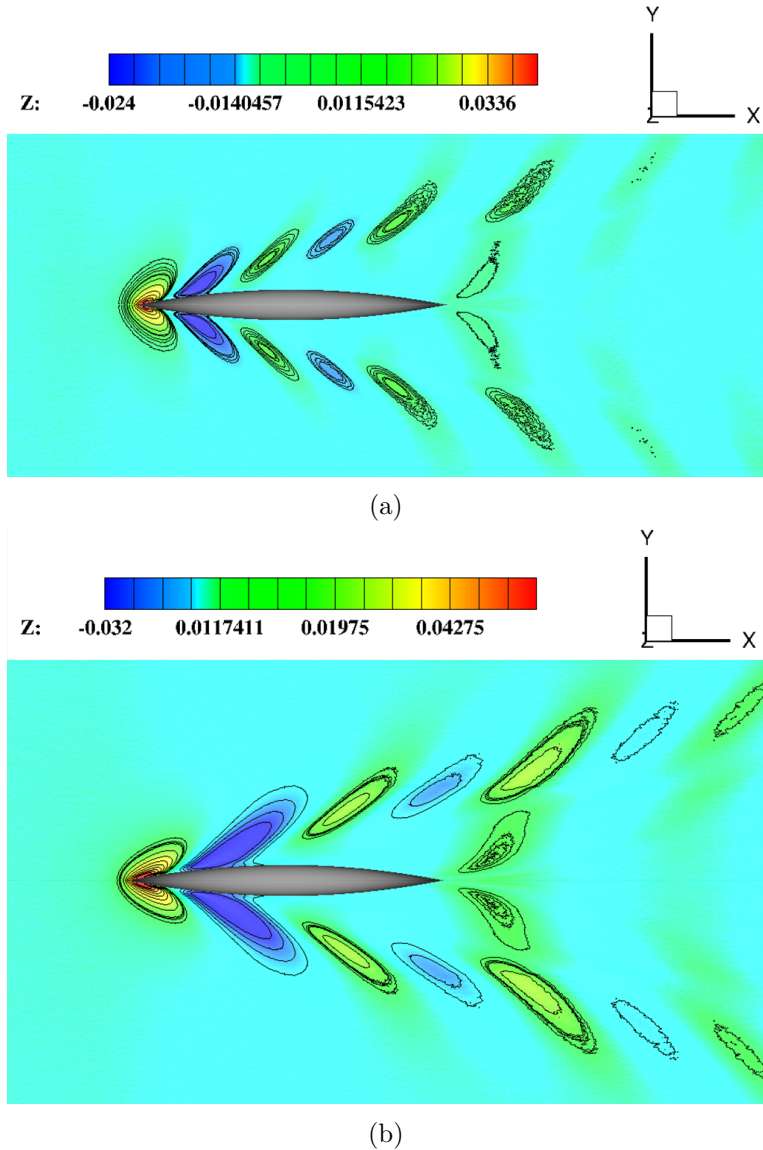


Figure 9.4: Wave elevation contours along the Wigley hull at (a) $Fr = 0.25$ and (b) $Fr = 0.316$. The contours are mirrored along the $X - Z$ plane owing to the symmetry in the hull geometry.

geometry is symmetric along the $X - Z$ plane, the contours are mirrored to obtain the Kelvin waves on both the sides of the hull. We next consider a more complicated geometry of the hull and analyze the effect of the free-surface ocean waves and current on the heave motion of the ship hull.

9.2 Ship hydrodynamics

We next study the problem of free heave of a ship model under the influence of surface waves and current. The hull geometry we employ for the ship is for the Navy surface combatant model DTMB 5415, which has been studied both experimentally and numerically in the literature. We utilize the Istituto Nazionale per Studi ed Esperienze di Architettura Navale (INSEAN) model which has a scale of 1:24.83. The details about the geometry of the model can be found in [206]. The length between perpendiculars of the ship hull is $L_{pp} = 5.72\text{m}$ with a draft of 0.248m and the displaced volume of water is 0.554m^3 . The volume, center of gravity and the mass moment of inertia of the ship hull are computed directly by meshing the ship hull and assuming its effective density.

9.2.1 Boundary conditions and key parameters

The computational domain and the boundaries are shown in Fig. 9.5. The inlet boundary Γ_{in} is exposed to the ocean current and linear Airy waves given by

$$u = U_\infty + \frac{\pi H_w}{T_w} \frac{\cosh(k_w(z+h))}{\sinh(k_w h)} \cos\left(k_w x - \frac{2\pi}{T_w} t\right), \quad (9.4)$$

$$v = 0, \quad (9.5)$$

$$w = \frac{\pi H_w}{T_w} \frac{\sinh(k_w(z+h))}{\sinh(k_w h)} \sin\left(k_w x - \frac{2\pi}{T_w} t\right), \quad (9.6)$$

$$\eta = \frac{H_w}{2} \cos\left(k_w x - \frac{2\pi}{T_w} t\right), \quad (9.7)$$

$$\phi = -\tanh\left(\frac{z-\eta}{\sqrt{2}\varepsilon}\right), \quad (9.8)$$

where $\mathbf{u}^f = (u, v, w)$ is the fluid velocity with its components, U_∞ is the freestream current velocity, H_w , T_w and k_w are the height, time period and wavenumber of the incoming linear waves, h and η are the depth of water and the fluid-fluid interface profile respectively. An outgoing current of U_∞ is enforced at the outlet boundary Γ_{out} to avoid any flow reversal. The side boundaries Γ_{side} are modeled with slip boundary condition with no-slip condition being satisfied at the bottom Γ_{bottom} and on the surface of the ship Γ_{ship} . Atmospheric condition of $p = 0$ is satisfied at the top boundary Γ_{top} . The physical properties of water and air are employed for the two fluid phases, i.e., $\rho_1^f = 1000$, $\mu_1^f = 1.002 \times 10^{-3}$, $\rho_2^f = 1.225$ and $\mu_2^f = 1.983 \times 10^{-5}$.

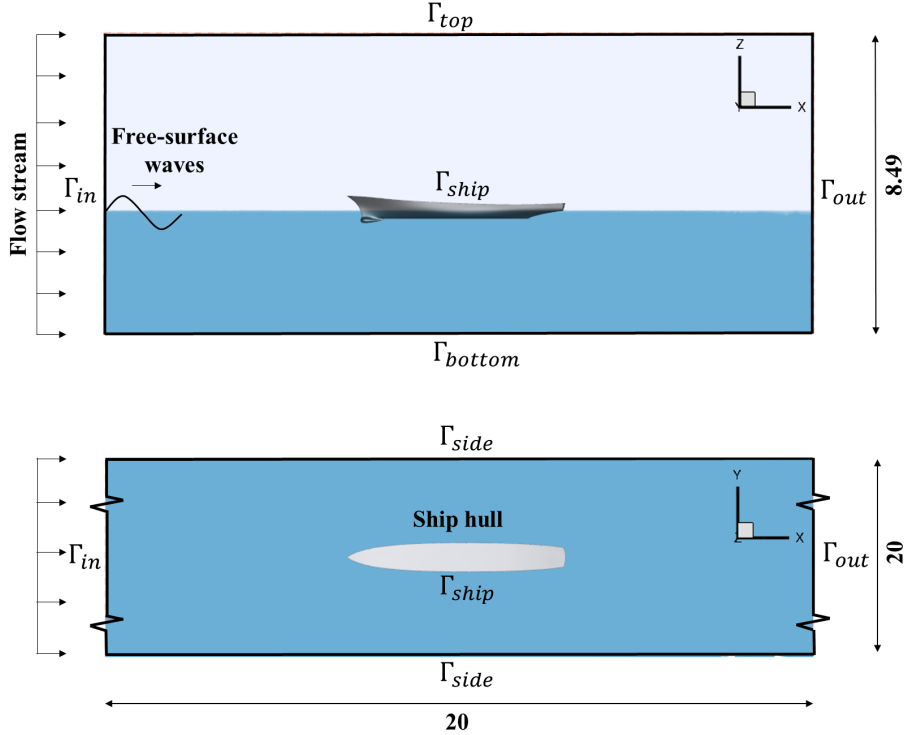


Figure 9.5: Schematic of the ship model 5415 with the computational domain. Γ_{in} and Γ_{out} denote the inlet and outlet boundaries with a combination of linear Airy waves and current at the inlet. Slip and no-slip boundary conditions are satisfied at the sides Γ_{side} and the ship hull surface Γ_{ship} respectively. Atmospheric condition is satisfied at Γ_{top} with no-slip condition at Γ_{bottom} .

The acceleration due to gravity is $\mathbf{g} = (0, 0, -9.81)$. For modeling the incoming turbulence, the eddy viscosity is equal to $\tilde{\nu} = 5\mu_1^f/\rho_1^f$ at the inlet boundary.

Based on the given data, the following non-dimensional numbers are employed where V_{disp} is the volume of the displaced fluid at equilibrium. All the variables are non-dimensionalized with the reference length L_{pp} and the freestream velocity U_∞ :

$$Re = \frac{\rho_1^f U_\infty L_{pp}}{\mu_1^f} = 1.069 \times 10^7, \quad \rho^* = \frac{\rho_1^f}{\rho_2^f} = 816, \quad m^* = \frac{m^s}{\rho_1^f V_{disp}} = 1,$$

$$\mu^* = \frac{\mu_1^f}{\mu_2^f} = 50, \quad Fr = \frac{U_\infty}{\sqrt{|\mathbf{g}| L_{pp}}} = 0.25.$$

9.2.2 Mesh characteristics

The mesh for the computational domain discussed in the previous section is constructed in the commercial meshing software Pointwise [207]. It consists of around 2 million nodes with

11.6 million four-node tetrahedron elements. A typical mesh is shown in Fig. 9.6. It can be

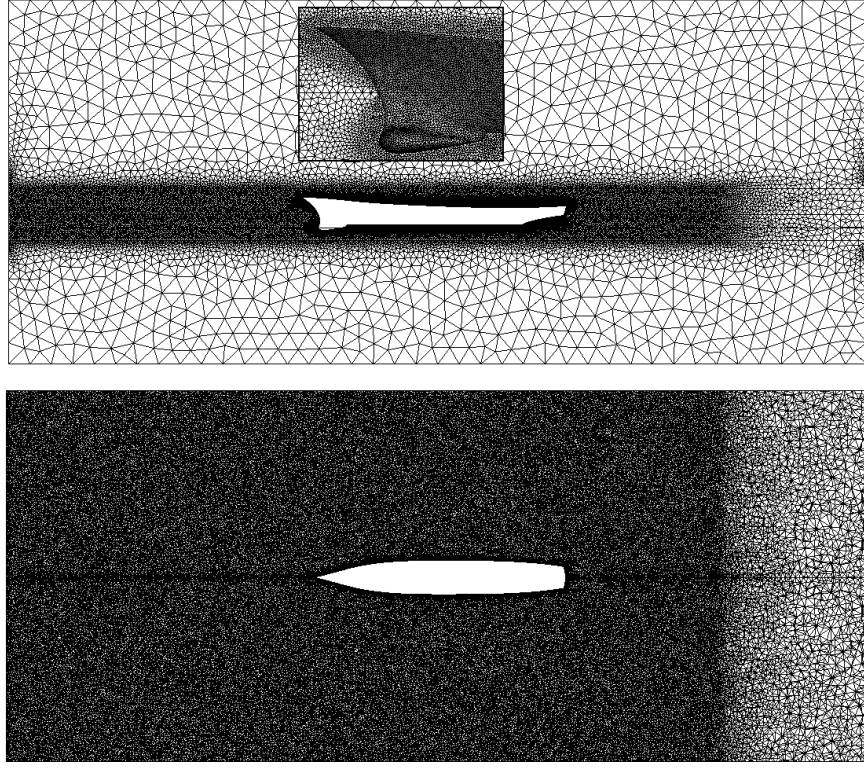


Figure 9.6: Computational mesh for the ship hull model 5415 with the top and side view. The mesh is refined near the fluid-fluid interface. The inset provides the discretization of the ship hull.

observed that a refined region is maintained to capture the fluid-fluid interface evolution. The mesh is coarsened at the outlet to damp the surface waves and avoid any reflection at the outlet boundary. The computation is performed using 136 processors with a non-dimensional time step size of $\Delta t U_\infty / L_{pp} = 3.27 \times 10^{-3}$. A total of 2,400 time steps took around 64 hours of computational time.

9.2.3 Results and discussion

A probe is introduced at $x/L_{pp} = 0.52$ from the inlet boundary Γ_{in} to measure the wave height. Based on the first harmonic of the Fourier transform of the elevation of the fluid-fluid interface obtained at the probe, the height of the wave is calculated as $H_w/L_{pp} = 0.056$. The wavenumber and time period of the wave are $k_w = 2\pi/L_{pp}$ and $T_w U_\infty / L_{pp} = 0.629$ respectively.

The heave response of the vessel is shown in Fig. 9.7 where the heave displacement (η_z^s / L_{pp}),

heave velocity ($\dot{\eta}_z^s/U_\infty$) and the vertical fluid force on the ship ($F_z/(\rho_1^f U_\infty^2 L_{pp}^2)$) are plotted with time (tU_∞/L_{pp}). It is observed that the time period of the heave response of the ship

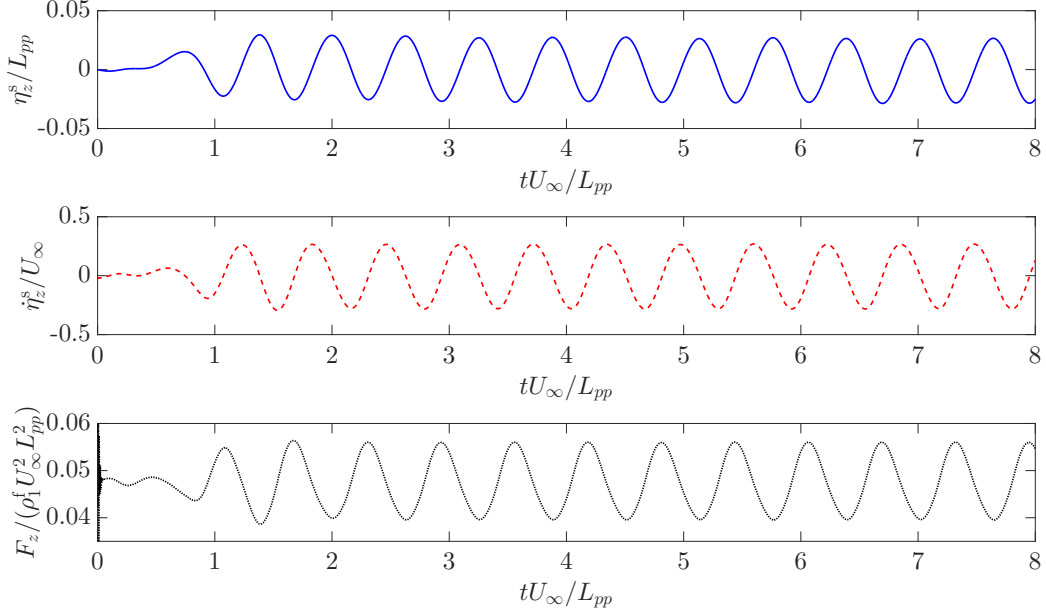


Figure 9.7: Heave displacement response (η_z^s/L_{pp}), heaving velocity ($\dot{\eta}_z^s/U_\infty$) and the vertical fluid force ($F_z/(\rho_1^f U_\infty^2 L_{pp}^2)$) on the ship model 5415 subjected to free-surface waves.

is $TU_\infty/L_{pp} = 0.628$ which is in synchronization with the time period of the incoming wave. The contour plots at the different non-dimensional time instances corresponding to the extreme displacements of the ship are presented in Fig. 9.8. We can observe the formation of the Kelvin waves near the rear of the ship. We next focus on the demonstration of the full-scale coupled drillship-riser system subjected to incoming ocean current and free-surface waves.

9.3 Drillship-riser system

We continue the study by presenting the full-scale demonstration of the coupled drillship-riser system. The ship hull is considered with the same geometry as the model 5415 with a scale of 1:1. This corresponds to a length between perpendiculars of $L_{pp} = 142\text{m}$ with a draft of 6.15m and displaced volume of water of 8424.4m^3 . A riser of diameter $D = 1\text{m}$ is attached to the bottom of the vessel and has an aspect ratio of $L/D = 200$. We present the response of the vessel and the riser which are subjected to the combined effects of turbulent ocean current and

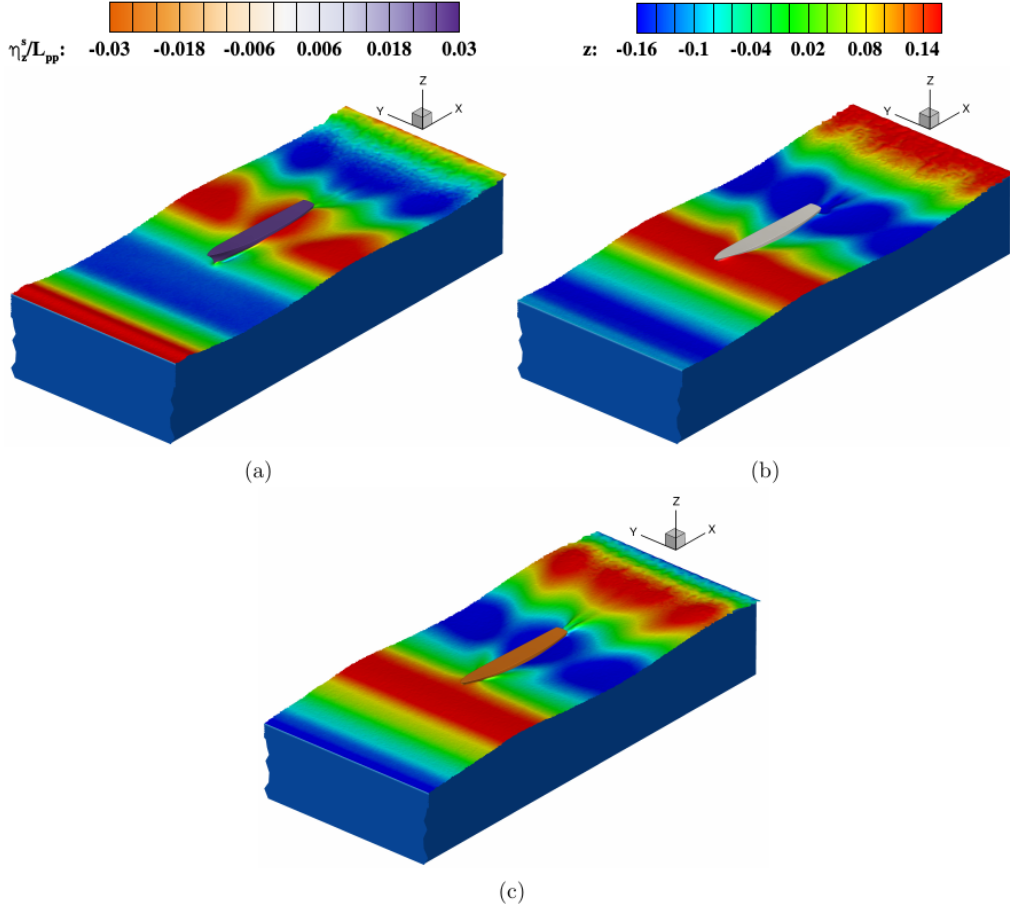


Figure 9.8: Heave motion of the 5415 vessel model at (a) $tU_\infty/L_{pp} = 3.27$, (b) $tU_\infty/L_{pp} = 6.22$ and (c) $tU_\infty/L_{pp} = 3.6$. The free-surface of the waves is represented by the iso-surface of the order parameter at $\phi = 0$ colored by the elevation. The ship surface is colored by the non-dimensional heave displacement.

the free-surface ocean waves.

9.3.1 Boundary conditions and key parameters

We employ boundary conditions similar to the INSEAN model case in the previous section. The computational domain is depicted in Fig. 9.9. The total length of the domain is 350m with second-order Stokes waves and a uniform flow current U_∞ at the inlet boundary Γ_{in} , while an outflow velocity of U_∞ is prescribed at the outlet boundary to prevent flow reversal. The side boundaries Γ_{side} satisfy the slip boundary condition, whereas the no-slip condition is imposed at the surfaces of the vessel, the riser, and the bottom boundary Γ_{bottom} . The atmospheric condition of zero pressure is prescribed at the top boundary. The ship is modeled as a rigid

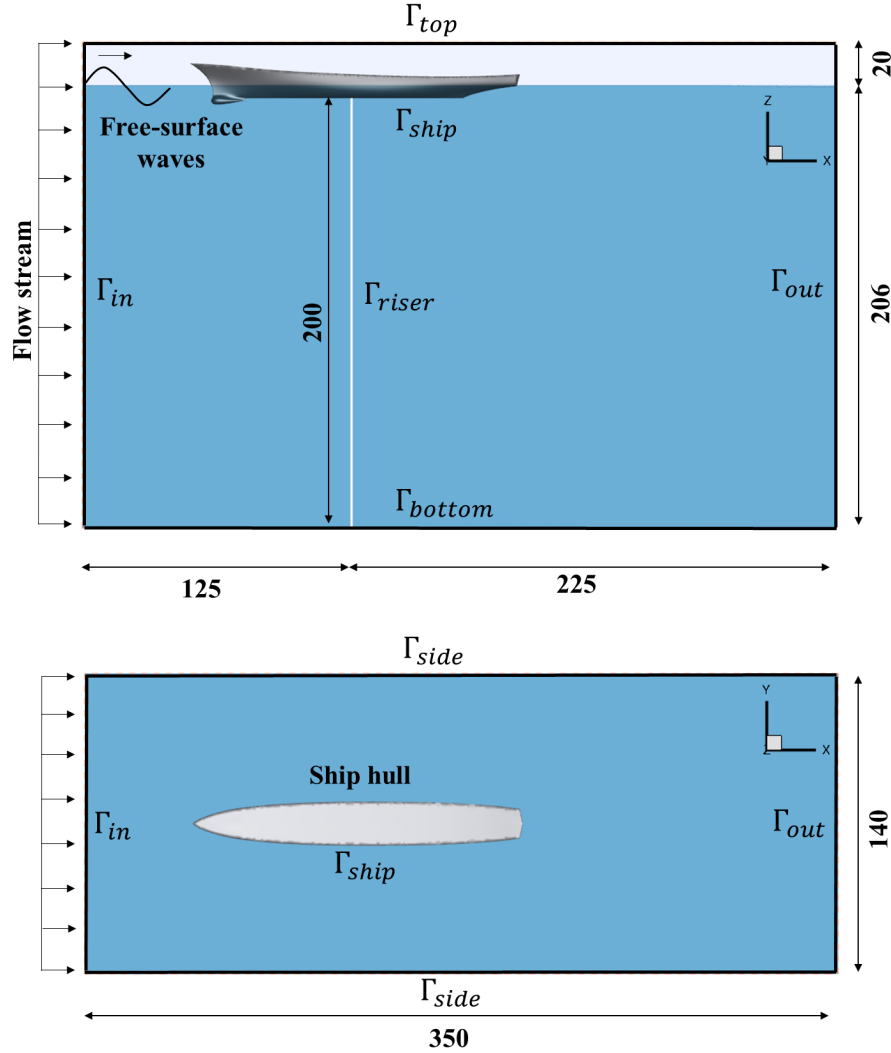


Figure 9.9: Schematic of the full-scale DTMB 5415 with the computational domain. Γ_{in} and Γ_{out} denote the inlet and outlet boundaries with a combination of nonlinear Stokes waves and current at the inlet. Slip and no-slip boundary conditions are satisfied at the sides Γ_{side} and the surfaces Γ_{ship} , Γ_{riser} respectively. Atmospheric condition is satisfied at Γ_{top} with no-slip condition at Γ_{bottom} .

body having three translational degrees of freedom, whereas the riser is solved as a nonlinear beam. The connection between the ship and the riser is assumed to be rigid, i.e., the response of the ship gets completely transferred to the riser and vice-versa. The second-order Stokes waves lead to the following conditions on the velocity ($\mathbf{u}^f = (u, v, w)$) at the inlet boundary Γ_{in} :

$$u = U_\infty + \frac{\pi H_w}{T_w} \frac{\cosh(k_w(z+h))}{\sinh(k_w h)} \cos\left(k_w x - \frac{2\pi}{T_w} t\right) + \frac{3\pi H_w^2 k_w}{8T_w} \frac{\cosh(2k_w(z+h))}{\sinh^4(k_w h)} \cos\left(2(k_w x - \frac{2\pi}{T_w} t)\right), \quad (9.9)$$

$$v = 0, \quad (9.10)$$

$$\begin{aligned} w &= \frac{\pi H_w}{T_w} \frac{\sinh(k_w(z+h))}{\sinh(k_w h)} \sin\left(k_w x - \frac{2\pi}{T_w} t\right) \\ &\quad + \frac{3\pi H_w^2 k_w}{8T_w} \frac{\sinh(2k_w(z+h))}{\sinh^4(k_w h)} \sin\left(2(k_w x - \frac{2\pi}{T_w} t)\right), \end{aligned} \quad (9.11)$$

$$\eta = \frac{H_w}{2} \cos\left(k_w x - \frac{2\pi}{T_w} t\right) + \frac{H_w^2 k_w}{16} \frac{\cosh(k_w h)(2 + \cosh(2k_w h))}{\sinh^3(k_w h)} \cos\left(2(k_w x - \frac{2\pi}{T_w} t)\right), \quad (9.12)$$

$$\phi = -\tanh\left(\frac{z - \eta}{\sqrt{2\varepsilon}}\right). \quad (9.13)$$

The physical parameters of water and air are the same as in Section 9.2. The non-dimensional parameters employed for the demonstration can be summarized as follows:

$$\begin{aligned} Re &= \frac{\rho_1^f U_\infty L_{pp}}{\mu_1^f} = 1.42 \times 10^8, & \rho^* &= \frac{\rho_1^f}{\rho_2^f} = 816, & \mu^* &= \frac{\mu_1^f}{\mu_2^f} = 50, \\ Fr &= \frac{U_\infty}{\sqrt{|\mathbf{g}|L_{pp}}} = 0.027, & m_{ship}^* &= \frac{m_{ship}^s}{\rho_1^f V_{disp}} = 1.0, & m_{riser}^* &= \frac{m_{riser}^s}{\rho_1^f D^2 L \pi / 4} = 2.23, \\ EI^* &= \frac{EI}{\rho_1^f U_\infty^2 D^4} = 2.1158 \times 10^7, & EA^* &= \frac{EA}{\rho_1^f U_\infty^2 D^2} = 1.7706 \times 10^8, & U_r &= \frac{U_\infty}{f_1 D} = 7.33, \end{aligned} \quad (9.14)$$

where m_{ship}^* and m_{riser}^* are the mass ratios of the ship and the riser respectively, EI^* and EA^* are the non-dimensional flexural and axial rigidity respectively and U_r is the reduced velocity of the riser assuming its first natural frequency using Eq. (4.56).

9.3.2 Mesh characteristics

A comparatively coarser mesh is constructed for the demonstration purpose, shown in Fig. 9.10. It consists of about 9 million grid points with 56 million four-node tetrahedron elements. The region near the fluid-fluid interface is refined to capture the free-surface waves. The computation is carried out using 600 processors. The non-dimensional time step size is selected as $\Delta t U_\infty / L_{pp} = 1.408 \times 10^{-4}$ and the computation ran for 13,200 time steps which amounted to be around 440 hours of computation.

9.3.3 Results and discussion

A probe is introduced at the location $x/L_{pp} = 0.176$ from the inlet boundary to measure the wave height. The first harmonic of the incoming wave revealed a wave height of $H_w/L_{pp} =$

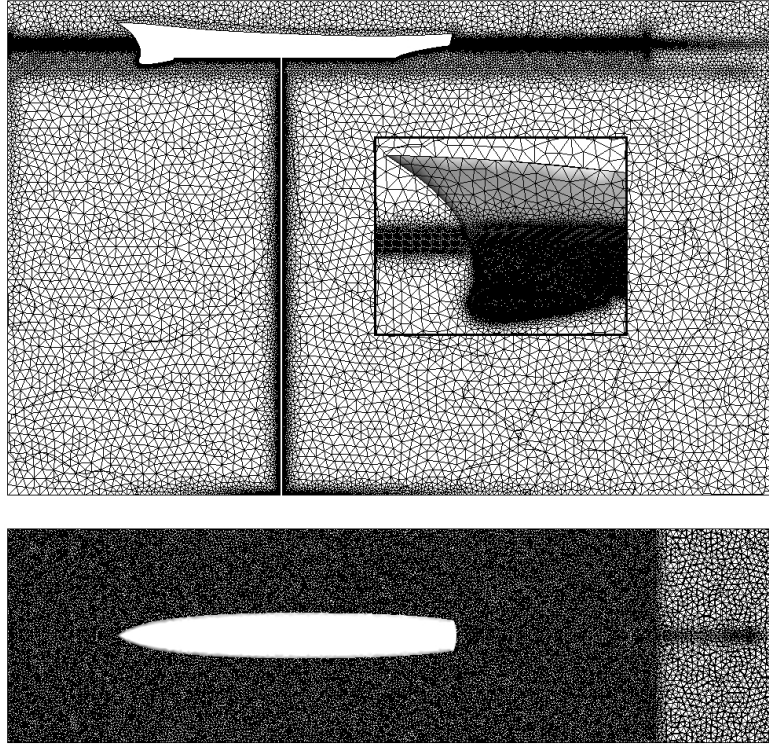


Figure 9.10: Computational mesh for the drillship-riser system with full-scale DTMB 5415 as the drillship. The mesh is refined near the fluid-fluid interface. The inset provides the discretization of the ship hull.

0.018 and a time period of $T_w U_\infty / L_{pp} = 0.0252$. The wavenumber of the incoming wave is $k_w = 2\pi/(0.141L_{pp})$.

The displacement response of the drillship is shown in Fig. 9.11 in the surge, sway and heave directions along with the hydrodynamic forces in Fig. 9.12. On the other hand, the displacement response of the riser midpoint at $z/L = 0.5$ is plotted in Fig. 9.13, corresponding to the location with the maximum amplitude response along the riser. The dominant frequencies obtained from the Fourier analysis of the responses are summarized in Table 9.2. The cross-flow response of the drillship manifests two frequencies with $fL_{pp}/U_\infty = 5.2$ being the dominant one. It is observed that the dominant in-line and cross-flow frequencies along the riser are in

Table 9.2: Non-dimensional frequencies (fL_{pp}/U_∞) of the displacement response.

Structure	In-line (x)	Cross-flow (y)
Drillship	6.5	5.2, 22.1
Riser	6.5	22.1

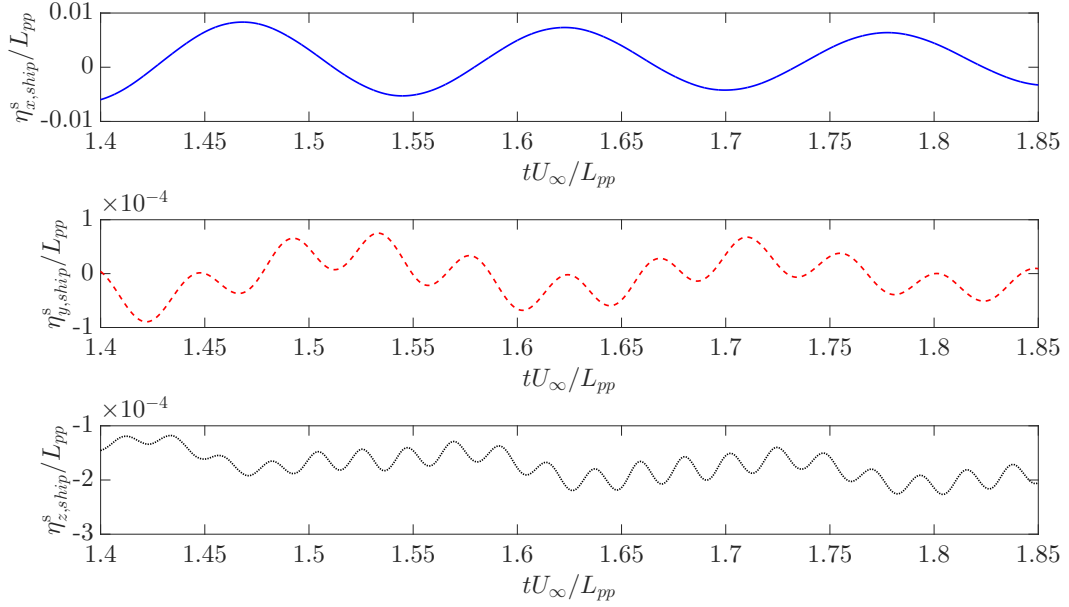


Figure 9.11: Displacement response (η_{ship}^s/L_{pp}) of the drillship in the surge (x), sway (y) and heave (z) directions.

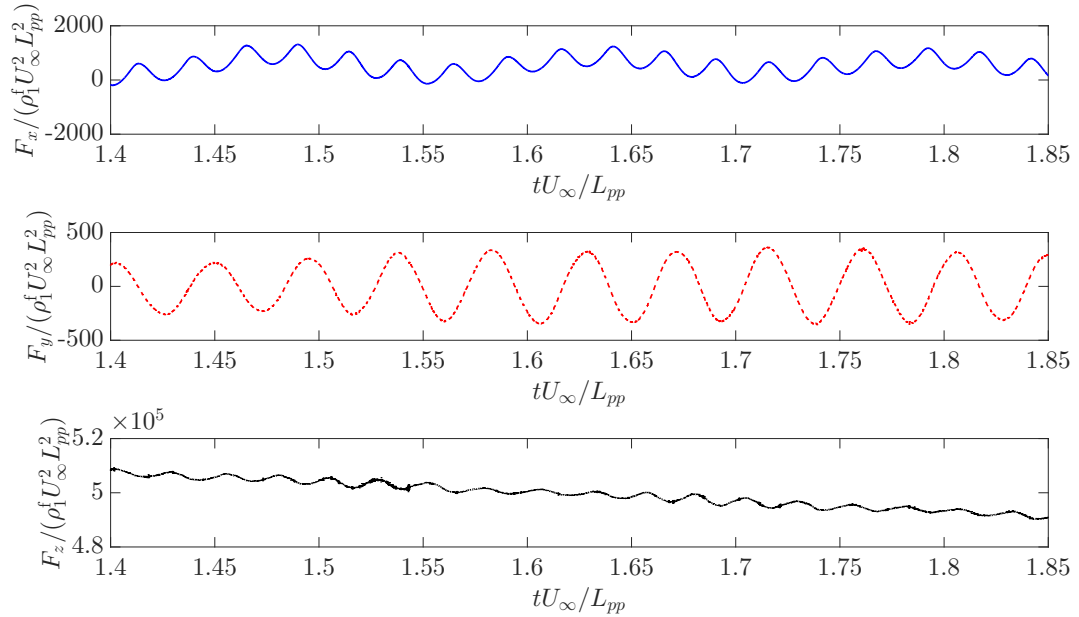


Figure 9.12: Fluid force ($F/(\rho_1^f U_\infty^2 L_{pp}^2)$) on the drillship in the surge (x), sway (y) and heave (z) directions.

synchronization with the surge and sway frequencies of the drillship. The riser oscillates with a high amplitude ($\sim \mathcal{O}(D)$) albeit its reduced velocity being away from the typical “lock-in”

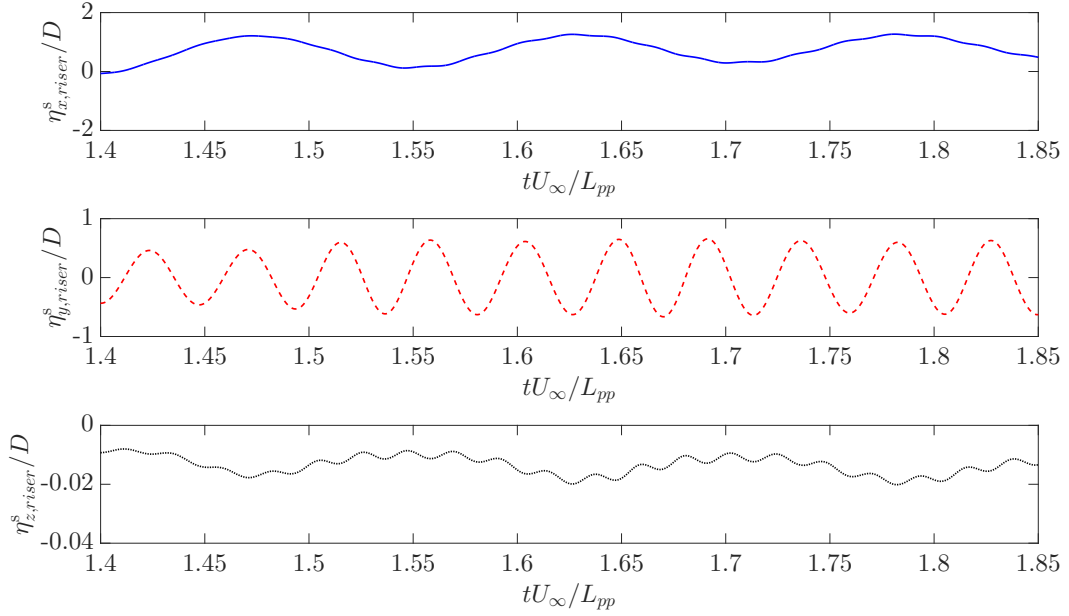


Figure 9.13: Displacement response (η_{riser}^s/D) of the riser of diameter D in the surge (x), sway (y) and heave (z) directions at the midpoint of the riser at $z/L = 0.5$.

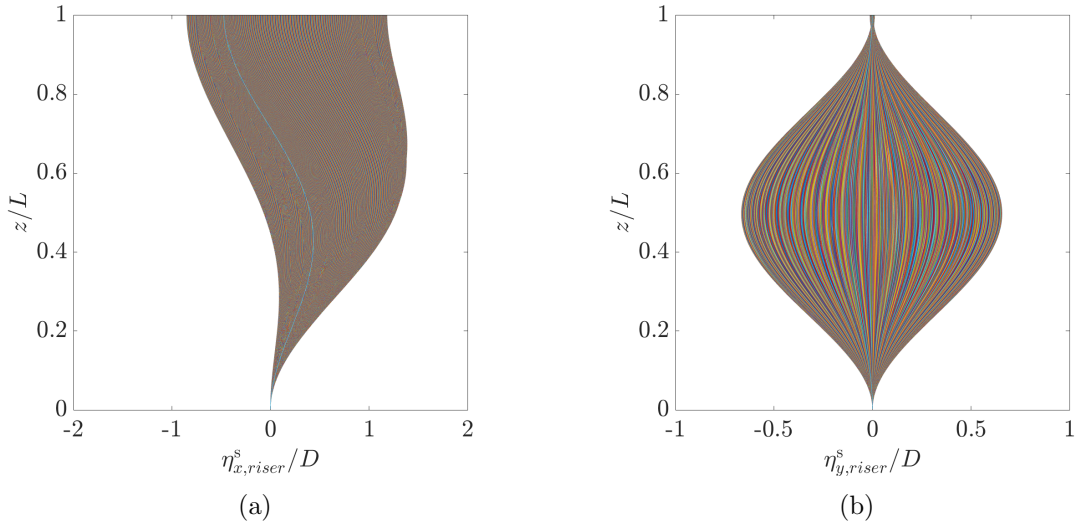


Figure 9.14: Response envelope along the span of the riser in (a) in-line (x) direction, and (b) cross-flow (y) direction.

range of $U_r \in [4 - 6]$. This high amplitude may be attributed to the synchronization of the riser amplitude with that of the vessel, leading to vessel-induced motion of the riser. The response envelope of the riser depicting the amplitude response along the riser with temporal variation is shown in Fig. 9.14 where we observe a standing wave-like pattern in the cross-flow response.

The contour plot of the vessel and the riser at $tU_\infty/L_{pp} = 1.535$ is shown in Fig. 9.15 where

we observe the formation of the Kelvin waves downstream of the vessel and the vortex shedding process along the riser. Note that the computational mesh employed for the demonstration is coarse. Further analyses employing a finer mesh is required for detailed physical understanding.

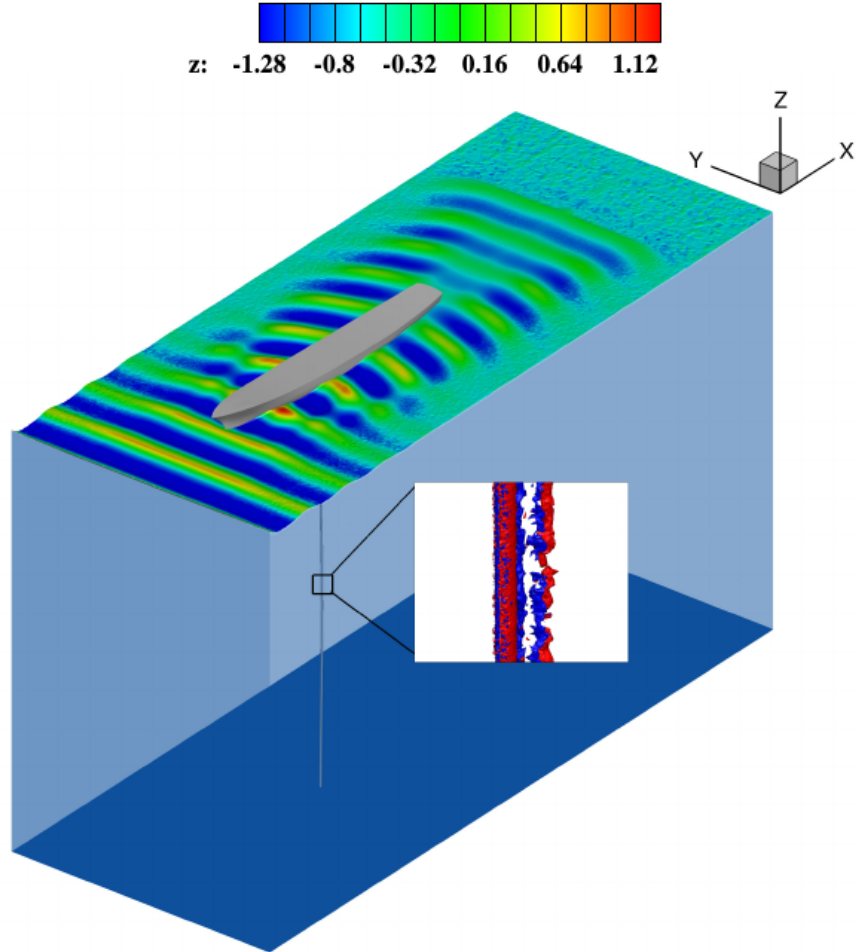


Figure 9.15: Coupled vessel riser system subjected to free-surface waves and ocean current at $tU_\infty/L_{pp} = 1.535$. The free-surface of the waves is represented by the iso-surface of the order parameter at $\phi = 0$ colored by the elevation. The inset provides the Z -vorticity contours along the riser surface with red and blue colors representing positive and negative vorticities respectively.

9.4 Summary

Integrating the different elements of the developed variational framework, the ultimate problem of the drillship-riser system is demonstrated in the present chapter. Some of the observations

Chapter 9. Application to Coupled Vessel Riser System

are:

- The coupled two-phase turbulent fluid-structure interaction solver is robust and stable for large-scale practical problems,
- The response of the drillship affects the response of the riser leading to a synchronization in the displacement frequencies between them, and
- The riser oscillates with high response amplitude in the coupled system, although its reduced velocity is away from the “lock-in” regime, owing to the vessel-induced motion.

Chapter 10

Conclusions and Recommendations

In this chapter, we provide a concluding summary of the present dissertation and suggest some recommendations for future work in the present area of research.

10.1 Concluding remarks

The present work discusses a novel **three-dimensional** computational framework for solving single and two-phase fluid-structure interaction problems and its application to large-scale drilling vessel-riser system. The study began by analyzing the convection-diffusion-reaction (CDR) equation, which forms the most canonical representation of the continuum differential equations. A variational method was developed to get a **stabilized and positivity preserving** solution for the CDR equation over a range of convection- and reaction-dominated regimes. The methodology is generic and applicable to any type of transport equation with convection or reaction effects.

With the goal of modeling two-phase flows, the PPV technique was extended to the **phase-field Allen-Cahn** equation. The diffuse-interface phase-field model gave an advantage by averting complex geometric manipulations to estimate the fluid-fluid interface and capturing the topologically deforming interface successfully with an Eulerian fixed grid. Several test problems such as Laplace-Young law, liquid sloshing in a tank, dam breaking and run-up on a vertical truncated cylinder established the capability of the formulation to handle **high density and viscosity ratios** of the two phases of the fluid. Further improvement in accuracy of the solution was observed by a adaptive mesh algorithm based on the residual error estimates of

the Allen-Cahn equation.

The coupling of the rigid and flexible structural equations with the two-phase flow formulation paved way for an integrated framework for single and two-phase FSI. The exact fluid-structure interface-tracking based on arbitrary Lagrangian-Eulerian technique and the phase-field fluid-fluid interface-capturing formed a **hybrid FSI formulation**. A **partitioned block-type coupling** was employed for the fluid and structure with the nonlinear iterative force correction at the fluid-structure interface to stabilize the solution at **low structure-to-fluid mass ratios**. This type of block coupling increases the flexibility and ease of implementation to the existing variational CFD solvers with minimal efforts. The PPV technique was also extended to the hybrid RANS/LES turbulence transport equation for turbulence modeling, where the benefits of both RANS and LES were combined to form a computationally less expensive turbulent formulation.

As a practical demonstration and **generality** of the developed framework for large-scale industrial systems, we demonstrated several relevant applications, viz., the vortex-induced vibration (VIV) of long riser with internal two-phase flow, subjected to external flow field, the VIV of long flexible riser of aspect ratio $L/D = 481.5$ exposed to turbulent flow and the fully coupled drilling vessel-riser system in a complex ocean environment consisting of free-surface waves and turbulent flow streams.

10.2 Future recommendations

The current work motivates a number of recommendations for the future extension which we allude to the discussions throughout this dissertation. They are summarized as follows:

- Introducing higher-order Lagrange polynomial interpolations for the shape functions of an element increases the accuracy of the solution in the variational framework [208]. However, stabilization terms have to be modified to circumvent the Babuška-Brezzi condition for equal-order interpolations. Furthermore, use of higher-order spline interpolation functions like NURBS and Bernstein polynomials is also one of the options to improve accuracy and reduce the degrees of freedom in the computation [209].
- In the current formulation, we have not performed any specific modification to solve the

Chapter 10. Conclusions and Recommendations

issue of turbulence at the free-surface, which is an open problem for the researchers. The treatment of the free-surface waves satisfies the inviscid potential theory, where the flow is assumed to be irrotational and free of vortices. However, the turbulent effects are present in the immediate neighbourhood of the interface inside the bulk phases. This modeling of the turbulence at the fluid-fluid interface while satisfying the irrotational flow condition needs further study.

- The mesh adaptive procedure presented in Chapter 6 only considers the refinement/coarsening algorithm in two-dimensions. While there is no limitation of the extension of the variational formulation to three-dimensions as shown by the three-dimensional simulations in Chapters 5 and 7, the newest vertex bisection algorithm, especially the coarsening procedure, needs some effort for its extension in three-dimensions.
- We considered the connection between the drilling vessel and the riser as a rigid joint in Chapter 9, i.e., complete transfer of the forces from the vessel to the riser and vice-versa. However, from the industrial point of view, such joints are telescopic and consist of a tensioner system to reduce the transfer of the forces. Further modeling of these connections needs to be carried out for an accurate representation of the riser tensioner system.

Bibliography

- [1] R. Codina. A discontinuity-capturing crosswind-dissipation for the finite element solution of the convection-diffusion equation. *Computer Methods in Applied Mechanics and Engineering*, 110:325–342, 1993.
- [2] H. G. Lee. High-order and mass conservative methods for the conservative Allen-Cahn equation. *Computers & Mathematics with Applications*, 72(3):620 – 631, 2016.
- [3] H. Sauerland and T-P. Fries. The extended finite element method for two-phase and free-surface flows: A systematic study. *Journal of Computational Physics*, 230(9):3369 – 3390, 2011.
- [4] M. Morris-Thomas. *An investigation into wave run-up on vertical surface piercing cylinders in monochromatic waves*. PhD thesis, The University of Western Australia, 2003.
- [5] J. Kim, R. Jaiman, S. Cosgrove, and J. O’Sullivan. Numerical wave tank analysis of wave run-up on a truncated vertical cylinder. In *ASME 30th International Conference on Ocean, Offshore and Arctic Engineering (OMAE)*, Rotterdam, The Netherlands, 2011.
- [6] S. Ito. *Study of the transient heave oscillation of a floating cylinder*. PhD thesis, Massachusetts Institute of Technology, 1971.
- [7] A. Calderer, S. Kang, and F. Sotiropoulos. Level set immersed boundary method for coupled simulation of air/water interaction with complex floating structures. *Journal of Computational Physics*, 277:201 – 227, 2014.
- [8] K. H. Jung, K. A. Chang, and H. J. Jo. Viscous effect on the roll motion of a rectangular structure. *Journal of Engineering Mechanics*, 132(2):190–200, 2006.

Bibliography

- [9] C. Norberg. *Effects of Reynolds number and a low-intensity free-stream turbulence on the flow around a circular cylinder*. Publication 87/2. Department of Applied Thermodynamics and Fluid Mechanics. Chalmers University of Technology, Sweden, 1987.
- [10] D. P. Rizzetta, M. R. Visbal, and G. A. Blaisdell. A time-implicit high-order compact differencing and filtering scheme for large-eddy simulation. *International Journal for Numerical Methods in Fluids*, 42(6):665–693, 2003.
- [11] A. Roshko. Experiments on the flow past a circular cylinder at very high Reynolds number. *Journal of Fluid Mechanics*, 10(2):345–356, 1961.
- [12] J. W. G. van Nunen. Pressure and forces on a circular cylinder in a cross flow at high Reynolds numbers. In E. Naudascher, editor, *Flow Induced Structural Vibrations*, pages 748–754. Springer-Verlag, Berlin, 1974.
- [13] A. Travin, M. Shur, M. Strelets, and P. Spalart. Detached-Eddy Simulations past a circular cylinder. *Flow, Turbulence and Combustion*, 63(1):293–313, 2000.
- [14] P. Parnaudeau, J. Carlier, D. Heitz, and E. Lamballais. Experimental and numerical studies of the flow over a circular cylinder at Reynolds number 3900. *Physics of Fluids*, 20(8):85101, 2008.
- [15] A. G. Kravchenko and P. Moin. Numerical studies of flow over a circular cylinder at $Re_D = 3900$. *Physics of Fluids*, 12(2):403–417, 2000.
- [16] L. M. Laurencio and C. Shih. *Characteristics of the plane turbulent near wake of a circular cylinder. A particle image velocimetry study*. Private communication. (data taken from “B-Spline methods and zonal grids for numerical simulations of turbulent flows”, Kravchenko, A. G., 1998), 1993.
- [17] V. V. Khatavkar, P. D. Anderson, P. C. Duineveld, and H. H. E. Meijer. Diffuse interface modeling of droplet impact on a pre-patterned solid surface. *Macromolecular Rapid Communications*, 26(4):298–303, 2005.
- [18] E. Fried and M. E. Gurtin. Dynamic solid-solid transitions with phase characterized by an order parameter. *Physica D: Nonlinear Phenomena*, 72(4):287 – 308, 1994.

Bibliography

- [19] F. Xie, X. Zheng, M. S. Triantafyllou, Y. Constantinides, Y. Zheng, and G. E. Karniadakis. Direct numerical simulations of two-phase flow in an inclined pipe. *Journal of Computational Physics*, 825:189 – 207, 2017.
- [20] S. Vist and J. Pettersen. Two-phase flow distribution in compact heat exchanger manifolds. *Experimental Thermal and Fluid Science*, 28(2):209 – 215, 2004. The International Symposium on Compact Heat Exchangers.
- [21] R. M. Sorensen. *Basic Wave Mechanics: For Coastal and Ocean Engineers*. A Wiley-Interscience publication. Wiley, 1993.
- [22] S. K. Chakrabarti. *Hydrodynamics of Offshore Structures*. Springer Verlag, 1987.
- [23] T. Li, P. Troch, and J. De Rouck. Interactions of breaking waves with a current over cut cells. *Journal of Computational Physics*, 223:865 – 897, 2007.
- [24] R. D. Blevins. Flow-induced vibration. Van Nostrand Reinhold, New York, 1990.
- [25] M. P. Paidoussis, S. J. Price, and E. de Langre. *Fluid-Structure Interactions: Cross-Flow-Induced Instabilities*. Cambridge University Press, 2010.
- [26] M. Stynes. Steady-state convection-diffusion problems. *Acta Numerica*, 14:445–508, 2005.
- [27] T. J. R. Hughes. *Finite Element Methods for Convection Dominated Flows*, volume 34. ASME, New York, 1979.
- [28] A. N. Brooks and T. J. R. Hughes. Streamline upwind/Petrov-Galerkin formulations for convection dominated flows with particular emphasis on the incompressible Navier-Stokes equations. *Computer Methods in Applied Mechanics and Engineering*, 32(1):199–259, 1982.
- [29] A. Mizukami and T. J. R. Hughes. A Petrov-Galerkin finite element method for convection-dominated flows: An accurate upwinding technique for satisfying the maximum principle. *Computer Methods in Applied Mechanics and Engineering*, 50(2):181–193, 1985.

Bibliography

- [30] J. G. Rice and R. J. Schnipke. A monotone streamline upwind finite element method for convection-dominated flows. *Computer Methods in Applied Mechanics and Engineering*, 48(3):313–327, 1985.
- [31] R. J. LeVeque. *Numerical methods for conservation laws*. Birkhäuser Verlag, Basel; Boston, 1992.
- [32] T. J. R. Hughes, M. Mallet, and A. Mizukami. A new finite element formulation for computational fluid dynamics: II. Beyond SUPG. *Computer Methods in Applied Mechanics and Engineering*, 54(3):341–355, 1986.
- [33] A. C. Galeão and E. G. Dutra do Carmo. A consistent approximate upwind Petrov-Galerkin method for convection-dominated problems. *Computer Methods in Applied Mechanics and Engineering*, 68(1):83–95, 1988.
- [34] E. G. Dutra do Carmo and G. B. Alvarez. A new stabilized finite element formulation for scalar convection-diffusion problems: the streamline and approximate upwind/Petrov-Galerkin method. *Computer Methods in Applied Mechanics and Engineering*, 192:3379–3396, 2003.
- [35] T. J. R. Hughes, L. P. Franca, and G. M. Hulbert. A new finite element formulation for computational fluid dynamics: VIII. The Galerkin/least-squares method for advective-diffusive equations. *Computer Methods in Applied Mechanics and Engineering*, 73(2):173–189, 1989.
- [36] L. P. Franca and E. G. Dutra do Carmo. The Galerkin gradient least-squares method. *Computer Methods in Applied Mechanics and Engineering*, 74:41–54, 1989.
- [37] F. Shakib, T. J. R. Hughes, and Z. Johan. A new finite element formulation for computational fluid dynamics: X. The compressible Euler and Navier-Stokes equations. *Computer Methods in Applied Mechanics and Engineering*, 89:141–219, 1991.
- [38] R. Codina. Comparison of some finite element methods for solving the diffusion-convection-reaction equation. *Computer Methods in Applied Mechanics and Engineering*, 156(1):185–210, 1998.

Bibliography

- [39] T. J. R. Hughes. Multiscale phenomena: Green's functions, the Dirichlet-to-Neumann formulation, subgrid scale models, bubbles and the origins of stabilized methods. *Computer Methods in Applied Mechanics and Engineering*, 127(1):387–401, 1995.
- [40] T. J. R. Hughes, G. R. Feij  o, L. Mazzei, and J. B. Quincy. The variational multiscale method-a paradigm for computational mechanics. *Computer Methods in Applied Mechanics and Engineering*, 166:3–24, 1998.
- [41] Y. Bazilevs, V. M. Calo, J. A. Cottrell, T. J. R. Hughes, A. Reali, and G. Scovazzi. Variational multiscale residual-based turbulence modeling for large eddy simulation of incompressible flows. *Computer Methods in Applied Mechanics and Engineering*, 197(1):173–201, 2007.
- [42] I. Akkerman, Y. Bazilevs, V. M. Calo, T. J. R. Hughes, and S. Hulshoff. The role of continuity in residual-based variational multiscale modeling of turbulence. *Computational Mechanics*, 41(3):371–378, 2008; 2007.
- [43] E. O  ate. Derivation of stabilized equations for numerical solution of advective-diffusive transport and fluid flow problems. *Computer Methods in Applied Mechanics and Engineering*, 151:233–265, 1998.
- [44] E. O  ate, J. Miquel, and G. Hauke. Stabilized formulation for the advection-diffusion-absorption equation using finite calculus and linear finite elements. *Computer Methods in Applied Mechanics and Engineering*, 195:3926–3946, 2006.
- [45] E. O  ate, F. Zarate, and S. R. Idelsohn. Finite element formulation for the convective-diffusive problems with sharp gradients using finite calculus. *Computer Methods in Applied Mechanics and Engineering*, 195:1793–1825, 2006.
- [46] E. O  ate, J. Miquel, and F. Zarate. Stabilized solution of the multidimensional advection-diffusion-absorption equation using linear finite elements. *Comput. Fluids*, 36:92–112, 2007.
- [47] J. P. Boris and D. L. Book. Flux-corrected transport. I. SHASTA, a fluid transport algorithm that works. *Journal of Computational Physics*, 11:38–69, 1973.

Bibliography

- [48] S. T. Zalesak. Fully multidimensional flux-corrected transport algorithms for fluids. *Journal of Computational Physics*, 31:335–362, 1979.
- [49] D. Kuzmin, R. Löhner, and S. Turek. *Flux-corrected Transport: Principles, Algorithms and Applications*. Springer, 2005.
- [50] A. Harten. High resolution schemes for hyperbolic conservation laws. *Journal of Computational Physics*, 49:357–393, 1983.
- [51] T. E. Tezduyar and Y. J. Park. Discontinuity-capturing finite element formulations for nonlinear convection-diffusion-reaction equations. *Computer Methods in Applied Mechanics and Engineering*, 59:307–325, 1986.
- [52] S. R. Idelsohn, N. Nigro, M. Storti, and G. Buscaglia. A Petrov-Galerkin formulation for advective-reaction-diffusion problems. *Computer Methods in Applied Mechanics and Engineering*, 136:27–46, 1996.
- [53] I. Harari and T. J. R. Hughes. Stabilized finite element methods for steady advection-diffusion with production. *Computer Methods in Applied Mechanics and Engineering*, 115:165–191, 1994.
- [54] S. R. Idelsohn, J. C. Heinrich, and E. Oñate. Petrov-Galerkin methods for the transient advective-diffusive equation with sharp gradients. *International Journal for Numerical Methods in Engineering*, 39(9):1455–1473, 1996.
- [55] R. Codina. On stabilized finite element methods for linear systems of convection-diffusion-reaction equations. *Computer Methods in Applied Mechanics and Engineering*, 188(1):61–82, 2000.
- [56] L. P. Franca and F. Valentin. On an improved unusual stabilized finite element method for the advective-reactive-diffusive equation. *Computer Methods in Applied Mechanics and Engineering*, 190:1785–1800, 2001.
- [57] G. Hauke and A. Garcia-Olivares. Variational subgrid scale formulations for the advection-diffusion-reaction equation. *Computer Methods in Applied Mechanics and Engineering*, 190:6847–6865, 2001.

Bibliography

- [58] G. Hauke. A simple subgrid scale stabilized method for the advection-diffusion-reaction equation. *Computer Methods in Applied Mechanics and Engineering*, 191:2925–2947, 2002.
- [59] G. Houzeaux, B. Eguzkitza, and M. Vázquez. A variational multiscale model for the advection-diffusion-reaction equation. *Communications in Numerical Methods in Engineering*, 25:787–809, 2009.
- [60] J. Principe and R. Codina. On the stabilization parameter in the subgrid scale approximation of scalar convection-diffusion-reaction equations on distorted meshes. *Computer Methods in Applied Mechanics and Engineering*, 199(21):1386–1402, 2010.
- [61] P. Nadukandi, E. Oñate, and J. Garcia. A high-resolution Petrov-Galerkin method for the 1D convection-diffusion-reaction problem. *Computer Methods in Applied Mechanics and Engineering*, 199:525–546, 2010.
- [62] P. Nadukandi, E. Oñate, and J. Garcia. A high-resolution Petrov-Galerkin method for the convection-diffusion-reaction problem. Part II-A multidimensional extension. *Computer Methods in Applied Mechanics and Engineering*, 213–216:327–352, 2012.
- [63] A. Prosperetti and G. Tryggvason. *Computational Methods for Multiphase Flow*. Cambridge University Press, 2007.
- [64] S. O. Unverdi and G. Tryggvason. A front-tracking method for viscous, incompressible, multi-fluid flows. *Journal of Computational Physics*, 100(1):25 – 37, 1992.
- [65] R. Vignjevic and James Campbell. *Review of Development of the Smooth Particle Hydrodynamics (SPH) Method*, pages 367–396. Springer US, Boston, MA, 2009.
- [66] J. Donea, S. Giuliani, and J. P. Halleux. An arbitrary Lagrangian-Eulerian finite element method for transient dynamic fluid-structure interactions. *Computer Methods in Applied Mechanics and Engineering*, 33(1):689 – 723, 1982.
- [67] J. U. Brackbill, D. B. Kothe, and C. Zemach. A continuum method for modeling surface tension. *Journal of Computational Physics*, 100(2):335 – 354, 1992.
- [68] R. Scardovelli and S. Zaleski. Direct numerical simulation of free-surface and interfacial flow. *Annual Review of Fluid Mechanics*, 31(1):567–603, 1999.

Bibliography

- [69] W. J. Rider and D. B. Kothe. Reconstructing volume tracking. *Journal of Computational Physics*, 141(2):112 – 152, 1998.
- [70] J. A. Sethian and P. Smereka. Level set methods for fluid interfaces. *Annual Review of Fluid Mechanics*, 35:341, 2003. Copyright - Copyright Annual Reviews, Inc. 2003; Last updated - 2014-05-18.
- [71] L. Zhao, X. Bai, T. Li, and J. J. R. Williams. Improved conservative level set method. *International Journal for Numerical Methods in Fluids*, 75(8):575–590, 2014. FLD-13-0333.R1.
- [72] M. Sussman and E. Fatemi. An efficient, interface-preserving level set redistancing algorithm and its application to interfacial incompressible fluid flow. *SIAM Journal on Scientific Computing*, 20(4):1165–27, 1999. Copyright - Copyright] © 1999 Society for Industrial and Applied Mathematics; Last updated - 2012-02-15.
- [73] D. Peng, B. Merriman, S. Osher, H. Zhao, and M. Kang. A PDE-based fast local level set method. *Journal of Computational Physics*, 155(2):410 – 438, 1999.
- [74] G. Russo and P. Smereka. A remark on computing distance functions. *Journal of Computational Physics*, 163(1):51 – 67, 2000.
- [75] D. Enright, R. Fedkiw, J. Ferziger, and I. Mitchell. A hybrid particle level set method for improved interface capturing. *Journal of Computational Physics*, 183(1):83 – 116, 2002.
- [76] D. Enright, F. Losasso, and R. Fedkiw. A fast and accurate semi-Lagrangian particle level set method. *Comput. Struct.*, 83(6-7):479–490, February 2005.
- [77] C. G. Koh, M. Gao, and C. Luo. A new particle method for simulation of incompressible free surface flow problems. *International Journal for Numerical Methods in Engineering*, 89(12):1582–1604, 2012.
- [78] M. Sussman and E. G. Puckett. A coupled level set and volume-of-fluid method for computing 3D and axisymmetric incompressible two-phase flows. *Journal of Computational Physics*, 162(2):301 – 337, 2000.

Bibliography

- [79] Z. Wang, J. Yang, B. Koo, and F. Stern. A coupled level set and volume-of-fluid method for sharp interface simulation of plunging breaking waves. *International Journal of Multiphase Flow*, 35(3):227 – 246, 2009.
- [80] X. Yang, A. J. James, J. Lowengrub, X. Zheng, and V. Cristini. An adaptive coupled level-set/volume-of-fluid interface capturing method for unstructured triangular grids. *Journal of Computational Physics*, 217(2):364 – 394, 2006.
- [81] E. Olsson and G. Kreiss. A conservative level set method for two phase flow. *Journal of Computational Physics*, 210(1):225 – 246, 2005.
- [82] E. Olsson, G. Kreiss, and S. Zahedi. A conservative level set method for two phase flow II. *Journal of Computational Physics*, 225(1):785 – 807, 2007.
- [83] D. M. Anderson, G. B. McFadden, and A. A. Wheeler. Diffuse-interface methods in fluid mechanics. *Annual Review of Fluid Mechanics*, 30(1):139–165, 1998.
- [84] D. M. Anderson and G. B. McFadden. A diffuse-interface description of fluid systems. In *NIST IR 5887 (National Institute of Standards and Technology)*, 1996.
- [85] S. M. Allen and J. W. Cahn. A microscopic theory for antiphase boundary motion and its application to antiphase domain coarsening. *Acta Metallurgica*, 27(6):1085 – 1095, 1979.
- [86] J. W. Cahn and J. E. Hilliard. Free energy of a nonuniform system. I. Interfacial free energy. *The Journal of Chemical Physics*, 28(2), 1958.
- [87] G. Tierra and F. Guillén-González. Numerical methods for solving the Cahn-Hilliard equation and its applicability to related energy-based models. *Archives of Computational Methods in Engineering*, 22(2):269–289, 04 2015.
- [88] Q. Du and R. A. Nicolaides. Numerical analysis of a continuum model of phase transition. *SIAM Journal on Numerical Analysis*, 28(5):1310–1322, 1991.
- [89] J. Rubinstein and P. Sternberg. Nonlocal reaction-diffusion equations and nucleation. *IMA Journal of Applied Mathematics*, 48(3):249–264, 1992.
- [90] L. Bronsard and B. Stoth. Volume-preserving mean curvature flow as a limit of a nonlocal Ginzburg-Landau equation. *SIAM Journal on Mathematical Analysis*, 28(4):769–39, 07

Bibliography

1997. Copyright - Copyright] © 1997 Society for Industrial and Applied Mathematics;
Last updated - 2012-02-29.

- [91] Z. Zhang and H. Tang. An adaptive phase field method for the mixture of two incompressible fluids. *Computers & Fluids*, 36(8):1307 – 1318, 2007.
- [92] X. Yang, J. J. Feng, C. Liu, and J. Shen. Numerical simulations of jet pinching-off and drop formation using an energetic variational phase-field method. *Journal of Computational Physics*, 218(1):417 – 428, 2006.
- [93] D. F. M. Vasconcelos, A. L. Rossa, and A. L. G. A. Coutinho. A residual-based Allen-Cahn phase field model for the mixture of incompressible fluid flows. *International Journal for Numerical Methods in Fluids*, 75(9):645–667, 2014.
- [94] M. Brassel and E. Bretin. A modified phase field approximation for mean curvature flow with conservation of the volume. *Mathematical Methods in the Applied Sciences*, 34(10):1157–1180, 2011.
- [95] J. Kim, S. Lee, and Y. Choi. A conservative Allen-Cahn equation with a space-time dependent Lagrange multiplier. *International Journal of Engineering Science*, 84:11 – 17, 2014.
- [96] D. Jeong and J. Kim. Conservative Allen-Cahn-Navier-Stokes system for incompressible two-phase fluid flows. *Computers & Fluids*, 156(Supplement C):239 – 246, 2017. Ninth International Conference on Computational Fluid Dynamics (ICCFD9).
- [97] J. Kim, D. Jeong, S.-D. Yang, and Y. Choi. A finite difference method for a conservative Allen-Cahn equation on non-flat surfaces. *Journal of Computational Physics*, 334(Supplement C):170 – 181, 2017.
- [98] J. Shin, S. K. Park, and J. Kim. A hybrid FEM for solving the Allen-Cahn equation. *Applied Mathematics and Computation*, 244(Supplement C):606 – 612, 2014.
- [99] T. J. R. Hughes and M. Mallet. A new finite element formulation for computational fluid dynamics: IV. A discontinuity-capturing operator for multidimensional advective-diffusive systems. *Computer Methods in Applied Mechanics and Engineering*, 58(3):329–336, 1986.

Bibliography

- [100] R. Löhner. *Applied Computational Fluid Dynamics Techniques*, pages 269–297. John Wiley & Sons, Ltd, 2008.
- [101] R. E. Bank and R. K. Smith. A posteriori error estimates based on hierarchical bases. *SIAM Journal on Numerical Analysis*, 30(4):921–935, 1993.
- [102] O. C. Zienkiewicz and J. Z. Zhu. A simple error estimator and adaptive procedure for practical engineering analysis. *International Journal for Numerical Methods in Engineering*, 24(2):337–357, 1987.
- [103] R. Verfürth. A posteriori error estimation and adaptive mesh-refinement techniques. *J. Comput. Appl. Math.*, 50(1-3):67–83, May 1994.
- [104] R. Verfürth. *A review of a posteriori error estimation and adaptive mesh-refinement techniques*. Wiley-Teubner, 1996.
- [105] R. Verfürth. Adaptive finite element methods. Lecture notes, Fakultät für Mathematik, Ruhr-Universität, Bochum, Germany.
- [106] A. Schmidt and K. G. Siebert. *Design of adaptive finite element software*. Springer, 2005.
- [107] D. Kessler, R. H. Nochetto, and A. Schmidt. A posteriori error control for the Allen–Cahn problem: Circumventing Gronwall’s inequality. *ESAIM: Mathematical Modelling and Numerical Analysis*, 38(1):129–142, 2004.
- [108] S. Bartels, R. Müller, and C. Ortner. Robust a priori and a posteriori error analysis for the approximation of Allen–Cahn and Ginzburg–Landau equations past topological changes. *SIAM Journal on Numerical Analysis*, 49(1):110–134, 2011.
- [109] E. H. Georgoulis and C. Makridakis. On a posteriori error control for the Allen-Cahn problem. *Mathematical Methods in the Applied Sciences*, 37(2):173–179, 2014.
- [110] S. Bartels. A posteriori error analysis for time-dependent Ginzburg-Landau type equations. *Numerische Mathematik*, 99(4):557–583, Feb 2005.
- [111] X. Feng and H. Wu. A posteriori error estimates and an adaptive finite element method for the Allen-Cahn equation and the mean curvature flow. *Journal of Scientific Computing*, 24(2):121–146, Aug 2005.

Bibliography

- [112] J. Zhang and Q. Du. Numerical studies of discrete approximations to the Allen-Cahn equation in the sharp interface limit. *SIAM Journal on Scientific Computing*, 31(4):3042–3063, 2009.
- [113] Z. Tan, K. M. Lim, and B. C. Khoo. An adaptive mesh redistribution method for the incompressible mixture flows using phase-field model. *Journal of Computational Physics*, 225:1137–1158, 2007.
- [114] B. S. Kirk, J. W. Peterson, R. H. Stogner, and G. F. Carey. libmesh: a C++ library for parallel adaptive mesh refinement/coarsening simulations. *Engineering with Computers*, 22(3):237–254, Dec 2006.
- [115] L. Chen and C. Zhang. A coarsening algorithm on adaptive grids by newest vertex bisection and its applications. *Journal of Computational Mathematics*, 28(6):767–789, 2010.
- [116] R. Mittal and G. Iaccarino. Immersed boundary methods. *Annual Review of Fluid Mechanics*, 37(1):239–261, 2005.
- [117] F. Sotiropoulos and X. Yang. Immersed boundary methods for simulating fluid-structure interaction. *Progress in Aerospace Sciences*, 65:1 – 21, 2014.
- [118] J. Hron and S. Turek. A monolithic FEM/multigrid solver for an ALE formulation of fluid-structure interaction with applications in biomechanics. In Hans-Joachim Bungartz and Michael Schäfer, editors, *Fluid-Structure Interaction*, pages 146–170, Berlin, Heidelberg, 2006. Springer Berlin Heidelberg.
- [119] Y. Bazilevs, V. M. Calo, T. J. R. Hughes, and Y. Zhang. Isogeometric fluid-structure interaction: Theory, algorithms, and computations. *Computational Mechanics*, 43(1):3–37, Dec 2008.
- [120] M. W. Gee, U. Küttler, and W. A. Wall. Truly monolithic algebraic multigrid for fluid-structure interaction. *International Journal for Numerical Methods in Engineering*, 85(8):987–1016.

Bibliography

- [121] J. Liu, R. K. Jaiman, and P. S. Gurugubelli. A stable second-order scheme for fluid–structure interaction with strong added-mass effects. *Journal of Computational Physics*, 270:687 – 710, 2014.
- [122] D. Corson, R. Jaiman, and F. Shakib. Industrial application of RANS modelling: Capabilities and needs. *International Journal of Computational Fluid Dynamics*, 23(4):337–347, 2009.
- [123] J. Fröhlich and D. von Terzi. Hybrid LES/RANS methods for the simulation of turbulent flows. *Progress in Aerospace Sciences*, 44(5):349 – 377, 2008.
- [124] P. R. Spalart. Detached-Eddy Simulation. *Annual Review of Fluid Mechanics*, 41(1):181–202, 2009.
- [125] S. R. Allmaras, F. T. Johnson, and P. R. Spalart. Modifications and clarifications for the implementation of the Spalart-Allmaras turbulence model. In *7th Conference on Computational Fluid Dynamics*, Big Island, Hawaii, 2012.
- [126] P. R. Spalart and S. R. Allmaras. A one-equation turbulence model for aerodynamic flows. *AIAA-92-0439*, 1992.
- [127] E. Lorin, A. Ben Haj Ali, and A. Soulaimani. A positivity preserving finite element-finite volume solver for the Spalart-Allmaras turbulence model. *Computer Methods in Applied Mechanics and Engineering*, 196:2097–2116, 2007.
- [128] D. Moro, N. C. Nguyen, and J. Peraire. Navier-Stokes solution using hybridizable discontinuous Galerkin methods. *AIAA-2011-3407*, 2011.
- [129] Y. Modarres-Sadeghi, F. Chasparis, M. S. Triantafyllou, M. Tognarelli, and P. Beynet. Chaotic response is a generic feature of vortex-induced vibrations of flexible risers. *Journal of Sound and Vibration*, 330(11):2565 – 2579, 2011.
- [130] A. Ongoren and D. Rockwell. Flow structure from an oscillating cylinder Part 2. Mode competition in the near wake. *Journal of Fluid Mechanics*, 191:225, 1988.

Bibliography

- [131] T. Srikanth, H. N. Dixit, R. Tatavarti, and R. Govindarajan. Vortex shedding patterns, their competition, and chaos in flow past inline oscillating rectangular cylinders. *Physics of Fluids*, 23:073603, 2011.
- [132] J. Vandiver. Drag coefficients of long flexible cylinders. In *Offshore Technology Conference*, Texas, USA, 1983.
- [133] J. M. Dahl. Vortex-induced vibration of a circular cylinder with combined in-line and cross-flow motion, 2008.
- [134] A. D. Trim, H. Braaten, H. Lie, and M. A. Tognarelli. Experimental investigation of vortex-induced vibration of long marine risers. *Journal of Fluids and Structures*, 21(3):335 – 361, 2005. Marine and Aeronautical Fluid-Structure Interactions.
- [135] Vortex induced vibration data repository- Datasets from ExxonMobil (Test case 1103) (<http://web.mit.edu/towtank/www/vivdr/downloadpage.html>).
- [136] J. K. Vandiver, S. Swithenbank, V. Jaiswal, and H. Marollo. The effectiveness of helical strakes in the suppression of high-mode-number VIV. In *Offshore Technology Conference, OTC 18276*, Houston, TX, 2006.
- [137] M. A. Tognarelli, S. Taggart, and M. Campbell. Actual VIV fatigue response of full scale drilling risers: with and without suppression devices. In *ASME 27th International Conference on Offshore Mechanics and Arctic Engineering (OMAE)*, Estoril, Portugal, 2008.
- [138] M. M. Zdravkovich. Flow induced oscillations of two interfering circular cylinders. *Journal of Sound and Vibration*, 101(4):511 – 521, 1985.
- [139] S. Holmes, O. H. Oakley, and Y. Constantinides. Simulation of riser VIV using fully three dimensional CFD simulations. In *ASME 25th International Conference on Offshore Mechanics and Arctic Engineering (OMAE)*, Hamburg, Germany, 2006.
- [140] Y. Constantinides and O. H. Oakley. Numerical prediction of bare and straked cylinder VIV. In *ASME 25th International Conference on Offshore Mechanics and Arctic Engineering (OMAE)*, Hamburg, Germany, 2006.

Bibliography

- [141] R. K. Jaiman, F. Shakib, O. H. Oakley, and Y. Constantinides. Fully coupled fluid-structure interaction for offshore applications. In *ASME Offshore Mechanics and Arctic Engineering OMAE09-79804 CP*, 2009.
- [142] Y. Constantinides and O. H. Oakley. Numerical prediction of VIV and comparison with field experiments. In *ASME 27th International Conference on Offshore Mechanics and Arctic Engineering (OMAE)*, Estoril, Portugal, 2008.
- [143] R. Bourguet, G. E. Karniadakis, and M. S. Triantafyllou. Vortex-induced vibrations of a long flexible cylinder in shear flow. *Journal of Fluid Mechanics*, 677:342–382, 6 2011.
- [144] K. Huang, H. C. Chen, and C. R. Chen. Vertical riser VIV simulation in uniform current. *Journal of Offshore Mechanics and Arctic Engineering*, 132(3):031101-1–031101-10, 2010.
- [145] E. Wang and Q. Xiao. Numerical simulation of vortex-induced vibration of a vertical riser in uniform and linearly sheared currents. *Ocean Engineering*, 121:492–515, 2016.
- [146] H. Kajitani, H. Miyata, M. Ikehata, H. Tanaka, H. Adachi, M. Nanimatsu, and S. Ogigawa. The summary of the cooperative experiment on Wigley parabolic model in Japan. In *17th ITTC Resistance Committee Report*, 1983.
- [147] J. Farmer, L. Martinelli, and A. Jameson. A fast multigrid method for solving incompressible hydrodynamic problems with free surfaces. *AIAA Journal*, 32(6):1175 – 1182, 1993.
- [148] R. Löhner, C. Yang, E. Oñate, and S. Idelsohn. An unstructured grid-based, parallel free surface solver. *Applied Numerical Mathematics*, 31(3):271 – 293, 1999.
- [149] I. Akkerman, Y. Bazilevs, C.E. Kees, and M.W. Farthing. Isogeometric analysis of free-surface flow. *Journal of Computational Physics*, 230(11):4137 – 4152, 2011. Special issue High Order Methods for CFD Problems.
- [150] A. Olivieri, F. Pistani, A. Avanzini, F. Stern, and R. Penna. Towing tank experiments of resistance, sinkage and trim, boundary layer, wake, and free surface flow around a naval combatant INSEAN 2340 model. *IIHR Technical Report No. 421*, 2001.

Bibliography

- [151] P. Voxaklis. Ship hull resistance calculations using CFD methods. Master's thesis, Massachusetts Institute of Technology, 2012.
- [152] I. Akkerman, Y. Bazilevs, D. J. Benson, M. W. Farthing, and C. E. Kees. Free-surface flow and fluid-object interaction modeling with emphasis on ship hydrodynamics. *Journal of Applied Mechanics*, 79(1):10905, 2012.
- [153] J. Chung and G. M. Hulbert. A time integration algorithm for structural dynamics with improved numerical dissipation: The generalized- α method. *Journal of Applied Mechanics*, 60(2):371–375, 1993.
- [154] D. Kuzmin. *A Guide to Numerical Methods for Transport Equations*. Friedrich-Alexander-Universität, Erlangen-Nürnberg, 2010.
- [155] I. Harari and T. J. R. Hughes. What are C and h?: Inequalities for the analysis and design of finite element methods. *Computer Methods in Applied Mechanics and Engineering*, 97(2):157–192, 1992.
- [156] R. Codina, E. Oñate, and M. Cervera. The intrinsic time for the streamline upwind/Petrov-Galerkin formulation using quadratic elements. *Computer Methods in Applied Mechanics and Engineering*, 94:239–262, 1992.
- [157] R. Codina and O. Soto. Approximation of the incompressible Navier-Stokes equations using orthogonal subscale stabilization and pressure segregation on anisotropic finite element meshes. *Computer Methods in Applied Mechanics and Engineering*, 193(15-16):1403–1419, 2004.
- [158] S. Mittal. On the performance of high aspect ratio elements for incompressible flows. *Computer Methods in Applied Mechanics and Engineering*, 188:269–287, 2000.
- [159] T. K. Sengupta, A. Dipankar, and P. Sagaut. Error dynamics: Beyond von Neumann analysis. *Journal of Computational Physics*, 226(2):1211 – 1218, 2007.
- [160] T. K. Sengupta. *High accuracy computing methods: Fluid flows and wave phenomena*. Cambridge University Press, 2013.

Bibliography

- [161] R. F. Warming and B. J. Hyett. The modified equation approach to the stability and accuracy analysis of finite-difference methods. *Journal of Computational Physics*, 14:159–179, 1974.
- [162] R. Codina. A finite element formulation for the numerical solution of the convection-diffusion equation. *CIMNE, Barcelona*, 1993.
- [163] M. Casey and T. Wintergerste. Best practice guidelines for industrial computational fluid dynamics. *ERCOFTAC*, 2000.
- [164] K. E. Jansen, C. H. Whiting, and G. M. Hulbert. A generalized- α method for integrating the filtered Navier-Stokes equations with a stabilized finite element method. *Computer Methods in Applied Mechanics and Engineering*, 190(3–4):305 – 319, 2000.
- [165] T. J. R. Hughes and G. Wells. Conservation properties for the Galerkin and stabilised forms of the advection-diffusion and incompressible Navier-Stokes equations. *Computer Methods in Applied Mechanics and Engineering*, 194:1141–1159, 2005.
- [166] M. Hsu, Y. Bazilevs, Calo V., T. Tezduyar, and T. J. R. Hughes. Improving stability of multiscale formulations of fluid flow at small time steps. *Computer Methods in Applied Mechanics and Engineering*, 199:828–840, 2010.
- [167] T. E. Tezduyar, S. Mittal, S. Ray, and R. Shih. Incompressible flow computations with stabilized bilinear and linear equal-order interpolation velocity-pressure elements. *Computer Methods in Applied Mechanics and Engineering*, 95:221–242, 1992.
- [168] L. Franca and S. Frey. Stabilized finite element methods: II. The incompressible Navier-Stokes equations. *Computer Methods in Applied Mechanics and Engineering*, 99:209–233, 1992.
- [169] C. Johnson. *Numerical solutions of partial differential equations by the finite element method*. Cambridge University Press, 1987.
- [170] P. S. Gurugubelli, R. Ghoshal, V. Joshi, and R. K. Jaiman. A variational projection scheme for nonmatching surface-to-line coupling between 3D flexible multibody system and incompressible turbulent flow. *Computers and Fluids*, 165:160 – 172, 2018.

Bibliography

- [171] J. Kim. Phase-field models for multi-component fluid flows. *Communications in Computational Physics*, 12(3):613–661, 009 2012.
- [172] J. Kim. A continuous surface tension force formulation for diffuse-interface models. *Journal of Computational Physics*, 204(2):784 – 804, 2005.
- [173] R. W. Ogden. *Non-linear elastic deformations*. Ellis Horwood, 1984.
- [174] J. Bonet and R. D. Wood. *Nonlinear continuum mechanics for finite element analysis*. Cambridge University Press, 1997.
- [175] A. Lew, J. E. Marsden, M. Ortiz, and M. West. Variational time integrators. *International Journal for Numerical Methods in Engineering*, 60(1):153–212, 2004.
- [176] Y. Saad and M. H. Schultz. GMRES: A generalized minimal residual algorithm for solving nonsymmetric linear systems. *SIAM J. Sci. Stat. Comput.*, 7(3):856–869, July 1986.
- [177] MPI webpage (www mpi-forum.org). Technical report, 2009.
- [178] J. C. Martin and W. J. Moyce. Part IV. An experimental study of the collapse of liquid columns on a rigid horizontal plane. *Philosophical Transactions of the Royal Society of London. Series A, Mathematical and Physical Sciences*, 244(882):312–324, 1952.
- [179] S. Koshizuka. A particle method for incompressible viscous flow with fluid fragmentation. *Computational Fluid Dynamics Journal*, 4:29, 1995.
- [180] E. Walhorn. *Ein simultanes Berechnungsverfahren für Fluid-Struktur-Wechselwirkungen mit finiten Raum-Zeit-Elementen*. PhD thesis, Technische Universität Braunschweig, 2002.
- [181] T. Kleefsman. *Water impact loading on offshore structures*. PhD thesis, University of Groningen, The Netherlands, 2005.
- [182] K. M. T. Kleefsman, G. Fekken, A. E. P. Veldman, B. Iwanowski, and B. Buchner. A volume-of-fluid based simulation method for wave impact problems. *Journal of Computational Physics*, 206(1):363 – 393, 2005.

Bibliography

- [183] R. Issa and D. Violeau. Test-case 2, 3D dambreaking, Release 1.1 (<http://app.spheric-sph.org/sites/spheric/tests/test-2>). Technical report, Electricité De France, Laboratoire National d’Hydraulique et Environnement, 2006.
- [184] R. N. Elias and A. L. G. A. Coutinho. Stabilized edge-based finite element simulation of free-surface flows. *International Journal for Numerical Methods in Fluids*, 54(6-8):965–993, 2007.
- [185] I. Akkerman, Y. Bazilevs, C. E. Kees, and M. W. Farthing. Isogeometric analysis of free-surface flow. *Journal of Computational Physics*, 230(11):4137 – 4152, 2011. Special issue High Order Methods for CFD Problems.
- [186] G. G. Stokes. *On the Theory of Oscillatory Waves*, volume 1 of *Cambridge Library Collection - Mathematics*, pages 197–229. Cambridge University Press, 2009.
- [187] K. P. Thiagarajan and N. Repalle. Wave run-up on columns of deepwater platforms. *Proceedings of the Institution of Mechanical Engineers, Part M: Journal of Engineering for the Maritime Environment*, 227(3):256–265, 2013.
- [188] C. Geuzaine and J. F. Remacle. Gmsh: A 3-D finite element mesh generator with built-in pre- and post-processing facilities. *International Journal for Numerical Methods in Engineering*, 79(11):1309–1331, 2009.
- [189] L. Chen and C. Zhang. AFEM@MATLAB: A MATLAB package of adaptive finite element methods. Technical report, University of Maryland.
- [190] W. Dörfler. A convergent adaptive algorithm for Poisson’s equation. *SIAM Journal on Numerical Analysis*, 33(3):1106–1124, 1996.
- [191] R. K. Jaiman, N. R. Pillalamarri, and M. Z. Guan. A stable second-order partitioned iterative scheme for freely vibrating low-mass bluff bodies in a uniform flow. *Computer Methods in Applied Mechanics and Engineering*, 301:187–215, 2016.
- [192] C. Brezinski. A classification of quasi-Newton methods. *Numerical Algorithms*, 33(1):123–135, Aug 2003.

Bibliography

- [193] C. Brezinski. *Projection methods for systems of equations*, volume 7. North-Holland, Amsterdam, 1997.
- [194] R. K. Jaiman, M. Z. Guan, and T. P. Miyanawala. Partitioned iterative and dynamic subgrid-scale methods for freely vibrating square-section structures at subcritical Reynolds number. *Computers and Fluids*, 133:68–89, 2016.
- [195] E. Nogueira and R. M. Cotta. Heat transfer solutions in laminar co-current flow of immiscible liquids. *Wärme - und Stoffübertragung*, 25(6):361–367, Nov 1990.
- [196] P. R. Spalart and S. R. Allmaras. A one-equation turbulence model for aerodynamic flows. *La Rech. Aérospatiale*, 1:5–21, 1994.
- [197] P. R. Spalart. Young-person’s guide to Detached-Eddy Simulation grids. *NASA/ CR-2001-211032*, 2001.
- [198] R. Zhao, J. Liu, and C. Yan. Detailed investigation of detached-eddy simulation for the flow past a circular cylinder at $Re=3900$. In *Progress in Hybrid RANS-LES Modelling: Papers Contributed to the 4th Symposium on Hybrid RANS-LES Methods, Beijing, China, September 2011*, pages 401–412. Springer Berlin Heidelberg, Berlin, Heidelberg, 2012.
- [199] L. Ong and J. Wallace. The velocity field of the turbulent very near wake of a circular cylinder. *Experiments in Fluids*, 20(6):441–453, 1996.
- [200] G. S. Cardell. *Flow past a circular cylinder with a permeable splitter plate*. PhD thesis, California Institute of Technology, 1993.
- [201] R. P. Hansen and J. R. Forsythe. Large and Detached Eddy Simulations of a circular cylinder using unstructured grids. *AIAA 2003-0775*, 2003.
- [202] Y. Constantinides and O. H. Oakley. Numerical simulation of cylinder VIV focusing on high harmonics. In *ASME 28th International Conference on Ocean, Offshore and Arctic Engineering*, Honolulu, USA, 2009.
- [203] J. K. Vandiver, V. Jaiswal, and V. Jhingran. Insights on vortex-induced, traveling waves on long risers. *Journal of Fluids and Structures*, 25:641–653, 2009.

Bibliography

- [204] V. Joshi and R. K. Jaiman. A variationally bounded scheme for delayed detached eddy simulation: Application to vortex-induced vibration of offshore riser. *Computers and Fluids*, 157:84 – 111, 2017.
- [205] J. M. Dahl, F. S. Hover, and M. S. Triantafyllou. Resonant vibrations of bluff bodies cause multivortex shedding and high frequency force. *Physical Review Letters*, 99(144503):1–4, 2007.
- [206] US Navy Combatant, DTMB 5415 (<http://www.simman2008.dk/5415/combatant.html>).
- [207] Gridgen User Manual “POINTWISE”, ver. 15, 2013.
- [208] R. J. Labeur and G. N. Wells. Energy stable and momentum conserving hybrid finite element method for the incompressible Navier-Stokes equations. *SIAM Journal on Scientific Computing*, 34(2):25, 2012.
- [209] H. Gómez, V. M. Calo, Y. Bazilevs, and T. J.R. Hughes. Isogeometric analysis of the Cahn–Hilliard phase-field model. *Computer Methods in Applied Mechanics and Engineering*, 197(49):4333 – 4352, 2008.
- [210] M. A. Christon, M. J. Martinez, and T. E. Voth. Generalized Fourier analyses of the advection-diffusion equation-Part I: one-dimensional domains. *International Journal for Numerical Methods in Fluids*, 45(8):839–887, 2004.
- [211] G. Hauke and M. H. Doweidar. Fourier analysis of semi-discrete and space-time stabilized methods for the advective-diffusive-reactive equation: II. SGS. *Computer Methods in Applied Mechanics and Engineering*, 194:691–725, 2005.
- [212] G. Hauke and M. H. Doweidar. Fourier analysis of semi-discrete and space-time stabilized methods for the advective-diffusive-reactive equation: I. SUPG. *Computer Methods in Applied Mechanics and Engineering*, 194:45–81, 2005.
- [213] F. Shakib and T. J. R. Hughes. A new finite element formulation for computational fluid dynamics: IX. Fourier analysis of space-time Galerkin/Least-Squares algorithms. *Computer Methods in Applied Mechanics and Engineering*, 87:35–58, 1991.

Bibliography

- [214] T. K. Sengupta, Y. G. Bhumkar, M. K. Rajpoot, V. K. Suman, and S. Saurabh. Spurious waves in discrete computation of wave phenomena and flow problems. *Applied Mathematics and Computation*, 218:9035 – 9065, 2012.
- [215] T. E. Voth, M. J. Martinez, and M. A. Christon. Generalized Fourier analyses of the advection-diffusion equation-Part II: two-dimensional domains. *International Journal for Numerical Methods in Fluids*, 45(8):889–920, 2004.
- [216] T. K. Sengupta, M. K. Rajpoot, S. Saurabh, and V. V. S. N. Vijay. Analysis of anisotropy of numerical wave solutions by high accuracy finite difference methods. *Journal of Computational Physics*, 230:27 – 60, 2011.

Appendix A

One-dimensional analysis of the local element matrix

In this section, we analyze the steady-state CDR equation and identify different regimes where the local element matrix fails to satisfy the positivity property. Consider the steady-state CDR equation in one-dimension:

$$u \frac{d\varphi}{dx} - k \frac{d^2\varphi}{dx^2} + s\varphi = f. \quad (\text{A.1})$$

For simplicity, assume that only Dirichlet boundary conditions are specified and $f = 0$. The variational formulation gives: find $\varphi_h(\mathbf{x}) \in \mathcal{S}_\varphi^h$ such that $\forall w_h \in \mathcal{V}_\varphi^h$,

$$\int_{\Omega(t)} \left(w_h u \frac{d\varphi_h}{dx} + \frac{dw_h}{dx} k \frac{d\varphi_h}{dx} + w_h s \varphi_h \right) d\Omega = 0. \quad (\text{A.2})$$

After linear finite element discretization in one-dimension, the above equation can be written as a system of linear equations, $\mathbf{A}\boldsymbol{\varphi} = \mathbf{b}$. Let \mathbf{A}^e be the local matrix at the element level. Using Eq. (3.35),

$$\mathbf{A}^e = \begin{bmatrix} -\frac{u}{2} + \frac{k}{h} + \frac{sh}{3} & \frac{u}{2} - \frac{k}{h} + \frac{sh}{6} \\ -\frac{u}{2} - \frac{k}{h} + \frac{sh}{6} & \frac{u}{2} + \frac{k}{h} + \frac{sh}{3} \end{bmatrix}. \quad (\text{A.3})$$

Case 1. Convection-reaction equation ($k = 0$): Let $Da = sh/u$ be the non-dimensional number representing the ratio of reaction to convection effects. Note that in this case, the first row non-diagonal element is positive for positive convection velocity and reaction coefficient, thus violating the positivity property (Eq. (3.29)). Although it seems that \mathbf{A}^e is violating the positivity property for all cases when $u > 0$ and $s > 0$, the method behaves well until $Da = 2.5$

Appendix A. One-dimensional analysis of the local element matrix

(observed in the performed numerical simulations). This can be explained by the fact that the conditions of positivity are sufficient but not necessary. Therefore, the convection-reaction equation solution behaves as positivity preserving for some small Da .

Case 2. Diffusion-reaction equation ($u = 0$): Let $\psi = sh^2/k$ be the representative non-dimensional number for this case. It is observed from Eq. (A.3) that the non-diagonal elements are positive when the reaction effects are in excess to those of the diffusion, i.e., when $(k/h) < (sh/6)$ or $\psi > 6$.

Case 3. Convection-diffusion equation ($s = 0$): $Pe = uh/2k$ is the non-dimensional number depicting the ratio of convection to diffusion effects. The non-diagonal element of the first row is positive when the convection effects are dominating to those of the diffusion, i.e., when $(u/2) > (k/h)$ or $Pe > 1$.

Since the positivity property is violated for many different regimes, we enforce this property with the help of the discrete upwind operator. For matrix \mathbf{A}^e , the operator is given by

$$\mathbf{D}^e = \begin{bmatrix} \max\left\{\frac{|u|}{2} - \frac{k}{h} + \frac{sh}{6}, 0\right\} & -\max\left\{\frac{|u|}{2} - \frac{k}{h} + \frac{sh}{6}, 0\right\} \\ -\max\left\{\frac{|u|}{2} - \frac{k}{h} + \frac{sh}{6}, 0\right\} & \max\left\{\frac{|u|}{2} - \frac{k}{h} + \frac{sh}{6}, 0\right\} \end{bmatrix} = \frac{k^{\text{add}}}{h} \begin{bmatrix} 1 & -1 \\ -1 & 1 \end{bmatrix}, \quad (\text{A.4})$$

where k^{add} can be considered as the added diffusion to the original equation which is expressed as

$$k^{\text{add}} = \max\left\{\frac{|u|h}{2} - k + \frac{sh^2}{6}, 0\right\}. \quad (\text{A.5})$$

This diffusion matrix when added to \mathbf{A}^e transforms it as (for positive u):

$$\tilde{\mathbf{A}}^e = \mathbf{A}^e + \mathbf{D}^e = \begin{bmatrix} \frac{sh}{2} & 0 \\ -u & u + \frac{sh}{2} \end{bmatrix}. \quad (\text{A.6})$$

The above matrix is positivity preserving since it has positive row-sum and non-diagonal elements are less than or equal to zero. The above simple formulation confirms that the positivity and local boundedness can be restored in the finite element method in a relatively simple manner.

Appendix B

The positivity condition for convective transport equation

We present a brief description of the positivity condition for the stabilized finite element method.

Consider a simplified form of Eq. (3.1) with only convection effects:

$$\partial_t \varphi + \mathbf{u} \cdot \nabla \varphi = 0. \quad (\text{B.1})$$

The positivity preserving variational formulation of the above problem will lead to the following finite element based stencil form:

$$\varphi_i^{n+1} = \varphi_i^n + C^+(\varphi_{i+1}^n - \varphi_i^n) - C^-(\varphi_i^n - \varphi_{i-1}^n), \quad (\text{B.2})$$

where

$$C^+ = -\frac{u\Delta t}{2h} + \frac{u^2\tau\Delta t}{h^2} + \frac{\chi\Delta t}{h^2} \frac{|\mathcal{R}(\varphi)|}{|\nabla\varphi|} \max\left\{\frac{uh}{2} - \tau u^2, 0\right\}, \quad (\text{B.3})$$

$$C^- = \frac{u\Delta t}{2h} + \frac{u^2\tau\Delta t}{h^2} + \frac{\chi\Delta t}{h^2} \frac{|\mathcal{R}(\varphi)|}{|\nabla\varphi|} \max\left\{\frac{uh}{2} - \tau u^2, 0\right\}, \quad (\text{B.4})$$

where h is the element length in one-dimension, Δt is the time step, τ is the linear stabilization parameter given by Eq. (3.19) and $\chi = 1/u$. All the parameters are defined by taking the diffusion and reaction coefficients to be null in the transient convection-diffusion-reaction equation.

For the scheme to be positivity preserving, the coefficients C^+ and C^- need to satisfy

$$C^+ \geq 0, \quad C^- \geq 0, \quad C^+ + C^- \leq 1. \quad (\text{B.5})$$

Next, we consider two scenarios as follows:

Appendix B. The positivity condition for convective transport equation

Case 1: Element nodes far from the discontinuity or diffusion-dominated regime, i.e., either $\mathcal{R}(\varphi) \rightarrow 0$ or $uh/2 - \tau u^2 < 0$. For these conditions, the coefficients will be

$$C^+ = -\frac{u\Delta t}{2h} + \frac{u^2\tau\Delta t}{h^2}, \quad (\text{B.6})$$

$$C^- = \frac{u\Delta t}{2h} + \frac{u^2\tau\Delta t}{h^2}, \quad (\text{B.7})$$

$$C^+ + C^- = \frac{2u^2\tau\Delta t}{h^2} = \left(\frac{u\Delta t}{h}\right)\left(\frac{2u\tau}{h}\right). \quad (\text{B.8})$$

Now we satisfy the positivity condition for this case.

$$\frac{uh}{2} - \tau u^2 < 0 \implies \frac{u\Delta t}{2h} - \frac{\tau u^2\Delta t}{h^2} < 0 \implies -\frac{u\Delta t}{2h} + \frac{\tau u^2\Delta t}{h^2} > 0 \implies C^+ > 0. \quad (\text{B.9})$$

Since u , Δt , h and τ are all positive, $C^- > 0$. Furthermore, the stabilization parameter τ can be expressed for the one-dimensional problem as

$$\tau = \left[\left(\frac{2}{\Delta t} \right)^2 + \left(\frac{2u}{h} \right)^2 \right]^{-1/2} \implies \frac{2u\tau}{h} = \left[\left(\frac{h}{u\Delta t} \right)^2 + 1 \right]^{-1/2}. \quad (\text{B.10})$$

The explicit scheme employed here satisfies the Courant-Friedrichs-Lowy condition for stability, i.e., $Co = u\Delta t/h \leq 1$. Therefore,

$$\frac{2u\tau}{h} = \left[\left(\frac{1}{Co} \right)^2 + 1 \right]^{-1/2} < 1, \quad (\text{B.11})$$

which implies that $C^+ + C^- \leq 1$ and the scheme satisfies the positivity condition. The definition of the stabilization parameter τ puts a bound to the term $2u\tau/h$ while satisfying the positivity condition.

Case 2: Element nodes near the discontinuity with optimal discrete upwind operation, i.e., $uh/2 - \tau u^2 > 0$ and $\chi|\mathcal{R}(\varphi)|/|\nabla\varphi| \approx 1$. The coefficients can be written as

$$C^+ = -\frac{u\Delta t}{2h} + \frac{u^2\tau\Delta t}{h^2} + \frac{u\Delta t}{2h} - \frac{u^2\tau\Delta t}{h^2} = 0, \quad (\text{B.12})$$

$$C^- = \frac{u\Delta t}{2h} + \frac{u^2\tau\Delta t}{h^2} + \frac{u\Delta t}{2h} - \frac{u^2\tau\Delta t}{h^2} = \frac{u\Delta t}{h} > 0, \quad (\text{B.13})$$

$$C^+ + C^- = \frac{u\Delta t}{h} \leq 1. \quad (\text{B.14})$$

We have employed the Courant-Friedrichs-Lowy condition and the fact that $Co > 0$ for satisfying the inequalities above. The above two cases show the behavior of the presented variational scheme to maintain the positivity property. The nonlinear residual term acts as a limiter function to regulate the stabilization terms.

Appendix C

Fourier analysis of the CDR equation in one-dimension

In this section, we perform one-dimensional Fourier analysis on the stabilized CDR equation to assess the GLS and SGS methods in more detail. The boundary conditions are assumed to be periodic throughout the domain. Similar to [210], let us express the exact solution of the transient CDR equation as a Fourier series

$$\varphi = A e^{\nu t + i K x}, \quad (\text{C.1})$$

where K is the spatial wave number and ν denotes the evolution of the solution with respect to time. ν can be written as

$$\nu = -\xi - i\omega, \quad (\text{C.2})$$

ξ and ω being the damping coefficient and frequency respectively and $i = \sqrt{-1}$. Substituting (C.1) and (C.2) in the transient form of Eq. (A.1), we get

$$\xi = s + k K^2, \quad (\text{C.3})$$

$$\omega = u K. \quad (\text{C.4})$$

We define the phase speed for the continuous CDR equation by

$$c = \frac{\omega}{K}. \quad (\text{C.5})$$

Appendix C. Fourier analysis of the CDR equation in one-dimension

The group velocity is defined by [210, 160]

$$v_g = \frac{\partial \omega}{\partial K} = c = u. \quad (\text{C.6})$$

Discretizing the continuous equation using the finite element method, we obtain the following three-point semi-discrete stencil for the linear GLS method:

$$\begin{aligned} & \frac{h}{6} [1 \ 4 \ 1] \dot{\varphi}_h + \frac{u\tau}{2} [1 \ 0 \ -1] \dot{\varphi}_h + \frac{s\tau h}{6} [1 \ 4 \ 1] \dot{\varphi}_h + \frac{u}{2} [-1 \ 0 \ 1] \varphi_h \\ & - \frac{k}{h} [1 \ -2 \ 1] \varphi_h + \frac{sh}{6} [1 \ 4 \ 1] \varphi_h - \frac{u^2\tau}{h} [1 \ -2 \ 1] \varphi_h + \frac{u\tau s}{2} [1 \ 0 \ -1] \varphi_h \\ & + \frac{u\tau s}{2} [-1 \ 0 \ 1] \varphi_h + \frac{\tau s^2 h}{6} [1 \ 4 \ 1] \varphi_h = \mathbf{0}, \end{aligned} \quad (\text{C.7})$$

where $\dot{\varphi}_h$ represents the time derivative of the unknown variable vector φ_h .

C.1 Semi-discrete analysis

In the semi-discrete domain, the solution is assumed as $\varphi_h(x_j, t) = Ae^{\nu^h t + iKjh}$, where $\nu^h = -\xi^h - i\omega^h$, ξ^h and ω^h being the algorithmic damping coefficient and algorithmic frequency respectively and A is a constant. Moreover, it is assumed that the time discretization has negligible error. For the discrete equation, the phase speed is given by

$$c^h = \frac{\omega^h}{K}. \quad (\text{C.8})$$

The group velocity for a numerical scheme is defined by [210]

$$v_g^h = \frac{\partial \omega^h}{\partial K}, \quad (\text{C.9})$$

which is not equal to the group velocity of the continuous differential equation, i.e., c or u .

Putting the above expressions in the stencil formula Eq. (C.7), it can be shown that

$$\nu_{\text{GLS}}^h = \frac{2(\cos(Kh) - 1)(k + u^2\tau) - \frac{sh^2}{3}(\cos(Kh) + 2)(1 + s\tau) - ih\sin(Kh)}{\frac{h^2}{3}(\cos(Kh) + 2)(1 + s\tau) - ihu\tau\sin(Kh)}. \quad (\text{C.10})$$

Similarly, for the SGS method,

$$\nu_{\text{SGS}}^h = \frac{2(\cos(Kh) - 1)(k + u^2\tau) - \frac{sh^2}{3}(\cos(Kh) + 2)(1 - s\tau) - ih\sin(Kh)(1 - 2s\tau)}{\frac{h^2}{3}(\cos(Kh) + 2)(1 - s\tau) - ihu\tau\sin(Kh)}. \quad (\text{C.11})$$

Further analysis is carried out to quantify the phase velocity ratio (or algorithmic frequency ratio) and the diffusivity (or algorithmic damping ratio) of the method by evaluating ω^h and ξ^h . The phase velocity ratio for the semi-discrete numerical scheme is defined by $c^h/c = \omega^h/\omega$. The

Appendix C. Fourier analysis of the CDR equation in one-dimension

algorithmic damping ratio is given by ξ^h/ξ while the group velocity ratio is given by v_g^h/c . The non-dimensional wave number $\bar{K} = Kh$ is defined such that it is equal to the element Damköhler number, $Da = sh/u$. The parameters u , k and K are kept constant and the element length (h) is varied from 0 to π/K . These ratios are plotted against the non-dimensional wavenumber Kh in Fig. C.1. The ideal continuous problem will have no phase error and damping ratio, shown as $\omega^h/\omega = 1$ and $\xi^h/\xi = 1$ respectively and the group velocity will be equal to the convection velocity $v_g^h = c$. It is observed from Fig. C.1 that SGS method has high phase error and is highly

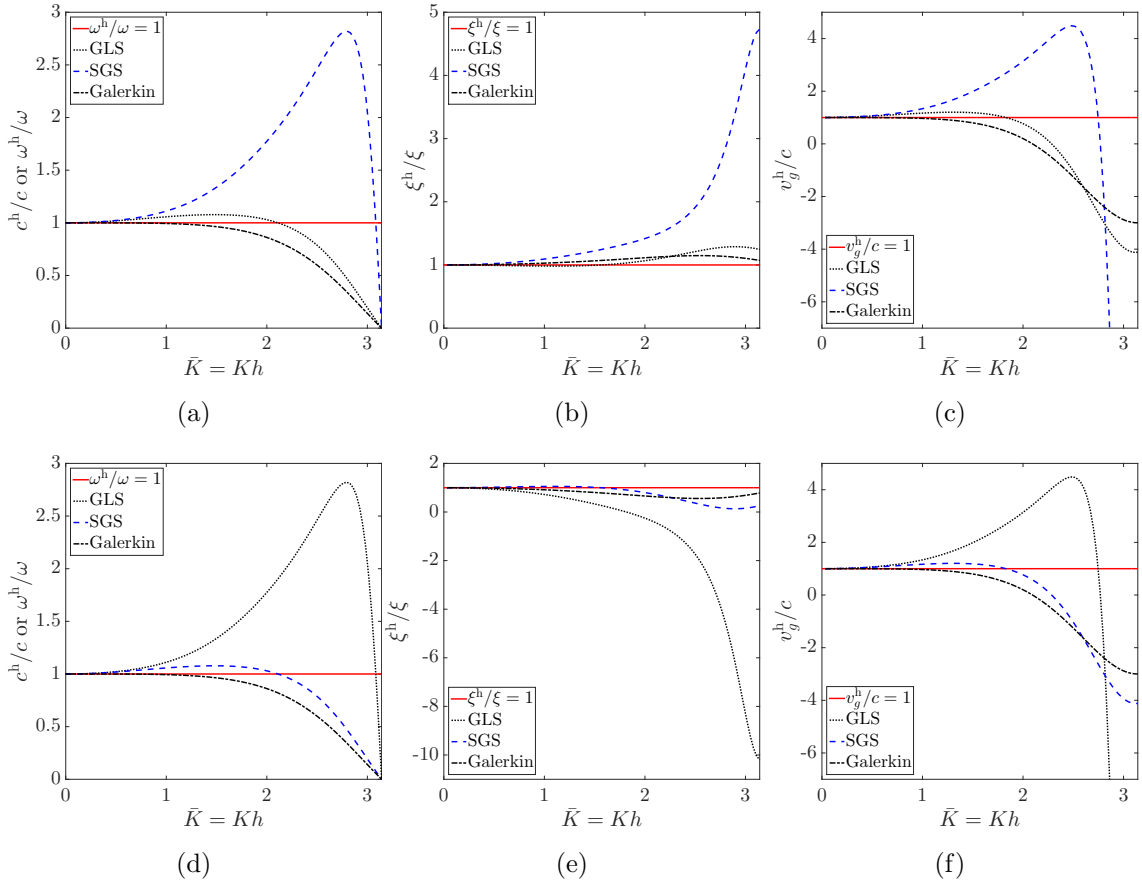


Figure C.1: Variation of phase velocity, damping and group velocity ratios with $\bar{K} = Kh$ for convection-diffusion-reaction problem for different numerical schemes: Phase velocity ratio for (a) positive reaction, (d) negative reaction; Damping ratio for (b) positive reaction, (e) negative reaction; Group velocity ratio for (c) positive reaction, (f) negative reaction. The plots for the proposed method will be similar to those of GLS method for positive reaction and those of SGS method for negative reaction.

damped at high positive Da . However, GLS method adds an appropriate amount of damping or diffusion. When the reaction coefficient is negative, SGS method performs better than GLS with respect to the phase error in both phase velocity as well as group velocity ratios. It also

Appendix C. Fourier analysis of the CDR equation in one-dimension

provides sufficient damping while damping of GLS is more negative compared to that of the Galerkin method. The accuracy of the scheme can be analyzed by expanding the expressions for algorithmic frequency and algorithmic damping coefficients as follows:

$$\omega_{\text{GLS}}^h = uK + ukK^3\tau - \left(\frac{uK^5}{180}\right)h^4 + \mathcal{O}(\tau\Delta t, \Delta t^2, \tau^2, h^6), \quad (\text{C.12})$$

$$\xi_{\text{GLS}}^h = s + kK^2 - skK^2\tau + \left(\frac{kK^4}{12}\right)h^2 + \mathcal{O}(\tau\Delta t, \Delta t^2, \tau^2, h^4). \quad (\text{C.13})$$

Similarly, for the SGS method,

$$\omega_{\text{SGS}}^h = uK + ukK^3\tau - \left(\frac{uK^5}{180}\right)h^4 + \mathcal{O}(\tau\Delta t, \Delta t^2, \tau^2, h^6), \quad (\text{C.14})$$

$$\xi_{\text{SGS}}^h = s + kK^2 + skK^2\tau + \left(\frac{kK^4}{12}\right)h^2 + \mathcal{O}(\tau\Delta t, \Delta t^2, \tau^2, h^4). \quad (\text{C.15})$$

The order of accuracy of ω^h and ξ^h depends on the reliance of the stabilization parameter τ on h . For Galerkin method ($\tau = 0$), ω^h and ξ^h are fourth-order and second-order accurate respectively. Stability and accuracy analysis for the SGS and SUPG methods was also performed in [211] and [212] respectively, however, the expression for the stabilization parameter τ was different. Moreover, constant Damköhler number and element length were assumed with varying wavenumber unlike the above analysis where the wavenumber is defined equal to the element Damköhler number.

C.2 Fully discrete analysis

In the fully discrete domain, the solution is assumed as $\varphi^h(x_j, t^n) = Ae^{\nu^h n\Delta t + iKjh}$, where Δt and n are the discretized time step size and the time step respectively. Let $\zeta^h = e^{\nu^h \Delta t}$ be the amplification factor of the scheme. Putting the above expressions in the stencil formula, it can be shown that for the backward Euler implicit time integration scheme,

$$\zeta_{\text{GLS}}^h = \frac{(2 + \cos\bar{K})(1 + \bar{s}\bar{\tau}) - i3\bar{u}\bar{\tau}\sin\bar{K}}{(2 + \cos\bar{K})(1 + \bar{s}\bar{\tau})(1 + \bar{s}) + 6(\bar{k} + \bar{u}^2\bar{\tau})(1 - \cos\bar{K}) + i3\bar{u}\sin\bar{K}(1 - \bar{\tau})}, \quad (\text{C.16})$$

where all the variables are non-dimensionalized as follows:

$$\bar{K} = Kh, \quad \bar{u} = \frac{u\Delta t}{h}, \quad \bar{k} = \frac{k\Delta t}{h^2}, \quad \bar{s} = s\Delta t, \text{ and } \bar{\tau} = \frac{\tau}{\Delta t}. \quad (\text{C.17})$$

Appendix C. Fourier analysis of the CDR equation in one-dimension

A similar fully discrete analysis was carried out in [213]. For the SGS method,

$$\zeta_{\text{SGS}}^h = \frac{(2 + \cos \bar{K})(1 - \bar{s}\bar{\tau}) - i3\bar{u}\bar{\tau}\sin \bar{K}}{(2 + \cos \bar{K})(1 - \bar{s}\bar{\tau})(1 + \bar{s}) + 6(\bar{k} + \bar{u}\bar{\tau})(1 - \cos \bar{K}) + i3\bar{u}\sin \bar{K}(1 - \bar{\tau} - 2\bar{s}\bar{\tau})}. \quad (\text{C.18})$$

For further analysis, we notice that ζ^h has both real and imaginary parts. Let $\zeta^h = \zeta_{\text{real}}^h +$

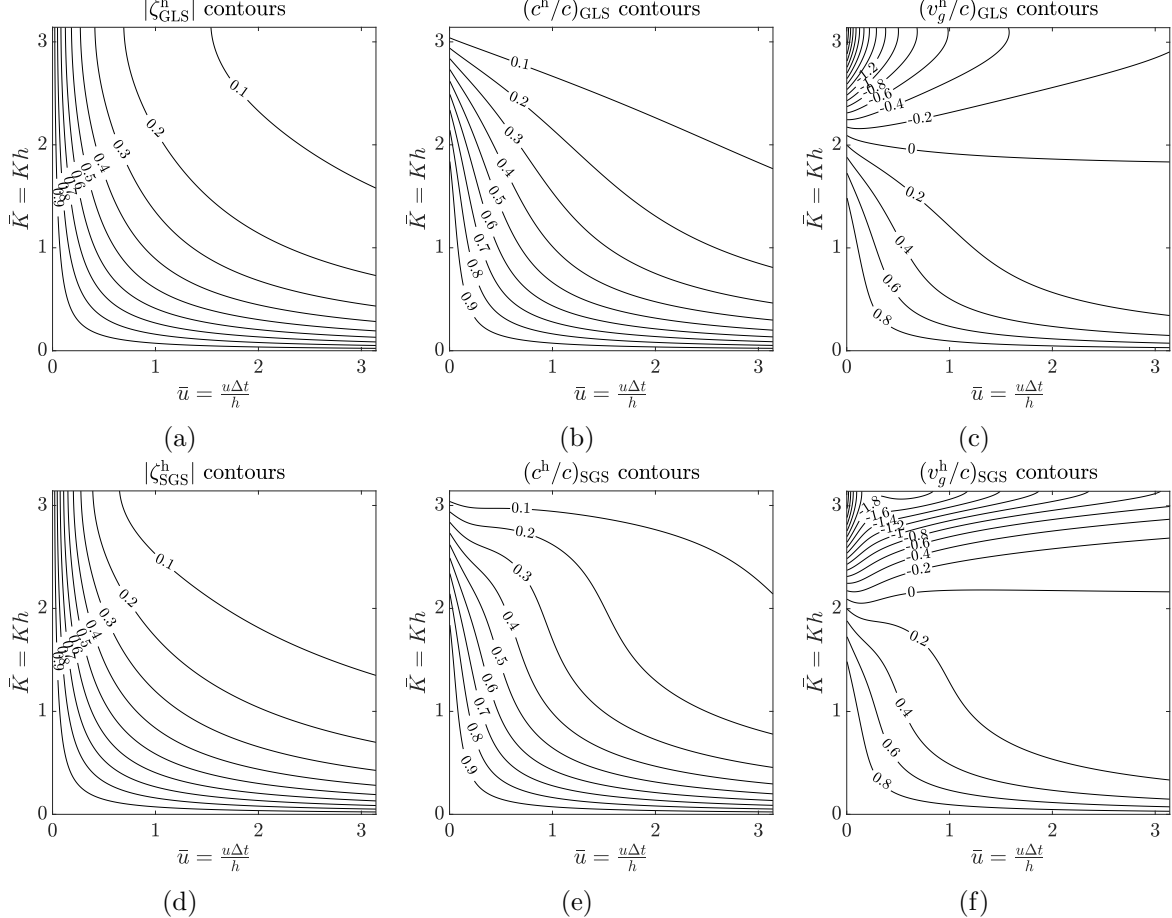


Figure C.2: Contours of the magnitude of the amplification factor ($|\zeta^h|$), the phase velocity ratio (c^h/c) and the group velocity ratio (v_g^h/c) for GLS and SGS methods when the reaction coefficient is positive ($s > 0$).

$i\zeta_{\text{imag}}^h$, where ζ_{real}^h and ζ_{imag}^h are the real and imaginary parts of the amplification factor for the respective scheme. Some of the quantities are defined below which are used in the analysis [159, 160, 214]:

$$|\zeta^h| = \left([\zeta_{\text{real}}^h]^2 + [\zeta_{\text{imag}}^h]^2 \right)^{1/2}, \quad (\text{C.19})$$

$$\tan \beta = -\frac{\zeta_{\text{imag}}^h}{\zeta_{\text{real}}^h}, \quad (\text{C.20})$$

$$\frac{c^h}{c} = \frac{\beta}{\omega \Delta t} = \frac{\beta}{c K \Delta t}, \quad (\text{C.21})$$

Appendix C. Fourier analysis of the CDR equation in one-dimension

$$\frac{v_g^h}{c} = \frac{1}{h\bar{u}} \frac{d\beta}{dK}, \quad (\text{C.22})$$

where $|\zeta^h|$ is the amplitude of the amplification factor of the scheme, c^h is the numerical phase velocity, β is known as the phase shift, ω is the frequency of the continuous CDR equation defined earlier, v_g^h is the numerical group velocity and c is the group velocity of the continuous CDR equation, i.e., $c = u$. The contours of these quantities are depicted in Figs. C.2 and C.3 for

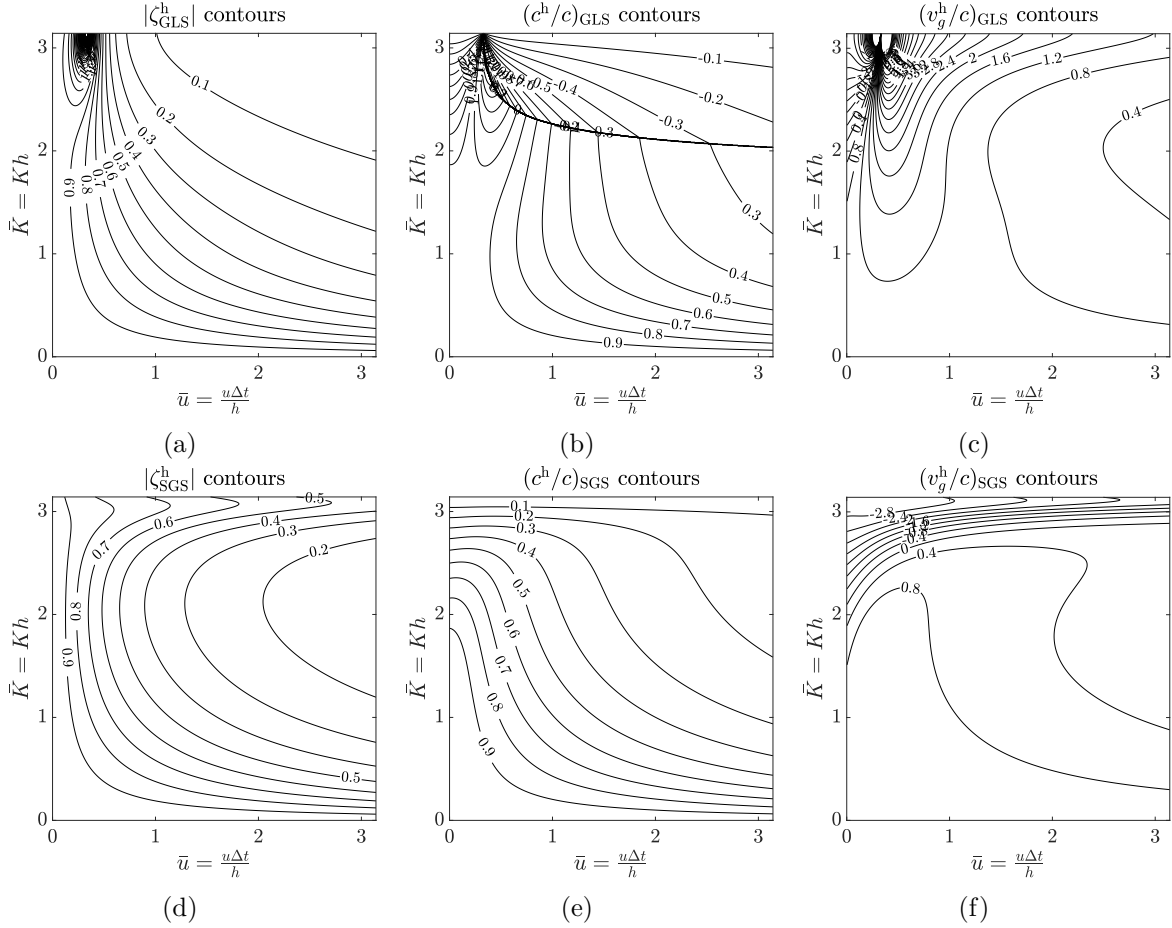


Figure C.3: Contours of the magnitude of the amplification factor ($|\zeta^h|$), the phase velocity ratio (c^h/c) and the group velocity ratio (v_g^h/c) for GLS and SGS methods when the reaction coefficient is negative ($s < 0$).

positive and negative reaction coefficients respectively. The abscissa shows the Courant number $\bar{u} = u\Delta t/h$ and the ordinate represents the non-dimensional wavenumber $\bar{K} = Kh$ which is assumed to be equal to the Damköhler number. The parameters u , k and K are kept constant and the element length (h) is varied from 0 to π/K . Δt is varied such that the Courant number \bar{u} varies from 0 to π . When the reaction coefficient is positive, $|\zeta^h| \leq 1$ over the whole plot for both GLS and SGS methods. Moreover, the phase and group velocity ratio plots are similar for

Appendix C. Fourier analysis of the CDR equation in one-dimension

both the methods.

However, due to excess diffusion in SGS method, we choose GLS in this regime. For the case when the reaction coefficient is negative, SGS seems to be stable for the whole regime. Furthermore, the phase velocity ratio becomes negative and has a jump discontinuity for the GLS method. The group velocity ratio plot shows negative values for both GLS and SGS methods, but SGS is better in this case since the minimum ratio is -3.085 compared to that in GLS where it is -6123.188 . These negative values of the group velocity ratio represent the upstream propagation of the signal waves which was also observed for the pure convection in [160, 214].

Such detailed analysis dealing with the Galerkin method, SUPG for linear interpolation functions and higher-order interpolations for convection equation was carried out in [160]. The proposed PPV method is a combination of GLS and SGS methods. It behaves as GLS method when $s \geq 0$ and as SGS when $s < 0$ for linear and multilinear elements. This ensures that the phase and accuracy of the method are maintained to the highest possible level.

Appendix D

Fourier analysis of the CDR equation in two-dimensions

We carry out the Fourier analysis in two-dimensions for the stabilized CDR equation in this section. The procedure is similar to that followed in [215]. Let the wave vector be $\mathbf{K} = K \cos \alpha_k \mathbf{i} + K \sin \alpha_k \mathbf{j}$ and the velocity vector be $\mathbf{u} = u \mathbf{i} + v \mathbf{j}$ in two dimensions with α_k denoting the wave propagation direction. The wave vector and the velocity vectors are assumed to be aligned in the same direction for simplicity so that $u = |\mathbf{u}| \cos \alpha_k$ and $v = |\mathbf{u}| \sin \alpha_k$. The nodal locations are given by mh_x and nh_y for a point (x_m, y_n) with aspect ratio, $\gamma_k = h_y/h_x$ with h_x and h_y denoting the grid size in the two coordinate axes respectively. Let us express the exact solution of the transient CDR equation as a Fourier series

$$\varphi = A e^{\nu t + i \mathbf{K} \cdot \mathbf{x}}, \quad (\text{D.1})$$

where \mathbf{K} is the spatial wave vector, \mathbf{x} is the position vector and ν denotes the evolution of the solution with respect to time. The damping coefficient and the frequency for the continuous CDR equation in two-dimensions can be obtained as

$$\xi = s + k K^2, \quad (\text{D.2})$$

$$\omega = |\mathbf{u}| K. \quad (\text{D.3})$$

The following semi-discrete stencil is used for the linear GLS method in two-dimensions (contains a total of 9 nodes with a node of coordinate (x_m, y_n) at the center surrounded by four elements):

Appendix D. Fourier analysis of the CDR equation in two-dimensions

$$\begin{aligned}
& \frac{h_x h_y}{36} \begin{bmatrix} 1 & 4 & 1 \\ 4 & 16 & 4 \\ 1 & 4 & 1 \end{bmatrix} \dot{\varphi}_h + \frac{u\tau h_y}{12} \begin{bmatrix} 1 & 0 & -1 \\ 4 & 0 & -4 \\ 1 & 0 & -1 \end{bmatrix} \dot{\varphi}_h + \frac{v\tau h_x}{12} \begin{bmatrix} -1 & -4 & -1 \\ 0 & 0 & 0 \\ 1 & 4 & 1 \end{bmatrix} \dot{\varphi}_h \\
& + \frac{s\tau h_x h_y}{36} \begin{bmatrix} 1 & 4 & 1 \\ 4 & 16 & 4 \\ 1 & 4 & 1 \end{bmatrix} \dot{\varphi}_h + \frac{uh_y}{12} \begin{bmatrix} -1 & 0 & 1 \\ -4 & 0 & 4 \\ -1 & 0 & 1 \end{bmatrix} \dot{\varphi}_h + \frac{vh_x}{12} \begin{bmatrix} 1 & 4 & 1 \\ 0 & 0 & 0 \\ -1 & -4 & -1 \end{bmatrix} \dot{\varphi}_h \\
& + \frac{sh_x h_y}{36} \begin{bmatrix} 1 & 4 & 1 \\ 4 & 16 & 4 \\ 1 & 4 & 1 \end{bmatrix} \dot{\varphi}_h - \frac{\tau}{6} \begin{bmatrix} u^2 \frac{h_y}{h_x} - 3uv + v^2 \frac{h_x}{h_y} & -2u^2 \frac{h_y}{h_x} + 4v^2 \frac{h_x}{h_y} & u^2 \frac{h_y}{h_x} + 3uv + v^2 \frac{h_x}{h_y} \\ 4u^2 \frac{h_y}{h_x} - 2v^2 \frac{h_x}{h_y} & -8(u^2 \frac{h_y}{h_x} + v^2 \frac{h_x}{h_y}) & 4u^2 \frac{h_y}{h_x} - 2v^2 \frac{h_x}{h_y} \\ u^2 \frac{h_y}{h_x} + 3uv + v^2 \frac{h_x}{h_y} & -2u^2 \frac{h_y}{h_x} + 4v^2 \frac{h_x}{h_y} & u^2 \frac{h_y}{h_x} - 3uv + v^2 \frac{h_x}{h_y} \end{bmatrix} \dot{\varphi}_h \\
& + \frac{s\tau uh_y}{12} \begin{bmatrix} -1 & 0 & 1 \\ -4 & 0 & 4 \\ -1 & 0 & 1 \end{bmatrix} \dot{\varphi}_h + \frac{s\tau vh_x}{12} \begin{bmatrix} 1 & 4 & 1 \\ 0 & 0 & 0 \\ -1 & -4 & -1 \end{bmatrix} \dot{\varphi}_h + \frac{u\tau sh_y}{12} \begin{bmatrix} 1 & 0 & -1 \\ 4 & 0 & -4 \\ 1 & 0 & -1 \end{bmatrix} \dot{\varphi}_h + \frac{v\tau sh_x}{12} \begin{bmatrix} -1 & -4 & -1 \\ 0 & 0 & 0 \\ 1 & 4 & 1 \end{bmatrix} \dot{\varphi}_h \\
& + \frac{s^2 \tau h_x h_y}{36} \begin{bmatrix} 1 & 4 & 1 \\ 4 & 16 & 4 \\ 1 & 4 & 1 \end{bmatrix} \dot{\varphi}_h - \frac{k}{6} \begin{bmatrix} \frac{h_y}{h_x} + \frac{h_x}{h_y} & -2\frac{h_y}{h_x} + 4\frac{h_x}{h_y} & \frac{h_y}{h_x} + \frac{h_x}{h_y} \\ 4\frac{h_y}{h_x} - 2\frac{h_x}{h_y} & -8(\frac{h_y}{h_x} + \frac{h_x}{h_y}) & 4\frac{h_y}{h_x} - 2\frac{h_x}{h_y} \\ \frac{h_y}{h_x} + \frac{h_x}{h_y} & -2\frac{h_y}{h_x} + 4\frac{h_x}{h_y} & \frac{h_y}{h_x} + \frac{h_x}{h_y} \end{bmatrix} \dot{\varphi}_h = 0. \tag{D.4}
\end{aligned}$$

The $\dot{\varphi}_h$ denotes the time derivative of the unknown variable and periodic boundary condition is assumed over the entire domain. Also, for simplicity, the analysis is carried out in the semi-discrete form assuming that negligible error occurs in the time discretization. In the discrete domain, the solution is assumed as $\varphi_h((m, n), t) = A e^{v^h t + i K h_x (m \cos \alpha_k + n \gamma_k \sin \alpha_k)}$. Substituting this expression in the stencil formula, we get

$$\begin{aligned}
\nu_{\text{GLS}}^h &= \frac{1}{\gamma_k h_x^2 M_x M_y (1 + s\tau) - i\tau h_x (u\gamma_k M_y \sin \alpha_x + v M_x \sin \alpha_y)} \times \\
&\left[\frac{2M_x(\cos \alpha_y - 1)}{\gamma_k} (k + \tau v^2) + 2M_y(\cos \alpha_x - 1)\gamma_k(k + \tau u^2) - 2\tau u v \sin \alpha_x \sin \alpha_y \right. \\
&\left. - s\gamma_k h_x^2 M_x M_y (1 + s\tau) - i h_x (u\gamma_k M_y \sin \alpha_x + v M_x \sin \alpha_y) \right], \tag{D.5}
\end{aligned}$$

where

$$\alpha_x = K h_x \cos \alpha_k, \tag{D.6}$$

$$\alpha_y = K h_y \sin \alpha_k = K \gamma_k h_x \sin \alpha_k, \tag{D.7}$$

Appendix D. Fourier analysis of the CDR equation in two-dimensions

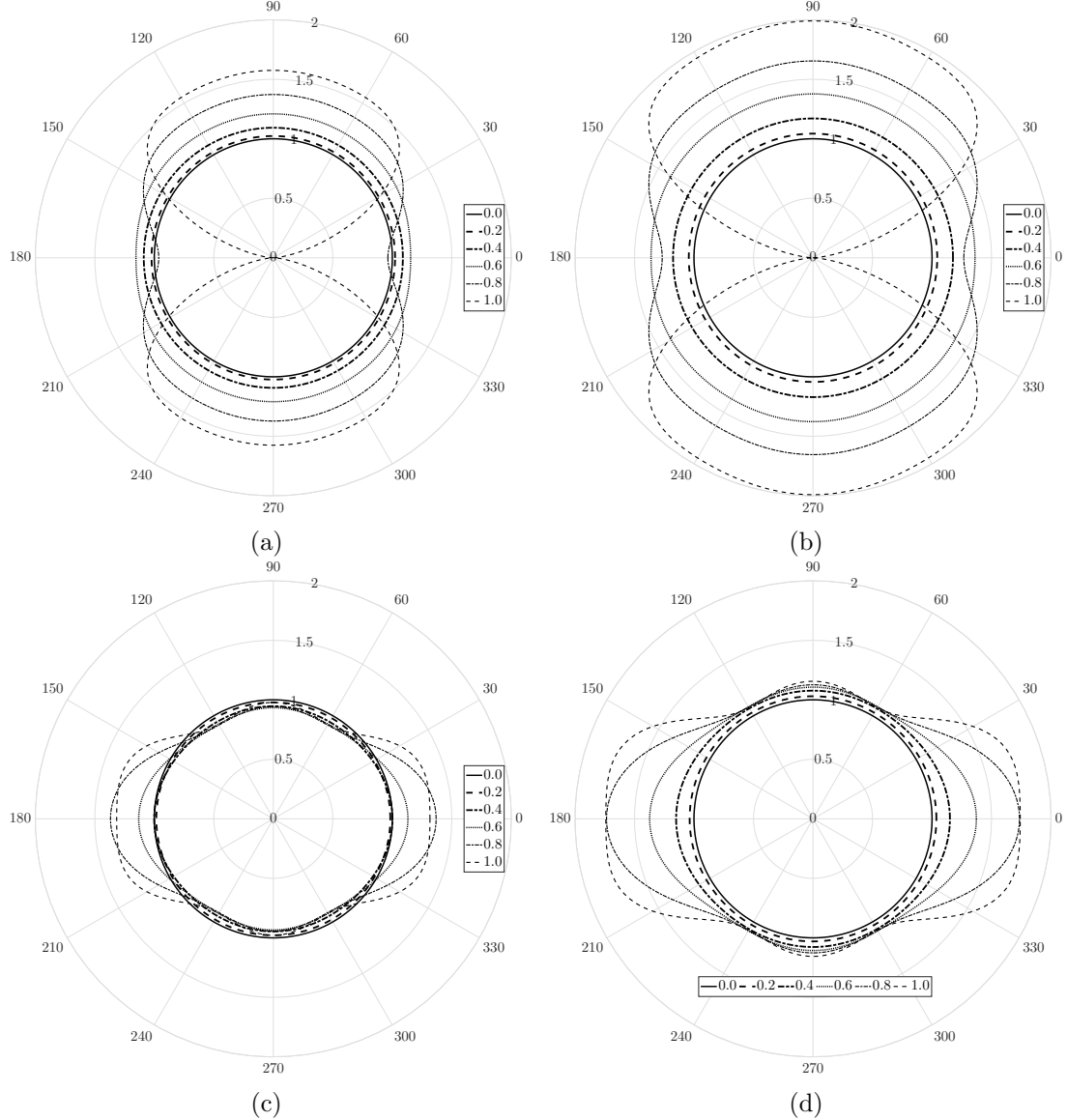


Figure D.1: Variation of phase velocity and damping ratios with α_k for different $Kh_x/\pi \in [0, 1]$ for convection-diffusion-reaction problem with positive reaction: Phase velocity ratio for (a) GLS, (b) SGS; Damping ratio for (c) GLS, (d) SGS. The plots for the proposed method will be similar to those of GLS method in this regime.

$$M_x = \frac{\cos\alpha_x + 2}{3}, \quad (D.8)$$

$$M_y = \frac{\cos\alpha_y + 2}{3}. \quad (D.9)$$

Similarly, for the SGS method,

$$\begin{aligned} \nu_{SGS}^h = & \frac{1}{\gamma_k h_x^2 M_x M_y (1 - s\tau) - i\tau h_x (u\gamma_k M_y \sin\alpha_x + v M_x \sin\alpha_y)} \times \\ & \left[\frac{2M_x(\cos\alpha_y - 1)}{\gamma_k} (k + \tau v^2) + 2M_y(\cos\alpha_x - 1)\gamma_k (k + \tau u^2) - 2\tau u v \sin\alpha_x \sin\alpha_y \right] \end{aligned}$$

Appendix D. Fourier analysis of the CDR equation in two-dimensions

$$-s\gamma_k h_x^2 M_x M_y (1 - s\tau) - i h_x u \gamma_k M_y \sin \alpha_x (1 - 2s\tau) - i h_x v M_x \sin \alpha_y (1 - 2s\tau) \Big]. \quad (\text{D.10})$$

One can observe the similarity in the above expressions compared with those of one-dimensional

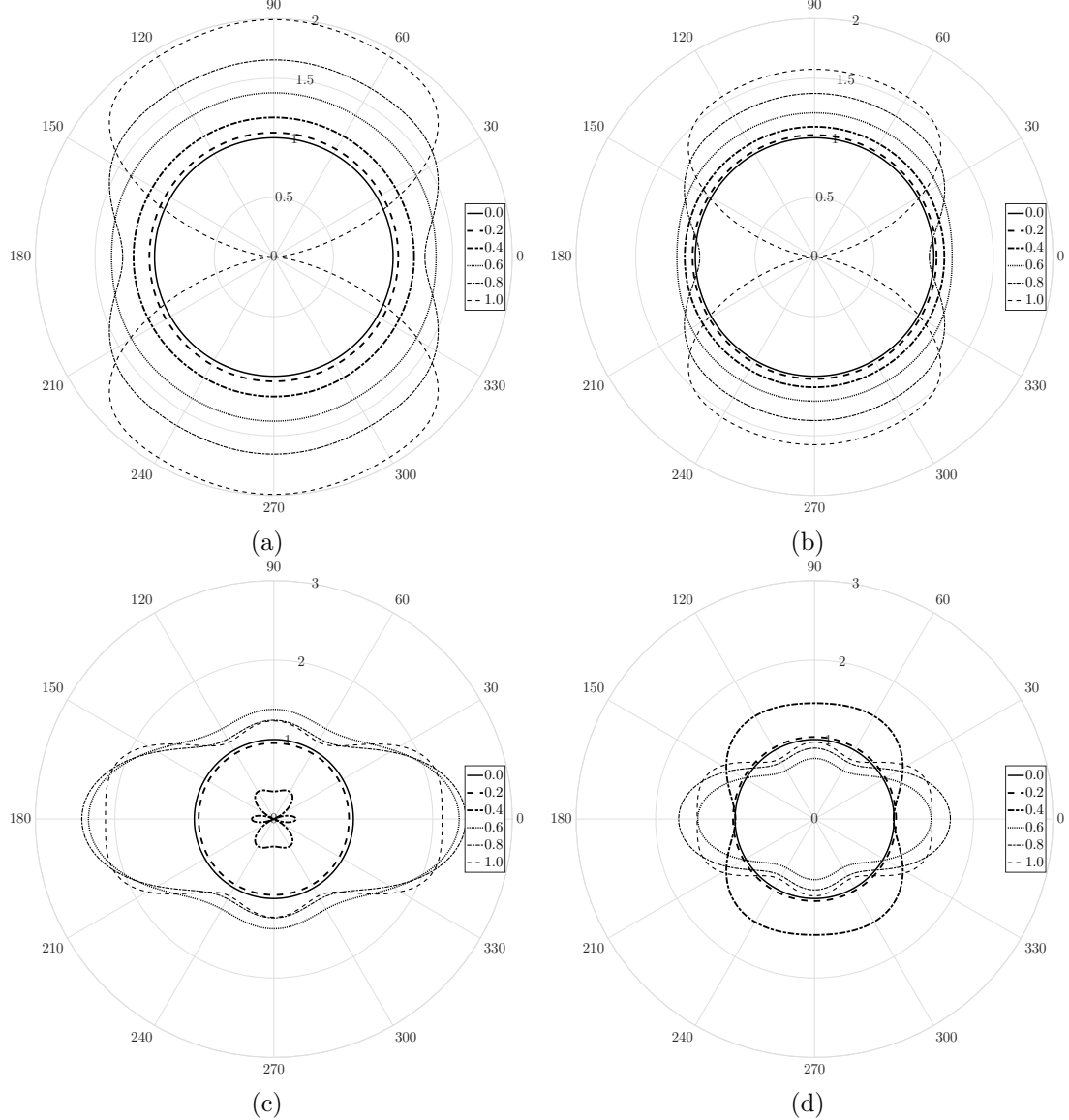


Figure D.2: Variation of phase velocity and damping ratios with α_k for different $Kh_x/\pi \in [0, 1]$ for convection-diffusion-reaction problem with negative reaction: Phase velocity ratio for (a) GLS, (b) SGS; Damping ratio for (c) GLS, (d) SGS. The plots for the proposed method will be similar to those of SGS method in this regime.

analysis. The two-dimensional expression reduces to the one-dimensional one along the coordinate directions. The phase velocity ratio is defined as ω^h/ω and the damping ratio as ξ^h/ξ . Since the wave propagation direction α_k is an extra parameter, polar plots with α_k as azimuthal coordinate and the phase velocity ratio or the algorithmic damping ratio as the radial coordi-

Appendix D. Fourier analysis of the CDR equation in two-dimensions

nate with the aspect ratio of $\gamma_k = 1/2$ are shown in Figs. D.1 and D.2 for positive and negative reaction respectively. Similar observations as in one-dimensional analysis can be made for the two-dimensional results from the polar plots. The semi-discrete wave velocity will be equal to the continuous wave velocity in the absence of phase error from $h \rightarrow 0$ to the grid Nyquist limit. Therefore, the ideal phase speed ratio curves are circular with $\omega^h/\omega = 1$. For positive reaction coefficient (Figs. D.1(a) and (b)), the GLS method has less phase error compared to the SGS method since it is closer to the ideal circular curve of zero phase error. Moreover, SGS is more diffusive than the GLS method (Figs. D.1(c) and (d)). In the negative reaction regime (Fig. D.2), SGS method behaves quite well with less phase error and damping than the GLS method.

A similar analysis for finite difference methods was carried out in [216] for the pure convection problem where the dispersion error was characterized in terms of the phase velocity and group velocity ratios in the two independent directions. Convection-diffusion equation under the finite element framework was analyzed in [215].

Appendix E

Exact solutions of the CDR equation in one-dimension

For the sake of completeness, we present analytical solution of the one-dimensional CDR equation:

$$u \frac{d\varphi}{dx} - k \frac{d^2\varphi}{dx^2} + s\varphi = f. \quad (\text{E.1})$$

Let L be the length of the computational domain, A and B be the Dirichlet conditions specified at the left-hand and right-hand extreme nodes respectively. Let $m_1 = \frac{-u+\sqrt{u^2+4ks}}{-2k}$, $m_2 = \frac{-u-\sqrt{u^2+4ks}}{-2k}$. If,

$$C_1 = \frac{Ae^{m_2 L} - \frac{f}{s}(e^{m_2 L} - 1) - B}{e^{m_2 L} - e^{m_1 L}}, \quad (\text{E.2})$$

$$C_2 = A - C_1 - \frac{f}{s}, \quad (\text{E.3})$$

then, the exact solution is given by

$$\varphi(x) = C_1 e^{m_1 x} + C_2 e^{m_2 x} + \frac{f}{s}. \quad (\text{E.4})$$

The exact solution for each of the canonical cases, i.e., convection-reaction, diffusion-reaction and convection-diffusion can be derived similarly in a simple manner.

Appendix F

Discrete energy stability proof for the Allen-Cahn equation

Here, we derive the statement of discrete energy stability for our variational phase-field formulation based on the convective Allen-Cahn equation presented in Section 5.2.2. We show that our proposed formulation is provably energy-stable. We will take one particular case when $\alpha_m^f = \gamma^f = 0.5$. To prove the energy stability, we choose the following approximation

$$\phi^{n+\alpha^f} = \frac{\phi^{n+1} + \phi^n}{2}, \quad (\text{F.1})$$

$$\partial_t \phi^{n+\alpha_m^f} = \frac{\phi^{n+1} - \phi^n}{\Delta t}. \quad (\text{F.2})$$

For simplicity, we assume that $\hat{\mathbf{u}} = \mathbf{0}$. The discrete variational formulation is now given as

$$\begin{aligned} & \int_{\Omega^f(t)} \left(\hat{w}_h \partial_t \phi_h + \nabla \hat{w}_h \cdot (\hat{k} \nabla \phi_h) + \hat{w}_h \hat{s} \phi_h - \hat{w}_h \hat{f} \right) d\Omega \\ & + \sum_{e=1}^{n_{el}} \int_{\Omega^e} \chi \frac{|\mathcal{R}(\phi_h)|}{|\nabla \phi_h|} k_c^{\text{add}} \nabla \hat{w}_h \cdot \mathbf{I} \cdot \nabla \phi_h d\Omega^e = 0. \end{aligned} \quad (\text{F.3})$$

Now, substituting $\hat{w}_h = \phi^{n+1} - \phi^n$, each term of Eq. (F.3) can be written as follows:

$$\text{Inertia term : } \int_{\Omega^f(t)} \hat{w}_h \partial_t \phi_h d\Omega = \int_{\Omega^f(t)} (\phi^{n+1} - \phi^n) \frac{(\phi^{n+1} - \phi^n)}{\Delta t} d\Omega = \frac{1}{\Delta t} \|\phi^{n+1} - \phi^n\|_0^2, \quad (\text{F.4})$$

$$\begin{aligned} \text{Diffusion term : } & \int_{\Omega^f(t)} \nabla \hat{w}_h \cdot (\hat{k} \nabla \phi_h) d\Omega = \int_{\Omega^f(t)} \varepsilon^2 \nabla (\phi^{n+1} - \phi^n) \cdot \nabla \left(\frac{\phi^{n+1} + \phi^n}{2} \right) d\Omega \\ & = \frac{\varepsilon^2}{2} \|\nabla \phi^{n+1}\|_0^2 - \frac{\varepsilon^2}{2} \|\nabla \phi^n\|_0^2, \end{aligned} \quad (\text{F.5})$$

$$\text{Reaction/source terms : } \int_{\Omega^f(t)} \hat{w}_h (\hat{s} \phi_h - \hat{f}) d\Omega$$

Appendix F. Discrete energy stability proof for the Allen-Cahn equation

$$\begin{aligned}
&= \int_{\Omega^f(t)} (\phi^{n+1} - \phi^n) F'(\phi) d\Omega - \beta(t) \int_{\Omega^f(t)} (\phi^{n+1} - \phi^n) \sqrt{F(\phi)} d\Omega \\
&= \int_{\Omega^f(t)} (F(\phi^{n+1}) - F(\phi^n)) d\Omega - \beta(t) \int_{\Omega^f(t)} (K(\phi^{n+1}) - K(\phi^n)) d\Omega \\
&= \int_{\Omega^f(t)} (F(\phi^{n+1}) - F(\phi^n)) d\Omega,
\end{aligned} \tag{F.6}$$

$$\begin{aligned}
\text{PPV stabilization term :} & \sum_{e=1}^{n_{el}} \int_{\Omega^e} \chi \frac{|\mathcal{R}(\phi_h)|}{|\nabla \phi_h|} k_c^{\text{add}} \nabla \hat{w}_h \cdot \nabla \phi_h d\Omega^e \\
&= \int_{\Omega^f(t)} \chi \frac{|\mathcal{R}(\phi_h)|}{|\nabla \phi_h|} k_c^{\text{add}} \nabla (\phi^{n+1} - \phi^n) \cdot \nabla \left(\frac{\phi^{n+1} + \phi^n}{2} \right) d\Omega \\
&= \frac{\chi}{2} \frac{|\mathcal{R}(\phi_h)|}{|\nabla \phi_h|} k_c^{\text{add}} \|\nabla \phi^{n+1}\|_0^2 - \frac{\chi}{2} \frac{|\mathcal{R}(\phi_h)|}{|\nabla \phi_h|} k_c^{\text{add}} \|\nabla \phi^n\|_0^2.
\end{aligned} \tag{F.7}$$

The third line of Eq. (F.6) is obtained by substituting the corresponding discretizations of $F'(\phi)$ and $\sqrt{F(\phi)}$ which are expressed in Eqs. (5.16) and (5.17) respectively. Equation (5.11) further helps to simplify the expression in Eq. (F.6). By substituting the expressions in Eq. (F.3) and after some algebraic arrangements, we get the following discrete energy statement:

$$\mathcal{E}(\phi^{n+1}) - \mathcal{E}(\phi^n) = -\frac{1}{\Delta t} \|\phi^{n+1} - \phi^n\|_0^2 \leq 0, \tag{F.8}$$

where $\mathcal{E}(\phi)$ is the modified energy functional given as

$$\mathcal{E}(\phi) = \int_{\Omega^f(t)} \left(\frac{1}{2} (\varepsilon^2 + \chi \frac{|\mathcal{R}(\phi_h)|}{|\nabla \phi_h|} k_c^{\text{add}}) |\nabla \phi|^2 + F(\phi) \right) d\Omega. \tag{F.9}$$

Therefore, the presented scheme is unconditionally energy-stable. In other words, the discrete Allen-Cahn phase-field equation possesses the energy functional that is bounded for all time, with the bound depending only on the problem data. A similar proof can be derived for the θ -family of time integration methods (which are specific cases of the generalized- α method) with the condition of unconditional energy stability as $\theta \geq 0.5$.

Appendix G

Discrete mass conservation for the Allen-Cahn equation

In this section, we prove the mass conservation property of the discrete Allen-Cahn equation presented in Eq. (5.25). Consider $\hat{w}_h = 1$ in Eq. (5.25). With the aid of boundary conditions in Eqs. (5.7-5.9), the incompressibility condition and the Gauss divergence theorem, we have

$$\int_{\Omega^f(t)} \hat{\mathbf{u}} \cdot \nabla \phi_h d\Omega = \int_{\Gamma} (\hat{\mathbf{u}} \phi_h) \cdot \mathbf{n} d\Gamma - \int_{\Omega^f(t)} \phi_h (\nabla \cdot \hat{\mathbf{u}}) d\Omega = 0. \quad (\text{G.1})$$

Since $\nabla \hat{w}_h = 0$, Eq. (5.25) can be rewritten as

$$\int_{\Omega^f(t)} \left(\partial_t \phi_h + \hat{s} \phi_h \right) d\Omega = 0, \quad (\text{G.2})$$

$$\implies \int_{\Omega^f(t)} \left(\partial_t \phi_h + F'(\phi) - \beta(t) \sqrt{F(\phi)} \right) d\Omega = 0, \quad (\text{G.3})$$

$$\implies \int_{\Omega^f(t)} \partial_t \phi_h d\Omega + \int_{\Omega^f(t)} F'(\phi) d\Omega - \beta(t) \int_{\Omega^f(t)} \sqrt{F(\phi)} d\Omega = 0. \quad (\text{G.4})$$

Using the definition of $\beta(t)$ in Eq. (5.10), we obtain

$$\int_{\Omega^f(t)} \partial_t \phi_h d\Omega + \int_{\Omega^f(t)} F'(\phi) d\Omega - \int_{\Omega^f(t)} F'(\phi) d\Omega = 0. \quad (\text{G.5})$$

Since $\partial_t \phi_h$ is evaluated at $n + \alpha^f$, we can write

$$\int_{\Omega^f(t)} \partial_t \phi^{n+\alpha^f} d\Omega = 0, \quad (\text{G.6})$$

which can be expressed as follows using Eqs. (5.12) and (5.13),

$$\int_{\Omega^f(t)} \partial_t \phi^n - \frac{\alpha_m^f}{\gamma^f} \partial_t \phi^n + \frac{\alpha_m^f}{\gamma^f \Delta t} (\phi^{n+1} - \phi^n) d\Omega = 0, \quad (\text{G.7})$$

Appendix G. Discrete mass conservation for the Allen-Cahn equation

which implies that the mass will only be conserved when $\alpha_m^f = \gamma^f$. This completes the proof of discrete mass conservation. All the simulations performed in the present study consider $\alpha_m^f = \gamma^f = \alpha^f = 0.5$.

Appendix H

Temporal accuracy of the discrete Allen-Cahn equation

Through the Taylor series argument and the truncation error analysis, we show the second-order accuracy of the temporally discretized conservative Allen-Cahn equation with $\hat{\mathbf{u}} = \mathbf{0}$. The continuous Allen-Cahn phase-field equation can be expressed without any temporal approximation as

$$\partial_t \phi^{n+\alpha_m^f} - \varepsilon^2 \nabla^2 \phi^{n+\alpha^f} + F'(\phi^{n+\alpha^f}) - \beta(t^{n+\alpha^f}) K'(\phi^{n+\alpha^f}) = 0. \quad (\text{H.1})$$

Here, we take a particular case of $\alpha_m^f = \gamma^f = \alpha^f = 0.5$. After the approximations between $[t^n, t^{n+1}]$, we have

$$\underbrace{\frac{\phi^{n+1} - \phi^n}{\Delta t}}_{\text{Inertia}} - \underbrace{\frac{\varepsilon^2}{2} \left(\nabla^2 \phi^{n+1} + \nabla^2 \phi^n \right)}_{\text{Diffusion}} + \underbrace{\frac{F(\phi^{n+1}) - F(\phi^n)}{\phi^{n+1} - \phi^n}}_{\text{Double-well potential}} - \underbrace{\beta(t^{n+1}, t^n) \frac{K(\phi^{n+1}) - K(\phi^n)}{\phi^{n+1} - \phi^n}}_{\text{Lagrange multiplier}} = 0, \quad (\text{H.2})$$

where $\beta(t^{n+1}, t^n)$ is the time dependent part of the Lagrange multiplier written using the mid-point approximation as

$$\beta(t^{n+1}, t^n) = \frac{\int_{\Omega^f(t)} \frac{F(\phi^{n+1}) - F(\phi^n)}{\phi^{n+1} - \phi^n} d\Omega}{\int_{\Omega^f(t)} \frac{K(\phi^{n+1}) - K(\phi^n)}{\phi^{n+1} - \phi^n} d\Omega}. \quad (\text{H.3})$$

Appendix H. Temporal accuracy of the discrete Allen-Cahn equation

Expanding the variables for each component using the Taylor series, we have the following terms:

$$\phi^{n+1} = \phi^{n+1/2} + \frac{1}{2}\Delta t \partial_t \phi^{n+1/2} + \frac{1}{2}\left(\frac{1}{2}\Delta t\right)^2 \partial_{tt} \phi^{n+1/2} + \frac{1}{6}\left(\frac{1}{2}\Delta t\right)^3 \partial_{ttt} \phi^{n+1/2} + \mathcal{O}(\Delta t^5), \quad (\text{H.4})$$

$$\phi^n = \phi^{n+1/2} - \frac{1}{2}\Delta t \partial_t \phi^{n+1/2} + \frac{1}{2}\left(\frac{1}{2}\Delta t\right)^2 \partial_{tt} \phi^{n+1/2} - \frac{1}{6}\left(\frac{1}{2}\Delta t\right)^3 \partial_{ttt} \phi^{n+1/2} + \mathcal{O}(\Delta t^5), \quad (\text{H.5})$$

$$\nabla^2 \phi^{n+1} = \nabla^2 \phi^{n+1/2} + \frac{1}{2}\Delta t \partial_t (\nabla^2 \phi^{n+1/2}) + \frac{1}{2}\left(\frac{1}{2}\Delta t\right)^2 \partial_{tt} (\nabla^2 \phi^{n+1/2}) + \mathcal{O}(\Delta t^3), \quad (\text{H.6})$$

$$\nabla^2 \phi^n = \nabla^2 \phi^{n+1/2} - \frac{1}{2}\Delta t \partial_t (\nabla^2 \phi^{n+1/2}) + \frac{1}{2}\left(\frac{1}{2}\Delta t\right)^2 \partial_{tt} (\nabla^2 \phi^{n+1/2}) - \mathcal{O}(\Delta t^3), \quad (\text{H.7})$$

$$F(\phi^{n+1}) = F(\phi^{n+1/2}) + \frac{1}{2}(\Delta t) F'(\phi^{n+1/2}) \partial_t \phi^{n+1/2} + \mathcal{O}(\Delta t^2), \quad (\text{H.8})$$

$$F(\phi^n) = F(\phi^{n+1/2}) - \frac{1}{2}(\Delta t) F'(\phi^{n+1/2}) \partial_t \phi^{n+1/2} + \mathcal{O}(\Delta t^2), \quad (\text{H.9})$$

$$K(\phi^{n+1}) = K(\phi^{n+1/2}) + \frac{1}{2}(\Delta t) K'(\phi^{n+1/2}) \partial_t \phi^{n+1/2} + \mathcal{O}(\Delta t^2), \quad (\text{H.10})$$

$$K(\phi^n) = K(\phi^{n+1/2}) - \frac{1}{2}(\Delta t) K'(\phi^{n+1/2}) \partial_t \phi^{n+1/2} + \mathcal{O}(\Delta t^2). \quad (\text{H.11})$$

After substituting Eqs. (H.4) and (H.5) in the inertia term and Eqs. (H.6) and (H.7) in the diffusion term, we obtain:

$$\underline{\text{Inertia}} : \frac{\phi^{n+1} - \phi^n}{\Delta t} = \partial_t \phi^{n+1/2} + \mathcal{O}(\Delta t^2), \quad (\text{H.12})$$

$$\underline{\text{Diffusion}} : \frac{-\varepsilon^2}{2} (\nabla^2 \phi^{n+1} + \nabla^2 \phi^n) = -\varepsilon^2 \nabla^2 \phi^{n+1/2} + \mathcal{O}(\Delta t^2). \quad (\text{H.13})$$

We next estimate the truncation error in the double-well potential and the Lagrange multiplier terms for which we need an expression to evaluate the error in the ratio of $F(\phi^{n+1}) - F(\phi^n)$ and $\phi^{n+1} - \phi^n$ (for the double-well potential term) and the ratio of $K(\phi^{n+1}) - K(\phi^n)$ and $\phi^{n+1} - \phi^n$ (for the Lagrange multiplier term). Suppose we have a quantity $R_3 = R_1/R_2$ and the error in evaluating R_1 and R_2 are ΔR_1 and ΔR_2 respectively. By assuming the continuous differential property of the error functions R_1 and R_2 , the error in R_3 can be expressed via the quotient rule as

$$\frac{\Delta R_3}{R_3} = \frac{\Delta R_1}{R_1} - \frac{\Delta R_2}{R_2}. \quad (\text{H.14})$$

Appendix H. Temporal accuracy of the discrete Allen-Cahn equation

Substituting Eqs. (H.8), (H.9), (H.4) and (H.5) in the double-well potential term, we can construct:

$$F(\phi^{n+1}) - F(\phi^n) = (\Delta t)F'(\phi^{n+1/2})\partial_t\phi^{n+1/2} + \mathcal{O}(\Delta t^3), \quad (\text{H.15})$$

$$\phi^{n+1} - \phi^n = (\Delta t)\partial_t\phi^{n+1/2} + \mathcal{O}(\Delta t^3). \quad (\text{H.16})$$

To evaluate the truncation error in the ratio of these quantities, we utilize Eq. (H.14). Let $R_1 = (\Delta t)F'(\phi^{n+1/2})\partial_t\phi^{n+1/2}$ with error $\Delta R_1 = \mathcal{O}(\Delta t^3)$ and $R_2 = (\Delta t)\partial_t\phi^{n+1/2}$ with error $\Delta R_2 = \mathcal{O}(\Delta t^3)$. Therefore, the truncation error in $R_3 = R_1/R_2$ is given by

$$\Delta R_3 = \left(\frac{\Delta R_1}{R_1} - \frac{\Delta R_2}{R_2} \right) R_3 = \frac{(1 - F'(\phi^{n+1/2}))}{\partial_t\phi^{n+1/2}} \mathcal{O}(\Delta t^2). \quad (\text{H.17})$$

The truncation error in the double-well potential term can thus be written as

$$\text{Double - well potential : } \frac{F(\phi^{n+1}) - F(\phi^n)}{\phi^{n+1} - \phi^n} = \frac{R_1 + \Delta R_1}{R_2 + \Delta R_2} = R_3 + \Delta R_3 = F'(\phi^{n+1/2}) + \mathcal{O}(\Delta t^2). \quad (\text{H.18})$$

Through the similar arguments, it is observed that the spatial part of the Lagrange multiplier can be expressed as

$$\frac{K(\phi^{n+1}) - K(\phi^n)}{\phi^{n+1} - \phi^n} = K'(\phi^{n+1/2}) + \mathcal{O}(\Delta t^2). \quad (\text{H.19})$$

Now, let us look into the time dependent part of the Lagrange multiplier $\beta(t^{n+1}, t^n)$ which can be reduced using Eqs. (H.18) and (H.19) as

$$\beta(t^{n+1}, t^n) = \frac{\int_{\Omega^f(t)} F'(\phi^{n+1/2}) + \mathcal{O}(\Delta t^2) d\Omega}{\int_{\Omega^f(t)} K'(\phi^{n+1/2}) + \mathcal{O}(\Delta t^2) d\Omega}. \quad (\text{H.20})$$

With the help of the error estimation for the ratio of two quantities in Eq. (H.14), the error in $\beta(t^{n+1}, t^n)$ is $\mathcal{O}(\Delta t^2)$ and therefore,

$$\beta(t^{n+1}, t^n) = \frac{\int_{\Omega^f(t)} F'(\phi^{n+1/2}) d\Omega}{\int_{\Omega^f(t)} K'(\phi^{n+1/2}) d\Omega} + \mathcal{O}(\Delta t^2) = \beta(t^{n+1/2}) + \mathcal{O}(\Delta t^2). \quad (\text{H.21})$$

Substituting Eqs. (H.19) and (H.21) in the Lagrange multiplier term,

$$\text{Lagrange multiplier : } \beta(t^{n+1}, t^n) \frac{K(\phi^{n+1}) - K(\phi^n)}{\phi^{n+1} - \phi^n} = \beta(t^{n+1/2}) K'(\phi^{n+1/2}) + \mathcal{O}(\Delta t^2). \quad (\text{H.22})$$

Appendix H. Temporal accuracy of the discrete Allen-Cahn equation

Finally, substituting Eqs. (H.12), (H.13), (H.18) and (H.22) in Eq. (H.2), we get

$$\partial_t \phi^{n+1/2} - \varepsilon^2 \nabla^2 \phi^{n+1/2} + F'(\phi^{n+1/2}) - \beta(t^{n+1/2}) K'(\phi^{n+1/2}) + \mathcal{O}(\Delta t^2) = 0, \quad (\text{H.23})$$

which implies that the present temporal discretization is second-order accurate. This has been further confirmed in Fig. 5.2(b) via numerical experiments.

Appendix I

Residual error estimates for the Allen-Cahn equation

We derive the residual error estimates for the Allen-Cahn equation following a similar procedure as in [105]. Let the time interval $[0, T]$ be subdivided into intervals of length $\Delta t = t^{n+1} - t^n$, $n = 0, 1, 2, \dots$. For each time t^n , an affine equivalent, admissible and shape-regular partition \mathcal{T} of the domain $\Omega^f(t)$ which consists of elements Ω_e , is chosen such that $\Omega^f(t) = \cup_{e=1}^{n_{el}} \Omega_e$ and $\emptyset = \cap_{e=1}^{n_{el}} \Omega_e$, where n_{el} is the number of elements. Let the finite element space of trial solution in the partition be denoted by $\mathcal{S}_\phi^h \in \mathbb{V}^h$ and the space of test functions be represented by $\mathcal{V}_\phi^h \in \mathbb{V}^h$, where $\mathbb{V}^h \in \mathbb{V}$ is the finite element space on the partition \mathcal{T} . For simplicity, we only consider the Galerkin discretization of the Allen-Cahn equation in Eq. (5.25) which can be written as: find $\phi_h(\mathbf{x}^f, t^{n+\alpha^f}) \in \mathcal{S}_\phi^h$ such that for all $\hat{w}_h \in \mathcal{V}_\phi^h$,

$$\int_{\Omega^f(t)} \left(\hat{w}_h \partial_t \phi_h + \hat{w}_h (\hat{\mathbf{u}} \cdot \nabla \phi_h) + \nabla \hat{w}_h \cdot (\hat{k} \nabla \phi_h) + \hat{w}_h \hat{s} \phi_h - \hat{w}_h \hat{f} \right) d\Omega = 0. \quad (I.1)$$

Let Γ be the Lipschitz continuous boundary of the domain $\Omega^f(t)$, Γ_D and Γ_N be the Dirichlet and Neumann boundaries of $\Omega^f(t)$ respectively such that $\Gamma = \Gamma_D \cup \Gamma_N$. Furthermore, let \mathcal{E} denote the set of edges for all the elements in the domain, \mathcal{E}_Γ , \mathcal{E}_{Γ_D} and \mathcal{E}_{Γ_N} be the set of edges on the boundary Γ , Γ_D and Γ_N respectively. Consider \mathcal{E}_{Ω_e} to be the set of edges of an element Ω_e and \mathcal{E}_Ω be the set of all the interior edges of $\Omega^f(t)$. Suppose the left-hand-side of Eq. (I.1) is denoted by LHS. It can thus be expressed as:

$$\text{LHS} = \int_{\Omega^f(t)} \hat{w}_h \partial_t \phi_h d\Omega + \int_{\Omega^f(t)} \hat{w}_h (\hat{\mathbf{u}} \cdot \nabla \phi_h) d\Omega - \int_{\Omega^f(t)} \hat{w}_h (\hat{k} \nabla^2 \phi_h) d\Omega$$

Appendix I. Residual error estimates for the Allen-Cahn equation

$$+ \sum_{e=1}^{n_{el}} \int_{\mathcal{E}_{\Omega_e}} \hat{w}_h \hat{k} (\mathbf{n}_{\mathcal{E}_{\Omega_e}} \cdot \nabla \phi_h) d\Omega_e + \int_{\Omega^f(t)} \hat{w}_h \hat{s} \phi_h d\Omega - \int_{\Omega^f(t)} \hat{w}_h \hat{f} d\Omega \quad (I.2)$$

$$= \int_{\Omega^f(t)} \hat{w}_h (\partial_t \phi_h + \hat{\mathbf{u}} \cdot \nabla \phi_h - \hat{k} \nabla^2 \phi_h + \hat{s} \phi_h - \hat{f}) d\Omega + \sum_{e=1}^{n_{el}} \int_{\mathcal{E}_{\Omega_e}} \hat{w}_h \hat{k} (\mathbf{n}_{\mathcal{E}_{\Omega_e}} \cdot \nabla \phi_h) d\Omega_e \quad (I.3)$$

$$= \sum_{e=1}^{n_{el}} \int_{\Omega_e} \hat{w}_h \mathcal{R}_{\Omega_e}(\phi_h) d\Omega_e + \sum_{E \in \mathcal{E}} \int_E \hat{w}_h \mathcal{R}_E(\phi_h) dE, \quad (I.4)$$

where $\mathbf{n}_{\mathcal{E}_{\Omega_e}}$ is the normal to the element edge \mathcal{E}_{Ω_e} , \mathcal{R}_{Ω_e} and \mathcal{R}_E are the element and edge based residuals given as,

$$\mathcal{R}_{\Omega_e} = \partial_t \phi_h + \hat{\mathbf{u}} \cdot \nabla \phi_h - \hat{k} \nabla^2 \phi_h + \hat{s} \phi_h - \hat{f}, \quad (I.5)$$

$$\mathcal{R}_E = \begin{cases} -\mathbb{J}_E(\mathbf{n}_E \cdot \hat{k} \nabla \phi_h), & \text{if } E \in \mathcal{E}_\Omega, \\ -\mathbf{n}_E \cdot \hat{k} \nabla \phi_h, & \text{if } E \in \mathcal{E}_{\Gamma_N}, \\ 0, & \text{if } E \in \mathcal{E}_{\Gamma_D}, \end{cases} \quad (I.6)$$

where $\mathbb{J}_E(\cdot)$ is the jump of the argument across the element edge E and \mathbf{n}_E is the normal to the edge E . Using the property of Galerkin orthogonality in Eq. (I.4), we obtain

$$\text{LHS} = \sum_{e=1}^{n_{el}} \int_{\Omega_e} (\hat{w}_h - w_{\mathcal{T}}) \mathcal{R}_{\Omega_e}(\phi_h) d\Omega_e + \sum_{E \in \mathcal{E}} \int_E (\hat{w}_h - w_{\mathcal{T}}) \mathcal{R}_E(\phi_h) dE. \quad (I.7)$$

By choosing $w_{\mathcal{T}} = \mathcal{I}_{\mathcal{T}} \hat{w}_h$ where $\mathcal{I}_{\mathcal{T}}$ is the quasi-interpolation operator and using the Cauchy-Schwarz inequality for integrals:

$$\text{LHS} \leq \sum_{e=1}^{n_{el}} \|\mathcal{R}_{\Omega_e}\|_{\Omega_e} \|\hat{w}_h - \mathcal{I}_{\mathcal{T}} \hat{w}_h\|_{\Omega_e} + \sum_{E \in \mathcal{E}} \|\mathcal{R}_E\|_E \|\hat{w}_h - \mathcal{I}_{\mathcal{T}} \hat{w}_h\|_E. \quad (I.8)$$

The properties of the interpolation operator $\mathcal{I}_{\mathcal{T}}$ further reduces the inequality to

$$\text{LHS} \leq \sum_{e=1}^{n_{el}} \|\mathcal{R}_{\Omega_e}\|_{\Omega_e} c_1 h_{\Omega_e} \|\hat{w}_h\|_{H^1(\tilde{\omega}_{\Omega_e})} + \sum_{E \in \mathcal{E}} \|\mathcal{R}_E\|_E c_2 h_E^{1/2} \|\hat{w}_h\|_{H^1(\tilde{\omega}_E)}, \quad (I.9)$$

where h_{Ω_e} is the diameter of the element Ω_e , h_E is the length of the edge, c_1 and c_2 are constants which depend upon the shape of the partition \mathcal{T} , and $\tilde{\omega}_{\Omega_e}$ and $\tilde{\omega}_E$ are defined as:

$$\tilde{\omega}_{\Omega_e} = \bigcup_{N_{\Omega_e} \cap N'_{\Omega_e} \neq \emptyset} \Omega'_e, \quad \tilde{\omega}_E = \bigcup_{N_E \cap N'_{\Omega_e} \neq \emptyset} \Omega'_e, \quad (I.10)$$

Appendix I. Residual error estimates for the Allen-Cahn equation

where N_{Ω_e} are the vertices of Ω_e and N_E are the vertices of an edge E . Again, with the help of the Cauchy-Schwarz inequality for the sums,

$$\text{LHS} \leq \max\{c_1, c_2\} \left\{ \sum_{e=1}^{n_{el}} h_{\Omega_e}^2 \|\mathcal{R}_{\Omega_e}\|_{\Omega_e}^2 + \sum_{E \in \mathcal{E}} h_E \|\mathcal{R}_E\|_E^2 \right\}^{1/2} \left\{ \sum_{e=1}^{n_{el}} \|\hat{w}_h\|_{H^1(\tilde{\omega}_{\Omega_e})}^2 + \sum_{E \in \mathcal{E}} \|\hat{w}_h\|_{H^1(\tilde{\omega}_E)}^2 \right\}^{1/2}. \quad (\text{I.11})$$

Moreover, using the shape regularity assumption for the partition \mathcal{T} ,

$$\left\{ \sum_{e=1}^{n_{el}} \|\hat{w}_h\|_{H^1(\tilde{\omega}_{\Omega_e})}^2 + \sum_{E \in \mathcal{E}} \|\hat{w}_h\|_{H^1(\tilde{\omega}_E)}^2 \right\}^{1/2} \leq c \|\hat{w}_h\|_{H^1(\Omega^f(t))}. \quad (\text{I.12})$$

Therefore, for some constant c^* , we obtain the following desired result:

$$\text{LHS} \leq c^* \left\{ \sum_{e=1}^{n_{el}} h_{\Omega_e}^2 \|\mathcal{R}_{\Omega_e}\|_{\Omega_e}^2 + \sum_{E \in \mathcal{E}} h_E \|\mathcal{R}_E\|_E^2 \right\}^{1/2} \|\hat{w}\|_{H^1(\Omega^f(t))}. \quad (\text{I.13})$$

Finally, we use the residual-error equivalence that the norm of the error in \mathbb{V} is bounded from above and below by the norm of the residual in the dual space \mathbb{V}' which is established using the Friedrichs and Cauchy-Schwarz inequalities. Thus, the residual error estimate becomes

$$\|\phi - \phi_h\| \leq c^* \left\{ \sum_{e=1}^{n_{el}} h_{\Omega_e}^2 \|\mathcal{R}_{\Omega_e}\|_{\Omega_e}^2 + \sum_{E \in \mathcal{E}} h_E \|\mathcal{R}_E\|_E^2 \right\}^{1/2} \|\hat{w}\|_{H^1(\Omega^f(t))}, \quad (\text{I.14})$$

which can also be written as

$$\|\phi - \phi_h\| \leq c^* \left\{ \sum_{e=1}^{n_{el}} h_{\Omega_e}^2 \|\mathcal{R}_{\Omega_e}\|_{\Omega_e}^2 + \sum_{e=1}^{n_{el}} \sum_{E \in \mathcal{E}_{\Omega_e} \cap \mathcal{E}} h_E \|\mathcal{R}_E\|_E^2 \right\}^{1/2} \|\hat{w}\|_{H^1(\Omega^f(t))}. \quad (\text{I.15})$$

Let η_{Ω_e} denote the error indicator of the triangular element Ω_e on the mesh. The error estimate can be recast as

$$\|\phi - \phi_h\| \leq \eta = \left(\sum_{e=1}^{n_{el}} \eta_{\Omega_e}^2 \right)^{1/2}, \quad (\text{I.16})$$

$$\eta_{\Omega_e}^2 = h_{\Omega_e}^2 \|\mathcal{R}_{\Omega_e}\|_{\Omega_e}^2 + \sum_{E \in \mathcal{E}_{\Omega_e} \cap \mathcal{E}} h_E \|\mathcal{R}_E\|_E^2, \quad (\text{I.17})$$

where η is the error estimate and η_{Ω_e} is the error indicator for the element Ω_e . The above estimate is utilized to quantify the residual error for the nonlinear adaptive variational partitioned procedure presented in the current study.